Debris-flow erosion and deposition dynamics

SCHÜRCH, PETER

Debris-flow erosion and deposition dynamics

Peter Schürch

A Thesis presented for the degree of

Doctor of Philosophy

Institute of Hazard, Risk and Resilience
Department of Geography
University of Durham
United Kingdom

July 2011

Dedicated to

Maja my wife, who's support was crucial,

and to Fabio, who is such a star.

Debris-flow erosion and deposition dynamics

Peter Schürch

Submitted for the degree of Doctor of Philosophy

July 2011

Abstract

Debris flows are a major natural hazard in mountains world wide, because of their destructive potential. Prediction of occurrence, magnitude and travel distance is still a scientific challenge, and thus research into the mechanics of debris flows is still needed. Poor understanding of the processes of erosion and deposition are partly responsible for the difficulties in predicting debris-flow magnitude and travel distance. Even less is known about the long-term evolution of debris-flow fans because the sequential effects of debris-flow erosion and deposition in thousands of flows are poorly documented and hence models to simulate debris-flow fans do not exist. Here I address the specific issues of the dynamics of erosion and deposition in single flows and over multiple flows on debris-flow fans by terrain analysis, channel monitoring and fan evolution modeling.

I documented erosion and deposition dynamics of debris flows at fan scale using the Illgraben debris-flow fan, Switzerland, as an example. Debris flow activity over the past three millenia in the Illgraben catchment in south-western Switzerland was documented by geomorphic mapping, radiocarbon dating of wood and cosmogenic exposure dating of deposits. In this specific case I also documented the disturbance induced by two rock avalanches in the catchment resulting in distinct patterns of deposition on the fan surface. Implications of human intervention and the significance of autogenic forcing of the fan system are also discussed.

Quantification and understanding of erosion and deposition dynamics in debris flows at channel scale hinges on the ability to detect surface change. But change detection is a fundamental task in geomorphology in general. Terrestrial laser scanners are increasingly used for monitoring down to centimeter scale of surface change resulting from a variety of geomorphic processes, as they allow the rapid generation of high resolution digital elevation models. In this thesis procedures were developed to measure surface change in complex topography such as a debris-flow chan-

nel. From this data high-resolution digital elevation models were generated. But data from laser scanning contains ambiguous elevation information originating from point cloud matching, surface roughness and erroneous measurments. This affects the ability to detect change, and results in spatially variable uncertainties. I hence developed techniques to visualize and quantify these uncertainties for the specific application of change detection. I demonstrated that use of data filters (e.g. minimum height filter) on laser scanner data introduces systematic bias in change detection.

Measurement of debris-flow erosion and deposition in single events was performed at Illgraben, where multiple debris flows are recorded every year. I applied terrestrial laser scanning and flow hydrograph analysis to quantify erosion and deposition in a series of debris flows. Flow depth was identified as an important control on the pattern and magnitude of erosion, whereas deposition is governed more by the geometry of flow margins. The relationship between flow depth and erosion is visible both at the reach scale and at the scale of the entire fan. Maximum flow depth is a function of debris flow front discharge and pre-flow channel cross section geometry, and this dual control gives rise to complex interactions with implications for long-term channel stability, the use of fan stratigraphy for reconstruction of past debris flow regimes, and the predictability of debris flow hazards.

Debris-flow fan evolution on time scales of decades up to ten thousands of years is poorly understood because the cumulative effects of erosion and deposition in subsequent events are rarely well documented and suitable numerical models are lacking. Enhancing this understanding is crucial to assess the role of autogenic (internal) and allogenic (external) forcing mechanisms on building debris-flow fans over long time scales. On short time scales understanding fan evolution is important for debris-flow hazard assessment. I propose a 2D reduced-complexity model to assess debris-flow fan evolution. The model is built on a broad range of qualitative and empirical observations on debris-flow behaviour as well as on monitoring data acquired at Illgraben as part of this thesis. I have formulated a framework of rules that govern debris-flow behaviour, and that allows efficient implementation in a numerical simulation. The model is shown to replicate the general behaviour of alluvial fans in nature and in flume experiments. In three applications it is demonstrated how fan evolution modeling may improve understanding of inundation patterns, surface age distribution and surface morphology.

Declaration

The work in this thesis is based on research carried out at the Department of Geography and Institute of Hazard, Risk and Resilience of Durham University, United Kingdom. No part of this thesis has been submitted elsewhere for any other degree or qualification and it is all my own work unless referenced to the contrary in the text.

Acknowledgements

So I recommended having fun because there is nothing better for people in this world than to eat, drink, and enjoy life. That way we will experience some hapiness along with all the hard work God gives them under the sun. In my search for wisdom and in my observation of people's burdens here on earth, I discovered that there is ceaseless activity, day and night. I realized that no one can discover everything no matter what they claim.

(Book of Ecclesiastes 8:15–17 NLT Study Bible, 2008)

The three years and four months I spent in Durham at the Geography Department and with the people 'of Geography' are amongst the most enjoyable years during my training and career as a geologist so far. The friendly and happy atmosphere made the search for wisdom fun right until the end of my PhD. There was always someone here to give encouragement and expert advice when necessary – I was not alone. For this I owe thanks to many people, not only at the Geography Department, but also to people from Emmanuel Church in Durham, neighbours in Bearpark, and to family, friends and colleagues in Switzerland. I will try to acknowledge the individual contributions here, but please forgive me if I forgot to mention your name explicitly.

My supervisors Alex Densmore and Nick Rosser have been great in challenging my thoughts and gently guiding my research. I value their scientific advice and rigour, which have been crucial for the success of this work. Their support and indestructible humour during fieldwork was much appreciated, as days at Illgraben were long and hot, and the generator heavy. The fact that I am still, as I'm writing this, enjoying my PhD, is very much their merit and how they managed their student.

A special thanks goes to the people at the Swiss Federal Institute for Forest, Snow and Landscape Research (WSL). Brian McArdell facilitated this research in many ways, most importantly by providing access to precious WSL data on debris flows at Illgraben in Switzerland. Catherine Berger was my contact person for many queries I had about Illgraben data, and she patiently and carefully answered all of them. Christof Graf shared his expertise regarding the alarm system with me.

My PhD project involved quite a bit of fieldwork. A large number of people supported me in this in many ways: First of all I want to thank my parents Ernst and Elke, who prepared, maintained, stored and organized all sorts of equipment when needed, and had it ready for me to pick up. Various people let me borrow their car for fieldwork (!!!): Christian Schürch, Alex de Graaf, Marco Quinter, and again my parents. Urs Juon and his colleagues from BSAP Ingenieure AG, Visp, Switzerland, lent me surveying equipment for free, which I otherwise would have had to ship over from the UK. I thank them for trusting me, and for meeting all my last minute requests, often on weekends, this was much appreciated. My hosts at Illgraben, Kurt and Magdalena Baltensperger are acknowledged for letting me stay in their appartment at no cost in my first summer. Later I stayed many times at the house of Silvia and Leander Tscherrig, where I could also deposit equipment between my visits to Illgraben. They also took a great interst in my work and introduced me to the local wine. Hermann Rovina and colleagues let me access their archive with geological reports about the Illgraben fan and provided me with photographs of various debris flows at Illgraben. The land owners, Burgschaft Leuk (Stefan Eggo) and Paul Passeraub (Turtmann), are acknowledged for giving permission for sampling boulders. Stuart Lane let me join the Arolla field trip, which meant I could carry out fieldwork the same time and had a field crew of senior scientists to help me. A number of people came out to Illgraben just to help with fieldwork, this was much appreciated: Vreni and Gerhard Kiefer, Matthias Weil, Brian McArdell, Maja Schürch, and Michael Lim. The support staff in the Geography Department, particularly Mervyn Brown, Samatha Waugh, and the IT people have been a great help with day-to-day problems. I thank Emma Norman for constantly rearranging her fieldwork around my fieldwork schedule.

Thanks to the Sedymont project, led by Fritz Schlunegger, I was able to attend the European Geoscience Union meeting in Vienna in 2009 and the TopoEurope meeting in fall 2010 in Oslo. Also the Sedymont meetings in Leuk were very enjoyable, and discussions with members of the Sedymont team, particularly Georgie Bennet and Fritz Schlunegger, have been very useful in

focusing my ideas. Exposure dating of boulders on the Illgraben fan would not have been possible without the help of Susan Ivy-Ochs, Florian Kober, Vassili Alfimov and Peter Kubik from ETH Zurich. Preparation of wood samples and dating by the radiocarbon lab of the Physical Institute of the University of Bern was facilitated by Fritz Schlunegger and funded by the Swiss National Science Foundation (20T021-120464).

I also owe thanks to all those people who have thoroughly reviewed parts of this thesis: Dave Milledge, Michael Lim, Susan Ivy-Ochs, Florian Kober, Tristram Hales, Jason Kean, Oliver Korup, Nick Cox, Bob Hilton and several anonymous reviewers. I thank M. Imran for preparing the LaTeX template used for this thesis.

Whilst writing my acknowledgements a number of names crossed my mind; probably for a reason, so I shall thank them here for their help (in no particular order): Emma Raven, Tori Milledge, Andreas Vieli and Gwendolyn Vieli-Leisinger, Ed Llwellin, Emma Marsh, Thomas van Stiphout, Dirk Rieke-Zapp, Pat Thee, Pam and Dave Bulman, Edna and Maurice Abbott, Pam and Alan McKendrick, Nick Odoni, Rich Hardy, Chris Stokes, Louise Bracken, Jeff Warburton, Carly Maynard, Claire and Gideon Copestake, Patrice Carbonneau.

Without funding this PhD project would have been impossible, and I owe thanks to a range of institutions for providing support: Fieldwork was funded by a NERC grant NE/G009104/1 and a Royal Geographical Society fieldwork grant. My living expenses were covered by a Durham University Doctoral Fellowship.

Most importantly I want to thank my wife for constant encouragement, for letting me go on field work or to conferences and spending many days away from home and for checking references. My son Fabio was a constant source of joy, irrespective of whether I had a good or bad day at work. Finally I thank my parents Elke and Ernst, who raised me to be curious and perseverant enough to start and finish a PhD.

Contents

List of Figures

List of Tables

Chapter 1

Introduction

1.1 Definition of debris flows

Debris flows are fast, avalanche-like, moving mixtures of water, air, and variable fractions of sediment: silt, sand, gravel, stones and boulders, or even wood (Varnes, 1978). Debris flows initiate from landslides, from entrainment of bed material at times of high discharge or from direct failure of water-saturated sediment in headwater channels (Takahashi, 2007). Debris flows show a behaviour intermediate between shallow landsliding and hyper-concentrated flows, and the flow properties vary with water and sediment content, and sediment size and sorting (Costa and Fleisher, 1984). Although inhabitants of mountain areas were aware of the phenomenona for a long time and had named it in a variety of ways, such as Ja-nuke (The run off of king snake, Japan), Rüfe, Mure or Murgang (Germany, Switzerland, Austria), it was only in the second half of the 20^{th} century that the first photographs and films of debris flows were captured (Costa and Garnett, 1984; Okuda et al., 1977). Only thereafter did formal scientific investigation of the phenomena commence.

1.2 Motivation

Debris flows are a common phenomena and a major hazard in mountainous regions around the world (Bezzola et al., 2008; Jakob and Hungr, 2005; Rickenmann and Chen, 2003; Takahashi, 2007). Devastating events with hundreds of casualities and severe damage to infrastructure in the 19th and 20th century have promoted debris-flow research mainly in Japan, Europa and North

America. As a result, research has often been driven by the necessity to mitigate against this natural hazard.

Research on debris flow mitigation strategies can be grouped into three broad themes.

- How can debris-flow inititation be inhibited, or what measures can be taken to limit event magnitude (e.g. Remaitre et al., 2008; Takahashi, 2007)?
- How can debris flows be retained before they reach vulnerable elements (e.g. Wu and Chang, 2003)?
- How can debris flows be routed safely past vulnerable structures (e.g. Jakob et al., 2004)?

In pursuing these aims, much research effort has been spent on mapping debris flow hazard (e.g. Berti and Simoni, 2007; Griswold and Iverson, 2008), predicting run-out distance (e.g. Cannon, 1989; Rickenmann, 1999, 2005), determining magnitude-frequency relationships (e.g. Hungr et al., 2008; Innes, 1985; van Steijn, 1996; Zimmermann et al., 1997) or debris-flow behaviour modeling (e.g. Arattano and Savage, 1994; Iverson, 1997; Iverson and Denlinger, 2001; Patra et al., 2005; Pudasaini et al., 2005; Takahashi, 2007).

Debris flows are capable of eroding bedrock (Hsu et al., 2008; Stock and Dietrich, 2006) and are therefore regarded as important agents of landscape evolution, leaving a distinct fingerprint in catchments and on alluvial fans (Benda and Dunne, 1997b; Stock and Dietrich, 2003; Whipple and Dunne, 1992). The sedimentary record of debris-flow fans has attained growing interest because of the potential to yield information about temporal changes in the nature and rates of geomorphic processes, past climate and tectonics (Densmore et al., 2007; Dühnforth et al., 2008, 2007; Hornung et al., 2010).

Advances depend on how good understanding is of the fundamental processes of erosion and deposition during debris flows; both, at the local scale of a single channel, and at the scale of a debris-flow fan. Erosion and deposition affect the channel system locally but also control the behaviour of the flow as it continues to travel across topography, due to changes in flow volume (Iverson et al., 2011). The effects of erosion and deposition resulting from a succession of debris flows of varying magnitudes across such spatially and temporally variable topography constitute a complicated and still poorly understood feedback mechanism (Chapter 4).

With this thesis I aim at providing the scientific basis for a better understanding of two key issues: First, the controls on debris flow erosion and deposition, and second, the implications of these findings for debris flow fan evolution over time spans of decades to tens of thousands of years.

Debris flows occuring in mountain areas are often of described as 'granular' because they carry substantial amounts of coarse discrete particles (Berti and Simoni, 2007). In steep tributary valleys and over short distances of only a few kilometers debris flows may entrain large volumes of sediment, which usually leads to overbank deposition when joining the main valley and possibly the devastation of infrastructure or loss of life (Arattano et al., 2010; Scheuner et al., 2009). I focus on these mature and fully established debris flows (Takahashi, 2007) defined by high concentrations of coarse-grained particles that are dominated by Coulomb friction stress (Iverson, 1997) and on the associated landforms such as debris-flow fans, levee-bound channels and depositional lobes (Blair and McPherson, 1998; Major and Iverson, 1999; Whipple and Dunne, 1992). In the next section I review the broader debris-flow literature in the context of the processes of deposition and erosion.

1.3 Current understanding of debris-flow erosion and deposition

Erosion and deposition during a debris flow affect the volume of the current flow and hence the hazard it poses downstream. Alongside this, the channel geometry undergoes change, which changes the boundary conditions for the next flow or flow surge in the same channel. To capture the breadth of the problem, a consideration of a broad range of scales is necessary. I first consider ways to classify debris flows according to their mechanical properties. From there I move on to an overview of work specific to erosion and deposition, followed by a assessment of the lessons from debris-flow models regarding erosion and deposition. Finally, I take a broader perspective and review work relating to the evolution of debris-flow fans.

1.3.1 Classification of debris flows

Debris flows are a process intermediate between a river at high flow (mostly water) and a landslide (mostly sediment). It is useful to define the phenomena of interest in a mechanical sense separating it from these endmembers. Two examples of such a classification are detailed in Iverson (1997) and Takahashi (2007), which I summarize below.

Iverson (1997) identified three key dimensionless parameters to discriminate debris flows from similar related phenomena: the Savage number N_{Sav}, the Bagnold number N_{Bag} and the Darcy number N_{Dar}. The Savage number describes the ratio between inertial shear stress resulting from

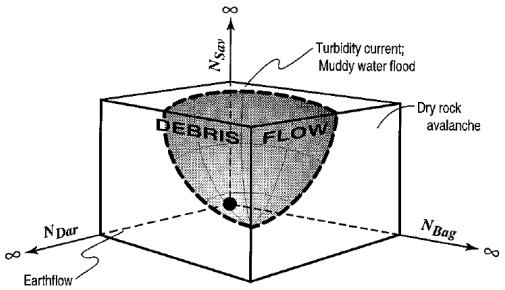

Figure 1.1: *Classification scheme for debris flows based on the Darcy number, N_{Dar}, the Savage number, N_{Sav}, and the Bagnold number, N_{Bag}. The debris-flow domain occupies an imprecisely defined region where the three parameters take intermediate values. The relation between debris flows and other mass movements such as earthflows, rock avalanches and mudflows is also indicated. Figure taken from Iverson (1997).*

grain collisions and the quasi-static shear stress arising from the weight and friction of the granular mass (Coulomb friction):

$$N_{Sav} = \frac{\dot{\gamma}^2 \rho_s \delta}{N(\rho_s - \rho_f) g \tan\phi} \tag{1.1}$$

where γ is shear strain rate, ρ_s and ρ_f are solid and fluid density, δ is representative grain diameter, N is number of grains above channel bed, g is gravitational acceleration and ϕ is angle of internal friction (see also p. 142). In debris flows the Savage number is suggested to be at most ≈ 0.2 (attained from flume experiments in the USGS debris-flow flume), or significantly smaller for larger events (Iverson, 1997), with friction stresses becoming dominant when $N_{Sav} \leq 0.1$. The Bagnold number is defined as the ratio between inertial grain stress and viscous shear stress:

$$N_{Bag} = \frac{C}{1-C} \frac{\rho_s \delta^2 \dot{\gamma}}{\mu} \tag{1.2}$$

where C is bulk sediment concentration and μ is dynamic viscosity of pore fluid with suspended fine sediment. For debris flows Iverson (1997) reports values of $N_{Bag} = 0.2 \ldots 400$. The Darcy number describes to what extent pore fluid pressure buffers grain interactions:

$$N_{Dar} = \frac{\mu}{C \rho_s \dot{\gamma} k} \tag{1.3}$$

Realistic values for debris flows are $\gtrsim 5000$ (Iverson, 1997). The domain of debris-flow occurrence can be understood as an imprecisely defined region (Figure 1.1) where the three parameters N_{Dar}, N_{Sav} and N_{Bag} take intermediate values. Figure 1.1 also highlights the distinction between debris flows and related mass-movement phenomena.

The classification proposed by Takahashi (2007) is similar to that of Iverson (1997) in the sense that it is based on an evaluation of three stresses (turbulent mixing stress, collision stress and viscous shear stress) used in the definition of the Savage, Bagnold and Darcy number and their relative importance. As a fourth component, the coarse sediment concentration is considered. According to this classification a debris flow requires at least a volume fraction of coarse sediment of $\gtrsim 0.2$. Takahashi (2007) distinguished between viscous, stony and muddy debris flows which are characterized by a high relative importance of viscous shear stress, collision stress and turbulent mixing stress respectively. At a coarse particle concentration of 0.2, the denominator of the Savage number (Equation 1.1), the Coulomb friction stress, still plays a negligible role in the total stress. Only when the concentration of coarse particles exceeds 0.5 does a debris flow of quasi-static motion develop (Takahashi, 2007) which is comparable to the flows with $N_{Sav} \ll 0.1$ as described by Iverson (1997). Many observations have confirmed that debris flows develop steep granular fronts (e.g. Costa and Fleisher, 1984; Iverson, 1997; Major and Iverson, 1999; McArdell et al., 2007; McCoy et al., 2010) because large particles on the flow surface travel faster than the body of the flow (Suwa, 1988), and accumulate at the flow front. Beside the difference in coarse sediment concentration between flow front and flow tail, the overall sediment concentration declines towards the flow tail also (McArdell et al., 2007). Iverson (1997) and McArdell et al. (2007) measured low hydrostatic pressures in the flow front compared to the tail. It is therefore evident that values of N_{Sav}, N_{Bag} and N_{Dar} in a debris flow must vary between flow front and tail.

In this work I focus on debris flows with granular fronts containing large clasts and bulk sediment concentrations of more than 0.2. These flows are common in mountain areas such as the Alps (Berti and Simoni, 2007) and they are responsible for building debris-flow fans with characteristic levee-bound channels and depositional lobes. This type of debris flows is very destructive because of the large clasts carried, the steep and high front and the high momentum. These flows fulfill the criteria defined by Iverson (1997) and those defined by Takahashi (2007) for dynamic debris flows with high importance of collisional stress ('stony type'), and for debris flows of quasi-static motion.

1.3.2 Erosion and deposition processes

A debris flow in motion undergoes a two-way exchange of material with its channel in the form of entrainment and deposition, often at the same time. This volume exchange per unit downstream distance (dV/dx) is termed the 'lag rate' (Cannon, 1989). There is overwhelming evidence that

debris flows may grow by several orders of magnitude after initiation as they erode material along the flow path (e.g. Fannin and Wise, 2001; Hungr et al., 2005; Rickenmann and Zimmermann, 1993; Scheuner et al., 2009), before they start to deposit their load. In order to understand sediment transfer in debris-flow systems and the hazard potential of a debris flow prone channel, it is important to investigate controls on lag rate.

Major advances with respect to erosion of bedrock by debris flows have been made by Stock and Dietrich (2006) and Hsu et al. (2008) who recognized that the properties of the granular debris-flow front are crucial in understanding this process. Stock and Dietrich (2006) proposed a bedrock incision law for debris flows based on the inertial stress on the bed by grain–bed impacts. The model predicts debris flows with long and coarse fronts and high shear rates (surface velocity / flow depth) to be most erosive. Hsu et al. (2008), using drum experiments, found a dependence of bedrock incision on grain diameter and to a lesser extent on shear rate of the flow, suggesting that most of wear occurs at the coarse granular flow front. Both suggested that the intensity of grain-bed impacts drive incision. Key parameters identified are grain size and shear rate. Recent spot measurements of entrainment from a bed of unconsolidated sediment have confirmed that erosion primarily takes place during passage of the flow front (Berger, McArdell, Fritschi and Schlunegger, 2010; Berger et al., 2011; Iverson et al., 2011). Results shown in Iverson et al. (2011) suggest that entrainment of unconsolidated sediment is driven by sharp rises in pore water pressure in the bed due to undrained loading induced by the advancing flow front. Where bed saturation is low, this process is shown to be less effective. Results presented in Berger et al. (2011) indicate that erosion starts before pore water pressure rises, but continues until about 20 s after passage of the flow front. The importance of grain-bed impacts for entrainment of unconsolidated bed sediment remains therefore unclear.

The rates of deposition in a debris flow are closely linked to the total travel distance. Deposition becomes progressively more important as channel gradients decrease, leading to a net loss of flow volume (Cannon, 1989; Fannin and Wise, 2001; Hürlimann et al., 2003; Rickenmann, 2005). As long as debris flows remain confined within channels and hence experience small net loss in volume, momentum is conserved and motion sustained at very low slopes (Whipple and Dunne, 1992). The rate of deposition increases dramatically when levee deposition is replaced by lobe formation upon inundating unconfined terrain such as open fan surfaces (Blair and McPherson, 1998). The limits of debris flow deposits are usually well defined since grain segregation

concentrates coarse grains at the deposit margins (Major and Iverson, 1999; Suwa, 1988) where Coulomb friction dominates (Iverson and Vallance, 2001). Several researchers have suggested that, beside the topographic boundary conditions, mobility and hence location of deposits is also influenced by properties of the flow itself such as granular temperature (defined as the mean square of particle velocity fluctuations, see Equation 1.13, Iverson, 1997; Iverson and Vallance, 2001), excess pore fluid pressure (McCoy et al., 2010) and sediment concentration (Takahashi, 2007). The time-dependent prediction of these state variables is suggested to be essential in understanding deposition, but poses a major challenge (Iverson and Vallance, 2001).

An important outcome from this review is that composition and shape of the flow front are critical for erosion and deposition. This is important for the analysis in Chapter 4 and the model development in Chapter 5.

1.3.3 Modeling debris flows

Flow depth, shear stress, granular temperature, sediment concentration and pore fluid pressure are important in understanding erosion and deposition. As debris flows are fluid-solid mixtures, a physically based derivation of these parameters is not simple; recently developed debris-flow models provide some guidance. These models fall in one of the following three broad categories: continuum constituent, discrete particle and empirical models. Continuum constituent models describe the debris mixture as a continuum using Eulerian forms of the continuity and momentum equations (e.g. Iverson, 1997; Iverson and Denlinger, 2001; Pudasaini et al., 2005). These models can be used to make predictions about shear stress at the flow base and within the flow body, pore fluid pressure and flow depth. The description of individual particles of granular flows allows detailed insights into the flow dynamics (Hill et al., 2003). Discrete particle models (e.g. Gray and Kokelaar, 2010) adopt this Lagrangian view and are capable of reproducing the naturally observed grain seggregation during debris-flow motion and observed grading patterns in the deposits (Costa and Fleisher, 1984; Major, 1997; Suwa, 1988) by solving the segregation equation first introduced by Savage and Lun (1988). Although these models give very detailed insight at a small scale, they require long computing times (Dalbey et al., 2008; Takahashi, 2007), which makes debris-flow modelling over large domains (e.g. a debris-flow fan) and over multiple events difficult. In addition to these approaches, a great variety of empirical and semi-empirical debris-flow models have been published (e.g. Berti and Simoni, 2007; Griswold and Iverson, 2008; Iverson et al.,

1998; Rickenmann, 1999, 2005) to predict bulk debris flow behaviour, such as peak discharge, runout or front velocity.

In the following sections, I introduce the mass and momentum conservation equations for debris flows, which form the physical basis of many debris-flow models. I assess which models are useful in predicting sediment concentration, shear stress, granular temperature, pore fluid pressure and flow depth.

Mass and momentum conservation equations for debris flows

The equations for mass and momentum conservation are the basis of many debris flow models (Arattano and Savage, 1994; Iverson, 1997; Iverson and Denlinger, 2001; Patra et al., 2005; Pudasaini et al., 2005). Depending on the specific application they are formulated for a single- or two-phase continuum. As an example, I show the equations formulated for a two-phase constituent model for general reference (Iverson, 1997). In this case the equations are formulated for a unit volume. Indices s and f stand for the solid and fluid phase respectively.

Mass conservation

$$\frac{\partial(\rho_s C)}{\partial t} + \nabla \cdot (\rho_s C u_s) = m_s \tag{1.4}$$

$$\frac{\partial(\rho_f (1-C))}{\partial t} + \nabla \cdot (\rho_f (1-C) u_f) = m_f \tag{1.5}$$

where m_s and m_f are the rates of solid or fluid mass addition per unit volume, u_s and u_f are the solid and fluid velocities and t is time (see also p. 142). Equations 1.4 and 1.5 are coupled by the sediment concentration C and can be added to gain a formula for the mixture. Incompressibility of the solid and fluid can usually be assumed, therefore the first term in Equations 1.4 and 1.5 can be neglected.

Momentum conservation

$$\rho_s C(\frac{\partial u_s}{\partial t} + u_s \cdot \nabla u_s) = \nabla \cdot T_s + \rho_s C g + F_i \tag{1.6}$$

$$\rho_f (1-C)(\frac{\partial u_f}{\partial t} + u_f \cdot \nabla u_f) = \nabla \cdot T_f + \rho_f (1-C) C g - F_i \tag{1.7}$$

where T_s and T_f are the solid and liquid phase stress tensors, and F_i is the interaction force between solid and fluid constituents.

Sediment concentration

Bagnold (1954) made fundamental observations for our understanding of granular flows and Takahashi (2007) investigated the controls on sediment concentration of debris flows in flume experiments. Debris flows with considerable fractions of coarse particles often show high mobility and run over slopes as gentle as 4° before stopping. The reason for this behaviour has been identified as the separation of the coarse particles by a supporting mechanism (Takahashi, 2007). At high concentrations of coarse particles (> 0.5), excess pressures in the interstitial fluid cause this effect. However, at lower concentrations of coarse particles only the repulsive forces of grain-to-grain collisions and turbulence within the flow appear capable of supporting grains in such a manner. Bagnold (1954) was the first to describe and measure the particle collision stress p_c in an experiment with neutrally buoyant spheres ($\rho_s = \rho_f$) within a liquid. He found that the shear stress, τ_c, was proportional to the square of the shearing rate λ if a uniform grain distribution was assumed (see p. 142 for notation):

$$p_c = \alpha_i \cos\alpha_i \rho_s \lambda^2 d_p^2 (\frac{du}{dz})^2 \tag{1.8}$$

where α_i is the collision angle of grains, and $\frac{du}{dz}$ the velocity gradient perpendicular to the bed. Bagnold (1954) repeated his experiments for a range of grain concentrations between 13.5% and 62.3% and found consistently that:

$$\frac{\tau_c}{p_c} \approx \tan\alpha_i \approx 0.32 \tag{1.9}$$

However, Iverson and Vallance (2001) emphasized that experiments by Bagnold (1954) do not prove that $\tau_c \propto (\frac{du}{dz})^2$ when grains are not neutrally buoyant (e.g. in a debris flow). Nevertheless one important outcome of this view of granular flows was the dilatant fluid model and a definition of the maximum sustainable coarse particle concentration (equilibrium concentration) C_∞ as a function of bed slope S and angle of internal friction ϕ, which has also been confirmed by experimental results (Takahashi, 2007):

$$C_\infty \equiv \frac{\rho_f S}{(\rho_s - \rho_f)(\tan\phi - S)} \tag{1.10}$$

This is an interesting result because it predicts that the equilibrium concentration decreases

with slope, and it implies that debris flows have to deposit coarse material (e.g. in the form of levees) when they reach lower slopes. Many field observations are compatible with this prediction (e.g. Blair and McPherson, 1998; Kim and Lowe, 2004; Whipple and Dunne, 1992). I will use the concept of maximum sustainable sediment concentration in the modelling (Chapter 5).

Shear stress

The shear stress in the flow can be investigated using Equations 1.6 and 1.7. Addition of these equations yields a momentum conservation equation for the bulk mixture and eliminates the complex interaction forces. In the simpler case of a steady uniform flow where the relative velocity between solids and fluids is neglected, the stress-balance equation becomes (Takahashi, 2007, and references therein)(notation see p. 142):

$$T_s + T_f = g \sin\theta \int_z^h \rho_b dz \tag{1.11}$$

where T_s and T_f are the shear stresses in the solid and liquid phases and $\rho_b = (\rho_s - \rho_f)C + \rho_f$ is the bulk density of the bulk mixture. By integrating over the flow depth h the total shear stress at the base of the flow becomes simply:

$$\tau_b = T_s + T_f = \rho_b g h \sin\theta \tag{1.12}$$

where h is measured perpendicular to the bed. Debris-flow monitoring at Illgraben, Switzerland over several events, showed that basal shear and normal stresses maintain a constant ratio of $\tau_b/\sigma \approx 0.1$ in a straight channel section with a slope of $S = \sin(5^\circ) \approx 0.1$ (e.g. Berger et al., 2011; McArdell et al., 2007). This result is a strong support for Equation 1.12.

For large mass movements (Volume $> 10^7$ m^3) Dade and Huppert (1998) suggest that upon failure the initial resisting stress (which leads to failure of the mass) drops approximately to the yield strength (i.e. the final resisting stress after deposition) which can be estimated after deposition in the field (Costa and Fleisher, 1984; Whipple and Dunne, 1992). This implies that the debris mass deforms in a purely plastic manner with a near constant shear stress in the proposed range of 10-100 kPa (Dade and Huppert, 1998).

Because I am considering smaller total volumes I will use Equation 1.12 to estimate basal shear stress in the interpretation of monitoring results in Chapter 4 and in the formulation of a debris-flow model in Chapter 5.

Granular temperature

Iverson (1997) explained granular temperature as a measure of grain agitation that results from bulk deformation of the flowing mass. The total velocity of grains in a debris flow can be described as the sum of the mean velocity and a fluctuating component: $v = \bar{v} + v'$. When granular temperature is defined as twice the kinetic energy due to velocity fluctuations (in analogy to gases) per unit mass of granular solids, it can be written as:

$$T = \left\langle v'^2 \right\rangle = \left\langle (v - \bar{v})^2 \right\rangle \tag{1.13}$$

where the angle brackets stand for a limited spatial and temporal average. Higher granular temperature results in a reduction in bulk density and enhanced mobility whereas a reduction would have the opposite effect (Iverson, 1997). For a uniform granular flow in an experimental flume with an erodible bed, Armanini et al. (2008) showed that granular temperature is largest at the flow surface, where the flow is in the collisional regime. Under the assumption that locally produced kinetic energy is locally dissipated by particle collisions, granular temperature is proportional to the square of the shear rate (Armanini et al., 2008). It remains unclear how granular temperature can be estimated from measurable quantities in a natural debris flow.

Pore fluid pressure

Many researchers have found that pore fluid pressure in debris flows is higher than hydrostatic pressure (Iverson, 1997; McArdell et al., 2007; McCoy et al., 2010). This excess fluid pressure results from the interaction of granular solids and the fluid. The total fluid pressure can be written as:

$$p_t = p_h + p_e = \rho_f g h \cos\theta + p_e \tag{1.14}$$

where p_e is the excess fluid pressure and p_h the hydrostatic pressure. So far no straight-forward method of estimating p_e has been found. For the calculation of p_h usually a fluid density $\rho_f > 1000$ kg/m^3 is used due to the suspended load increasing the fluid density. However, p_e can be inferred through simultaneous measurement of flow depth and basal total fluid pressure p_t. McArdell et al. (2007) estimated values for p_e of up to 6 kPa under the assumption of $\rho_f = 1100$ kg/m^3 or up to 3 kPa for $\rho_f = 1300$ kg/m^3 and a maxium flow depth of $\approx$1 m. Excess pore fluid pressure arises

when a flow is in the grain-inertial regime dominated by grain collisions, which is the case when the Savage number (see Equation 1.1) is small ($N_{sav} < 0.1$) (McArdell et al., 2007).

Flow depth

To predict flow depth (or more generally the flow hydrograph) for different locations along a debris flow path, empirical, semi-empirical and numerical models have been employed. Some of the methods used for modelling debris flows today have originaly been developed for volcanic mass flows (lahars). The semi-empirical model proposed by Iverson et al. (1998) provides a quick way of estimating the cross sectional area of the flow A from the total volume V. It is based on a dimensional analysis which requires that $A \propto V^{2/3}$. It is further assumed that the hydrographs of lahars (or debris flows) can be approximated by a triangular shape, that mass and density remain constant and that the propagation velocity follows $u \approx \sqrt{gh_r}$, where h_r is the hydraulic radius. From this Iverson et al. (1998) showed that a power-law relationship exists between flow cross sectional area and flow volume:

$$A = \varepsilon V^{2/3} \tag{1.15}$$

ε is assumed to be constant and can be calibrated for data sets of total flow volumes and cross sectional areas (Berti and Simoni, 2007; Griswold and Iverson, 2008; Iverson et al., 1998). However, it is important to remember that Equation 1.15 does not account for downstream attenuation of the hydrograph and hence provides a conservatively large estimate of the cross sectional area of the flow front. Values calculated with Equation 1.15 can then be used to estimate the flow depth in a given channel cross section. To estimate flow depth, a flow surface geometry has to be assumed – the simplest choice would be a horizontal flow surface (see Chapter 5). Then flow surface and channel cross section can be intersected so they enclose the flow cross section area estimated with Equation 1.15.

Alternatively the evolution of the flow hydrograph can be assessed with numerical or analytical models that solve the mass and momentum balance equations (Section 1.3.3). These methods become progressively more computationaly intensive as fewer simplifications are made. The kinematic wave approximation (Arattano and Savage, 1994) provides a 1D analytical solution for debris flows traveling in steep channels with an initial triangular shape (vertical front followed by a tail of defined length). It can be used to predict the evolution of the flow hydrograph as a function

of travel distance. The model explicitly does not account for changes in bed slope, erosion or deposition. Because of the underlying assumptions this model also does not predict travel distance. An alternative implementation of the kinematic wave approximation (Takahashi, 2007) accounts for temporal storage of debris flow material in a stagnation area near the channel. Arattano and Franzi (2010) extended the kinematic model to include diffusive effects in the momentum equation. For cases where the assumption of no erosion nor deposition is justified, predicted and observed hydrographs are in reasonable agreement (Arattano and Franzi, 2010; Arattano and Savage, 1994; Takahashi, 2007).

A much improved prediction of flow depth (and velocity) is possible when solving the mass and momentum conservation equation and when modeling is performed over natural, 3D terrain (Christen et al., 2010; Iverson and Denlinger, 2001; Patra et al., 2005; Pudasaini et al., 2005). These approaches however, rely on computer-intensive numerical solutions to Equations 1.4 to 1.7.

1.3.4 Evolution and morphology of debris-flow fans

In this section I discuss the current understanding of evolution and morphology of debris-flow fans. Little has been published on physical or numerical modeling of debris-flow fans. Nevertheless, insights gained from numerical modeling of alluvial fans may be valuable to identify common problems and potential differences between debris-flow and alluvial fans. Generally speaking the sudden change in flow confinement triggers deposition and hence fan formation, where tributary streams join higher-order valleys or when reaching the front of a mountain range (Bull, 1977). The boundary conditions for these two settings, tributary junction and mountain range front, are different. Fans evolving at tributary junctions are limited in their growth by the width of the higher-order valley. Upon reaching its maximum size, the fan toe will start to be eroded by the higher-order stream, which in flume experiments and in numerical models results in incision on the fan (Clarke et al., 2010; Nicholas and Quine, 2007a). At this point the further evolution is not only a function of the catchment delivering sediment and water to the fan, but also of the transport capacity of the higher-order stream (e.g. Schlunegger et al., 2009). The radial growth of fans evolving at mountain range fronts is not usually limited by space constraints. Over time scales of millions of years generation of accommodation due to subsidence inhibits radial fan growth (e.g. Densmore et al., 2007). Subsidence may result from a combination of tectonic deformation along the mountain front and isostatic and flexural adjustment of the crust due to loading. Fans

formed in alpine valleys since the beginning of the quaternary have short life spans due to frequent glaciations, and therefore the subsidence can be neglected. For the rest of this section I focus mainly on results from studies that neglect the generation of accommodation. I now consider three aspects of fan morphology: fan slope, avulsion frequency and fan head incision.

Environmental controls on fan slope

Many researchers have been curious about the links between fan slope and properties of the catchment, climate and transport processes (Bull, 1962, 1977; Clarke et al., 2010; Densmore et al., 2007; Harvey, 2002; Milana and Ruzycki, 1999; Schumm et al., 1987; Stock et al., 2008; Whipple et al., 1998). Fan slope is a common morphologic measure reported for fans in different settings and from flume experiments. Fan slope is easily measured in the field, from topographic maps or digital elevation models (DEMs). Average fan slopes are measured between a point close to the fan apex and the toe. However, fan long profiles are often not straight (Bull, 1977; Stock et al., 2008; Whipple et al., 1998). For many natural and experimental fans, long profiles are concave-up (Kim and Lowe, 2004; Stock et al., 2008; Whipple et al., 1998), which implies a downslope decline in slope. Whipple et al. (1998) found in long profiles of experimental fans a difference between bedload- and suspension-dominated fans. For suspension-dominated fans long profiles were convex-up in the upper part of the fan, and concave-up in the lower part of the fan.

The controls on fan slope have been studied in several experiments, which consistently showed that average fan slope increases with increasing sediment concentration of the input flux (Schumm et al., 1987; Whipple et al., 1998). In three experiments by Clarke et al. (2010) sediment to water ratio was held constant but the total discharge of the sediment-water mixture was doubled in each experiment. They found a decreasing fan slope with increasing discharge. In all experiments fan slope was either measured when sediment input equalled sediment output (Clarke et al., 2010) or when fan slope reached steady state under conditions of raising base level (Whipple et al., 1998). In a numerical model by Densmore et al. (2007) sensitivity of fan slope to perturbations in precipitation and uplift rate in the catchment was explored. The catchment was transport limited and the fan slope was assumed to be uniform, but accommodating all sediment efflux from the catchment. Densmore et al. (2007) found that fan slope decreased with increasing precipitation rate and increased with increasing uplift rate of the catchment relative to the basin. All of these experiments focused on fluvial sediment transport.

Milana and Ruzycki (1999) found that fans in arid regions are generally steeper than fans in humid regions for any given catchment area. If flood discharge in arid regions has generally higher sediment concentrations because sediment accumulated in the catchment is removed less frequently, then results shown by Milana and Ruzycki (1999) would be compatible with the findings of Schumm et al. (1987) and Whipple et al. (1998). Bull (1962) and Harvey (2002) show that fan slope decreases with increasing catchment area and suggest a relationship of the form $S = aA_c^{-b}$, where S is slope, A_c is drainage area and a, b regression coefficients. There is some debate whether this observation is an artefact resulting from concave-up long profiles (Stock et al., 2008). If drainage area A_c can be considered as a proxy for discharge, then this result would support the findings of Clarke et al. (2010) (decreasing fan slope with increasing discharge at constant sediment concentration, see above). As a whole, experimental and field evidence suggests that alluvial fan slope increases with increasing sediment concentration and decreasing total discharge. I am unaware of any studies considering specifically debris-flow fan slope. Tsai (2006) performed small flume experiments of debris flows with volumes of up to 50,000 cm^3 to investigate deposit geometry of single events. Unfortunately the authors do not report resulting fan slopes, and because only single flows were investigated an extrapolation to the fan scale is difficult.

Avulsion frequency

On fans the direction of the main flow and hence the location of deposition changes frequently, compared with the active lifespan of the fan. This process is called (channel) avulsion. On alluvial fans there is evidence from natural examples (Törnqvist, 1994) and experiments (Bryant et al., 1995; Reitz et al., 2010) that avulsion frequency increases with sedimentation rate. In alluvial systems in- and near-channel sedimentation leads to increasing superelevation of the channel above the neighboring fan surface, which promotes switching of flow into new (or previously-abandoned) channels (Bryant et al., 1995; Jerolmack and Paola, 2007). Field (2001) also recognized the role of small depositional flood events in setting the stage for a major avulsion. He proposes a mechanism by which channels gradually fill so that at some point only a minor fluctuation in sedimentation results in breeching of channel levees and establishment of a new flow path (see also examples in: Bryant et al., 1995; Clarke et al., 2010). Reitz et al. (2010) suggest that a characteristic avulsion period (i.e. the time between avulsion events) can be estimated as the time needed to fill a typical

channel of depth h, length $r(t)$ and width B at a given sediment input flux Q_s:

$$T_A(t) = hBr(t)/Q_s \tag{1.16}$$

While experimental results cited above described the mechanics of avulsion in systems under constant sediment feed, case studies highlight also the importance of the sequencing of events in increasing or reducing the probability of avulsion in the near future by systematically changing channel morphology (Field, 2001). On debris-flow fans sedimentation is a more stochastic, spatially concentrated process. Debris flows may come to a sudden halt and form elongated in-channel, plug-like deposits (Dühnforth et al., 2007; McCoy et al., 2010; Whipple and Dunne, 1992). Sudden in-channel deposition may then lead to abandonment of this flow path before the channel is filled from fan toe to apex (Whipple and Dunne, 1992). Therefore the frequency of avulsion events on debris flow fans might be more related to the probability of sudden stopping of flows, which probably depends on the time-dependent values of state variables such as granular temperature and pore fluid pressure (see section 1.3.2; Iverson, 1997; McCoy et al., 2010), as well as sediment concentration (Takahashi, 2007). Triggers of avulsion and their frequency of occurrence are important for the resurfacing of the fan, the age of fan lobes (Chapter 2), and for the hazard assessment on debris flow fans (Chapter 5).

Fan head incision

Fan head incision is a well documented feature of alluvial and debris-flow fans (Davies and Korup, 2007; Dühnforth et al., 2008; Harvey, 1984, 2002, and references therein) resulting in a cessation in deposition over large fractions of the fan surface (Dühnforth et al., 2007). Fan head incision on natural fans has been linked to external forcing in the form of changing base level (Harvey, 2002), changes in sediment supply (Dühnforth et al., 2008; Harvey, 1984), tectonic uplift at normal faults (Bull, 1977) or infrequent extreme events such as rock avalanches or landslides (Davies and Korup, 2007; Korup, 2004). However, case studies as described above, often provide only a snapshot of the morphology of a fan at a point in time. The picture is therefore always incomplete and it is impossible to say how a particular fan would have evolved in the absence of the described external forcing.

Physical modeling of alluvial fans shows that the patterns of inundation and deposition change in a systematic way over the lifespan of the fan (Jerolmack and Paola, 2007; Reitz et al., 2010). Kim and Jerolmack (2008) observed in flume experiments of fan deltas under constant sediment flux cycles of sheet flow with widespread deposition and times of channelization and incision. Whilst sheet flow resulted in a steeper fan slope, this was compensated by channelization and transfer of sediment from the fan to the fan margin, and hereby lowering of fan slope. Clarke et al. (2010) found a consistent sequence of four stages of fan development described as sheetflow dominated (stage 1), unstable channelised (stage 2), lateral channel migration (stage 3) and single channel (stage 4) in absence of changes in sediment or water input or change in base level. By the time stage 4 was reached, the fan toe had grown to the maximum possible lateral extent defined by a circular drainage channel marking the downstream model boundary. In a similar experiment Reitz et al. (2010) reported repeated cycles of fan channelization, channel backfilling from fan toe to fan head followed by an avulsion and widespread flooding and deposition on the fan in absence of external forcing. Clarke et al. (2010) propose that these cycles are controlled by a self-regulating feedback between incision and entrainment at steeper slopes resulting in a decrease in channel slope and channel backfilling resulting again in steepening.

Autogenic processes, as described above, can produce similar morphologies to external forcing such as changes in precipitation rate or rock uplift rate. But the response of an alluvial fan to external forcing is thought to be much slower than the frequency of autogenic fluctuations when assuming reasonable rates of change in external forcing (Densmore et al., 2007; Kim et al., 2006). Jerolmack and Paola (2010) propose that sedimentary systems only transmit variations in the input signal to the output signal under certain conditions defined by a minimum duration and event magnitude scale. Disturbances of shorter duration and smaller magnitude are obliterated by the autogenic variation. This means that only because a signal is detected in the stratigraphic record it does not mean that it is due to external forcing, and vice versa external forcing might not always be recorded by the sedimentary record.

Understanding the controls on and time scales of fan head incision has practical implications for the hazard on debris flow fans, because the more pronounced the incision, the less likely a catastrophic avulsion becomes (Chapter 2 and 5; Davies and Korup, 2007; Scheuner et al., 2009). Fan head incision has also implications for the role of fans as storage elements in a sediment routing system (Chapter 2, 4 and 5), because fan head incision promotes down-fan routing of sediment (Clarke et al., 2010; Kim and Jerolmack, 2008).

1.4 Research questions and road map

The main aim of this thesis is to enhance the understanding of erosion and deposition in debris flows at different spatial and temporal scales. In pursuing this aim I address the following specific areas of research:

Q1: How can the dynamics of debris-flow erosion and deposition be documented at the scale of an alluvial fan; what can be learned from the pattern of deposits and channels on a debris-flow fan with regard to the evolution of the fan?

Q2: How can debris-flow erosion and deposition be measured in sufficient spatial and temporal resolution to allow for a meaningful analysis of the underlying processes? What are the optimal field procedures to measure geomorphic change in debris-flow channels?

Q3: Can a robust proxy for the prediction of erosion and deposition in debris flows be established?

Q4: Can this proxy be used to formulate a model for debris-flow fan evolution? How can observations on the behaviour of single flows be implemented to simulate thousands of debris flows?

Q5: What are the implications for fan evolution under the assumptions of the proposed model? How can the interaction of individual flows with the fan environment be understood as the result of repeated erosion and deposition in thousands of flows?

The chapters of this thesis are structured as research papers. I briefly outline the logical connections between and the content of each paper. In Chapter 2 I introduce the field site at Illgraben, Switzerland, which provides a unique natural laboratory for debris-flow research because of frequent debris flows, an extraordinary set-up of monitoring devices (Badoux et al., 2008; McArdell et al., 2007) and a large fan which retains traces of past debris flows. The chapter documents the geomorphology of the Illgraben catchment and debris-flow fan, provides temporal constraints on channel bed fluctuations in the catchment and on debris-flow deposition on the fan, and closes with a conceptual model for fan evolution over the last three millenia, addressing research question Q1. The Illgraben debris-flow fan as the example investigated in this thesis, is the result of thousands of debris flows dynamically interacting with their environment through deposition and

erosion. Understanding a debris-flow fan requires an understanding of the underlying process in the form of the individual flow event. Investigation has to be undertaken at a scale small enough to be meaningful for the fundamental processes of deposition and erosion but also large enough to be meaningful at the scale of a debris-flow fan, otherwise the connection between the two is impossible.

In Chapter 3 I develop the methodology to monitor debris-flow erosion and deposition with high resolution at the scale of a channel reach of 300 m length using terrestrial laser scanning (TLS) (Q2). It is monitoring at this scale that is necessary to see variation in flow behaviour with changing channel geometry, which can then be linked to data at the fan scale. The focus in Chapter 3 lies on field procedures, handling of point cloud data, sources of error in TLS and error propagation. Special attention is paid to issues arising from complex topography and when dense point cloud data are used to generate digital elevation models (DEM) for detection of surface change. Measurement of surface change is a fundamental task in geomorphology, and the development of surveying techniques such as terrestrial laser scanning also require the development of new methods for error analysis. Therefore I conclude Chapter 3 with a widely applicable model to estimate volumetric uncertainty in change detection.

In Chapter 4 I address Q3 by investigating erosion and deposition at the level of single debris flows, and interpret two complementary data sets on erosion and deposition in debris flows from Illgraben. The first data set consists of high-resolution data on erosion and deposition acquired following the procedures outlined in Chapter 3 from the 300 m study reach at Illgraben of four debris flows. Second I present a comparison of debris-flow volumes calculated from stage measurements near the fan apex and at the toe of the fan for a sequence of 14 events. This second data set allows estimation of total volume change of flows as they traverse the fan. The two data sets, because collected at two complementary spatial scales covering multiple events, are then used to formulate a conceptual model of the evolution of debris-flow channels and fans over sequences of multiple flows. From the data a proxy for debris-flow erosion and deposition is suggested that is used in Chapter 5 to inform a numerical fan evolution model.

In Chapter 5 I outline the conceptual basis for a debris-flow fan evolution model that extrapolates observations from single flows such as data shown in Chapter 4 but also empirical observations from other researchers to the scale of a debris-flow fan (Q4). I then validate the model against independent data on fan evolution. Possible answers to Q5 are explored in Chapter 5 in

applications of the fan evolution model. I demonstrate how my model may be used to learn from the behaviour of thousands of flows about the characteristics of different stages of debris-flow fan evolution, and how the behaviour of single flows may be described in a probabilistic sense. In Chapter 6 I summarize the findings of this thesis, and I conclude with an assessment of potential avenues for future research following on from my own findings.

Chapter 2

Post-glacial fan evolution and sediment storage in an alpine debris-flow catchment

Abstract

[1] Over the Holocene, Alpine sediment routing systems have experienced dramatic changes in sediment availability in response to climate fluctuations and stochastic sediment input by landslides and rock avalanches. External forcing mechanisms operate in parallel to autogenic cycles of sediment storage and release. Whilst in flume experiments autogenic forcing can be studied by controlling external forcing, in field studies the accurate description of external forcing is crucial to assess the long-term system behaviour. In this chapter I document the post-glacial evolution of a debris-flow catchment and fan system at Illgraben, Switzerland, perturbed by rock avalanches. Rock avalanches exert a significant geomorphic impact on the landscape by inducing changes in base level, setting sediment supply, and regrading stream profiles. With the application of terrain analysis, radiocarbon dating of wood, cosmogenic ^{10}Be and ^{36}Cl exposure dating of deposits, I constrain the temporal evolution of the sediment routing system in the catchment and on the fan during the past 3,000 yr. I identify a rock-avalanche deposit near the fan apex and demonstrate how sediment was impounded upstream. I illustrate the downstream shift of the fan apex position upon breaching of the rock-avalanche dam and the subsequently altered pattern of deposition across the fan surface.

[1] This chapter is in preparation for submission to the *Swiss Journal of Geosciences*

2.1 Introduction

Landslides and rock avalanches are significant sources of sediment in mountain belts (Davies and Korup, 2007; Hovius et al., 1997; Korup et al., 2007, 2010; Malamud et al., 2004), and can have both an instant and longlasting impact on landscape and society (e.g. Dunning et al., 2007; Heim, 1882, 1932). More specifically landslides and rock avalanches exert strong external forcing on channel networks and alluvial fans through sediment retention upstream of landslide deposits and release to downstream portions of the sediment routing system (Davies and Korup, 2007; Korup, 2004; Lee et al., 2009; Pratt-Sitaula et al., 2004; Schürch et al., 2006). From flume experiments it is known that autogenic forcing on alluvial fans complicates the analysis of external forcing (Jerolmack and Paola, 2010; Kim and Jerolmack, 2008; Kim et al., 2006; Nicholas and Quine, 2007b; Whipple and Dunne, 1992). It is therefore clear that advances in understanding the role of autogenic forcing is only possible by thorough documentation of external forcing in order to separate respective responses from each other. In this chapter I contribute to this by presenting a case study of a debris-flow catchment and fan, where I constrain the response to external forcing over the last three millenia.

At Illgraben, Switzerland (Figure 2.1A), a rock avalanche blocked the outlet of the debris-flow prone catchment. The focus of this chapter is neither the mechanics nor the trigger of the rock avalanche; instead I document the temporal evolution of the sediment routing system in response to this rock avalanche in the context of continuous debris-flow activity. I employ geomorphic field mapping of the catchment and the fan, detailed terrain analysis aided by a high-resolution digital elevation model derived from airborne LiDAR, reconstruct fan apex migration, and apply various dating techniques to constrain terrace, rock avalanche and debris-flow deposition ages.

In the rest of the introduction I discuss published work regarding the geomorphic impact of rock avalanches, work on sediment storage and evacuation behind rock avalanche dams and in debris-flow catchments as well as depositional patterns on debris-flow fans. I conclude this with a review of the local geology, geomorphology and time frame of deglaciation of the study site.

2.1.1 Geomorphic impact of rock avalanches

Korup et al. (2010) and Hewitt et al. (2008) grouped the geomorphic effect of rock avalanches and landslides into impact on catchment size and shape, valley-floor morphology and sediment delivery or retention. For time scales of a few millenia, the second and third types of impact are

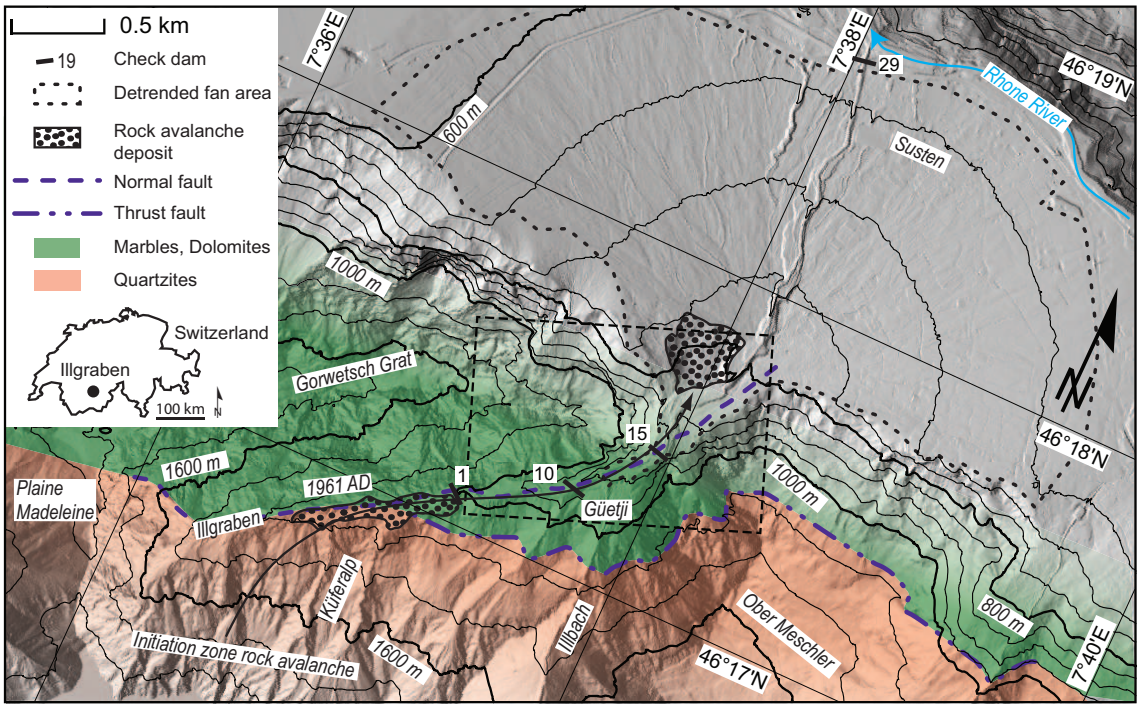

Figure 2.1: *Map of the Illgraben catchment and debris-flow fan in south-western Switzerland. The Illbach joins the Illgraben 0.5 km upstream of the fan apex. Geology and fault traces are adapted from Gabus et al. (2008). Contour interval on fan is 50 m up to the 1,000 meter contour, and 200 m above. Locations and numbers of check dams referred to in the text, are indicated on the map. Check dam 1 was built to stabilize the deposit of the rock avalanche that occured in 1961. A second rock avalanche deposit is indicated near the fan apex; its age is discussed in the text. The source area of this rock avalanche is suggested to be to the west of Küferalp (see text). Dashed box outlines extent of Figure 2.3. Digital elevation model DTM-AV©2011 published with permission from Swisstopo No: 5704 000 000.*

most relevant. Landslide or rock avalanche deposits are responsible for damming streams or rivers and storing sediment (e.g. Bonnard, 2004; Dunning et al., 2007; Hewitt et al., 2008; Lee et al., 2009; von Poschinger, 2005). Depending on the porosity, seepage, size and erodibility of the deposits, and the discharge of the dammed river, these dams and associated lakes can be transient features with lifetimes that span from days or months (e.g. Buzza di Biasca, southern Swizerland; Hattian Bala, Pakistan; Wenchuan earthquake, Sichuan Province, China; Bonnard, 2004; Dunning et al., 2007; Xu et al., 2009) to millenia (e.g. Flims, Eastern Switzerland, von Poschinger, 2005). The pulverization of the rock mass in the initial phase of failure and compaction when the rock avalanche stops, often results in deposits of low permeability (Hewitt et al., 2008). The failure of the debris dam is often catastrophic and may lead to loss of human lives (e.g. Buzza di Biasca, breached 20 months after emplacement on 20 May 1515, with 600 fatalities; Bonnard, 2004), widespread rapid downstream aggradation in valley floors (Korup, 2004; von Poschinger, 2005), channel avulsion (Korup, 2004) and deposition of distinctive sediment layers in distant lakes (e.g.

deposits in Lake Constance from the Flims rock slide, von Poschinger, 2005; Wessels, 1998). In regions where rock avalanches occur frequently, the disturbance of sediment transport and storage becomes a permanent feature of the system (Hewitt et al., 2008). On a smaller scale fluctuations in sediment storage and release due to rock avalanches and landslides have been linked to fan head trenching at the catchment outlet. Davies and Korup (2007) showed in flume experiments that infrequent sediment input caused aggradation and steepening of the fan head, followed by fan head incision when sediment flux declined subsequently. Fan head trenching may also result from other mechanisms such as autogenic processes (Clarke et al., 2010; Kim and Jerolmack, 2008; Kim and Muto, 2007; Kim et al., 2006; Nicholas and Quine, 2007b; Whipple et al., 1998) or sediment trapping due to glacial overdeepening during glaciations (Dühnforth et al., 2008).

2.1.2 Sediment storage and evacuation by debris flows

Many studies have found that debris flows are efficient at entraining sediment from low-order channels and conveying it farther downstream (Chapter 4; Benda and Dunne, 1997a; Berger, McArdell and Schlunegger, 2010; Berger et al., 2011; Fannin and Wise, 2001; Hungr et al., 2005; Lancaster and Casebeer, 2007; Schürch et al., 2011; Stock and Dietrich, 2003). These short- to medium-term observations are supported by evidence that catchments with frequent debris flows exhibit slope-area relationships that differ from predictions of fluvial-incision models. Stock and Dietrich (2003) found that at slopes of ≈ 0.03–0.1 and higher, inverse power laws of fluvial incision overpredict slope. This means that on the long-term debris-flow incision, and hence removal of sediment, is more efficient than fluvial erosion and incision in these settings. At the scale of individual debris flows, entrainment has been studied in flume experiments and field investigations. It has been argued that debris-flow entrainment is a function of impacts of boulders on the channel bed (Berger et al., 2011; Hsu et al., 2008; Stock and Dietrich, 2006), of peak discharge and channel geometry (Chapter 4), of sediment concentration in the flow and channel bed slope (Takahashi, 2007), and of bed saturation (Iverson et al., 2011). It remains unclear how these factors interact and a coherent view of the entrainment mechanism is still lacking. Nevertheless entrainment along the flow path may result in a volume increase of debris flows by several orders of magnitude within travel lengths of only a few kilometers (Berger, McArdell and Schlunegger, 2010; Coe et al., 2011; Fannin and Wise, 2001; Hungr et al., 1984).

It is clear that both large and infrequent events (e.g., large rock falls), and a low-magnitude high-frequency supply of sediment, contribute to replenishing the sediment reservoirs in low-order channels (Benda and Dunne, 1997a; Berger, McArdell and Schlunegger, 2010). The attempt to infer the nature and rate of the processes replenishing the sediment storage in the headwaters from debris flow volumes measured at catchment outlets (Bardou and Jaboyedoff, 2008) is inherently difficult, without considering the properties of the storage elements. Therefore two opposing views of how these storage elements operate exist: Lancaster and Casebeer (2007) proposed a linear reservoir model where likelihood of entrainment decreases linearly with storage size, while Nakamura and Kikuchi (1996) suggested that the likelihood of re-entrainment decreases with deposit age. Reported residence times of sediment for debris-flow dominated channel reaches range from years (Berger, McArdell and Schlunegger, 2010) to centuries (Lancaster and Casebeer, 2007), and storage in first and second order channels is often found to be out of phase. Berger, McArdell and Schlunegger (2010) and Benda and Dunne (1997b) reported that for example whilst first order channels are recharged, the second order channels are scoured by debris flows and vice versa. Whether a specific debris flow or landslide stops in a first- or second-order channel (and thereby replenishes the storage) or continues traveling downstream (and removes material from storage) is difficult to predict and depends on the properties of the channel network and properties of the flow (Chapter 4; Benda and Cundy, 1990; Benda and Dunne, 1997a; Major, 1997; Major and Iverson, 1999; McCoy et al., 2010; Takahashi, 2007).

2.1.3 Patterns of debris-flow deposition on fans

The large-scale patterns of deposition on debris-flow fans are similar to those observed on alluvial fans. The processes of inundation, sedimentation and flow path selection have been extensively studied in flume models of alluvial fans, in numerical models and models of fan deltas (Clarke et al., 2010; Field, 2001; Jerolmack and Paola, 2007; Reitz et al., 2010; Sun et al., 2002; Törnqvist, 1994). The general consensus is that the flow follows the steepest path, of which there can be several active at any one time. Deposition in the 'active' part of a fan leads to building of topography, and infilling of channels (Reitz et al., 2010). At some point the active flow path becomes less favourable due to a reduction in slope, the system avulses and adopts a new steepest flow path.

Debris-flow fans operate in a very similar style, with the main difference being that sediment transport is very episodic in time (Benda and Dunne, 1997b; Blair and McPherson, 1998; Dühnforth et al., 2007; Jakob and Friele, 2010; Suwa and Okuda, 1983). During debris flows

deposition and erosion can take place at high rates (Chapter 4; Scheuner et al., 2009), and may lead to sudden changes in flow path and channel geometry due to in-channel flow front deposition (Arattano et al., 2010; Blair and McPherson, 1998; Suwa et al., 2009; Whipple and Dunne, 1992). The surface morphology at scales of meters to 10s of meters of debris-flow fans is dominated by levee-bound channels and depositional lobes (Blair and McPherson, 1998; Kim and Lowe, 2004; Whipple and Dunne, 1992). Levees form due to increased friction along the margins of debris flows occupying unconfined slopes (Major and Iverson, 1999) and consist of an inversely graded assemblage of large boulders (Blair and McPherson, 1998; Kim and Lowe, 2004) that travelled on the flow surface to the front, at which point they were pushed aside and deposited (Gray and Kokelaar, 2010; Suwa, 1988). Pairs of levees left behind by a flow form single-event channels that might be incised by subsequent flow as a result of feedback mechanisms arising from particular combinations of channel geometry and peak discharge (Chapter 4). These incised channels are important in routing flows down-fan and may lead to long-term abandonment of significant portions of the fan (Dühnforth et al., 2007; Whipple and Dunne, 1992).

Lobe deposition occurs as a result of declining momentum, pore pressure and grain agitation, as well as an increase in sediment concentration (Iverson, 1997; Iverson et al., 2010; McCoy et al., 2010; Takahashi, 2007). It has been shown that with careful mapping and description of fan surface morphologies, a relative chronology of lobe deposition can be established (Blair and McPherson, 1998; Dühnforth et al., 2007). This mapping is the necessary basis for subsequent surface exposure dating of boulders to obtain absolute fan depositional ages (Dühnforth et al., 2007).

2.1.4 Field site

The Illgraben in south-western Switzerland (E 7.6334°, N 46.2938°) is a steep debris-flow catchment on the southern flank of the Rhone Valley (Figure 2.1). The catchment covers an area of $\approx$9.5 km^2 which connects to a debris-flow fan of $\approx$2 km radius built in the base of the Rhone Valley (Appendix A.1). The Illgraben catchment consists of two sub-catchments, the Illbach (southern branch) and the Illgraben (SW-branch). Almost all of the recent sediment discharge is generated from the Illgraben sub-catchment, where incision rates are suggested to be considerably higher, as the Illbach joins the Illgraben as a hanging valley (Berger, McArdell and Schlunegger, 2010). The Illgraben climate is temperate-humid, with mean annual precipitation varying between 700 mm in

the lower parts of the catchment to 1,700 mm in the summit region of the Illhorn (Berger, McArdell and Schlunegger, 2010). Two bedrock lithologies, which are both highly fractured, dominate the catchment (Gabus et al., 2008): the north west (left) bank of the Illgraben is underlain by Upper Triassic dolomites and marbles, steeply dipping to the south east, whilst the south east (right) bank is mainly underlain by Lower Triassic quartzites (Figure 2.1). The quarzites come in two varieties, a white quarzite and a light-green sericitic quarzite, both of which also dip steeply to the south-east. In large parts of the Illgraben sub-catchment bedrock is exposed, although a few patches of till deposits of uncertain age are found on the right valley flank at Küferalp (Figure 2.1, Gabus et al., 2008). The lowermost bedrock exposure along the Illgraben channel can be found just downstream of check dam 1 at 1,000 m a.s.l. (Figure 2.1). One kilometer downstream, at check dam 15, bedrock has been found in boreholes at an elevation of ≈790 m a.s.l. (or ≈80 m below the channel bed) and a paleosoil level is reported at ≈860 m a.s.l. The fan apex is at ≈800 m a.s.l. Badoux et al. (2008) estimated the fan volume[2] to be $\approx 500 \cdot 10^6$ m^3. Boreholes at the toe of the fan, in the village of Susten, did not reach bedrock in an end-depth of ≈610 m a.s.l., or 50 m below the surface (Gabus et al., 2008), but bedrock is exposed in the right bank of the Rhone River at the fan toe opposite the junction of the Illgraben. The currently active channel follows the approximate centre line of the fan and separates the western forested half from pasture land on the eastern half.

According to Ivy-Ochs et al. (2008) it is unlikely there was a glacier in this part of the Rhone Valley after the Gschnitz Stadial around 15.4±1.4 kyr. Therfore the Illgraben fan should be younger. It seems reasonable to assume that the Rhone Glacier removed and reworked most of any older fan from the last inter glacial, and that the fan visible today started to accumulate sediment after retreat of the Rhone Glacier from this area.

Historical reports of rock fall activity in the Illgraben catchment start in the 20$^{\text{th}}$ century. Remains of earlier undated events, one of which blocked the catchment outlet, are shown on the geologic map of the area (Gabus et al., 2008). Major rock fall activity was reported for 1920, 1928, 1934 and 1961 in Gabus et al. (2008) and Lichtenhahn (1971). In the Illgraben catchment two large rock avalanche deposits (10^6 m^3) are documented. The first is is $\approx 3.5 \cdot 10^6$ m^3 in volume, and occurred in 1961 with an initiation zone on the flank of the Gorwetsch Grat[3] (Fig-

[2] $V = \frac{\pi}{6} r^2 h = \frac{\pi}{6} (2{,}000 \text{ m})^2 \cdot 250 \text{ m} \approx 500 \cdot 10^6 \text{m}^3$

[3] Grat = Ridge

ure 2.1, Lichtenhahn, 1971, ; Appendix A.1), referred to herein as the rock avalanche in the upper Illgraben. The second rock avalanche deposit is located near the fan apex – its investigation is part of the objectives of this study. Berger, McArdell and Schlunegger (2010) documented eight rock fall events and two landslides from aerial imagery in 2008 and 2009 ranging in volume from 300–4,400 m^3.

Reports about debris flows in the Illgraben catchment resulting in disruption of the important trade route along the Rhone Valley date back to the 16^{th} century and are recorded in the archives of the Canton Wallis in Sitten (see references in Gabus et al., 2008). Marchand (1871) reported on the violent nature, the speed and noise of the debris flows at Illgraben and early efforts of debris-flow hazard mitigation. The author also mentioned an incident in 1868 when a debris flow blocked the Rhone river for about one hour, which must be attributed to a major debris flow that was routed in an established channel to the toe of the fan. A dendrogeomorphic analysis of trees affected (but not removed) by debris flows (Stoffel et al., 2008) reported six events that affected areas alongside the recently active channel between 1793 and 1931, but not the one event mentioned by Marchand (1871) in 1868. An unpublished report by a consulting firm (Zimmermann, 2000) documented a total of 42 debris flows between 1932 and 2000, with a noticeable gap after construction of a sediment retention dam (check dam 1 in Figure 2.1, Appendix A.1) during the early 1970s in response to the 1961 rock avalanche in the upper Illgraben catchment (Lichtenhahn, 1971). For this period the dendrogemorphic analysis (Stoffel et al., 2008) reports nine events, three of which are also identified in the analysis by Zimmermann (2000). Regular debris-flow activity resumed in 1982 when debris flows started to over-top the sediment retention dam (check dam 1). For the period up to the year 2000 estimates of debris flow volumes are vague; the largest reported event occurred on 3 June 1961 in response to the rock avalanche earlier in the same year and was estimated to have a volume of between 2.5–5.0·10^5 m^3 (Badoux et al., 2008; Zimmermann, 2000). Since 2000 the Federal Institute for Forest, Snow and Landscape Research (WSL) has maintained a debris flow observation station (Hürlimann et al., 2003) at the toe of the fan (Figure 2.1) where debris-flow volumes are recorded (Berger et al., 2011; McArdell et al., 2007; Schlunegger et al., 2009), with a median total annual discharge of $\approx 10^5$ m^3 (35 events between 2000 and 2009, McArdell and Berger, 2010). Since 2007 a debris-flow warning system has been installed, triggering an alarm when debris flows pass instrumentation installed at check dams 1 or 10 (Badoux et al., 2008). It is clear that the record of debris flow events is incomplete, in particular for the period before 2000.

But also after the year 2000 only debris flows were recorded that either triggered the observation station at the toe of the fan (Hürlimann et al., 2003) or the debris flow alarm system at check dams 1 and 10 (Figure 2.1, Badoux et al., 2008). Events depositing in the upper catchment above check dam 1 remain unacounted for. Seasonal debris flow activity peaks between May and October in response to convective storms (Badoux et al., 2008; McArdell et al., 2007; Schlunegger et al., 2009). The review of all reported debris-flow events above and an assessment of old topographic maps of the area since 1845 published as the 'Doufourkarte', sheet XVII, (Dufour, 1845) and since 1886 published as the 'Siegfriedkarte', sheet 482, by Siegfried (1886, 1907, 1915, 1924 and 1933) indicate that since 1793 no major avulsion has occured and that the present flow path down the centre line of the fan was established before the earliest documented debris flow.

From aerial imagery Berger, McArdell and Schlunegger (2010) quantified rock fall volumes and in-channel sediment storage change between 2007 and 2009 for the Illgraben catchment upstream of check dam 1. The authors found that rock fall activity recharged the channel network draining the valley walls. This rock fall debris was subsequently transported to the main Illgraben channel within less than 1 year. For the Illgraben channel Berger, McArdell and Schlunegger (2010) observed channel filling during winter and spring followed by net erosion between summer and autumn. On an annual basis the authors found that rock fall volumes and sediment volumes removed from the reach upstream of check dam 1 are orders of magnitude smaller than debris flow volumes recorded at the fan toe, which indicates the importance of storage in the Illgraben channel between the fan apex and check dam 1 (Chapter 4; Berger, McArdell and Schlunegger, 2010). Preliminary results at Illgraben from an analysis by Bennett et al. (2011) between 1963 and 2009 suggest that these fluctuations averaged out over time scales of decades.

Sedimentation rates on the fan are poorly constrained. Bardou et al. (2003) and Gabus et al. (2008) report the same results from carbon-14 dating of buried soils from the 'lower part of the cone' in outcrops along the present-day channel; exact sample locations are unfortunately not reported. These data suggest sedimentation of 5 m over $1,231 \pm 70$ yr and 2 m over $1,354 \pm 60$ yr at these locations, but cannot be extrapolated to the fan as a whole. Whether these buried soils correspond to those found in boreholes near check dam 15 (Figure 2.1) remains unclear.

2.2 Methods

2.2.1 Terrain analysis

In this section I describe the methods employed for gemorphic field mapping, terrain analysis of the digital elevation model, reconstruction of fan apex migration and surface exposure dating. The first task was to understand the inventory of and the spatial relationship between different components of the fan system. In the field I mapped terraces in the catchment, the extent of the rock avalanche deposit and depositional lobes on the debris-flow fan. This mapping was cross checked against the LiDAR-derived 'DTM-AV', a 2-m-resolution digital elevation model (DEM) with an elevation uncertainty of $1\sigma = \pm$ 0.5 m, based on a raw point density of 1 point per 2 m^2 (Bundesamt für Landestopographie, 2005). Subsequently I refer to these data as the DEM. To map the depositional lobes on the fan I detrended the DEM of the fan area (Figure 2.1): first by fitting a 2nd-order polynomial surface to the DEM outlined as the fan area in Figure 2.1. Second I subtracted the resultant 2nd order polynomial surface from the DEM yielding detrended surface topography, which I show as shaded relief in the background of Figure 2.2. The detrending procedure enhanced the visibility of the boundaries of depositional lobes substantially (compare Figure 2.1 with 2.2). To distinguish between depositional lobes (Figure 2.2) I recorded a qualitative description of the surface morphology (e.g. Dühnforth et al., 2007), including roughness, dimensions of channels and levees and the occurrence and size of boulders. The relative chronology and the boundaries of fan lobes were established on the basis of cross-cutting relationships between channels, and downlapping of depositional lobes creating traceable topographic steps. Distinction of lobes in the distal parts of the fan became increasingly difficult and speculative (see also Dühnforth et al., 2007), so my mapping is limited at a radial distance of approximately 1.2 km from the fan apex.

To estimate sediment storage in the catchment behind the rock avalanche deposit near the fan apex (RA in Figure 2.3) I performed a series of steps: In the catchment I mapped terraces between the rock avalanche deposit and check dam 1 on both channel banks (Figure 2.1). I manually picked elevation samples from the DEM to represent these terraces and fan lobe L9, and interpolated them with a 3rd-order polynomial surface (Figure 2.3) to reconstruct a terrace surface aligned with the present-day fan surface. This surface was then shifted vertically upwards by 24 m to match the top of the rock avalanche deposit (purple band in Figure 2.3). I assume that channel bed slope is more or less constant over time and hence the purple surface simulates the potential maximum elevation of sediment stored behind the rock avalanche deposit.

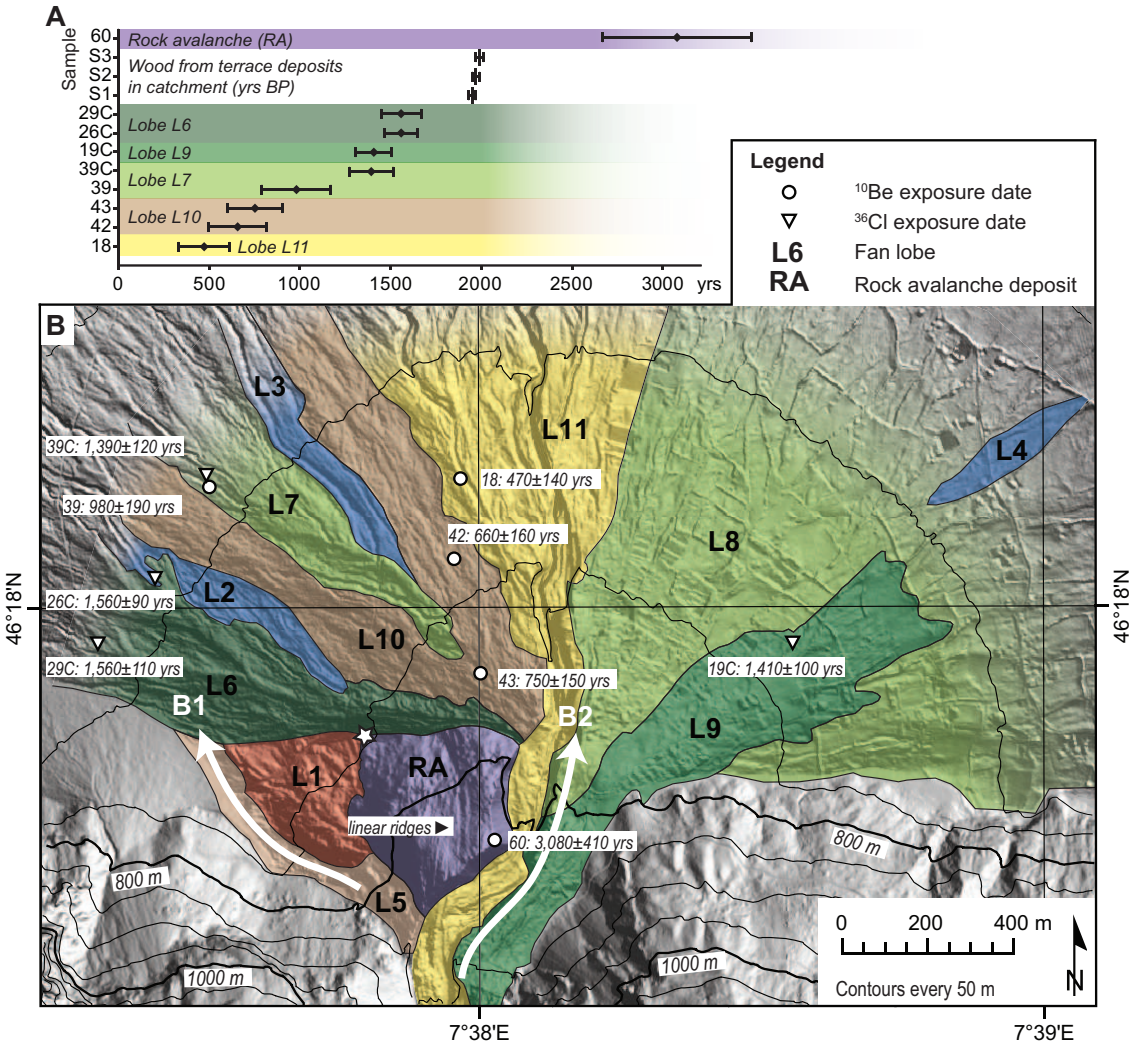

Figure 2.2: *Results from geomorphic mapping, radiocarbon dating of wood samples and exposure dating of boulders. Letter 'C' (e.g. 19C) denotes dolomite samples; other samples are quarzite samples. A: Rock and wood samples on vertical axis, see Tables 2.1 and 2.2 for details on sampled boulders. Horizontal axis age in years, errors are indicated with horizontal bar. Radiocarbon samples S1–S3 are in yr BP (see text for details). Colour bands correspond to colour of lobes in Figure 2.2B. B: Geomorphic map of depositional lobes based on cross cutting relationships of channels and deposits. Lobe L1 is suggested to be older than the rock avalanche (RA). Age of L2, L3 and L4 is unknown. Cross cutting relationships indicate that lobe L2 may be older than the rock avalanche (RA). B1: pathway of first breaching of rock avalanche dam across lobe L5. B2: secondary breaching of rock avalanche dam followed by resurfacing of the fan. Exposure ages of boulders are indicated where available. Star: north west corner of RA deposit; used as base elevation for volume calculation of RA deposit.*

I calculated a minimum volume for the rock avalanche deposit from the DEM based on the mapped outline of the deposit (Figure 2.2), a minimum thickness calculated from the lowest outcrop (at the north west corner, marked with a star in Figure 2.2) of the rock avalanche deposit at 747.8 m a. s. l., and an assumed horizontal, planar base. I estimated the storage volume created by blocking the catchment outlet with the rock avalanche deposit as the difference between the DEM and the purple surface and a downstream limit as indicated in Figure 2.3. I chose the downstream

limit of my calculation where the valley shape is still well defined, because downstream of this limit I do not know the exact extent and shape of the rock avalanche deposit. The storage volume calculated is therefore a conservative estimate.

In order to understand the effects of the rock avalanche on sediment transport pathways and deposition on the fan surface I examined the channel network on the fan surface. I reconstructed apex positions by visualizing the intersection pattern of channel fragments on the fan surface (Figure 2.4). For 75 channel fragments mapped on the fan surface I calculated the linear trend by connecting the start and end point of the mapped channel segments. I projected those trend lines to a search area for apex reconstruction (Figure 2.4) that was centered at coordinates 46.165703°N, 7.628309°E and had a size of 1.3 km (east–west) by 1.8 km (north–south). Within this area I defined a regular raster with a grid node every 10 m, and counted the number of channel trend lines that intersect with a circle of 150 m radius around each node. A radius of 150 m approximately matches the width of the catchment outlet, and allows to visualize the larger scale shifts in apex position.

2.2.2 Dating

Selection and sampling of boulders for cosmogenic exposure dating

To determine the absolute depositional chronology on the Illgraben fan and catchment I employed radiocarbon dating of wood fragments found in terrace deposits and cosmogenic exposure dating of boulders on the fan surface. Based on the relative fan lobe chronology I chose quarzite boulders for ^{10}Be and dolomite boulders for ^{36}Cl exposure dating. I identified a total of 47 potential candidate boulders for dating. The boulders consisted of sericitic quartzites, white quartzites and a few marbles and dolomites. From these I selected 16 boulders (Table 2.1 and 2.2) that were large in diameter (1.5–6.0 m), appeared to be situated in their original undisturbed geomorphic context, had a high quartz content based on visual inspection, had boulder upper surface slope of $\leq 25^{\circ}$ to minimize shielding (Dunne et al., 1999), and were clearly part of a debris flow deposit (as opposed to, for example, derived from rock fall from the north flank of the Gorwetsch Grat; Figure 2.1). Two sampled boulders (samples 46 and 60) are located on the rock avalanche deposit (Figure 2.2). At each location I took a sample of a maximum thickness of 4 cm as far from the boulder edges as possible, with a minimum weight of 0.5 kg. Elevations were obtained from the DEM. Posi-

tions were surveyed with a hand-held GPS reciever, then verified and adjusted against the DEM and the topographic map (Bundesamt für Landestopographie, 2006b). Locations near channels or prominent topographic features are accurate to about ± 2 m while locations in unstructured terrain were more difficult to verify and are less accurate (± 10 m). At each location I measured the angle to the local horizon of a number of azimuths (> 10) with a hand-held compass and clinometer to calculate the shielding correction (Table 2.1 and 2.2).

Laboratory proceedures for ^{10}Be and ^{36}Cl exposure age measurements

Here I give a brief overview over the laboratory procedures required for the cosmogenic exposure dating. Susan Ivy-Ochs, Florian Kober and Peter W. Kubik carried out sample preparation, quartz separation and Beryllium purification at the Department of Earth Sciences and the Laboratory of Ion Beam Physics, both of ETH Zurich (Switzerland). For silicate lithologies ^{10}Be was used and for calcareous lithologies ^{36}Cl. Standard procedures were followed to separate pure quartz from the bulk rock samples (0.2–0.8 mm grain size), and for the purification of Be (Ivy-Ochs, 1996; Kohl and Nishiizumi, 1992; Ochs and Ivy-Ochs, 1997; von Blanckenburg et al., 1996). Measurements of ^{10}Be/^{9}Be were made relative to in-house standards fixed to the 07KNSTD of Nishiizumi et al. (2007) and Balco (2009 and updates) at the accelerator mass spectrometry facility of the Laboratory Ion Beam Physics at ETH Zurich (Kubik and Christl, 2010). The weighted average ^{10}Be/^{9}Be long-term, full process blank ratio of $(2.60\pm0.43)\cdot10^{-15}$ was subtracted from the measured sample ratios. Exposure ages were calculated with the Cronus-Earth Be-10–Al-26 exposure age calculator (Balco, 2009 and updates) using a half-life of 1.39 Myr for ^{10}Be (Chmeleff et al., 2010; Korschinek et al., 2010). A production rate due to spallation of ^{10}Be (P10sp) of 4.41 ± 0.51 atoms g^{-1} yr^{-1} was adopted, valid at sea level and high latitude with muon contribution (Balco, 2009 and updates; Desilets et al., 2006).

Cl was extracted from the < 0.4 mm fraction of the crushed whole rock carbonates using sample preparation procedures described in Ivy-Ochs et al. (2004), which is based on the method of Stone et al. (1996). Samples were prepared at Ion Beam Physics using isotope dilution with a carrier of 99.9% pure ^{35}Cl (Desilets et al., 2006; Elmore et al., 1997; Ivy-Ochs et al., 2004). Cl ratios are measured with AMS at the Laboratory of Ion Beam Physics at ETH Zurich; ^{36}Cl/^{35}Cl sample ratios are normalized to the ETH internal standard K381/4 with a value of ^{36}Cl/Cl$= 15.6\cdot10^{-12}$, while the stable ^{37}Cl/^{35}Cl ratios were normalized to the natural ratio ^{37}Cl/^{35}Cl$= 31.98\%$ of the

K381/4 standard and machine blank. Measured sample $^{36}Cl/^{35}Cl$ ratios were corrected for a procedure blank of $5.6 \cdot 10^{-15}$, which amounted to a correction of less than 13% for the four samples. A SLHL (sea level – high latitude [$> 60°$]) production rate of 48.8 ± 1.7 atoms $^{36}Cl \cdot g(Ca)^{-1} \cdot yr^{-1}$ for was used for Ca spallation and of 5.3 ± 0.5 atoms $^{36}Cl \cdot g(Ca)^{-1} \cdot yr^{-1}$ production due to muon capture on Ca (Stone et al., 1996, 1998). Low energy capture of thermal and epithermal neutrons is calculated following Liu et al. (1994) and Phillips et al. (2001) using a production constant of 700 ± 400 neutrons$\cdot$(g air)$^{-1} \cdot yr^{-1}$ scaled with spallogenic scaling (see Alfimov and Ivy-Ochs, 2009, and references therein). Low natural Cl concentrations indicate that the contribution of non-cosmogenic subsurface production of ^{36}Cl is negligible (Fabryka-Martin, 1988). Shielding corrections for all samples were done following Dunne et al. (1999), and due to the expected young exposure ages (late Holocene) an erosion rate of zero was assumed for the sampled boulders. A rock density of 2.4 g/cm^3 was used for the carbonates and 2.65 g/cm^3 for the quartzites.

Radiocarbon dating of wood samples

To constrain the timing of sediment infilling behind the rock avalanche deposit at the catchment outlet, I searched for wood embedded in the terraces along the Illgraben channel between check dam 1 and 10. I sampled three slivers of wood (samples S1, S2 and S3, Appendix A.1) from whole sub-horizontally bedded logs, which were incorporated within a crudely-bedded boulder diamict on the right bank of the Illgraben channel. The sample locations were above the green surface and the terrace on the opposite (left) side of the channel but below the purple surface (Figure 2.3 and 2.5). The samples were prepared and dated in the Radiocarbon Lab of the Physical Institute of the University of Bern, Switzerland (lab numbers S1: B-9629, S2: B-9630 and S3: B-9631, Appendix A.2).

2.3 Results

2.3.1 Geomorphic mapping and terrain analysis

The surface of the Illgraben fan can be divided in the field into eleven distinct depositional lobes (L1–L11) and the rock avalanche deposit (RA, Figure 2.2). Cross-cutting relationships from field mapping and terrain analysis of the DEM suggest a decreasing age from L1 to L11. I place the occurrence of the rock avalanche after deposition of lobe L1 and before the onset of deposition on

lobes L5, L6 and L8 (Figure 2.2). The relative chronology of lobes L2, L3 and L4, and whether they predate the rock avalanche, could not be determined with certainty from mapping alone. Likewise the relative chronology of lobes on the east and west sides of the active channel (denoted lobe L11 in Figure 2.2) is uncertain due to a lack of cross-cutting relationships.

I now give a morphological description in chronological order of each lobe and of the rock avalanche deposit. Lobe L1 consists of one distinct channel of 15–20 m width and 1–2 m depth and many scattered boulders with diameters of up to 4 m on the unchannelized surface. The channel is clearly truncated by channels and levees of lobe L6 at its downstream end, and by the rock avalanche deposit at its upstream end. The rock avalanche deposit is downlapping onto the lobe L1 and the contact is marked by a distinct concave break in slope. Several debris-flow snouts are scattered across this lobe.

Lobe L2 consists of a series of short, sub-parallel channels (width $\approx$10 m, depth 1–2 m) with well-defined levees. Boulders in the levees are 1–2 m in diameter (largest: 4 m). At the upstream end, the channels are blocked by snouts of lobe L6.

Lobe L3 consists of one long channel of $\approx$15 m width and 1–3 m depth with broad and relatively smooth levees with no large boulders. The upstream end of this channel is clearly cut off by lobe L7. Two shorter channel fragments, which are possibly part of the same channel, are found to the east and are cut off by lobe L10.

Lobe L4 is only exposed in a small window surrounded by deposits of the younger lobe L8. It consists of a single poorly-defined, wide and shallow channel, which is truncated by deposits of lobe L8. There are no boulders exposed and the surface morphology outside the channel is smooth.

The surface of the rock avalanche deposit exhibits high roughness due to undulations of the deposit itself but also as a result of the abundance of very large boulders of $\gtrsim$10 m in diameter; the largest boulder found measured $\approx$20 m along its longest axis. The boulders on the surface of the rock avalanche are mostly unorganized. In a few places I found ridges of 1–3 m width extending north from the southern limit of the deposit, but these can only rarely be traced across the whole deposit (Figure 2.2) (Dufresne and Davies, 2009). Where these structures can be followed across the deposit, they are truncated by levees and channels of lobe L6. The western, southern and eastern margins of the rock avalanche deposit have been eroded by debris flows and are very steep (Figure 2.3 and profile 5 in Figure 2.5). The northern margin has a shallower surface slope

and probably represents the original depositional surface of the rock avalanche (profile 5 in Figure 2.5). The inner structure of the rock avalanche deposit is well exposed along the southern margin (Appendix A.1). The clasts found within and on top of the rock avalanche deposit are generally more angular than those found in the active channel and on the fan surface. They consist mainly of white and sericitic quarzite (Gabus et al., 2008) and are embedded in a matrix of silty sand with gravel. The rock avalanche deposit shows a clear inverse grading over the height of the erosion scar of ≈30 m with the largest clasts on the carapace. The lower parts of the exposed rock avalanche appear to be more stable than the upper, coarser layer.

Lobe L5 occupies a narrow strip between the rock avalanche deposit and L1 and the talus slopes beneath the Gorwetsch Grat (Figure 2.1). One steep channel with levees on both sides can be followed over parts of the lobe. The levees are built of rounded quarzite boulders of up to ≈4 m in diameter, while there are also scattered, more angular boulders of dolomite and marble (up to 3 m in diameter) that originate from rockfall from the Gorwetsch Grat. At its downstream end this lobe is truncated by levees and channels of lobe L6.

Lobe L6 is poorly channelized in the proximal part and almost free from channels in the distal part. Numerous lobate deposits and snouts create a highly undulating surface with only few large boulders; many boulders are smaller than 0.5 m in diameter. This lobe truncates structures in L1, L2 and L5.

Lobe L7 is well channelized with typical channel widths of ≈16 m and depths of 1–3 m and boulders of moderate size of up to 2 m. Channels in this lobe are truncated by deposits of L10.

Lobe L8 occupies most of the eastern half of the fan. Despite intensive agricultural land use, dry stone walls and irrigation channels, many channel fragments can still be traced over distances of ≈100 m. However, the surface morphology is smooth, boulders are scarce and the lobe boundaries with L4, L9 and L11 were difficult to determine precisely. This lobe is older than lobe L9, which shows a clear downlap contact onto L8. Lobe L9 is, apart from a distinct feeder channel at the top, unchannelized, with a few boulders (up to 3 m in diameter) towards the lower end .

Lobe L10 consists mainly of stacked lobate deposits and snouts, with a few boulders of up to 2 m in diameter but a generally smooth morphology. Its deposits truncate channels in lobes L2, L3 and L7.

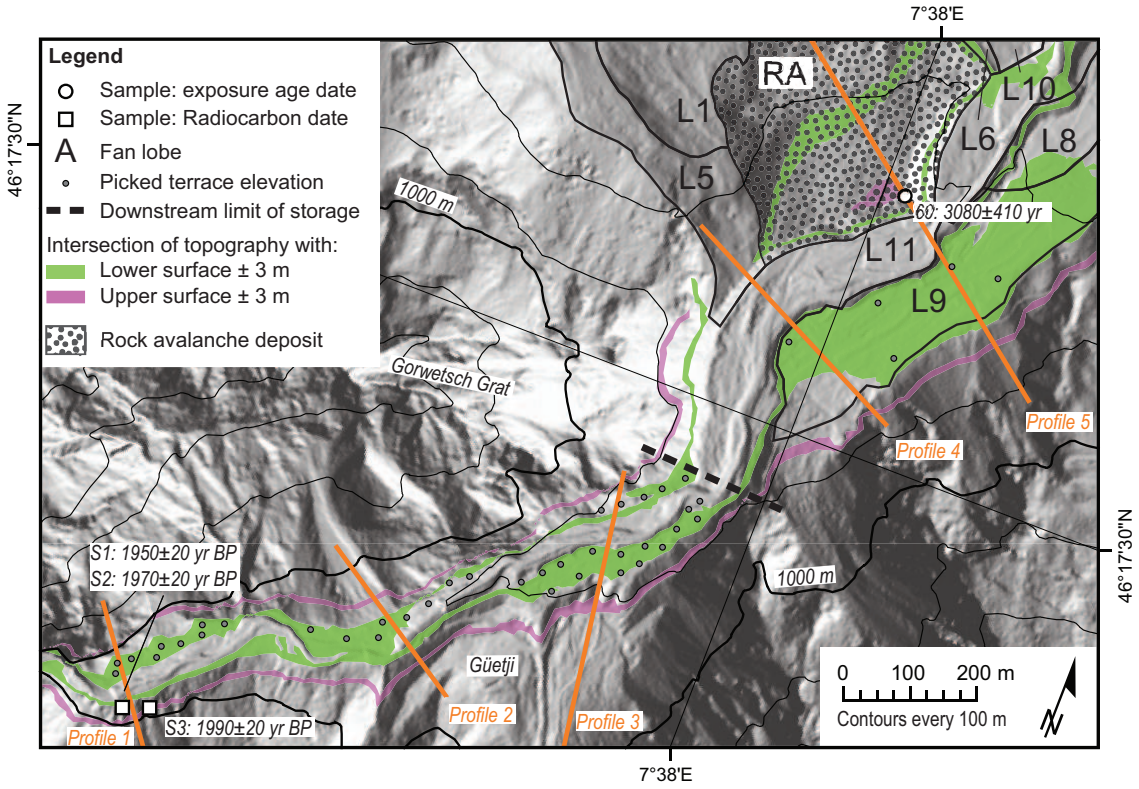

Figure 2.3: *Terrace reconstruction between check dam 1 and the rock avalanche deposit (RA). Topographic cross profiles (orange lines) are shown in Figure 2.5. Gray dots: Elevation samples for interpolation of the lower surface from the lower-most set of terraces and from fan lobe L9 (see text for details). Position of lower (green) and upper (purple) surface is indicated as the intersection of the surface, including a buffer, with present-day topography. The lower surface (green) is a 3rd-order polynomial interpolation of the elevation samples (gray dots) and represents an equilibrium valley fill aligned with the present-day fan surface (lobe L8/L9). The upper (purple) surface lies 24 m above the lower surface, and represents the maximum valley floor elevation of sediment stored behind the rock avalanche deposit at the fan apex (black dotted area). L1, L5, L6, L8–L11: distinct depositional lobes (see Figure 2.2). Location of wood samples and resulting radiocarbon ages in yrs BP are shown. A conservative estimate of sediment volume stored behind the rock avalanche deposit (RA) is shown in the text. The downstream limit of the area considered is indicated by the black dashed line. Digital elevation model DTM-AV©2011 published with permission from Swisstopo No: 5704 000 000.*

Lobe L11 forms the central part of the fan and also contains the currently active channel. East of the active channel a few distinct channels were found with widths of ≈10 m and depths of ≈4 m. Scattered large boulders are up to 3 m in diameter. The boundary with lobe L8 is however uncertain due to buildings and earthworks on this part of the fan. The active channel consists of two generations of inset terraces below the present-day fan surface. Its width decreases downfan from ≈70 m to ≈30 m, and its depth varies between ≈20 m near the fan apex and ≈10 m near the fan toe. To the west of the present channel, on the same lobe, one prominent channel of 35–45 m width and a maximum depth of 10 m stands out, and is lined by some scattered boulders. The dimensions are comparable to those of the active channel. The boundary with L10 is a distinct downlap relationship.

I show the terrace mapping in the catchment between the rock avalanche and check dam 1 in Figure 2.3. The channel in this section of the Illgraben is lined with fragments of terraces that lie between 5 m (upstream end) and 20 m (near downstream end) above the presently active channel. The 3rd-order polynomial interpolation from 42 elevations picked from these terraces (gray dots in Figure 2.3) yields a standard deviation of the residuals between known and interpolated elevations of $\sigma_r = 3$ m. This value is comparable to the expected variation in elevation due to channels, levees and boulders on such terrain depicted at this resolution. The purple surface in Figure 2.3 lies 24 m above the green surface, which equals the difference between the mean elevation of lobe L9 and the maximum elevation of the rock avalanche deposit in profile 5 (Figure 2.5). I found that this purple surface then passes through the downslope limit of the Güetji terrace (profile 2 and 3 in Figure 2.5) and lies above the sampled and dated wood embedded in terrace deposits on the right bank of the Illgraben farther upstream (profile 1 in Figure 2.5).

In Figure 2.4 I show the results of the apex reconstruction. The colour shading represents the number of intersections of channel trends within a 150 m search radius around each 10x10 m grid node. The area of highest intersection density has an elongated shape and is NNW–SSE oriented. Whilst the intersection density is highest at the present day apex, just north of the rock avalanche deposit, the colour shading indicates also that a considerable number of channel trends intersect in an area $\approx$ 500 m farther south. This secondary area lies just south of and partly beneath the rock avalanche deposit (Figure 2.4).

2.3.2 Depositional chronology and exposure ages from ^{10}Be and ^{36}Cl and ^{14}C dating of wood

In Table 2.1 and 2.2 and Figure 2.2 I show the results of exposure dating. Of the 16 boulders sampled, six did not yield enough pure quartz for successful dating, but exposure ages were determined for the remaining six quartzite and all four dolomite samples. Calculated exposure ages of these boulders range from $3,080 \pm 410$ yr (sample 60) to 470 ± 140 yr (sample 18). The oldest dated surface on the Illgraben fan is the rock avalanche deposit (sample 60). All other dated boulders show exposure ages that are $\approx 1,400$ years younger than the rock avalanche. Unfortunately I was unable to find suitable boulders for exposure dating on L3 and L4 and the samples taken from L1 and L2 did not yield enough quartz for reliable exposure dating.

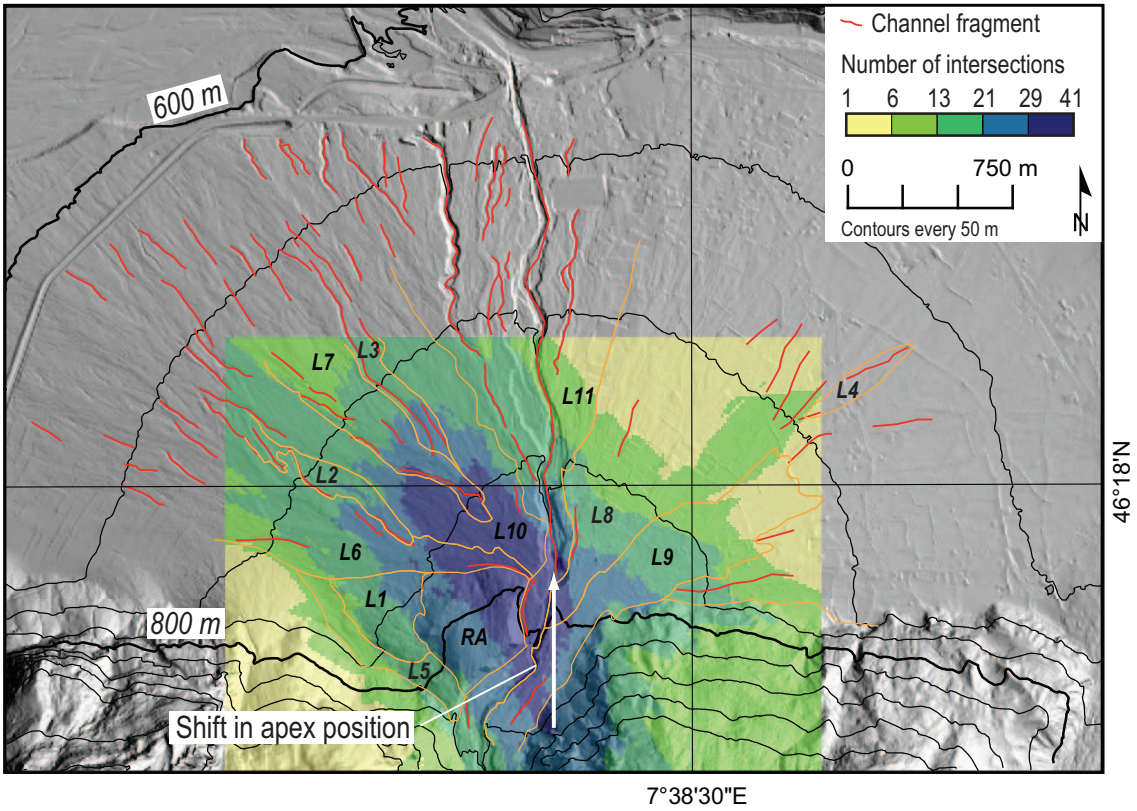

Figure 2.4: *Map of the Illgraben fan showing the apex reconstruction for mapped channel fragments (red lines). The colour shading indicates the number of intersections (termed 'intersection density') of channel trends within a 150 m search radius around grid nodes spaced 10 m. Mapped lobe boundaries are shown in orange and lobes are labeled in black. Digital elevation model DTM-AV©2011 published with permission from Swisstopo No: 5704 000 000.*

I determined the age of the rock avalanche (sample 60) as $3,080 \pm 410$ yrs ago and estimated the remaining volume of the deposit as $\approx 6 \cdot 10^6$ m^3. The emplacement of the rock avalanche at the catchment outlet undoubtedly led to creation of accommodation in the catchment and subsequent storage of sediment. Wood embedded in sediment, which I interpret as debris flow deposits due to high matrix content, poor sorting and chaotic structure, indicates a formerly higher channel bed elevation (Figure 2.3). The uncalibrated C-14 ages obtained for the wood samples S1, S2 and S3 are $1,950 \pm 20$ yrs BP, $1,970 \pm 20$ yrs BP and $1,990 \pm 20$ yrs BP, and are about 1,000 years younger than the rock avalanche deposit.

The cross cutting relationship between lobe L5 and lobe L6 suggests that lobe L5 is the first active (and preserved) lobe after the rock avalanche. Exposure ages from lobes L6, L7 and L9 (samples 19C, 26C, 29C, 39 and 39C) show that major resurfacing of the fan occurred around 1,500 yrs ago. Although L8 is undated, its morphologic relationships with lobe L9 and the rock avalanche deposit suggests depositional activity earlier than activity on L9, but after the rock

Table 2.1: *AMS-measured concentrations of ^{10}Be, surface exposure ages calculated with shielding correction, topography and dip. n/a: sample did not yield enough pure quartz for dating.*

Sample	Diameter [m]	Latitude [° N]	Longitude [° E]	Elevation [m a. s. l.]	Shielding correction	^{10}Be atoms/g rock	^{10}Be exposure age [yr]
18	3.0	46.3014	7.6318	727	0.975	3,459±957	470±140
26	4.0	46.2993	7.6229	693		n/a	
29	4.0	46.2980	7.6211	689		n/a	
34	5.0	46.2946	7.6272	752		n/a	
37	1.5	46.2958	7.6253	726		n/a	
39	2.0	46.3010	7.6242	691	0.982	7,096±110	980±190
42	1.5	46.2997	7.6316	740	0.979	4,898±109	660±160
43	1.8	46.2974	7.6324	767	0.980	5,727±945	750±150
44	3.0	46.2966	7.6291	750		n/a	
45	3.0	46.2975	7.6276	733		n/a	
46	6.0	46.2946	7.6324	824		n/a	
60	6.0	46.2946	7.6324	824	0.974	24,800±1,538	3,080±410

avalanche. Taking into account the uncertainties on the exposure dates, it seems reasonable to postulate that deposition on lobe L6 occurred first followed by activity on lobe L9 and L7.

Lobe L10 is the second youngest lobe on the fan, dated from two boulders (42 and 43) yielding similar deposition ages between around 500 and 900 yrs ago. On lobe L11, which includes the recently active channel, depositional activity started at least by 470 ± 140 yrs ago (boulder 18, Figure 2.2).

2.4 Discussion

In this section I discuss the findings of my analysis of the post-glacial evolution of the Illgraben sediment routing system. I first consider the results from exposure dating, and my interpretation with regard to the depositional chronology. Next I consider the effects of the earlier rock avalanche from 3,080 years ago on the fan morphology, sediment storage and release from the catchment, and the associated time scales. Finally, I discuss three possible mechanisms for the recent phase of incision of the Illgraben fan.

I established the chronology of lobe activity on the Illgraben fan mainly based on the cross-cutting relationships I found between different lobes, variations in surface morphology and the geometric relationship of these lobes with the rock avalanche deposit, following closely the methodology outlined in Dühnforth et al. (2007). Exposure dating confirmed my relative chronology and allowed, to my knowledge, the first absolute dating of debris-flow fan surfaces in the Alps by cosmogenic exposure dating. The ages presented have to be interpreted as a minimal age range of depositional activity on the different lobes, as I cannot assume that I have sampled the oldest

Table 2.2: *AMS-measured concentrations of ^{36}Cl, surface exposure ages calculated with shielding correction topography and dip.*

Sample	Boulder diameter [m]	Latitude [° N]	Longitude [° E]	Elevation [m a. s. l.]	Shielding correction	CaO wt. %	^{36}Cl atoms/g rock	Cl in rock ppm	^{36}Cl exposure age [yr]
19C	3.0	46.2980	7.6416	739	0.983	53.3	52,310±3,260	8.4±0.2	1,410±100
26C	3.0	46.2994	7.6229	694	0.966	47.7	57,320±2,940	36.2±0.4	1,560±90
29C	4.0	46.2980	7.6211	689	0.961	38.8	54,900±3,300	43.6±0.2	1,560±110
39C	1.5	46.3015	7.6243	690	0.982	55.7	52,310±4,030	12.6±0.1	1,390±120

nor the youngest boulder on each lobe (Dühnforth et al., 2007). The boundaries of the different lobes are based on geomorphic mapping only (Figure 2.2B). However, when considering the errors on the ages (Figure 2.2A, Tables 2.1 and 2.2), the distinction between the different lobes is less obvious. Lobe ages overlap due to measurement error, but also because deposition might have switched back and forth between two adjacent lobes before a definite abandonment of the older lobe. Inheritance of ^{10}Be or ^{36}Cl in the sampled boulders from previous exposure to comsogenic radiation could also be responsible for large age ranges within depositional lobes, and would lead to ages older than the true age of deposition (Ivy-Ochs et al., 2009; Ivy-Ochs and Schaller, 2009; Stock and Uhrhammer, 2010). Inheritance may arise from long residence times in the catchment or from reworking on the fan itself (Dühnforth et al., 2007). But on an annual basis sediment delivered to the main channel by small debris flows and rock fall in the upper Illgraben catchment (Figure 2.1) is evacuated to the fan by larger debris flows as shown by Berger, McArdell and Schlunegger (2010) from the analysis of aerial images. We therefore regard inheritance arising from long residence times of boulders in the catchment as insignificant. Abrasion of the boulders during transport in debris flows works towards resetting the exposure age clock, because ^{10}Be accumulated near the rock surface is removed, but abrasion of boulders in debris flows is difficult to quantify and I am unaware of any studies adressing this problem.

On the rock avalanche only one sample (sample 60) was dated. On one hand deposition can be assumed to have occurred instantaneously (Ivy-Ochs et al., 2009; Stock and Uhrhammer, 2010), on the other hand inherited ^{10}Be from previous exposure could have biased the age calculation yielding older ages than the true age of the rock avalanche. This is because boulders that were exposed on the rock face prior to the failure have been found to remain on top of the moving debris Ivy-Ochs et al. (2009); Ivy-Ochs and Schaller (2009); Stock and Uhrhammer (2010). Only additional dates from different boulders from the surface of the rock avalanche deposit can overcome this uncertainty.

The samples from lobes L6, L7, L9, L10 and L11 are all substantially younger than the rock avalanche deposit near the fan apex, and I conclude that most of the present day fan surface has been deposited by debris flows since this deposit was emplaced. With regard to the chronology of lobe deposition on the eastern half of the fan geomorphic evidence remains sparse. Centuries of agricultural land use and construction of dry-stone walls, roads, houses and irrigation ditches have destroyed important geomorphic evidence contained in relatively fragile landforms such as levees

that might exhibit local relief of as little as 1 m. The low number of channel fragments mapped on the eastern half of the fan is a reflection of these effects (Figure 2.4). The outline of lobe L9 is relatively well defined and sample 19C suggests depositional activity until at least $\approx 1,500$ yrs after the rock avalanche. I suggest that at least parts of L8 are younger than the rock avalanche, but farther downfan or close to the mountain front there could be surfaces that predate the rock avalanche.

The rock avalanche deposit consists of quartzites that crop out only on the north face of the Illhorn down to an elevation of about 1,000 m a.s.l. and below Ober Meschler down to an elevation of about 1,300 m a.s.l. (Figure 2.1, Gabus et al., 2008). The erosion scars on the southern and eastern side of the rock avalanche deposit suggest that the total volume must have been somewhat larger than my estimate of the present day volume of $6 \cdot 10^6$ m^3. The cliffs below Ober Meschler are still within the marbles, and can therefore be ruled out as source area. This leaves only a few options for the source area of the rock avalanche: either somewhere along the break in slope to the west of Ober Meschler but above the contact with the marbles (Figure 2.1), or farther south in the catchment on the north face of the Illhorn. The latter option appears more feasible because this allows for a reasonable ratio between runout and drop of 2–3:1. Dade and Huppert (1998) suggested such a ratio as a minimum for rock avalanches with a total volume on the order of 10^7 m^3 or above. For any source area closer to the catchment outlet I would have expected the maximum runout farther down-fan than observed. The south to north orientation of the ridges on top of the deposit indicate a similar flow direction (Dufresne and Davies, 2009), which would be incompatible with a source area beneath Ober Meschler.

The emplacement of the rock avalanche near the fan apex left a distinct fingerprint on the morphology of the fan as a whole. I interpret the cross-cutting relationships between lobes L1, L6 and the rock avalanche to indicate that L1 predates the rock avalanche. The preservation of lobe L1 is a direct result of the rock avalanche and of the pattern of subsequent incision: although early bypassing of the rock avalanche deposit occurred on its western side (lobe L5 in Figure 2.2), this period must have been short as it did not lead to a significant build-up of fan deposits in this area. Otherwise debris flows building lobe L6 could not have formed the strongly oriented pattern of levees and channels that indicate a dominant post avalanche flow direction from east to west (Figure 2.2). The presence of the rock avalanche deposit also sheltered the preserved part of lobe L1 from inundation from the west.

The apex reconstruction reported in Figure 2.4 suggests that some channel fragments mapped on the fan are associated with an apex location ≈ 500 m south of the present day apex, and thus would be projected to run underneath the rock avalanche deposit. The simplest interpretation is that these channel fragments thus predate the rock avalanche (e.g. on lobe L2). The apex location indicated by these channel fragments (Figure 2.4) corresponds to the position of the mountain front to the east and west of the Illgraben catchment outlet. Unfortunately, I could not confirm the hypothesis that lobe L2 predates the rock avalanche by exposure dating due to a lack of suitable sample material.

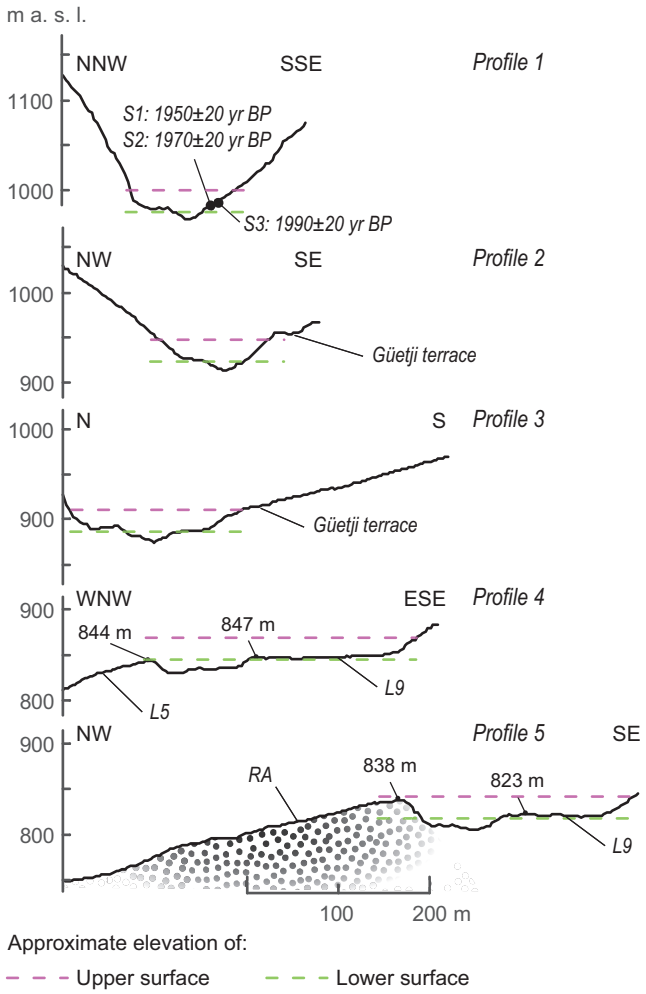

Figure 2.5: *Topographic profiles across the Illgraben channel in several locations illustrating the relationship between active channel, Güetji terrace, rock avalanche (RA) and present day fan surface (lobes L5 and L9). Approximate minimal cross-valley extent of rock avalanche deposit (RA) is indicated in profile 5 by black dots. See Figure 2.3 for location of profiles. S1–S3: wood samples for radiocarbon dating, ages in yrs BP. Lower surface (green) is interpolated from terraces in the catchment between check dam 1 and 15, upper surface indicates an estimate of maximum elevation of sediment ponded behind rock avalanche deposit (RA) at the fan apex (Figure 2.3). Profiles were extracted from the DEM and profile locations are marked on Figure 2.3.*

The rock avalanche deposit near the fan apex temporarily raised the base level for the catchment and created additional accommodation. If I assume that the green surface in Figure 2.3 represents an approximately stable long-term channel long-profile for the Illgraben, then a rise in base level to an elevation matching the paleo-top surface of the rock avalanche deposit (profile 5 in Figure 2.5) would yield a channel bed similar to the purple surface in Figure 2.3 and 2.5. The difference between this purple surface and the DEM yields a conservative estimate of the accommodation generated by the rock avalanche of $3 \cdot 10^6$ m^3. I interpret the Güetji terrace and the deposits containing the wood sampled for C-14 dating as remainders of the sediment stored in the catchment in response to damming by the rock avalanche, because the elevation of the toe of the Güetji terrace matches the purple surface, and also because the elevations of the sampled wood fall between the two surfaces (Figure 2.3 and 2.5). My interpretation is further supported by the dates obtained for the wood samples S1, S2 and S3, which yield a depositional age younger than the rock avalanche but older than the oldest exposure ages on the fan from lobe L6 (sample 26C and 29C) that clearly post-date the rock avalanche. Schlunegger et al. (accepted) offered an alternative explanation for the formation of the Güetji terrace and the deposits containing the wood samples. In agreement with my argumentation, the authors came to the conclusion that these deposits are related to a time when sediment transport capacity in the Illgraben catchment was low in comparison to the hillslope derived sediment input and that subsequently the relative dominance between the two fluxes has changed. In disagreement to my interpretation Schlunegger et al. (accepted) attributed this change in the relative importance of the hillslope and channel sediment flux to a regional trend observed across the Alps during the Holocene (Norton et al., 2008), while I attribute this to the rise and subsequent fall in local base level due to the rock avalanche emplacement.

Following this period of sediment accumulation in the Illgraben catchment, the system entered the recent phase of incision in the catchment, leading first to a resurfacing of the fan and second to the development of an incised channel that is visible on the fan surface today (Figure 2.1). Breaching of the rock avalanche dam occurred first in a narrow corridor to the North-West (lobe L5, Figure 2.2). This phase was followed by breaching in a northern direction and gradual removal of the sediment stored in the catchment. During this time debris flows lowered the bed elevation along the entire reach starting near check dam 1 and incised into the rock avalanche deposit. The data suggest that this incision was gradual, reaching an accumulated incision of ≈ 15 m by $\approx 1,500$ yrs ago using the oldest exposure ages from directly after the rock avalanche (sample

19C, 26C and 29C), and ≈ 32 m by today as measured at profile 5 (Figure 2.5). My interpretation is in strong contrast to a dendrogeomorphic analysis of growth disturbances in *Pinus sylvestris, Larix decidua* and *Picea abies* related to debris flows (Stoffel et al., 2008). In this study the authors attributed growth disturbances to debris flows impacting trees in vicinity of sample 60 for several years in the 19^{th} and 20^{th} century and as late as 1957. This would have required at least a temporary channel bed elevation at profile 5 (Figure 2.5) of almost 838 m a.s.l., or 15 m above the surface of lobe L9, followed by widespread and rapid incision over an area of several 10,000 m^2. However, such significant change of the channel bed in this area in such a short time cannot be confirmed either from the relevant topographic maps of the area between 1845 and 1933 (Dufour, 1845; Siegfried, 1886, 1907, 1915, 1924 and 1933) or from the 1:25,000 topographic map from 1966 (sheet Sierre 1287, Bundesamt für Landestopographie, 1954) and is also in disagreement with exposure dating of lobe L9 presented herein. It remains therefore unclear what has caused the documented growth disturbances in the trees analyzed by Stoffel et al. (2008).

The data and the inventory of debris flows at Illgraben lead me to conclude that depositional activity in the last 500 years was concentrated on lobe L11, and since 1845 was concentrated in or near the present-day channel based on an analysis of old maps (Dufour, 1845; Siegfried, 1886, 1907, 1915, 1924 and 1933) that do not show any significant changes in the course of the Illgraben-stream on the fan. This downstream shift in depositional activity is the result of fan head incision on the Illgraben fan. I identify three mechanisms, one autogenic and two external forcings, that may have been operating simultaneously, potentially re-enforcing each other: First, temporary development of incised channels on alluvial fans occurs naturally and periodically as has been shown in flume experiments (Clarke et al., 2010; Jerolmack and Paola, 2010; Kim and Jerolmack, 2008; Kim et al., 2006; Nicholas and Quine, 2007b; Reitz et al., 2010). For fans where radial growth is limited, Clarke et al. (2010) found that fans tend to develop an incised channel, with a significantly reduced avulsion frequency, once the fan toe has grown to the model boundaries, where sediment is constantly removed. These boundary conditions are similar to the situation of the Illgraben fan, where the Rhone River removes any sediment transported to the fan toe (Schlunegger et al., 2009). Apart from this clear field evidence for autogenic forcing is still lacking, and characteristic time scales for natural alluvial fans are unknown.

Second, a natural decline in sediment flux, while water discharge remains unchanged, may result in incision of the fan surface. At Illgraben, sediment discharge appears to have increased almost instantly after large rock fall events (e.g. 1961, Badoux et al., 2008; Lichtenhahn, 1971) and then gradually declined over a period of time. It seems reasonable that the Illgraben catchment is still responding to the rock avalanche deposit near the fan apex and to the one in the upper Illgraben catchment, and that the sudden increase and subsequent decline in sediment discharge is partly responsible for the observed incision on the fan (Davies and Korup, 2007).

Third, construction of check dam 1 (Figure 2.1 and 2.6) in response to the 1961 rock avalanche has led to a further, although short-lived, decrease in sediment delivery and subsequent incision (Lichtenhahn, 1971). Subsequent construction of the check dams on the fan enforced a relatively narrow channel cross profile that efficiently routes debris flows by maintaining a high flow depth (Chapter 4 and 5).

At century scale the Illgraben catchment is undergoing rapid incision and degradation of 4 mm/yr (Berger, McArdell and Schlunegger, 2010; Schlunegger et al., 2009). The two photographs (Figure 2.6) taken from identical positions in 1921 and 2009 give further support for this trend, and show a decrease in channel width in the lower catchment below check dam 10 (black arrow in Figure 2.6), which I interpret as a sign of incision into the valley fill.

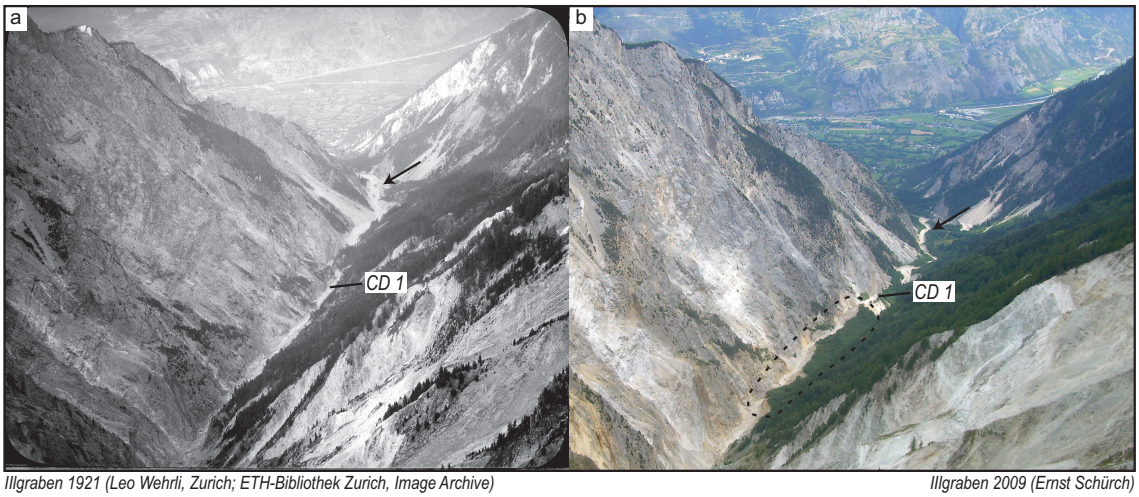

Figure 2.6: *Photographs taken from Plaine Madelaine (Figure 2.1) looking north east down the Illgraben channel. a) Illgraben in 1921. b) Illgraben in 2009. Forest cover in 2009 in the foreground is reduced compared to 1921. The rock avalanche deposit from 1961 is visible in the central part of the picture (marked by dashed line). Note decrease in active channel width between 1921 and 2009 (black arrows), which is interpreted as incision into the valley fill, and subsequent re-vegetation of the emerging terraces on both sides of the active channel. CD 1: location of check dam 1, the sediment retention dam built to stabilize to the 1961 rock avalanche deposit.*

2.5 Conclusions

In this chapter I reconstructed fan evolution and sediment storage in the Illgraben sediment routing system over the past 3,080 years. This reconstruction includes a detailed chronology of lobe deposition on the debris-flow fan by means of cosmogenic exposure dating of ten quartzite and dolomite boulders. A rock avalanche deposit of at least $6 \cdot 10^6$ m^3 volume dated to $3,080 \pm 410$ yrs occupies an area near the fan apex. I identified a likely source area of the rock avalanche on the north face of the Illhorn. The mapping and dating shows that the fan has been almost completely resurfaced by debris flows since emplacement of the rock avalanche at the fan apex. The rock avalanche left a distinct fingerprint on the fan and catchment which persists today. This fingerprint consists of a characteristic channel cross-cutting pattern that allowed approximate reconstruction of the pre-rock avalanche apex position. In the catchment I identified terrace deposits perched above the present-day channel, probably representing a valley fill in response to the damming of the catchment outlet by the rock avalanche deposit. The data and a review of reports on debris flow activity suggest that debris-flow activity during the last 500 years was concentrated on lobe L11 and since 1845 was concentrated in or near the present-day channel. This downstream focusing of deposition in combination with fan head incision is likely to be the result of three simultaneously operating mechanisms: autogenic fluctuations in sediment storage and release on the fan, a natural decline in sediment delivery as the rock avalanche deposit and retained sediment are gradually removed, and a man-made reduction in sediment delivery resulting from the construction of check dams in the catchment, which also led to a more efficient channel. The latter two mechanisms operate on very different time scales but also act to reinforce each other in this particular example; the relevant time scale for the first mechanism remains unknown. Whilst at Illgraben the effect of external forcing by rock avalanches and human activity of the alluvial fan has been demonstrated in this case study, it remains unclear how geomorphic features such as channels could be unambiguously attributed to autogenic forcing, without monitoring or reconstructing sediment fluxes in and out of the fan over prolonged periods of time.

Chapter 3

Detection of surface change in complex topography using terrestrial laser scanning: application to the Illgraben debris-flow channel

Abstract

[1] Detection of surface change is a fundamental task in geomorphology. Terrestrial laser scanners are increasingly used for monitoring surface change resulting from a variety of geomorphic processes, as they allow the rapid generation of high resolution digital elevation models. Irrespective of instrument specifics, survey design or data processing, such data are subject to a finite level of ambiguity in position measurement, a consideration of which must be taken into account when deriving change. The propagation of errors is crucial in change detection because even very small uncertainties in elevation can produce large uncertainties in volume when extrapolated over an area of interest. In this study we propose a methodology to detect surface change and to quantify the resultant volumetric errors in areas of complex topography such as channels, where data from multiple scan stations must be combined. We find that a commonly proposed source of error, laser

[1] Schürch P., Densmore A.L., Rosser N.J., Lim M., and Mc Ardell B.W. (2011). Detection of surface change in complex topography using terrestrial laser scanning: application to the Illgraben debris-flow channel, *Earth Surface Processes and Landforms,* doi: 10.1002/esp.2206

point elongation at low incidence angles, has a negligible effect on the quality of the final registered point cloud. Instead, ambiguities in elevation inherent to registered data sets have a strong effect on our ability to detect and measure surface change. Similarly we find that changes in surface roughness between surveys also reduce our ability to detect change. Explicit consideration of these ambiguities, when propagated through to volume calculations, allows us to detect volume change of 87 ± 5 m^3, over an area of $\approx 4,900$ m^2, due to passage of a debris flow down a 300 m reach of the Illgraben channel in Switzerland.

3.1 Introduction

Precise volumetric measurement of Earth surface change is a key component of many geomorphic investigations that aim to quantify sediment transport processes. Terrestrial laser scanning (TLS) is capable of deriving topographic data with resolutions of $\leq$1 m over large areas (10^4 m^2), making the detailed comparison of surface topography over discrete time intervals possible for the first time. Common to most published applications of change detection using TLS is a generally planar object geometry (e.g. braid plains, rock cliffs) with low relief in the scanner look direction compared to the lateral dimensions of the object (Brasington et al., 2003; Lim et al., 2005; Milan et al., 2007; Rosser et al., 2007). In such environments, measurement point density can be near-uniform when stations are well placed and occlusion from roughness elements is small, facilitating registration of multiple point clouds into coherent data sets. However, issues arising from complex surface geometry, as for example in a river or debris flow channel (Figure 3.1) with abrupt changes in slope, aspect, local surface roughness and high local relief, have not been fully addressed. In complex topography, point density need not be uniform and occlusion may be commonplace, leading to an increased chance of ambiguous point cloud matching (Figure 3.2).

For the purpose of change detection, inhomogeneous point clouds from TLS are often gridded (e.g Hodge et al., 2009; Milan et al., 2007; O'Neal and Pizzuto, 2011). When, depending on the specific application, surface roughness is of the same order of magnitude as the desired grid resolution, this gridding becomes a non-trivial task. A difficult choice must be made over how to best represent the elevation of a grid cell when multiple data points fall into a single cell. Although the absolute differences in elevation between different options for this choice might be small ($\approx$ 0.01–0.1 m), the effect of this difference can be significant in terms of volume change

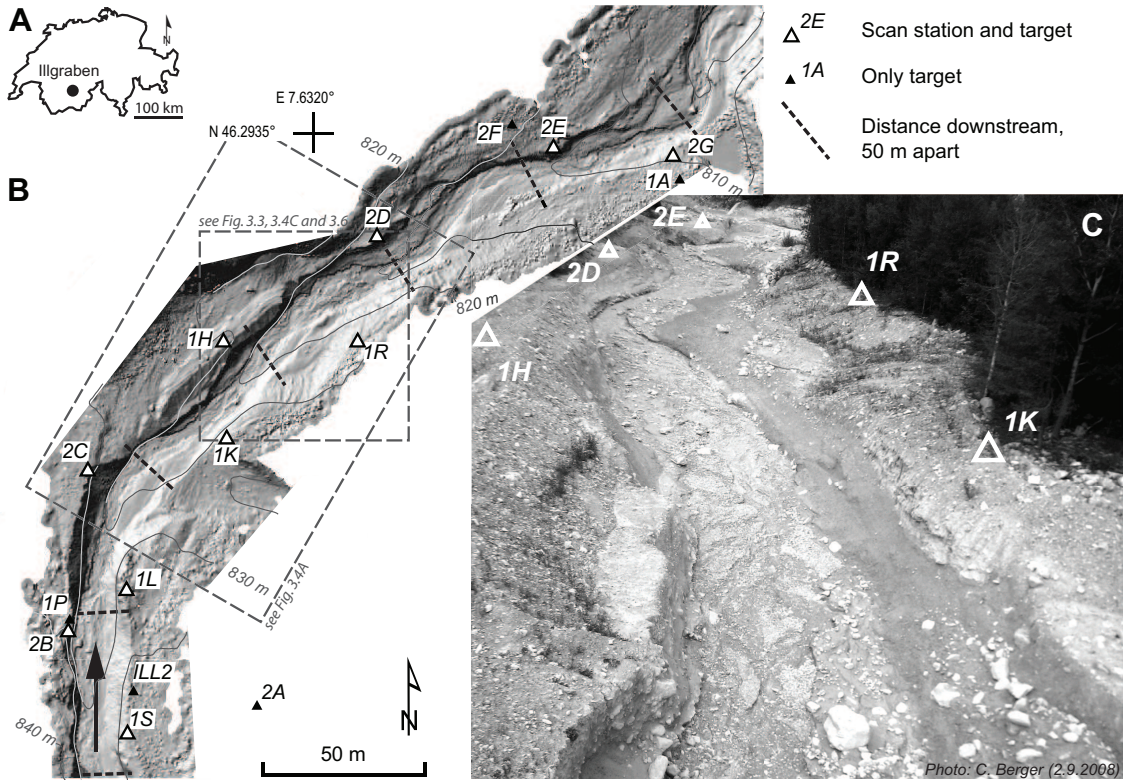

Figure 3.1: *(A) Location of Illgraben in south-western Switzerland. (B) Hillshaded DEM of the study reach surveyed on 30 and 31 July 2008 (survey 1). Elevations are given in meters above sea level according to vertical datum LHN02 (Bundesamt für Landestopographie, 2006a), contours are 5 m apart. Triangles denote benchmarks surveyed with differential GPS and used as scan stations and target positions (see text). Black arrow indicates flow direction of debris flows in the channel. Cross section markers are located at intervals of 50 m along the talweg. Dashed boxes outline the extent of the Figures 3.3, 3.4 and 3.6. (C) Photograph of the study reach downstream from benchmark 2C two days after the debris flow on 31 August 2008.*

when comparing digital elevation models (DEM) over large areas. Thus, the effects of these uncertainties on the calculation of volumetric change need to be accounted for in a rigorous and consistent manner. This paper presents a methodology to quantify the effect of elevation ambiguity on change detection.

Previous work that is relevant to uncertainty analysis can be grouped into two themes: 1) analysis of errors related to data acquisition with terrestrial laser scanners, and 2) analysis of errors in DEMs generated from point observation data. For time-of-flight based laser scanners the range measurement error is caused by errors in the pulse flight-time measurement (Petrie and Toth, 2008). When using a survey-grade instrument of adequate precision and at typical scanning ranges of ≈50 m, this error is negligible (e.g. σ = 1.4 mm, Trimble, 2005). Some work has been undertaken to identify and quantify other sources of error in TLS data (Abellán et al., 2009; Buckley et al., 2008; Hodge et al., 2009; Kaasalainen et al., 2008). These studies have suggested that in-

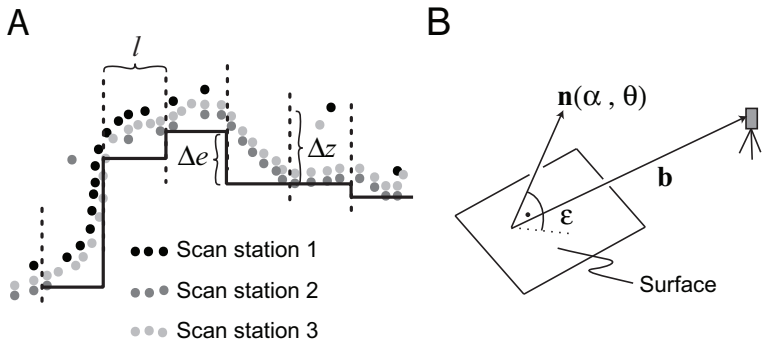

Figure 3.2: *(A) Cross section through a hypothetical point cloud matched from three scan stations (light gray, dark gray and black). Misalignment of data from individual scan stations results in a finite thickness of the point cloud. Point density varies as a function of incidence angle and occlusion. The solid black line represents the gridded topography (grid spacing l) after application of a lowest return filter to the raw data.* Δz *is the total range in elevation in a grid cell and* Δe *the expected variation over that cell due to topography. (B) Definition of incidence angle* ε *as the minimal angle between the surface and the vector* $\vec{b}$ *connecting the surface point with the laser scanner.* $\vec{n}$ *is the surface normal as a function of surface slope* θ *and surface azimuth* α*.*

creased laser footprint size at low incidence angles (Figure 3.2), variations in surface reflectance, variable point density and multiple reflections across sharp topographic edges cause erroneous points in the raw data. However, most studies have focused on small areas (Hodge et al., 2009), on artificial objects, or on data acquired from a single scan station (Abellán et al., 2009). The results of these studies can therefore not easily be generalized to a situation with multiple scan stations and complex topography, and it is unclear what the dominant sources of error are in such a situation.

Much work has also been undertaken in quantifying elevation errors in DEMs generated from point clouds and how these can be propagated into volume calculations. The classic approach in DEM validation is to compare the DEM to a finite number of check points surveyed by a total station or differential GPS (Brasington et al., 2003; Lane et al., 2003; Stojic et al., 1998). The difficulty in doing so is to collect a representative number and distribution of checkpoints (see full discussion in Brasington et al., 2003).

Many studies (Brasington et al., 2003; Fuller et al., 2003; Lane et al., 2003; Schürch et al., 2009) have adopted an approach for error propagation introduced by Bevington (1969) and Taylor (1982) to propagate uncertainties in DEMs into calculations involving multiple DEMs (e.g. differencing) or derivatives of DEMs (e.g. slope). A major drawback of these approaches is that they typically assume a normal distribution of, and sometimes independence of, errors in elevation, assumptions which may not necessarily be valid in all cases. A different approach to quantify DEM

uncertainty is based on a fuzzy inference system calibrated for different surface types (Wheaton et al., 2010). Uncertainties are assigned to the DEM based on local slope, point density and GPS quality. All of these approaches have been developed to analyse uncertainty of DEMs where the raw data density is lower than the DEM resolution (e.g. 0.3 points/m^2 for a grid resolution of 1 m in Wheaton et al., 2010), a condition not typically met in TLS studies. Also, none of these studies address issues particular to data consisting of multiple merged point clouds.

This study has three objectives: first, we define a novel spatial measure of point cloud quality that quantifies elevation ambiguity; second, we investigate the generation of elevation ambiguity in point clouds; and third, we quantify the volumetric error arising from this elevation ambiguity when differencing successive DEMs derived from point clouds. To demonstrate these concepts, we use a test data set from the Illgraben debris-flow channel in Switzerland.

3.2 Accquisition of test data

3.2.1 Field site

The Illgraben in south-western Switzerland (E 7.6334°, N 46.2938°) is a steep catchment with a drainage area of ≈9.5 km^2 that experiences regular seasonal debris-flow activity (McArdell et al., 2007; Schlunegger et al., 2009). Debris flows are triggered during convective storms from May to October (McArdell et al., 2007). We have monitored changes to the channel shape resulting from the transit of debris flows through a ≈300 m long study reach (Figure 3.1) just downstream of the fan apex. The study reach is located between two check dams and is cut into older debris-flow deposits. The channel is 10–20 m wide and about 2–4 m deep, and the surface roughness is dominated by grain sizes between sand and cobbles, and to a lesser extent by boulders of up to 2 m in diameter. The channel slope in the study reach is 4.5°–5.5°.

3.2.2 Terrestrial laser scanning procedure and survey layout for the test data set

We surveyed the channel (Figure 3.1) using a Trimble GS200 laser scanner on three occasions in 2008 (survey 1 on 30/31 July, survey 2 on 25/26 August and survey 3 on 30 September/1 October) in the aftermath of debris flows, yielding point clouds of ≈10^7 vertices each. Each survey consisted of 10 scan stations. Scan station positioning was constrained by a number of factors. Locations in the channel were considered too dangerous and transient to occupy repeatedly. The choice

Table 3.1: *(a) ID of control and check points, (b) 3D point quality from differential GPS, (c) residual 3D error from georeferencing the matched point cloud of survey 1 and (d) difference between elevation from differential GPS and elevations in gridded TLS data. n/a: check point not surveyed with differential GPS (2H) or used for georeferencing in survey 1 (1A, 2C, 2F, 1R). Stdev: Standard deviation of differences between GPS elevation and elevation in gridded TLS data.*

(a)	(b)	(c)	(d)		
Point ID	GPS Quality [m]	Georef. residual 3D error [m]	GPS Elevation - DEM Elevation [m]		
			Survey 1	Survey 2	Survey 3
1A	0.0116	0.024	n/a	-0.07	-0.01
1H	0.0160		-0.04	-0.01	-0.03
1K	0.0144		-0.05	-0.07	-0.11
1P	0.0165		0.05	0.07	0.05
1R	0.0133	0.095	n/a	-0.14	-0.07
2C	0.0150	0.079	n/a	0.09	0.05
2D	0.0155		-0.02	0.01	-0.01
2E	0.0150		0.02	0.02	0.07
2F	0.0156	0.059	n/a	-0.07	-0.09
2G	0.0101		0.04	0.03	0.01
2H	0.0165		n/a	-0.04	n/a
ILL2	0.0162		0.07	-0.09	0.11
		Median	0.023	-0.025	-0.009
		Mean	0.011	-0.022	-0.003
		Stdev	0.046	0.069	0.069

of locations on the channel banks was limited due to vegetation or steep and unstable terrain. We chose locations that were as high as possible above the channel bed (to maximise incidence angle), that were not more than $\approx$ 50 m apart (Figure 3.1), and that had a good view of other stations. Some additional positions (1P, ILL2, 2A, 2F and 1A in Figure 3.1) were identified as target locations for point cloud registration. Target and scan station locations were marked on the ground with survey markers. All locations were surveyed with a differential GPS (Table 3.1).

For our survey we specified a scan grid spacing of 50 mm at a range of 50–70 m from the scanner. To register the point clouds we used flat high-reflectivity Trimble targets (15 cm x 15 cm) mounted vertically on standard surveying tripods, and scanned at least five targets from each scan station (Table 3.2).

3.2.3 Point cloud registration

The survey was designed to allow for a target-based registration procedure of the ten scan stations. In the process of registering the data we encountered a series of challenges using the target-based registration. In this section we will discuss these issues and justify why we choose to employ iterative closest point (ICP) registration first introduced by Besl and McKay (1992) and Chen and

Table 3.2: *Target based registration errors for survey 1. (a) Scan stations from which the target was scanned. (b) Mean distance between the scanned target and the averaged target position (from all scans of one specific target). (c) Maximum distance between the averaged target position and the scanned target, in brackets the scan station from which this target scan was performed.*

Target	(a) Scanned from stations	(b) Mean residual error [m]	(c) Max residual error [m] (scanned from)
1A	2E, 2G	0.013	0.013 (2E, 2G)
1H	2B, 2C, 2D, 2E, 1K, 1R	0.020	0.034 (2C)
1K	2B, 2C, 2D, 1H, 1L, 1R,	0.037	0.093 (1L)
1L	2B, 2C, 1H, 1K, 1S	0.019	0.033 (1H)
1R	2C, 2D, 2E, 1H	0.050	0.097 (2C)
2A	2B, 2C, 1K, 1L, 1S	0.048	0.111 (1L)
2C	2B, 1H, 1R	0.028	0.041 (1R)
2D	2E, 2G, 1H, 1R	0.008	0.011 (1R)
2E	1R, 2D, 2G	0.011	0.012 (1R)
2F	2D, 2E, 2G	0.004	0.005 (2D)
ILL2	2B, 1K, 1L, 1S	0.015	0.023 (1L)
1P	1K, 1L, 1S	0.044	0.059 (1L)

Medioni (1992), and since tested for point cloud registration by Dalley and Flynn (2002) and von Hansen (2007). Target-based registration is very popular (e.g. Buckley et al., 2008; Hodge et al., 2009; Lim et al., 2009; Milan et al., 2007). This method of registration is implemented in software packages for point cloud manipulation and is relatively quick. We used the target-based registration tool provided in the RealWorks 6.0 (Trimble, 2006) software package to register the point clouds from the ten scan stations (Figure 3.1B). We report the target registration errors for survey 1 in Table 3.2. The performance of the target-based registration in the first survey was unsatisfactory, with mean residual errors (distance between scanned target and averaged target position) ranging from 0.004–0.050 m; the maximum residual error was 0.111 m (Table 3.2). An inspection of the point cloud revealed that the misalignment between point clouds scanned from different scan stations was even larger along the channel banks and in the channel. We found that the more target scans were matched together, the larger the mean residual errors. Only a few of our targets were located in the overlap zone between scan stations because we mainly used adjacent scan station locations as target locations. We suspect that target registration errors could be reduced by substantially increasing the number of targets located in the zone of overlap between adjacent scan stations, but this would require additional survey tripods and personnel and would result in a longer survey duration. Although the use of targets might be expected to achieve superior registration, providing control surfaces of calibrated reflectance, it seems that for this application the required number of targets to achieve a good result renders this approach unfeasible.

Table 3.3: *Root mean square (RMS) error of ICP matching of point clouds from individual scan stations (St) to adjacent scan stations for survey 1 (base line survey). The reported RMS errors refer to the matching of the combined point cloud of all previously matched stations with the next station. Matching started with station 1S and 1L. The last station to be incorporated was station 2G. Station locations are shown in Figure 3.1.*

St 1S	St 1L	St 1K	St 2B	St 2C	St 1H	St 1R	St 2D	St 2E	St 2G
0.040 m									
0.036 m									
0.049 m									
0.047 m									
0.031 m									
0.029 m									
0.040 m									
0.061 m									
0.055 m									

As an alternative we applied an iterative closest point (ICP) algorithm implemented in the RealWorks 6.0 software package (Trimble, 2006). The ICP algorithm calculates a root mean square (RMS) error based on the separation of the two populations of points in both point clouds and seeks to minimize this RMS error over a series of iterative rigid transformations. The registration process is initialized by a manual selection of three tie points in both point clouds. We found that the initialization and subsequent refinement is greatly helped when some prominent features are scanned at high resolution. An automated algorithm excludes all non-overlapping parts of the two point clouds prior to the ICP registration. This minimizes the deteriorating effects of differing view angles on the registration (personal communication David Hadden, Trimble, 2009). We find that after 5–8 iterations the RMS error stabilizes. In Table 3.3 we report these RMS errors of the ICP matching of survey 1 (baseline survey). We also looked at the competing effects of incidence angle of the laser beam on the surface and angular separation (of two adjacent scan stations) in determining quality of the ICP based registration but see no consistent correlation – we interpret this as being due to the complex nature of the overall point cloud, meaning that the different factors interact in ways that are not necessarily intuitive or predictable.

The procedure followed for the ICP matching of survey 1 is shown in Table 3.3. We started at the upstream limit of the study reach by matching the point clouds from station 1S and station 1L; subsequent stations were then matched to the combined point cloud of previous steps. The maximum RMS error of 0.061 m arises from matching station 2E to all upstream scan stations. As can be seen from Figure 3.1 this match relies mainly on the overlap with the data from station 2D on the gently sloping right channel bank. This area suffered from relatively different view angles

Table 3.4: *Root mean square (RMS) error of ICP matching between the reference point cloud of previous survey and the point clouds from individual scan stations from the subsequent survey. See Figure 3.1 for scan station locations.*

Scan station	RMS error [m] Survey 1 – Survey 2	RMS error [m] Survey 2 – Survey 3
Station 1S	0.022	0.029
Station 1L	0.025	0.032
Station 1K	0.025	0.021
Station 2B	0.031	0.031
Station 2C	0.030	0.023
Station 1H	0.030	0.031
Station 1R	0.032	0.033
Station 2D	0.031	0.038
Station 2E	0.026	0.033
Station 2G	0.019	0.022

and low incidence angles (low point density) from both stations, leading to a poorer performance of the ICP algorithm. In Table 3.4 we show the RMS errors for surveys 2 and 3 (subsequent surveys) where we matched point clouds from individual scan stations to a reference point cloud (of unchanged areas) selected from the previous survey (survey 1 and survey 2 respectively). The errors range from 0.019–0.038 m, and are mostly smaller than the mean residual errors from the target-based matching (Table 3.2).

We choose to match subsequent surveys to the previous (rather than the first) survey because we are interested in relative differences between subsequent surveys. Therefore we can sacrifice absolute accuracy in elevation to gain higher relative precision in elevation change detection. Our approach of using ICP registration for baseline and subsequent surveys achieves this. It ensures consistency across subsequent surveys because a systematic error between the true topography and the first survey is automatically included in subsequent surveys. This means that absolute errors in elevation are not propagated into any difference model calculated across successive surveys. We wish to emphasize that the registration procedure used here is optimized for change detection. If the aim was absolute elevation accuracy, the optimal registration procedure might well be different, but this question is beyond the scope of this paper.

3.2.4 Georeferencing, gridding and quality check of DEMs

We georeferenced the registered point cloud using five control points (1A, 1R, 2A, 2C and 2F in Table 3.1) and the locations of the respective ground control points in the registered point cloud. We removed laser reflections from vegetation both manually and with a grid-based minimum

height filter. We opted to use kriging without further testing of other algorithms for DEM interpolation since survey strategy appears to be more important in error generation than the choice of the interpolation algorithm (Bater and Coops, 2009; Heritage et al., 2009), particularly when point density is high enough to yield at least one data point for most of the grid cells. The point clouds were gridded at 0.2 m resolution.

We have deliberately not used GPS position data during point cloud registration in order to use these data as an independent check of the DEM quality. In Table 3.1 we provide a quality check of the resulting DEMs where we compare GPS elevations of check points visible to the scanner with the (gridded) DEM elevation. The residuals range from 0.01 m to 0.14 m. The maximum is found in the second survey at 1R. This highlights a general problem discussed by Brasington et al. (2003): The check point elevation is only an arbitrary point measurement. It is highly unlikely that the check point elevation will match the gridded surface elevation when there is substantial within-grid-cell surface roughness present (see our discussion of elevation ambiguity below). It is important to note that the errors do not increase from the first to the third survey (Table 3.1). This is in stark contrast to our experience with target-based registration, which gave inconsistent results in different surveys.

3.3 Elevation ambiguity of point cloud data

In this section we tackle our first objective: to define a spatial measure of point cloud quality. Elevation ambiguity of point cloud data emerges from erroneous points in the primary data, imperfect point cloud matching and high surface roughness. The distinction between erroneous points and surface roughness is only possible in special cases, so we develop a method to visualize this spatial ambiguity. Where the matching is imperfect the registered point cloud separates into distinct layered traces of points, with each layer containing data from one particular scan station, as shown for a hypothetical example in Figure 3.2A. Clearly, the smaller this layer separation, the better the matching at this particular location. However, matching is never perfect. Therefore, measuring this separation, or point cloud thickness, across the whole data set requires careful consideration. As Figure 3.2A illustrates, point cloud thickness is not just the difference between the maximum and minimum elevation (Δz) (Figure 3.3A), or the standard deviation of elevation σ_{elv} , within a given search window (l): these values are biased by 1) local slope, and 2) roughness elements that

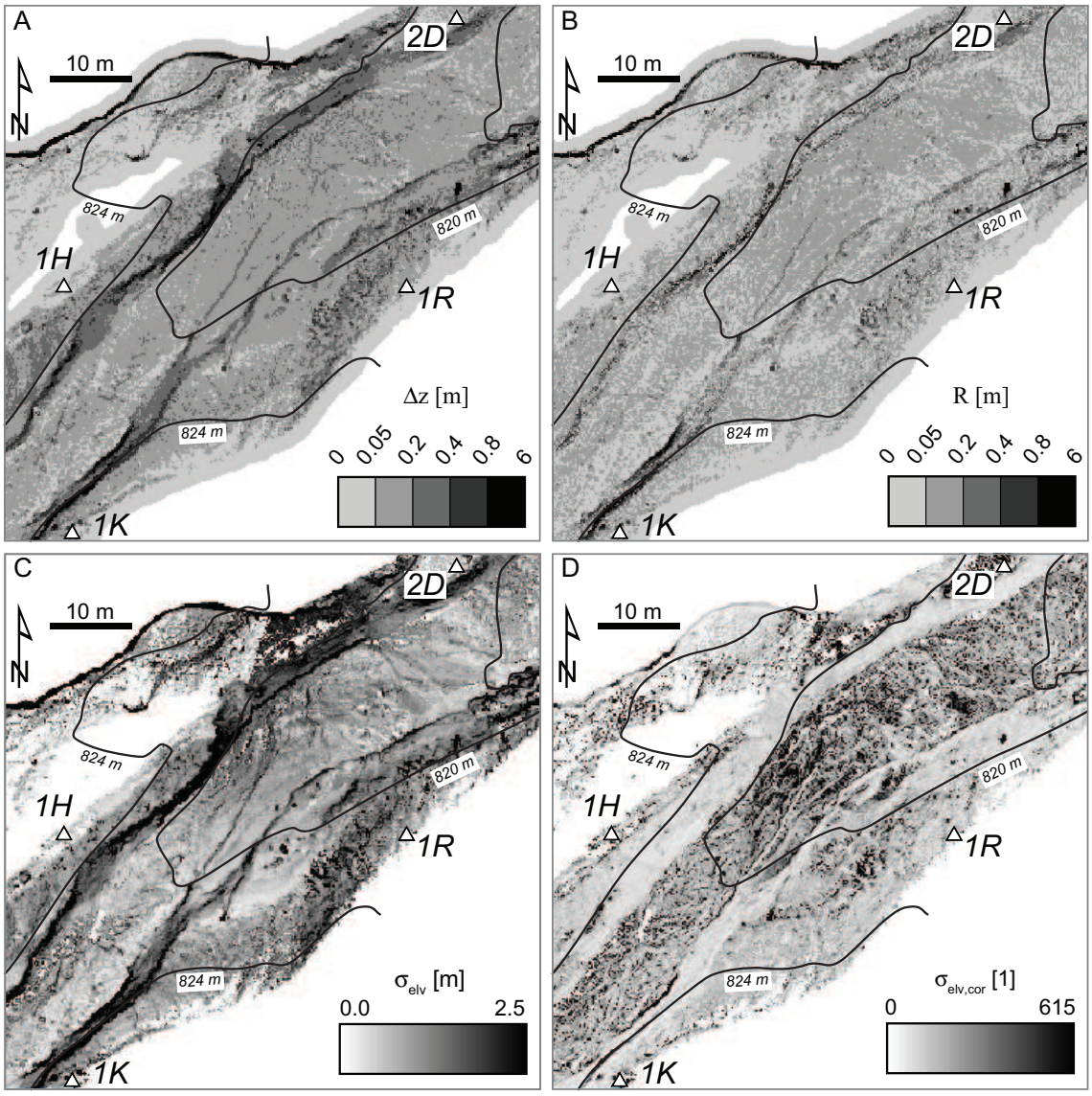

Figure 3.3: *Maps showing derived parameters of elevation ambiguity of the raw data from survey 2. See Figure 3.4C for the corresponding map of point density. Contours are 4 m apart. (A) Map of* Δz*, which is the range in elevation of the raw data that falls into each grid cell of 0.2 m x 0.2 m. (B) Map of topographically corrected range in elevation* $R = \Delta z - \Delta e$ *(Equation 3.1 and 3.2). (C) Map of standard deviation in elevation* σ_{elv} *in each grid cell. (D) Map of standard deviation in elevation corrected for topography* $\sigma_{elv,cor} = \sigma_{elv}/\sigma_{elv,exp}$ *(Equation 3.5).*

fall within the search window. They can easily be corrected for the effect of local slope by simply subtracting the expected change in elevation (Δe) over the distance l as result of local surface slope θ. Although we do not know the true topography, we can grid the point cloud to obtain a slope and an aspect map. Slope and aspect are spatially averaged because they are calculated on a moving window of 3 by 3 cells from the gridded data. We therefore expect uncertainties in elevation in individual cells of the order of $<$ 0.01–0.05 m to have little effect on the values of surface slope and aspect, given typical grid cell sizes of $\approx$0.1–1 m.

We can calculate the expected range in elevation (Δe) as:

$$\begin{aligned} \Delta e &= l \tan\theta \text{ ; when surface aspect is parallel to the grid axes} \\ \Delta e &= l\sqrt{2} \tan\theta \text{ ; when surface aspect is } 45^\circ \text{ to the grid axes} \end{aligned} \tag{3.1}$$

The range of elevation corrected for surface slope then becomes:

$$R = \Delta z - \Delta e \tag{3.2}$$

In Figure 3.3B we show the effect of correcting the range in elevation for topography for our sample data from Illgraben.

In a similar way we can define the standard deviation of elevation corrected for topography, $\sigma_{elv,cor}$, measured within a given search window l. As a measure of point cloud thickness this will be less sensitive than R to individual erroneous points lying above or beneath the main point cloud. To correct for surface slope we estimate the expected standard deviation in elevation $\sigma_{elv,exp}$ using the difference between a hypothetically highest (z_{max}) and lowest (z_{min}) point in every grid cell based on the gridded data (Figure 3.2A) and assuming linear variation of elevation between them. We derive the equation for $\sigma_{elv,exp}$ by calculating the standard deviation of two hypothetical data points (z_{min} and z_{max}, details in Apendix B). By substituting $\bar{z} = \frac{z_{max}-z_{min}}{2}$ and after rearranging we find:

$$\begin{aligned} \sigma_{elv,exp} &= \sqrt{\frac{1}{2}((z_{max}-\bar{z})^2 + (z_{min}-\bar{z})^2)} \\ &= \frac{1}{2}(z_{max} - z_{min}) \end{aligned} \tag{3.3}$$

Then we substitute $z_{max} - z_{min}$, the theoretical elevation range for a DEM grid cell Δe, in Equation 3.3 with Equation 3.1 to obtain a worst-case estimate of the expected standard deviation of elevation for a surface with zero within-cell roughness or misalignment and linear variation in elevation within the cell. Again we distinguish between two cases: a) aspect parallel to the grid axes, and b) aspect parallel to grid diagonals:

$$\sigma_{elv,exp} \leq \begin{cases} \frac{1}{2} l \tan\theta \text{ ; aspect parallel to grid} \\ \\ \frac{1}{\sqrt{2}} l \tan\theta \text{ ; aspect } 45^\circ \text{ to grid} \end{cases} \tag{3.4}$$

where l is the search window, θ the slope of each grid cell. We now define the topographically

corrected standard deviation of elevation as:

$$\sigma_{elv,cor} \equiv \frac{\sigma_{elv}}{\sigma_{elv,exp}} \tag{3.5}$$

$\sigma_{elv,cor}$ is the topographically corrected standard deviation of elevation. It is dimensionless due to the normalisation with the expected standard deviation of elevation $\sigma_{elv,exp}$. Figure 3.3C shows the standard deviation in elevation σ_{elv} over our test area, and Figure 3.3D the corrected value $\sigma_{elv,cor}$. The advantage of both measures, $\sigma_{elv,cor}$ and R, is that the calculation can be automated and performed across the whole data set. A thorough investigation of $\sigma_{elv,cor}$ or R for point clouds from individual scan stations could be used to develop algorithms to improve the quality assessment of ICP registration.

A drawback of calculating $\sigma_{elv,cor}$ and R for the matched point cloud is that we cannot distinguish easily between surface roughness and misalignment, since both will result in a higher value of these metrics. However, areas of poor point cloud matching will show up as either sudden changes or trends in maps of the respective parameter. Take for example a case of three matched point clouds where two overlap across 100% of their extent, and the third overlaps only 50% with the other two. Let us further assume that the third point cloud is slightly rotated around a horizontal axis relative to the others. Both of our measures of point cloud quality will visualize the nature and the spatial extent of the problem, with higher values of $\sigma_{elv,cor}$ or R where all three point clouds overlap. We would also notice an increase in the values away from the rotation axis of the third point cloud. Figure 3.3B and D can be read as maps of elevation ambiguity in the raw data and are helpful in identifying areas of poor point cloud matching, occurrence of erroneous points or areas of increased surface roughness. For example note areas of high ambiguity associated with surface roughness (e.g. in the channel) and with poor filtering of vegetation (10 m to the west of 1R).

3.4 Uncertainty in TLS-derived DEMs

3.4.1 Introduction

In this section we investigate the nature and relevance of processes that may introduce elevation ambiguity into point clouds matched from multiple scan stations (our second objective) and how this elevation ambiguity translates into volumetric uncertainty in change detection (third objec-

tive). Every measurement of a physical quantity is subject to error (Taylor, 1982). In order to deal with this fact we need to 1) understand where errors originate, 2) minimize errors where possible, and 3) quantify how they affect our end result. In our case the desired end result is a net elevation and volume change due to erosion or deposition within the study reach. This number is the product of an often lengthy work flow. During this work flow a number of decisions are required concerning scan resolution, survey layout, point cloud registration, data filtering and gridding. Yet we do not know a priori how the known uncertainties associated with individual aspects of the above list contribute to the combined error in the end product (Buckley et al., 2008). Therefore we tackle this question in a slightly different manner. The foremost problem is that we generally lack higher-quality check data to compare to TLS data. This means that we cannot quantify the absolute error in elevation of a TLS-generated point cloud (or any derivatives from it) in a spatially detailed way. A possible solution to this is to measure the ambiguity (see above) of the matched point cloud data in representing a natural surface and compare it with metrics of the error-generating processes. First we examine how choices of scan grid resolution affect the point density in complex topography. Next we look at the role of laser foot-print elongation as one of the most widely reported sources of error in TLS data (Abellán et al., 2009; Buckley et al., 2008; Hodge et al., 2009; Kaasalainen et al., 2008). Finally we propose a method to put meaningful boundaries of uncertainty on the elevation difference calculated from DEMs which are generated from two successive sets of TLS data. This final step is essential because surface roughness alone introduces elevation ambiguity, irrespective of whether we use matched or single-point-cloud data to generate a DEM.

3.4.2 Relationship between incidence angle and point density

Point density on the ground is controlled by angular scan resolution, distance to the object and incidence angle of the laser beam on the ground (Figure 3.2B). In complex topography, survey planning is essential to avoid data gaps due to occlusion and low point density due to low incidence angles. A good survey layout requires both carefully selected scan stations that provide a large field of view and a good overlap with adjacent scan stations, within the constraints of access and time in the field (Lim et al., 2009).

The maximal scan resolution is limited by the minimal angle at which the laser beam can be rotated between shots. In scanner control software the resolution is often expressed as the point spacing (scan grid) on a sphere with a chosen diameter around the scanner optical centre. This

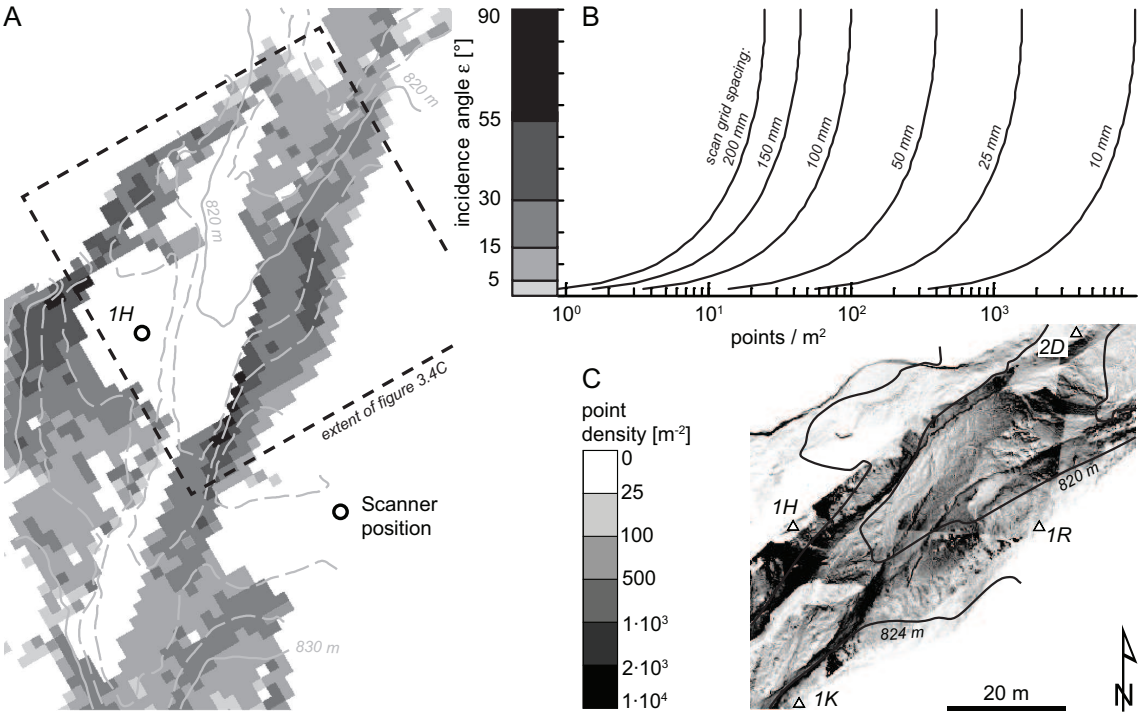

Figure 3.4: *(A) Predicted incidence angle* ε *from Equation 3.6 (see Figure 3.2B for definition) from scan station 1H (optical centre of instrument 1.6 m above ground) based on a DEM with 2 m grid resolution. The DEM was re-sampled from survey 2. White areas are not visible from the position of the instrument. (B) The expected point density on the surface that can be achieved with different settings of scan grid spacing at the distance of the point in question from the scanner. The calculation is based on Equation 3.8 and 3.9. (C) Map of point density for area marked with dashed box in (A). The map incorporates data from six scan stations: 2D, 1H, 1K, 1R and 2C, 2E outside of the test area.*

value can be misleading in terms of achievable point spacing if the laser beam is not normal to the object surface (Figure 3.4B), notably if sub-horizontal surfaces are surveyed. We calculate the incidence angle as a function of the vector between the surface and the laser scanner and the surface normal-vector (Figure 3.2B):

$$\varepsilon = \arcsin \frac{\vec{n} \cdot \vec{b}}{|n|\,|b|} \tag{3.6}$$

$$\vec{n} = \begin{pmatrix} \sin\theta \cdot \sin\alpha \\ \sin\theta \cdot \cos\alpha \\ \cos\theta \end{pmatrix} \tag{3.7}$$

where ε is the incidence angle, $\vec{n}$ is the surface normal vector, $\vec{b}$ is the vector pointing from the surface to the laser scanner optical centre, θ is the dip of the surface and α is the direction of surface dip. Figure 3.4 shows how scanner position, topography and chosen scan grid spacing

translate into point density. We base the incidence angle prediction (Figure 3.4A) on a coarse 2 m DEM of the debris flow channel to illustrate how coarse elevation information (e.g. from airborne LiDAR) could be used to plan a TLS survey. This figure shows that incidence angles of more than 30° only rarely occur on sub-horizontal surfaces. Larger incidence angles mainly occur on surfaces sloping steeply towards the scanner. The maximum point spacing on the surface, d, depends on the chosen scan grid spacing, G, as:

$$d = \frac{G}{\sin \varepsilon} \tag{3.8}$$

Equation 3.8 is a worst case estimate for the maximum point spacing along dip or strike if the projection of the scan grid on the surface is parallel to the strike and dip of the object surface. The minimum point spacing on the object equals the chosen scan grid spacing either along strike or dip and is minimal when $\varepsilon = 90°$. The point density on the surface P is calculated as:

$$P = \frac{1}{dG} \tag{3.9}$$

In Figure 3.4B we combine Equation 3.8 and 3.9 to calculate the point density as a function of the incidence angle for a range of scan grid settings. Figure 3.4 highlights an important problem: while only a small fraction of sub-horizontal areas are surveyed at incidence angles of $> 30°$ (Figure 3.4A), the achievable point density with a given scan grid spacing drops by about 50% when the incidence angle is decreased from 30° to 15° (Figure 3.4B). This implies that stations should be placed close enough to maximise coverage at incidence angles of more than $\approx 15°$. This recommendation potentially leads to a very high number of scan stations, depending on the complexity of the survey area. There are other reasons for minimizing the number of scan stations, such as complexity of the registration process or acquisition time, which we will discuss later.

3.4.3 Influence of laser footprint size on elevation ambiguity

Multiple reflections at sharp edges or at low incidence angles arising from increased laser footprint size result in erroneous points (Hodge et al., 2009). The laser footprint size grows as a function of distance due to beam divergence (Lichti et al., 2002), but also depends on the beam incidence angle. For scanners where the laser beam can be approximated as a cone with an opening angle β (e.g. the Trimble GS200 laser scanner), the laser footprint on a surface inclined to the laser beam

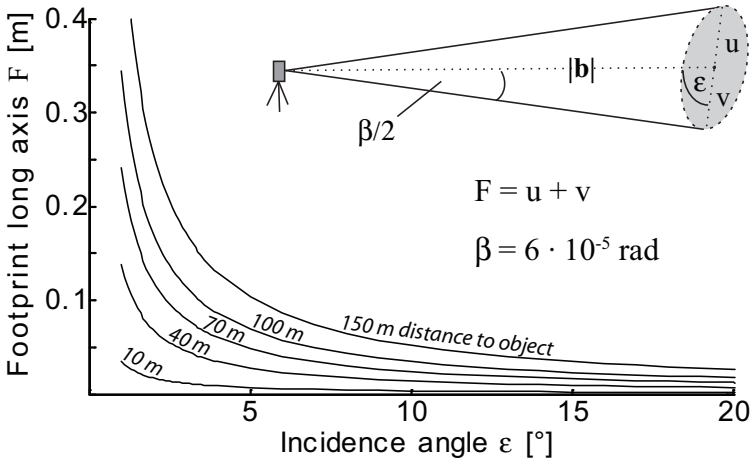

Figure 3.5: *Plot of incidence angle (Equation 3.6) versus laser footprint long axis (Equation 3.10) for a range of distances between laser scanner and object. Inset sketch defines the variables used to calculate footprint long axis (see text).*

is an ellipse, with the length of the long axis $F = u + v$ dependent on the incidence angle ε.

$$\begin{aligned} F = u + v &= \frac{\left|\vec{b}\right| \sin(\beta/2)}{\sin(\varepsilon - \beta/2)} + \frac{\left|\vec{b}\right| \sin(\beta/2)}{\sin(\pi - \varepsilon - \beta/2)} \\ &= \left|\vec{b}\right| \sin(\beta/2) \left(\frac{1}{\sin(\varepsilon - \beta/2)} + \frac{1}{\sin(\varepsilon + \beta/2)} \right) \end{aligned} \tag{3.10}$$

where $\vec{b}$ is the vector pointing from the object to the scanner. In Figure 3.5 we use the beam divergence of the GS200 laser scanner ($6 \cdot 10^{-5}$ rad, Trimble, 2005) to show the relationship between incidence angle ε and footprint size F. Figure 3.5 shows that footprint size only increases dramatically at low incidence angles and at large ranges. Equation 3.10 allows us to retrospectively calculate grids of laser footprint size for our surveys, and to compare the laser footprint size in every grid cell with the corrected standard deviation of elevation, to see whether areas with large laser footprint size coincide with areas of high corrected standard deviation of elevation. Because we are interested in the effect on matched data from multiple scan stations, we consider the area outlined in Figure 3.1 that contains data collected from six scan stations (2D, 1H, 1K, 1R, 2C and 2E). We calculated the laser footprint size grid for each scan station and created a combined grid (Figure 3.6A) using the maximum value of footprint size F_{max} from each scan station as the grid value. We used the maximum value rather than the average to consider the worst possible case. We found no relationship between F_{max} and $\sigma_{elv,cor}$ (Figure 3.6B), except that for small F_{max} (< 0.05 m) there was a slight tendency to lower values of $\sigma_{elv,cor}$. A similar pattern is seen for average rather than maximum footprint size over the six scan stations. The lack of a dramatic

increase in $\sigma_{elv,cor}$ for larger laser footprint sizes indicates that laser footprint elongation at this level of survey complexity (multiple scan stations, high surface roughness and complex topography) has no significant effect on the quality of the primary scan data and also has no effect on our ability to match these point clouds. Although there might be more erroneous points in areas of large laser footprint size than in other parts of the point cloud, these areas are also likely to be less significant in the ICP matching as a result of low point densities due to the low incidence angle (Figure 3.4B). This is beneficial, as laser footprint size is something the user has very little control over. With regard to elevation ambiguities in point clouds merged from multiple scan stations, we conclude that they arise mainly from the complexity of the problem of registering the data rather than from variations in the quality of the raw data of individual scans itself.

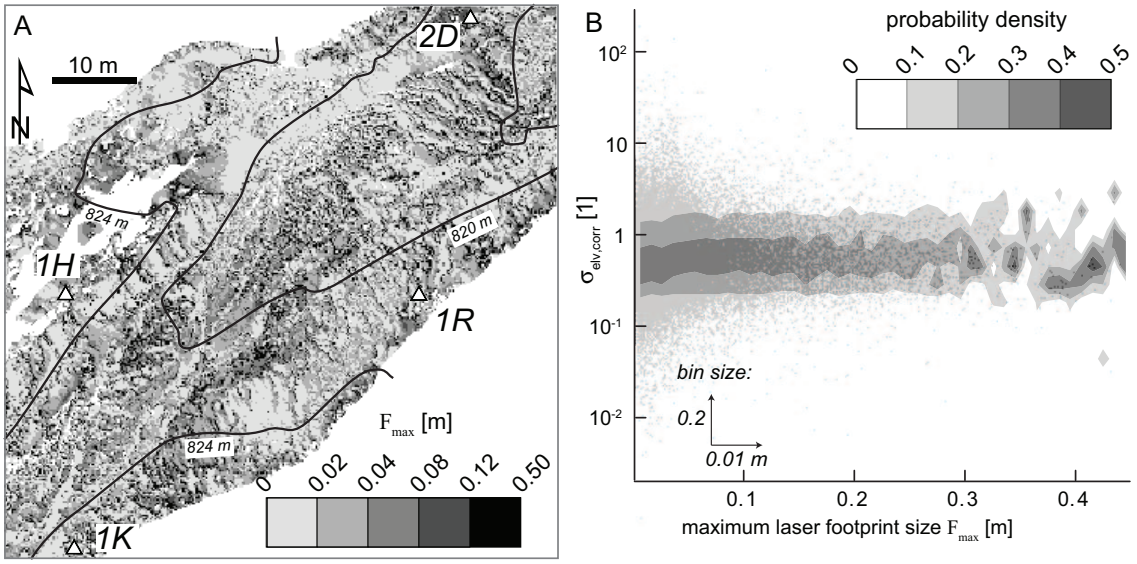

Figure 3.6: *(A) Map of maximum laser footprint long axis for the same six scan stations as in Figure 3.4C. Contours are 4 m apart and the raster data are shown on a 0.2 m grid. (B) Scatter plot of maximum laser footprint vs.* $\sigma_{elv,cor}$ *and probability density plot (data from Figures 3.6A and 3.3D).*

3.4.4 Mitigation of gridding error

The elevation ambiguity we described in previous sections has important implications for the post-processing of TLS data. These data are collected in the field with high point densities (10^2 to 10^4 points/m^2), which may be higher than required for the application. The point density is commonly spatially highly variable (Figure 3.4C). The heterogeneous and ambiguous (in elevation) point cloud that results is difficult to interpret. Gridding is one way of reducing the point cloud to a spatially homogenous format, but high point densities cause an over-defined problem because

every grid cell may contain tens to hundreds of points. Picking an elevation in such a grid cell is not trivial because of the elevation ambiguity: For example the application of a minimum elevation or 'lowest return' filter may not be appropriate because it ignores volume elements extending above this elevation (e.g. sediment grains sitting on the surface). It might also be a bad choice because it is affected by a potential misalignment of the point clouds or by erroneous points of other sources. We therefore identify a need to quantify how much any reasonable choice (given the observed data) for the elevation in each grid cell influences the outcome of a change analysis across two DEMs.

We can describe the elevation in the ith cell of DEM E as:

$$E_i = E'_i + \rho_i = E'_i + [0; R_i] \tag{3.11}$$

where the correction factor ρ_i is a value in the interval $[0; R_i]$ and E'_i denotes the elevation that would be calculated using a lowest return filter (Figure 3.2A). R_i is the topographically corrected range in elevation of the raw data points that fall into this particular grid cell (Equation 3.2). Our subsequent analysis of the effect of the elevation ambiguity on change detection uses R instead of $\sigma_{elv,cor}$ because it takes the dimenson of length and therefore allows calculation of a volumetric error (in m^3). We assume that the true elevation is given by Equation 3.11 but we have no means of obtaining its precise value. Consequently we define the difference model value D in grid cell i as the difference between two DEMs (E_1, E_2) as follows:

$$\begin{aligned} D_i &= E_{2,i} - E_{1,i} \\ &= E'_{2,i} + \rho_{2,i} - (E'_{1,i} + \rho_{1,i}) \\ &= E'_{2,i} - E'_{1,i} + \rho_{2,i} - \rho_{1,i} \\ &= D'_i + \rho_{2,i} - \rho_{1,i} \end{aligned} \tag{3.12}$$

where $\rho_{1,i} \in [0; R_{1,i}]$, $\rho_{2,i} \in [0; R_{2,i}]$ and D'_i is the difference model based on just differencing the lowest return DEMs. The value of the difference model and hence our ability to detect change now depends not only on the absolute differences in elevation but also on the difference in the correction factors applied. For example, if $R_{1,i}$ is larger than D'_i we cannot be sure whether this grid cell has experienced deposition or erosion, because the outcome depends strongly on the particular combination of $\rho_{1,i}$ and $\rho_{2,i}$. In order to quantify the value of the difference model at

a given location we need to consider the distribution of all possible combinations of $\rho_{2,i} - \rho_{1,i}$. In Figure 3.7A we show an example for $R_{1,i} = 0.15$ m and $R_{2,i} = 0.10$ m. Each cell represents a possible combination of $\rho_{1,i}$ and $\rho_{2,i}$. The cells in the top left corner represent outcomes with a net positive effect on the value of the difference model while those in the bottom right corner represent outcomes with a net negative effect. The relative proportions of positive and negative cells are controlled by the relative magnitudes of $R_{1,i}$ and $R_{2,i}$. This raster will be different for each grid cell in a difference model. In Figure 3.7B we show the frequency distribution of the cell values. For practical purposes we need to think about the probability of one particular combination of $\rho_{2,i} - \rho_{1,i}$ occurring, which is related to the issue of ambiguity in point cloud elevation. In every grid cell of each DEM we have recorded a number of points with the laser scanner. We do not know:

1. whether the distribution of elevation values recorded reflects the true distribution of elevation in nature; and

2. how much of R is due to misalignment in the point cloud or erroneous points and how much is due to surface roughness.

Because of this uncertainty, we make the conservative assumption of a uniform distribution to describe the probabilities of each outcome of $\rho_{2,i} - \rho_{1,i}$. This choice puts a high weight on the extreme outcomes (top left and bottom right) in Figure 3.7A, but justification of a different probability distribution would require a fundamentally better understanding of the data. By using a uniform probability distribution we also remove any bias towards our initial choice of E' generated using a lowest return filter. In other words, using a 'first return surface' and subtracting (instead of adding) R would yield the same result.

In this framework, the volume change across n grid cells in the difference model is simply:

$$\Delta V = \sum_{i=1}^{n} D_i \tag{3.13}$$

For each D_i we have a range of equally possible values (Equation 3.13). To investigate the effect of this on the total volume change we perform multiple simulations where we randomly pick a value from the respective $\rho_{2,i} - \rho_{1,i}$ distribution for each D_i value. Here we assume that the uncertainty in adjacent cells is independent. The procedure described accounts for the fact that

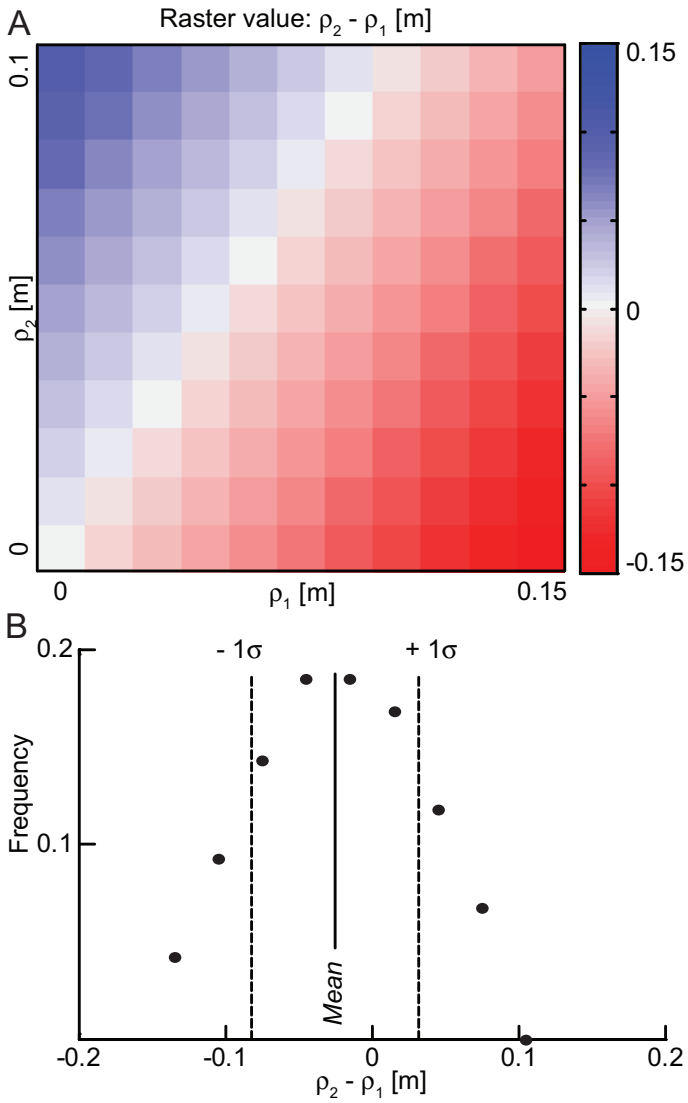

Figure 3.7: *(A) Example of a raster of* $\rho_2 - \rho_1$ *for values of* $R_1 = 0.15$ *m and* $R_2 = 0.10$ *m where* $\rho \in [0;R]$. *The raster shows all possible combinations when varying both values between zero and their respective maxima. (B) Relative frequency distribution of the raster values from (A). This example illustrates that if* $R_1 \neq R_2$ *the mean outcome of random sampling from the raster of* $\rho_2 - \rho_1$ *(A) is different from zero.*

the effects of the elevation ambiguity may to some degree cancel each other out over a larger area. We interpret the range in volumes resulting from this calculation as the aggregated error over the whole work flow. It is important to note that this error is specific to the quality of the raw data, the surface roughness, the work flow and this specific application of change detection.

3.5 Application to surface change calculation

In this section we apply the methodology for quantifying the volumetric error in change detection to two subsequent DEMs of the debris flow channel at Illgraben. We quantified the surface change due to the debris flow on 31 August 2008 using survey 2 and 3. The debris flow had a total volume of ≈11,000 m^3 and a peak discharge of ≈58 m^3/s (measured 500 m upstream of the study reach).

To understand how a debris flow evolves whilst travelling down a channel, it is useful to quantify gain (=erosion) and loss (=deposition) of material as function of down-stream distance. We therefore integrated the difference model along the flow path by dividing the channel into bands of 1 m width oriented perpendicular to the flow path and subsequently calculating the volume change in each band (Figure 3.8A). Note that positive values indicate entrainment (volume gain of the debris flow) and negative values indicate deposition (volume loss of the debris flow). From the DEMs of survey 2 and 3 we calculated maps of aspect and slope with a grid resolution of $l = 0.2$ m. From this we calculated maps of Δe (Equation 3.1) for both surveys. In Matlab we calculated maps of Δz also with a grid resolution of $l = 0.2$ m. Using Equation 3.2 we then calculated maps of corrected range in elevation (R_1, R_2) for both surveys. With this we were able to estimate the volumetric error as outlined in the previous section. We performed 100 simulations in which we picked a random value from the $\rho_{2,i} - \rho_{1,i}$ raster for each grid cell and used it in Equations 3.12 and 3.13. The volumetric error on this local volume change per cross section is shown in Figure 3.8B. The errors are largest where the channel has sub-vertical banks (Figure 3.1) near the top end of the study reach (between 0 and 50 m downstream distance). The width of the gray band reflects the range of deviation from the mean outcome shown in Figure 3.8A. It is worth noting that this deviation is not symmetric because the mean outcome (Figure 3.8A) is calculated based on the mean of all cell values in each $\rho_{2,i} - \rho_{1,i}$ matrix. This mean is different from zero if $R_{1,i}$ and $R_{2,i}$ are different (which is most likely), hence the asymmetry. This has important implications for the cumulative volume change along the study reach, which is summed over a total area of 4,947 m^2 (Figure 3.8C). The dashed line in Figure 3.8C is the result of the uncorrected calculation based on D', the difference model based on two 'lowest return' DEMs, while the solid line within the gray band is the calculation based on D and takes into account the ambiguity in elevation (Equation 3.12). This yields a total likely entrained volume of between 81 m^3 and 92 m^3 based on 100 random simulations, with a mean outcome of 87 m^3 of entrainment. The asymmetry of the

volumetric error causes the shift towards lower net entrainment in the cumulative volume change plot. This means that on average $R_{1,i} < R_{2,i}$. Surprisingly, the actual differences in the means are very small: $\bar{R}_1 = 0.10$ m and $\bar{R}_2 = 0.11$ m. These differences reflect slight changes in surface roughness, changes in data quality or both from one survey to the next. These differences have a significant effect – the difference between dashed and solid line in Figure 8C – on the result of a volume calculation and cannot be ignored.

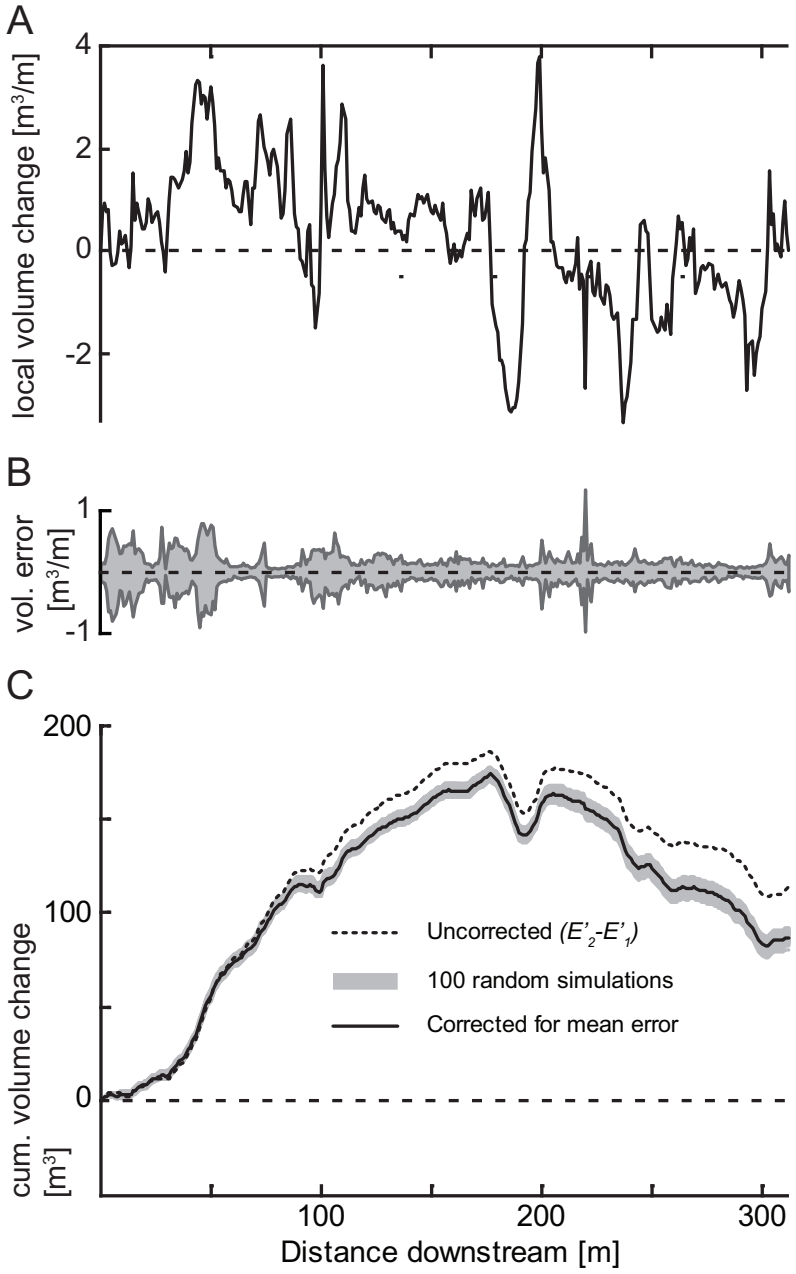

Figure 3.8: *Analysis of surface change as a result of the debris flow that occurred on 31 August 2008, based on the difference model between surveys 2 and 3. The change calculation is limited to the channel area indicated by cross section markers in Figure 3.1. (A) Local volume change in cross sections of 1 m width starting at the upstream end of the study reach. Positive values are entrainment (volume gain of the debris flow) and negative values are deposition (volume loss of debris flow). (B) Volumetric error on local volume change per 1 m downstream distance (A) from 100 random simulations. (C) Cumulative volume change for the uncorrected difference model (dashed black line), for 100 random simulations (gray) and for mean correction (solid black line).*

3.6 Discussion

Our results have some important but perhaps unexpected implications for surveying complex topography with a terrestrial laser scanner. Multiple surface reflections due to laser footprint elongation do not have a significant negative effect on the quality of a matched point cloud at this scale and in a multiple-station survey of this complexity. Also the relative positioning of scan stations has no consistent effect on the ability to register the data using ICP as long as sufficient overlap between both scan stations is provided. However, for any application that makes quantitative use of TLS data, the point cloud quality must be assessed in a spatially consistent manner. This is particularly true for matched point clouds from multiple scan stations. Point cloud quality is controlled by two factors, point density and elevation ambiguity, which we consider here in turn.

The choice of a certain scan grid spacing at a given distance can be very misleading in terms of actual point density on the ground. When scanning sub-horizontal surfaces, incidence angles are likely to be as low as 15° in parts of the scan. In order to collect an average of 100 points/m^2 on such areas (that is, on average one point every 100 mm) the scan grid spacing needs to be 50 mm or less at any given distance between scanner and object. In other words the choice of scan grid spacing should be based on the desired final point density, accounting for the expected incidence angle on the area of interest. Particularly at low incidence angles ($< 40°$), small changes in scan grid spacing have very large effects on point density. While point density far away from the scanner can be increased by decreasing the scan grid spacing, the problems of occlusion remain. Only additional scan stations from different directions with higher incidence angles can address this issue. This is particularly important in complex terrain, because high point densities help the ICP algorithm to converge when matching point clouds from different scan stations.

The second factor in point cloud quality is the elevation ambiguity at a given point. As indicators of point cloud quality we have proposed two measures of point cloud thickness; both include a correction factor for topography that is estimated from the data on a grid basis. The first is standard deviation of elevation $\sigma_{elv,cor}$ (Equation 3.5), a dimensionless measure of average relative point cloud thickness. The second is range in elevation R (Equation 3.2), which is much more sensitive to the extreme points contained in the data set. This use of R relies on two assumptions: firstly that the true surface elevation is somewhere within the range spanned by the data and secondly that the surface variability (that is, the highest and lowest points within a given search window) has been captured completely.

DEMs are a common and convenient way to represent topography, but their construction from point cloud data presents special challenges. Point density in TLS data is always highly variable. This means there will always be empty cells and conversely cells with multiple data points. Areas where there are no data can only be filled by interpolation and there is no way of constraining the uncertainty of the resulting DEM. If we have a number of data points in one grid cell, we can use their elevation information to make a more informed choice for the elevation of this particular grid cell. We have demonstrated one way of doing this in this paper, but there is certainly scope for other solutions. Quite apart from how we tackle the elevation ambiguity in TLS data, however, the choice of grid spacing is important. Clearly, more research is needed into how many data points should ideally be used to assess the elevation in one grid cell, particularly when there are large roughness elements (e.g. sediment grains) within single cells. The answer to this question depends on the surface roughness, the maximum achievable point density in the field and the level of detail we want to represent. However, a tricky problem remains: while the point density is highly variable, the grid spacing is a constant and will never be optimal for the whole data set. One way of dealing with this is the use of triangular irregular networks (Tucker et al., 2001) or other irregular grids, although these may raise other challenges in terms of their wider use and comparability with other data sets.

We have also demonstrated that lowest return filters are problematic for the application of change detection. In change detection it is important to use a volumetrically correct surface – that is, a surface where the positive and negative deviations of the natural surface arising from uncertainty in the point cloud or real roughness elements cancel each other out as much as possible. Otherwise volumes calculated from the comparison of two DEMs will be biased in an undeterminable manner (Figure 3.8C). It is of great importance to determine the value of this volumetric bias – the difference between dashed and solid black line in Figure 3.8C – as it is characteristic of each pair of point cloud data used in a specific change detection study.

However, the danger of using a lowest return filter (or indeed any filter) is that we remove essential information that might tell us where this volumetrically correct surface might be. Rather than trying to construct a volumetrically correct surface (by applying complicated filters) we have proposed a method to assess how our choice for the elevation of one particular grid cell in both surveys affects our ability to detect change (Figure 3.8B). The calculation of this volumetric error is possible because we used a relatively coarse grid spacing compared to the point spacing in the

raw data. With a grid spacing of 0.2 m, using our test data, 10% of cells are empty, another 10% contain only one data point, and 70% of cells contain six or more data points. It could be argued that an even larger grid spacing should be used in our example to reduce the number of empty or sparsely populated grid cells. However, without further investigations into how different grid spacing affects the range of simulation results in Figure 3.8B, it is hard to quantitatively determine the most appropriate grid spacing.

It is important to note that volumetric bias and error are partly dependent on the method of point cloud registration employed but they will never be zero. This is firstly because point cloud matching is never perfect and secondly because changes in surface roughness between surveys are highly likely in many geomorphic environments.

3.7 Conclusions

We have developed a method to quantify volumetric uncertainty in change detection specific to data from terrestrial laser scanning. This method is based on the ambiguity in elevation in the point cloud arising from surface roughness elements, erroneous points and misalignment of multiple point clouds. By deliberately choosing a relatively large grid spacing for the DEMs, we can use the range in elevation of all raw data points that fall into one grid cell to constrain uncertainty in elevation. We estimate the volumetric uncertainty by randomly varying the surface elevation within a reasonable range obtained from the raw data. We have measured an entrained volume of between 81 m^3 and 92 m^3 over an area of 4,947 m^2. This volumetric error is almost completely independent of the measurement error of the instrument, but is strongly affected by survey and processing parameters such as surface roughness, overall complexity of the survey layout, actual point density and DEM grid spacing.

The elevation ambiguity in data from surveys of complex topography, incorporating multiple scan stations, appears to arise primarily from imperfect point cloud registration and surface roughness. Previously-documented effects such as multiple surface reflections due to laser footprint elongation on meter-scale objects (Hodge et al., 2009) appear to have no significant effect on point cloud quality at the level of survey complexity and size presented in this study.

The main difficulty in TLS surveying is to ensure a minimum point density in all areas of interest. Point density is very sensitive to the incidence angle and to the user-defined scan grid

spacing. The minimum point density required should be informed by the surface roughness and the desired grid spacing of the DEM. Areas of higher surface roughness should be scanned at higher resolutions to ensure capture of the full range in elevation of a surface. Point density should be high enough for most DEM cells to contain multiple data points. Locations for scan stations should therefore be chosen in order to maximise incidence angle (at least 15° for most of the scanned area). With regard to point cloud registration we recommend to ensure significant overlap between scan stations; the specific scan station positioning is of minor importance.

Chapter 4

Dynamic controls on erosion and deposition on debris-flow fans

Abstract

[1] Debris flows are amongst the most hazardous and unpredictable of surface processes in mountainous areas. This is partly because debris-flow erosion and deposition are poorly understood, resulting in major uncertainties in flow behavior, channel stability and sequential effects of multiple flows. Here we apply terrestrial laser scanning and flow hydrograph analysis to quantify erosion and deposition in a series of debris flows at Illgraben, Switzerland. We identify flow depth as an important control on the pattern and magnitude of erosion, whereas deposition is governed more by the geometry of flow margins. The relationship between flow depth and erosion is visible both at the reach scale and at the scale of the entire fan. Maximum flow depth is a function of debris flow front discharge and pre-flow channel cross section geometry, and this dual control gives rise to complex interactions with implications for long-term channel stability, the use of fan stratigraphy for reconstruction of past debris flow regimes, and the predictability of debris flow hazards.

[1] Schürch P., Densmore A.L., Rosser N.J. and Mc Ardell B.W. (2011). Dynamic controls on erosion and deposition on debris-flow fans,*Geology*, doi: 10.1130/G32103.1

4.1 Introduction

Debris flows are a ubiquitous hazard in mountain areas, not least because of their ability to avulse from an existing channel and inundate adjacent areas on debris-flow fans (Jakob and Hungr, 2005; Rickenmann and Chen, 2003). The avulsion probability is controlled mainly by the ratio of flow peak discharge and channel conveyance capacity. While the latter can be estimated from field measurements (Whipple and Dunne, 1992), both parameters can change rapidly during a flow due to erosion and deposition along the flow path (Fannin and Wise, 2001). This not only makes it difficult to predict the temporal evolution of an individual flow, but also changes the boundary conditions for the next flow in that channel. There results a critical need to understand the dynamic relationships and feedbacks between debris flow volume and the changes in channel topography due to erosion and deposition as the flows traverse a fan.

Previous studies have focused more on debris-flow deposition than on the mechanics of erosion, and published work on erosion is partly contradictory. Takahashi (2007) found that the concentration of coarse particles in a debris flow increases with bed slope, and that erosion is only possible when the flow is undersaturated in coarse particles. But field observations, however, indicate that erosion occurs mostly during passage of the granular flow front (Berger et al., 2011), and is likely associated with impacts of coarse sediment on the bed. Iverson et al. (2011) explored the role of bed properties and found a positive correlation between erosional scour depth and bed water content. Debris-flow deposition has been related to channel gradient (Cannon, 1989; Fannin and Wise, 2001; Hungr et al., 2005; Hürlimann et al., 2003), downstream channel widening (Cannon, 1989; Fannin and Wise, 2001), or flow volume, based on an observed power-law relationship between flow volume and total inundated area (Griswold and Iverson, 2008). More generally, detailed monitoring of experimental flows (Major and Iverson, 1999) and physically-based description of fluid-solid mixtures (Iverson, 1997) have related flow mobility to granular temperature, defined as the mean square of particle velocity fluctuations, and excess pore-fluid pressure (McCoy et al., 2010). These effects are counteracted by friction at the dry coarse-grained flow margins (Major and Iverson, 1999).

The objective of this study is to understand the interaction between a debris flow and the channel bed by systematically measuring erosion and deposition in a series of natural flows at both the reach and fan scales. We hypothesize, based on the results of Berger et al. (2011), that

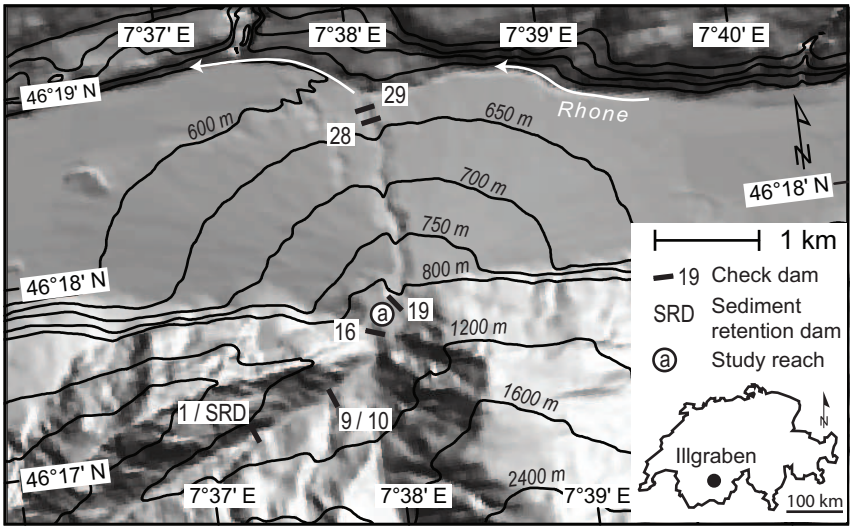

Figure 4.1: *Overview of the Illgraben catchment and fan in southeastern Switzerland. Tributary joining downstream of check dam (CD10) is inactive due to hydro-power dam in headwaters. Geophones are mounted on CDs 1, 9, 10, 28 and 29. Flow stage measurements are taken at CD10 (radar) and 29 (laser and radar). Study reach is located between CD16 and 19. Contour interval is 50 m on the fan and 400 m for altitudes above 800 m a.s.l. Digital elevation model DTM-AV©2011 published with permission from Swisstopo No: 5704 000 000.*

local bed elevation change is related to basal shear stress (and thus to maximum flow depth) and flow volume. We use a terrestrial laser scanner (TLS) to determine high-resolution reach-scale measurements of erosion and deposition in a natural channel caused by four debris flows. We then relate these data both to flow depth and to fan-scale flow volume changes estimated from debris-flow hydrographs.

4.2 Study area

The Illgraben debris flow fan is situated in the Rhone valley, Switzerland (Figure 4.1) and has a long history of debris flows (Lichtenhahn, 1971; Marchand, 1871). The fan has an area of 6.6 km^2 with a radius of 2 km and a gradient that decreases from 10% to 8% down-fan (Schlunegger et al., 2009). The bedrock geology in the catchment is dominated by schist, dolomite breccia and quarzite (Gabus et al., 2008). The lowermost bedrock along the Illgraben channel outcrops just below a sediment retention dam (check dam 1, Figure 4.1); downstream the channel bed consists of unconsolidated sediments. Convective storms from May to September trigger three to five debris flows per year (McArdell et al., 2007). In the 1970s a series of concrete check dams (CD) were constructed to limit erosion and control the channel position on the fan (Lichtenhahn, 1971). Flow hydrograph and onset data are available from two gauging stations at CD10 near the fan apex

(Figure 4.1 Badoux et al., 2008) and CD29 at the fan toe (McArdell et al., 2007). Since 2007 we have monitored the channel bed using TLS in an unconfined 300 m study reach between CD16 and 19 (Figure 4.1).

4.3 Methods

We surveyed the study reach before and after debris flows using a Trimble GS200 terrestrial laser scanner yielding point clouds of $\approx 10^7$ vertices per survey. Data from individual scan positions and subsequent surveys were merged into one coordinate system using an iterative closest point matching algorithm (Besl and McKay, 1992). We gridded the data to a 0.2 m resolution DEM and calculated difference models (Figure 4.2) from subsequent surveys; this yields a conservative estimate for erosion because it includes deposition in the falling limb of the flow hydrograph (Berger et al., 2011). For each flow, we mapped maximum inundation limits from levees and mudlines along the channel, and interpolated these to a 0.2 m resolution maximum flow stage surface. Our estimated uncertainty on this surface is ± 0.25 m, given the difficulties in identifying the mudline in the field due to splashing and poor preservation. The maximum flow stage surface is a lower estimate as the flow surface is generally convex up in cross section. Flow depth was taken as the difference between the maximum flow stage surface and the pre-event DEM. We analyzed the relationship between flow depth and channel change via a cell-by-cell comparison of flow depth with the difference model (Fig. 3A).

To understand how fan-scale flow volume change relates to flow properties, we estimated volumes and debris flow front heights from the first surge for 14 debris flows in 2007–2009 (Table C.1 in Appendix C) from flow hydrographs measured at the CD10 and CD29 gauging stations. From measurement of the front velocity of each flow, we calibrated a Manning-type friction relation (Schlunegger et al., 2009) to estimate mean flow velocity as a function of flow stage (Appendix C). The friction relation is then used to integrate the hydrograph over the event duration to obtain the total flow volumes at both the apex (CD10) and toe (CD29) of the fan.

4.4 Results

The difference DEMs for events 11 and 14 (Figure 4.2) show that both events caused net erosion within the study reach, leading to increases in flow volume of 87 $\pm$ 6 m^3 and 2,039 $\pm$4 m^3, respectively, but that the spatial patterns of erosion and deposition are very different. Event 11

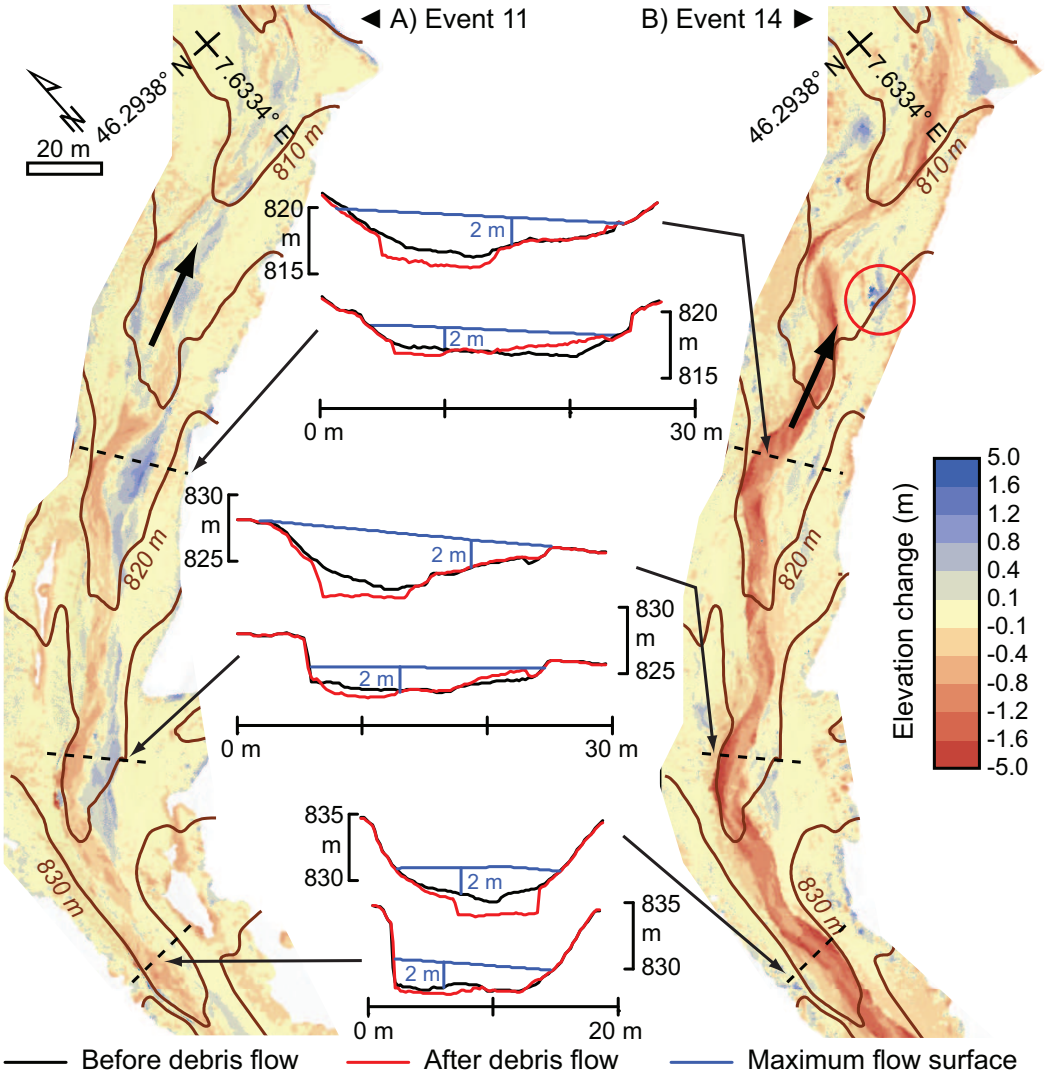

Figure 4.2: *Difference DEMs (0.2 m cell size) for (A) flow 11 and (B) flow 14. See Appendix, Table C.1, for flow details. The background hillshade image represents pre-event topography. Color scale values indicate surface elevation change during the flow; elevation change less than ±0.1 m is shown in white due to uncertainty caused by small-scale surface roughness. Center panels show elevation change in selected cross sections; black line indicates pre-event topography, red line indicates post-event topography, and blue line indicates maximum flow stage in the channel. Contour interval is 5 m. Red circle (panel B): boulders deposited over-bank.*

shows alternating regions of erosion and deposition, with erosion along the deepest parts of the channel and on the outside of bends, and discontinuous levee deposits along the flow margins and on shallow terraces (Figure 4.2A). The maximum discharge in this event was 60 m^3/s calculated at CD10. In event 14, the deepest parts of the channel were eroded continuously throughout the reach; zones of deposition correspond to localized over-bank spill and several large boulders (Diameter 2 m) have been emplaced along the flow margins (Figure 4.2B). The average flow depth in the channel was substantially larger than in event 11 and we estimate a maximum discharge of 630 m^3/s at CD10.

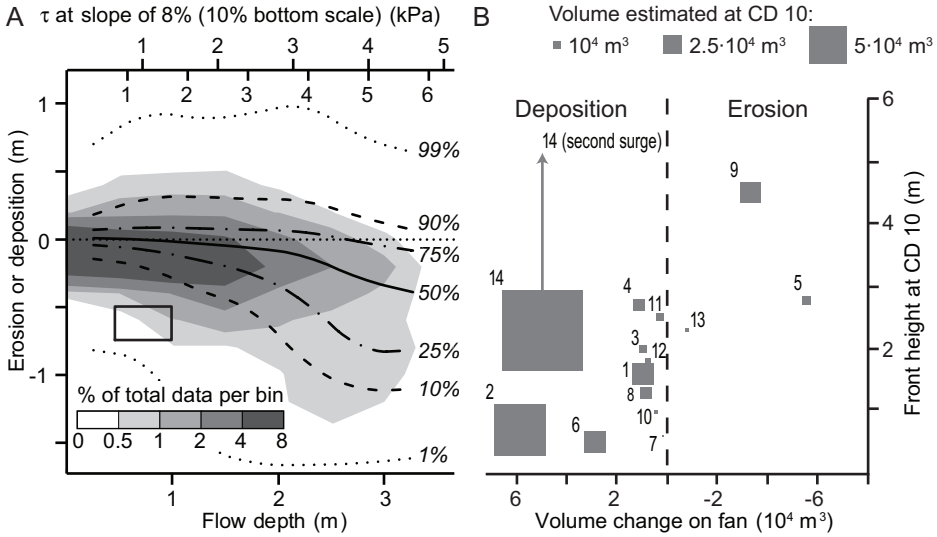

Figure 4.3: *A: Percentile plot of cell by cell comparison of elevation change (erosion or deposition) against maximum flow depth for events 9, 11, 12, and 14. Top axis shows estimated basal shear stress for channel slopes of 8% (above) and 10% (below). Gray shades show contours of raw data density based on bin size of 0.5 m in flow depth (shown by solid box). Ensemble of percentile lines illustrates frequency distribution of elevation change at any given flow depth. Total number of data points is 565,344. For individual events, see Appendix C. B: Fan-scale flow volume change against flow front depth at check dam 10 (CD10) for 14 events between 2007 and 2009. Numbers next to symbols indicate event number. For flow details, see Appendix, Table C.1. Box width indicates event volume at CD10. Volumes include both water and sediment. Arrow indicates height of second surge in event 14.*

By combining estimated maximum flow depth in each grid cell with the measured elevation change in that cell for events 9, 11, 12 and 14, we can evaluate the effect of flow depth on the probability of erosion or deposition (Figure 4.3A). The data illustrate two important observations: that substantial erosion is more likely with increased flow depth, but also that a broad range of outcomes is possible at any given flow depth.

Flow depth also appears to control debris-flow behavior at the fan scale. Of the 14 events in Figure 4.3B, 11 led to net deposition on the fan and three (5, 9, 13) to net erosion when comparing flow volumes at CD10 and CD29. All erosive events had front heights greater than 2.3 m, and all depositional events (except 14) had front heights less than 2.7 m. Event 14 consisted of two surges within the first 17 s with front heights of 2.3 m and 5.2 m respectively. By CD29, only a single surge was discernable, with a front height of 2.5 m. At the fan scale this event was clearly depositional (Figure 4.3A). However, visual inspection of the channel showed that it was highly erosive on the upper part of the fan (between CD10 and 19), including the study reach (Figure 4.2B), while downstream of CD19 we observed widespread deposition on inset terraces.

4.5 Discussion and conclusions

We have established a unique record showing correlation between flow depth and erosion or deposition in debris flows (Figure 4.3A). At flow depths of less than 1.5 m the probability distribution function (PDF) of bed elevation change approaches symmetry around zero: erosion and deposition are equally likely. As flow depth increases, the PDF widens to include the possibility of high erosion values, while the probability of deposition decreases moderately. At a flow depth of 1–2 m the probability of deposition is up to 50%, while at a depth of 3 m the probability of deposition is less than 25%. Flow depth exerts a much stronger influence in the erosional domain: the 10%, 25% and 50% quantiles of erosion all show an increase at flow depths greater than ≈ 2 m. Furthermore, between 2 and 3 m flow depth, the likely amount of erosion at any given probability level approximately doubles.

Flow depth is largest at the debris flow front (Iverson, 1997; McArdell et al., 2007) and the majority of erosion takes place during its passage (Berger et al., 2011). The flow depth at the front influences the forces acting on the channel bed via three mechanisms: higher basal shear stress, the impact stresses of coarse particles recirculating in the flow front (Hsu et al., 2008; Stock and Dietrich, 2006; Suwa, 1988), and hydraulic pressure at the flow front that may cause rapid undrained loading (Hungr et al., 2005) and liquefaction of the channel bed (Sassa and Wang, 2005). Although all three processes may be relevant here, we lack data on the second and third mechanisms. We can evaluate the first by converting flow depth to basal shear stress (Figure 4.3A), defined as $\tau_b = \rho_b g h S$ where ρ_b is density, g is gravity, h is flow depth and S is channel slope. Taking an observed median density of debris flow fronts at Illgraben of 1,800 kg/m^3 (35 events) and slopes of 8%–10%, we find that substantial erosion takes place when a basal shear stress of 3–4 kPa is exceeded, which is consistent with erosion monitoring near CD29 (Berger et al., 2011). Whether this shear stress reflects an effective strength of bed material, or is instead analogous to a threshold shear stress for fluvial entrainment, is not clear from our data. Other effects such as grain impact (Berger et al., 2011) or antecedent moisture conditions of the bed (Iverson et al., 2011) are relevant as well.

In contrast, debris-flow deposition occurs dominantly along the flow margins and where the flows spread over low-relief areas adjacent to the channel (Figure 4.2). As has been argued elsewhere (e.g. Cannon, 1989; Fannin and Wise, 2001; Major and Iverson, 1999) this pattern is consis-

tent with the triggering of deposition by increased friction along the flow margins, and by changes in local channel geometry. This is illustrated in Figure 4.2 by substantial deposition in the lower, wider cross-sections rather than the narrow upstream section of the reach.

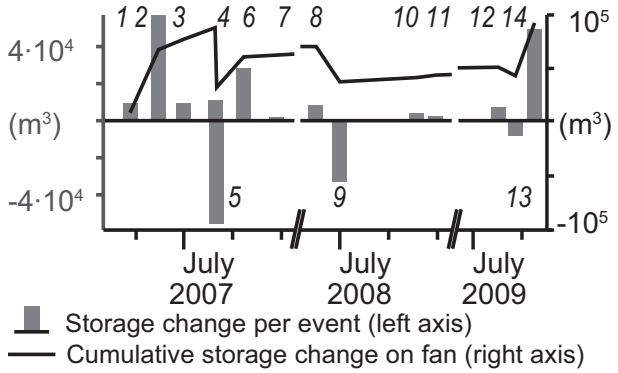

Figure 4.4: *Time series of erosional (negative) or depositional (positive) volume change per event, calculated as the difference between volumes at CD10 and 29 (gray bars) with event numbers (Appendix, Table C.1) and cumulative volume change (black line).*

If debris-flow front height is a key variable in determining flow behavior, then what are its primary controls? Front height is proportional to discharge but is dynamically adjusted as the channel cross-section geometry changes along the flow path. Sudden changes in channel geometry can reduce the maximum flow depth and cause both over-bank deposition and, critically, a decrease in basal shear stress within the channel, potentially leading to the onset of in-channel deposition (Cannon, 1989). Front height is also likely to vary with the proportion of the coarse sediment fraction. Coarse debris flow fronts have very low fluid pressures (Iverson, 1997; McArdell et al., 2007), leading to the analogy of these steep and dry flow fronts as mobile dams (Major and Iverson, 1999). As a thought experiment, consider such a mobile dam with a triangular cross-section in a channel ~ 4 m deep and 10 m wide, implying a total of ~ 160 m^3 of material to build. Because coarse particles are recirculated in the flow front (Iverson, 1997; Suwa, 1988) a debris flow probably requires a multiple of this volume to sustain the mobile dam, but even this is a small amount of material compared to typical Illgraben flow volumes (Appendix, Table C.1). Thus, the loss of even moderate volumes of coarse debris to levee deposition may lead to a fundamental downstream change in behavior as flow height decreases. Event 14, which showed a rapid downstream transition from dominantly erosional to dominantly depositional behavior, may represent an example of this process.

Our findings also have implications for the channel evolution over the course of sequential events. Figure 4.4 shows per-event and cumulative fan-scale changes in flow volume, indicating three phases of aggradation each followed by an erosive event. The state of the channel changes as a result of these events: in events with a very high front we expect deposition on the channel banks and erosion along the center-line (e.g., Figure 4.2B); a medium front height in the same channel might only erode along the center line; and events with even smaller flow fronts might gradually fill the channel by deposition of lobes and inset levees. As a result, similar consecutive events entering the apex of the fan will experience a different channel cross-section than their predecessors and will undergo different downfan changes in volume increase or loss. The cycles of filling and evacuating the channel observed here are evocative of larger-scale autocyclic storage and release of sediment on alluvial fans (Kim and Muto, 2007; Kim et al., 2006) and have major implications for the preservation of debris-flow fan stratigraphy, even in the absence of temporal variations in external controls such as climate, tectonics or changes in sediment supply. In addition, the lack of correlation ($R^2 = 0.0004$) between flow volume and front height (Figure 4.3B) means that (perhaps counter-intuitively) flows with larger total volumes may not necessarily pose the greatest hazard of avulsion. The dependence of flow volume change on the local channel characteristics and the history of previous flows are likely to complicate efforts to define hazard by establishing magnitude-frequency distributions for particular catchments (Hungr et al., 2008; Jakob, 2010; Jakob and Friele, 2010; Zimmermann et al., 1997) without a better understanding of downstream flow evolution.

Chapter 5

Debris-flow fan evolution modeling using a reduced-complexity model

Abstract

[1] Debris-flow fan evolution on time scales of decades to tens of thousands of years is poorly understood because the cumulative effects of erosion and deposition in successive events are rarely well documented, and numerical models which attempt to simulate this are lacking. Enhancing this understanding is crucial to assess the role of both autogenic (internal) and allogenic (external) forcing mechanisms on building debris-flow fans. Over short time scales understanding fan evolution is intimately linked to debris-flow hazard assessment. In this paper I propose a new 2D reduced-complexity model to assess debris-flow fan evolution. The model builds on a broad range of qualitative and empirical observations on debris-flow behaviour, as well as on direct monitoring data from active debris-flow channels. I formulate a framework of rules that govern debris-flow behaviour, that allows efficient implementation in a numerical simulation of fan construction. I demonstrate that my model replicates the general behaviour of alluvial fans in both nature and in flume experiments. Using three applications of the model I demonstrate how fan evolution modeling improves understanding and interpretation of inundation patterns, fan surface age distribution and fan surface morphology.

[1] This chapter is in preparation for submission to *Journal of Geophysical Research – Earth Surface*, but the conceptual framework of the model is already published in: Schürch P., Densmore A.L., Rosser N.J., Mc Ardell B.W. (2011). A novel debris flow fan evolution model based on debris flow monitoring and LIDAR topography, *in* R. Genevois, D. Hamilton and A. Prestininzi (eds), *5th International conference on debris-flow hazards – mitigation, mechanics, prediction and assessment; Padua, Italy 14–17 June 2011*, Casa Editrice Universita La Sapienza. p.263–272

5.1 Introduction

Debris-flow fan evolution on time scales of decades to millenia is poorly understood, but understanding behaviour at this time-scale is crucial to assess the role of external forcing such as catchment processes, climate, changes in base level or tectonics. A large number of researchers have investigated the morphology of debris-flow deposits at both the scale of individual flows (Blair and McPherson, 2008; Costa and Fleisher, 1984; Kim and Lowe, 2004; Major, 1997; Major and Iverson, 1999) or at fan-scale (Dühnforth et al., 2007; Frankel and Dolan, 2007; Helsen et al., 2002; Jakob and Friele, 2010; Stock et al., 2008; Volker et al., 2007). Interpretation of fan morphology is hindered by a lack of understanding how debris-flow properties, such as input flow volumes, deposit geometry, bed saturation or sediment concentration affect fan morphology over time.

The role of autogenic processes acting on debris-flow fans is poorly understood (Chapter 4; Dühnforth et al., 2008; Whipple and Dunne, 1992). For alluvial fans it has been shown convincingly that the separation of autogenic and allogenic processes is important, but not always possible, to understand fan stratigraphy and morphology (Bryant et al., 1995; Clarke et al., 2010; Jerolmack and Paola, 2010; Kim and Muto, 2007; Kim et al., 2006).

Debris-flow properties such as volume, sediment concentration and boulder concentration in natural debris flows are highly variable and originate from poorly understood mechanisms operating in the catchment-fan system (Hürlimann et al., 2003; Marchi et al., 2002; McArdell and Berger, 2010; Okuda et al., 1977; Schlunegger et al., 2009; Suwa, 1988; Suwa et al., 2009; Suwa and Okuda, 1988; Whipple and Dunne, 1992). Whilst these parameters are difficult and expensive to measure in the field, numerical flow modeling and systematic observation of flows suggests that this variability exerts a strong control on the flow velocity, peak discharge, pore-fluid pressure, flow mobility and deposit geometry (Chapter 4; Griswold and Iverson, 2008; Iverson, 1997; Iverson et al., 2010; Julien and Paris, 2010; Major and Pierson, 1992; McCoy et al., 2010; Whipple and Dunne, 1992).

By implication there is an urgent need to incorporate such observations on debris-flow behaviour at the level of individual flows into a numerical fan evolution model. Such a model will then allow investigation of the interactions between process and developing form on debris-flow fans over multiple events, and it will increase understanding of the controls on some of the most

simple measurable features of fan morphology such as slope, roughness, and presence or absence of channels. In this chapter I propose such a model, where I formulate rules for debris flows based on monitoring data (Chapter 4; Berger et al., 2011) and more general observed behaviour (Berti and Simoni, 2007; Blair and McPherson, 1998; Cannon, 1989; Fannin and Wise, 2001; Griswold and Iverson, 2008; Iverson et al., 1998; Takahashi, 2007).

First, I review existing work on numerical modeling of alluvial fans and debris flows, which I use to justify the modelling approach chosen. Next I consider what is known about the relationship between fan morphology and characteristics of the input flux of water and sediment to a fan system. This is important to assess the validity of the proposed model in absence of actual direct calibration data. A detailed review on the mechanics of erosion and deposition at the level of single debris flows together with my own observations at Illgraben are given in Chapter 4.

5.1.1 Numerical modeling of alluvial fans

A first class of models has been developed to examine the filling of accommodation over geological time scales by sediment which is transported by fluvial processes. Such alluvial fan or fan-delta models were commonly based on general formulations of sediment transport and flow resistance that average deposition in space and time (De Chant et al., 1999; Parker et al., 1998). For example, in the model of Hardy and Gawthorpe (1998) sediment was transported at a constant rate by a random walk algorithm from the source to the shore line.

These models had no actual representation of channels in the topography, although a more recent model by Sun et al. (2002) was based on a cellular approach capable of representing channelized flow. Many of these models have operated on a rectangular grid (e.g. Coulthard et al., 2000; Sun et al., 2002), but model behaviour can be very sensitive to the grid orientation and spacing (Nicholas and Quine, 2007a). Nicholas and Quine (2007a) proposed a numerical fan evolution model with a radial grid focused at the fan apex to represent the fan surface and a channel network represented by node positions, and explicitly included a process-form feedback at the channel scale in order to regulate the system response to erosion and deposition. The approach followed by Nicholas and Quine (2007a) seems to be an interesting starting point for a debris-flow fan evolution model because of the use of a radial grid and explicit inclusion of channels.

However these alluvial fan models cannot be used to model debris flows because of a range of reasons: Fluvial processes operate more continuously in time, changes to the surface morphology

take place gradually and the sediment flux and maximum transportable grain size are typically limited by the flow velocity or the available stream power. In contrast debris flows are events with a finite duration and a well defined spatial extent. Debris flows self-channelize by thalweg erosion and deposition of levees (Blair and McPherson, 2008) but may be subject to abrupt avulsion, whereby relatively small sediment volumes deposited in critical places along the channel can force subsequent flows or flow surges in new directions (Blair and McPherson, 2008; Whipple, 1992). In a single debris flow all available grain sizes are transported such that debris flow deposits show limited or no down-fan fining (Blair and McPherson, 2008; Kim and Lowe, 2004). Observations imply that erosion in debris flows may be largely a function of the inertial stresses induced by coarse particles carried in the flow front and impacting on the bed (Chapter 4; Hsu et al., 2008; Stock and Dietrich, 2006). None of the first class of models includes these effects explicitly.

5.1.2 Modeling debris flows

The second class of models was designed to model sediment transport by single debris flows in a physically correct manner (Chapter 1; Christen et al., 2010; Denlinger and Iverson, 2001; Iverson, 1997; Patra et al., 2005; Pudasaini et al., 2005; Scheuner et al., 2009; Takahashi, 2007). They are based on grain-fluid mixture theory and yield depth-averaged equations for momentum and mass conservation. At the moment they assume constant mass. A major finding from simulations based on these models was that the total flow resistance depended more on boundary geometry than on boundary shear stress (Denlinger and Iverson, 2001). This is important for understanding how channel geometry affects flow behaviour. These models are not suitable for simulating fan development over long time scales because of their numerical complexity and long run times. Individual model runs can take from several minutes up to several hours depending on size and resolution of the model space. This problem was discussed in detail in Dalbey et al. (2008) with the application of hazard assessment in mind, where due to the uncertainty of input parameters hundreds of runs are necessary to explore the range of possible outcomes.

Empirical and semi-empirical approaches (e.g. Berti and Simoni, 2007; Gamma, 1999; Griswold and Iverson, 2008; Iverson et al., 1998; Rickenmann, 1999, 2005; Scheidl and Rickenmann, 2011) were often written with an application in regional hazard assessment in mind. These models run much faster, but make compromises with regard to the representation of the physics of debris flows.

For some applications the main interest lies in predicting only the inundation area of a flow of given volume over given terrain. This can be achieved at lower computational costs using empirical or semi-empirical relationships. Griswold and Iverson (2008); Iverson et al. (1998) and Berti and Simoni (2007) found a power-law relationship between total flow volume V and inundated planimetric area B:

$$B = \alpha V^{2/3} \tag{5.1}$$

where α is a site-specific coefficient determined by regression. The smallest values of $\alpha = 6$–7 were reported by Crosta et al. (2003) for 138 granular debris flows with volumes of 2 to 10^5 m^3 (Central Italian Alps). A value of $\alpha = 20$ was reported by Griswold and Iverson (2008) from a worldwide data set of 44 non-volcanic debris flows ranging in volume from 10 to 10^7 m^3. Berti and Simoni (2007) suggested $\alpha = 33$ based on a data set of 24 granular debris flows with volumes of 500 to $5{\cdot}10^5$ m^3 in the Italian Alps.

The rate of deposition or erosion is a key parameter for understanding how debris flows interact with their bed and banks, and thus build topography. This two-way exchange of material between the debris flow in motion and the channel bed is called the lag or yield rate (Cannon, 1989; Hungr et al., 1984). The lag rate is defined as a volume per unit downstream distance that is lost ($dV/dx < 0$) or gained ($dV/dx > 0$) by the flow. Most difficult to predict is the erosion depth for transport-limited conditions (Abanco and Hürlimann, 2011; Gertsch, 2009; Hungr et al., 2005, 1984), and it is highly variable in different settings (Hungr et al., 2005). Material can be incorporated into the flow by lateral erosion of the banks, bank collapse or entrainment of material from the channel bed, and only repeat monitoring of debris flow channels before and after flows provides the necessary data to understand and quantify these processes (Chapter 4; Berger et al., 2011; Iverson et al., 2011; Jakob, 2010). More details on the mechanism of entrainment are discussed in Chapter 4.

The rates of deposition in a debris flow are closely linked to the runout length (Cannon, 1989; Fannin and Wise, 2001; Rickenmann, 2005). As a debris flow enters channel reaches with lower gradients, deposition becomes progressively more important, and eventually comes to dominate over erosion, leading to a net loss of flow volume (Cannon, 1989; Fannin and Wise, 2001; Hungr et al., 2005; Hürlimann et al., 2003; Rickenmann, 2005). The rate of deposition may increase dramatically on the lower parts of a fan where levee deposition is replaced by lobe formation (Blair

and McPherson, 2008). Despite these general observations, there remains no simple rule for the onset of deposition. Fannin and Wise (2001) have shown that channel confinement plays a major role in triggering deposition. Cannon (1989) showed for one particular debris flow that channel geometry (triangular vs. rectangular section), channel width and strength or rheology of the flowing debris influence the rate of deposition. Other researchers have proposed that deposition starts at a particular bed slope angle, ranging from 3.5° to 40° Hungr et al. (2005). These data are derived from a great variety of debris flows, comprising ranges in for example volume, composition, channel geometry, and show that slope alone is not a good predictor for the onset of deposition. Work by Iverson (1997) suggested that flow behaviour is best described by the granular temperature (Chapter 1 and 4) in the sense that material with a high granular temperature is more likely to keep moving, whilst declining granular temperature inhibits flow.

All these observations are important for understanding the controls on debris flow deposition but they provide little guidance on how to predict the lag rate for a specific flow. I am only aware of one relationship that can be adapted to estimate the lag rate. Iverson et al. (1998) and Griswold and Iverson (2008) proposed an empirical relationship between total flow volume V of a debris flow and the cross sectional area of the flow A:

$$A = \varepsilon V^{2/3} \tag{5.2}$$

where $\varepsilon = 0.1$ (regression based on 50 non-volcanic debris flows, worldwide). For granular debris flows in the Italian Alps (19 events) Berti and Simoni (2007) suggested $\varepsilon = 0.03$. This relationship can be interpreted as an upper limit on the rate of deposition, i.e. according to Equation 5.2 a debris flow cannot deposit more than A m^3 of sediment per 1 m channel length. Where only levees are deposited, the lag rate will necessarily be less because most of the flow cross section is made up by the channel. Note, too, that Equation 5.2 does not allow for dependence on the channel geometry or gradient.

From field evidence it is known that debris flows can stop suddenly in a channel, forming a snout of coarse particles (e.g. McCoy et al., 2010; Whipple and Dunne, 1992). This can cause the next flow to avulse into a new channel and leads to fundamental changes in the locus of sedimentation (Bryant et al., 1995; Dühnforth et al., 2008; Field, 2001; Reitz et al., 2010; Whipple, 1992). Bryant et al. (1995) found an increase in avulsion frequency with increased sedimentation

rates in a laboratory experiment of an alluvial fan. For understanding avulsion on debris-flow fans it is crucial to think about the conditions required to stop debris flows in a channel. McCoy et al. (2010) suggested that excess pore pressures in the flow causes high mobility and long runout. Nevertheless the process of debris flow deposition is not understood well enough to make precise predictions of the location of the depositional snout along a particular flow path.

Flow routing over sequences of multiple flows is a function of the very distinctive surface morphology of debris-flow fans consisting of amalgamated levees and lobes (e.g. Blair and McPherson, 2008; Cannon, 1989; Kim and Lowe, 2004; Whipple, 1992). Whilst the large-scale landform of a fan is convex and promotes flow spreading, small-scale elements such as levees and channels produce local concavities which act as flow attractors (Field, 2001; Reitz et al., 2010). It is these two divergent behaviours enforced by the landform that make modeling of debris-flow fans a challenge, but both need to be considered to fully represent the system behaviour.

5.1.3 Specifications of a debris-flow fan evolution model

To conclude the introduction I will now briefly outline the requirements of a new debris-flow fan evolution model. The model must operate on a radial grid which is the most appropriate representation of a conical fan and allows for more realistic flow routing, as opposed to a rectangular grid. The model must run fast so that the sequential effects of thousands of flows can be investigated. For this reason the two empirical relationships Equation 5.1 and 5.2 are appealing. Erosion and deposition rules should be explicitly modeled. This necessitates a realistic description of deposit geometry, based upon findings on the geometry of debris-flow deposits (Chapters 2 and 4). The model should allow for variable debris-flow input volumes, an initial sediment concentration, bed saturation and characteristic flow behaviour. The ability to track the evolution of single flows and of the whole fan in response to these variable input parameters is necessary. This includes capture of resulting topography and fan surface age in pre-defined time steps, and detailed event specific data such as evolution of flow volume, sediment concentration and modification of flow path geometry as flows traverse the fan. I expect such a model to conform to widely observed data regarding the controls on fan geometry in response to variations in sediment flux, sediment concentration and bed saturation (Iverson et al., 2011; Leeder and Mack, 2001; Milana and Ruzycki, 1999; Schumm et al., 1987; Whipple et al., 1998). I also expect the model to evolve and behave in a familiar pattern in flume experiments (Clarke et al., 2010; Kim et al., 2006; Reitz et al., 2010).

The rest of the chapter is structured as follows. I start with a detailed description of the proposed model and the parameter space. Next I experimentally demonstrate that the model replicates fundamental features of a debris-flow fan systems observed both in nature and in flume studies. I then use the model to investigate a range of questions related to the evolution of a fan over multiple events or to a quasi-stable state. These questions are important for both landscape evolution and debris-flow hazard as I will demonstrate with three specific applications of the model.

Each application consists of a short introduction, a description of the experiments and a presentation of the results and a discussion. First I will consider the temporal and spatial modulation of defined input flow-volume distributions as flows sampled from these distributions are routed across a debris-flow fan. Second I investigate the relationship between avulsion behaviour and final fan deposit geometry. Third I demonstrate system response to an external disturbance of the fan apex by a rock avalanche. This last experiment is motivated by findings presented in Chapter 2. In the discussion I critically assess the proposed model and outline how representation of processes could be further improved and noting how the model may be used to formulate hypotheses of fan evolution that are testable by either fieldwork, or by the use of more sophisticated models.

5.2 Model description

5.2.1 General framework

I start the model description with a brief overview before I explain the different components in detail. I route debris flows through consecutive topographic cross sections. The geometry of these cross sections is such that they are approximately perpendicular to the expected flow direction. This means that they take the shape of concentric semi-circles for a fan resulting in a radial grid centered at the fan apex (Nicholas and Quine, 2007a). A flow routing algorithm determines a steepest flow path through all cross sections, and a set of rules govern erosion and deposition in each cross section. The flow properties (volume and sediment concentration) are updated before assessing the next cross section. I draw initial debris-flow volumes and sediment concentrations from a user-defined distribution. The model space topography is updated after every flow before the flow-routing algorithm determines the flow path for the next event. Output data consist of downstream changes in individual flow volume, sediment concentration and bed elevation, as well as 2D flow tracks. In addition fan topography and surface age are captured at user-defined intervals.

5.2.2 Model space geometry

Figure 5.1 shows the model space geometry. It consists of an input chute of defined initial slope and length followed by the fan area. The chute simulates the feeder channel within the mountain front, and is divided into equally spaced straight cross sections. It ensures that the apex elevation is free to vary in response to elevation changes of the channel bed in the chute ('the catchment') and not as a result of boundary effects due to flow initiation. In the unconfined areas the grid takes the shape of semi-circles (subsequently termed arcs) with the same separation downslope separation as in the chute. Node spacing is equal along all arcs and can be chosen independently from arc spacing. To optimize computing time, arc spacing can be chosen to be larger than node spacing. This is defendable because because debris-flow channels and depositional lobes are elongated features arranged in a radial fashion, and hence topographic variability is larger across the fan (along the arcs) than in the downfan direction. The chute width is equal to the radius of the first arc, which equals twice the arc spacing (Figure 5.1).

5.2.3 Data management and storage

Data management and storage in this framework are more complicated than for a simple regular rectangular grid. I adapted a scheme proposed by Tucker et al. (2001). For the purposes of modification during a model run, the node elevations along each arc are stored in columns of a matrix (termed the radial grid matrix RG). The node positions are triangulated as a Delaunay network. In addition to RG the model maintains a database that contains for each node information on the parent arc, position within the arc, cartesian x-y coordinates, elevation (z), IDs of neighbouring nodes and area of the Voronoi polygon associated with the node, termed TIN. Node positions are kept fixed and only the node elevation changes as the model evolves. Node elevations in TIN are updated when necessary from the values in RG. The cartesian xyz coordinates in TIN can be extracted on demand to produce a digital elevation model at a desired resolution.

5.2.4 Flow routing

The flow routing algorithm always finds the steepest path between a start node in arc i and a node in arc $i+1$ within a defined downslope search angle $\zeta = 90^\circ$ (Figure 5.1) aligned symmetrical around the steepest path on the fan surface. All selected nodes form the talweg of the next debris flow.

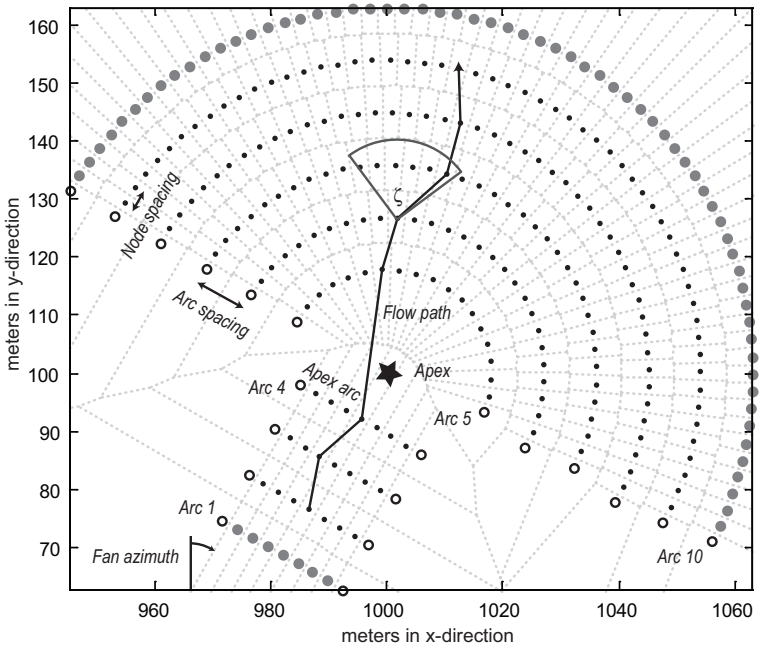

Figure 5.1: *Sketch of model space geometry. A model space consists of a chute with straight cross sections and a fan area with semi-circular cross sections (termed arcs). Dotted gray lines: boundaries of Voronoi polygons associated with each node. Open circles indicate nodes with an initial elevation of 9,999 m that serve as hard model boundaries (never occupied). Gray circles indicate nodes that are never occupied because area of Voronoi polygons is not defined; these are taken to represent base level. Filled circles are nodes that can be occupied by flows, their horizontal position is fixed. Arc 10 is a permeable model boundary (see text). A sample flow path is shown with a search angle ζ for flow routing indicated at arc 6. Debris flows are initiated in arc 2. Fan azimuth is 30° and coordinates of apex (star) are $x = 1000$ m and $y = 100$ m. Model space size (i.e. number of arcs), arc and noce spacing may be varied depending on the specific application.*

The slopes between the start node in arc i and candidate nodes in arc $i+1$ are calculated based on elevation difference and horizontal separation. If there are no nodes with a lower elevation in arc $i+1$ (because the flow has reached a pit) the algorithm selects the node with the lowest upward slope. Successive nodes along a flow path are never part of the same arc, forcing flows to always move radialy away from the fan apex (Figure 5.1), even if the surface is horizontal. The predicted path is searched for topographic pits and locates for each talweg node the minimum fill elevation that is required to overcome the next topographic threshold. The last operation on the pit-filled flow path is the calculation of along-track slope for node i as the slope between node i and $i+1$. With this I ensure that flows behave consistently with the topography ahead of them (i.e. no erosion when entering a flat reach or pit).

5.2.5 Governing equations and principles

I now describe the governing equations and principles that control the models behaviour. These operations are performed in the same order as described. This procedure is repeated for every arc until the flow has either deposited its complete volume or until the flow has reached the model boundary at the last downslope arc.

At each arc (Figure 5.1) I need to estimate two key parameters: flow depth as a function of cross sectional geometry and average deposit thickness d_c (Figure 5.2). To predict flow depth for different positions along a debris flow path empirical, semi-empirical and numerical models have been employed. For this purpose I need a computationally efficient approach and hence chose a semi-empirical model. Consequently I ignore dynamic effects, and do not solve the momentum conservation equation as for example in Iverson (1997). Instead, the semi-empirical LAHARZ model presented by Iverson et al. (1998), originally developed for lahars, then refined for debris flows in Griswold and Iverson (2008), provides a quick way of estimating the cross sectional area of the flow A from the total volume V (Equation 5.2). Once the flow cross sectional area is known, the flow depth can be calculated as a function of the cross sectional geometry (see below). The semi-empirical model in Equation 5.2 is based on a dimensional analysis which requires that $A \propto V^{2/3}$. It is further assumed that the hydrographs of lahars (or debris flows) can be approximated by a triangular shape, that mass and density remain constant and that the propagation velocity follows $u \approx \sqrt{gh_r}$. From this Iverson et al. (1998) showed that a power-law relationship should exist between flow cross sectional area and flow volume. ε in Equation 5.2 is assumed to be constant and can be calibrated for data pairs of total flow volume and cross sectional area (Berti and Simoni, 2007; Griswold and Iverson, 2008; Iverson et al., 1998). However, it is important to remember that Equation 5.2 does not account for downstream attenuation of the debris-flow front and hence provides a conservatively large estimate of the flow cross sectional area. Values calculated with Equation 5.2 can then be used to estimate the flow depth in a given channel cross section under the assumption of a (e.g. horizontal) flow surface. Typical values for ε [dimensionless] are < 0.1 as reported by Griswold and Iverson (2008) and Berti and Simoni (2007). Unlike the LAHARZ model (Iverson et al., 1998) I recalculate A as the flow progresses at every arc, because in my model flow volume itself changes due to deposition or erosion. This approach results from the observation that debris flows can erode substantial volumes while traversing a fan (Chapter 4; Scheuner et al., 2009).

The minimum deposit thickness d_c determines the amount of deposition occurring when the debris-flow discharge exceeds channel capacity and the flow inundates adjacent over-bank areas (Figure 5.2). I use a relationship also used in the LAHARZ model proposed by Iverson et al. (1998), between flow volume V and inundation area B (Equation 5.1). This relationship follows from the same dimensional analysis as in Equation 5.2 and is subject to the same simplifications and assumptions. Berti and Simoni (2007) proposed a slightly modified version where they substituted inundation area B by minimum deposit thickness ($B = V/d_c$):

$$d_c = 1/\alpha V^{1/3} \tag{5.3}$$

where α [dimensonless] is an empirical coefficient with a typical range of 6–33 for natural debris flows (Berti and Simoni, 2007; Crosta et al., 2003; Griswold and Iverson, 2008). The value of d_c controls two things: first it determines the thickness of the deposits when the flow can spread laterally and second it defines the flow depth below which no erosion occurs. If the flow depth at a node is larger than d_c the rules for erosion (see below) are invoked (Figure 5.2). After calculation of these key values the model checks whether the current talweg node is in a pit. If this is the case the model searches for all laterally adjacent nodes that have an elevation lower than the minimum fill elevation as determined by the flow routing. All selected nodes are inundated and sediment is deposited to this minimum fill level.

Next I determine the inundation limits based on the predicted flow cross section A (Equation 5.2), minimum deposit thickness d_c (Equation 5.3) and cross section topography A. Starting from the talweg node, the cross section is inundated by stepwise filling in small increments (0.1 m) in flow stage. The input topography is read from RG. After each incremental rise in flow stage, flow cross sectional area is calculated and compared with A. To simulate the lateral spreading with thickness d_c I buffer the topography with d_c and require the flow stage to reach at least a level of the node elevation $+d_c$ before the flow is allowed to spread laterally over bank (Figure 5.2). This procedure yields lateral limits of inundation and the flow depth for each inundated node.

I then classify the inundated nodes in those with flow depth $h \leq d_c$ and those where $h > d_c$ (Figure 5.2). In the former case I deposit the full flow depth. In the latter case elevation change is sampled from a probability distribution function of elevation change versus flow depth (PDF, Chapter 4) acquired from topographic monitoring of a debris-flow channel using a terrestrial laser

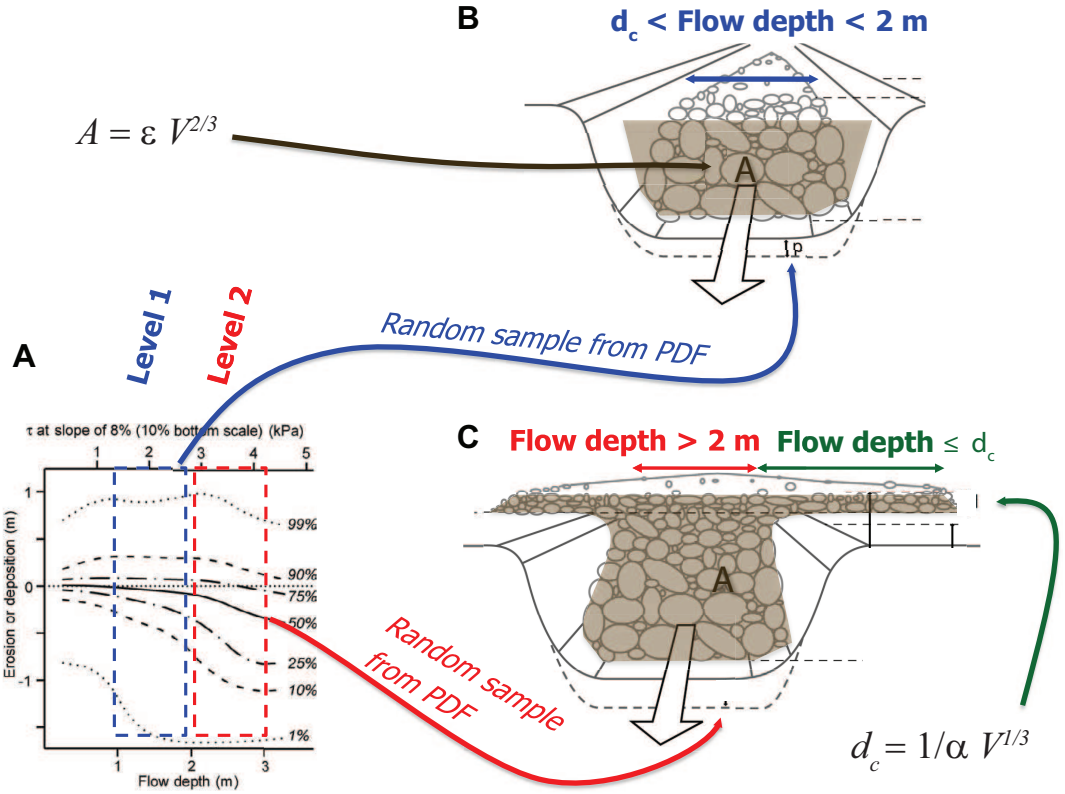

Figure 5.2: *Sketch of model operations to determine erosion and deposition. A: Probability density function (PDF) of basal shear stress versus bed elevation change, derived from data presented in Chapter 4. The PDF informs erosion and deposition in the model where flow depth is larger than d_{crit} (see text, Equation 5.3). B: Example of a debris flow contained within the channel. C: Example of a debris flow with peak discharge exceeding channel conveyance capacity and depositing over-bank.*

scanner (Chapter 3). I convert flow depth at each node to basal shear stress ($\tau = \rho_b g h S$; Iverson, 1997; Takahashi, 2007, see also a review in Section 1.3.3) using a bulk density ρ_b of 1,800 kg/m^3, which is the median density from 35 debris flows observed at the Illgraben debris-flow observation station (McArdell et al., 2007; McArdell and Berger, 2010). Figure 4.3 in Chapter 4 shows that the shape of the PDF is dependent on flow depth. I therefore divide the data into 1-m bins and calculate separate PDFs for each bin. Because in the model slope will vary and will be different from the slope in the study reach ($S = 0.09$) as reported in Chapter 4, I transform the bin boundaries to basal shear stress using the above values for S and ρ_b. The bin boundaries become then: 0, 1,487, 2,974, 4,461 and 5,949 Pa. To determine erosion or deposition for the nodes where $h > d_c$ I sample a random value of elevation change for each band of basal shear stress from the corresponding PDF.

Flows are released into the model space with an initial random sediment concentration sampled with uniform probability across a range of possible concentrations: $\{C_{min}...C_{max}\}$. Bed material

has a user-defined porosity s. Entrainment of bed material results in a change in sediment concentration $C_{old} \rightarrow C_{new}$, depending on the water content of the bed material w, which is set uniformly for each flow. The probability of the bed being wet for a particular flow is defined by setting p_{wet} to a value between 0 and 1. The new sediment concentration C_{new} as a function of change in flow volume ΔV_i and flow volume V_i at arc i becomes then:

$$C_{new} = \frac{V_i C_{old} + \Delta V_i(1-s)}{V_i + \Delta V_i(1-s+w)} \tag{5.4}$$

Equation 5.4 accounts for volume contraction when entraining unsaturated sediment (pore space vanishes). Deposition does not affect the sediment concentration, because the fresh deposit material is assumed to have the same concentration as the local flow. As the flow travels down-slope its sediment concentration is likely to increase due to entrainment. Takahashi (2007) found that debris flows tend to deposit when an equilibrium concentration C_∞ of coarse particles is reached. He suggested that this equilibrium concentration is dependent on rock and fluid density, angle of internal friction and channel slope. This model does not treat coarse and fine particles separately, hence Takahashi's (2007) relationship is not directly applicable. He suggested a maximum value for C_∞ of 0.5, but this value is lower than bulk maximum sediment concentrations observed in debris flows for example at Illgraben, Switzerland (Brian Mc Ardell, pers. comm., 2010). I apply Takahashi's (2007) concept in a simplified way and define a slope-independent critical concentration C_{crit} higher (e.g. 0.8) than the value reported by Takahashi (2007).

When $C > C_{crit}$ force the flow to deposit at higher rates to form depositional lobes. I implement this by simply depositing at every subsequent arc a volume equivalent to the flow depth of each inundated node multiplied by the total area of the Voronoi polygons involved. This switch in behaviour is irreversible. When the total remaining volume drops below 1 m^3 the flow has reached the final runout distance and is stopped. I correct the deposition depth h_{dep} for the escape of water and assume that bed porosity s is re-established to the original value:

$$h_{dep} = \frac{hC}{1-s} \tag{5.5}$$

where h is flow depth. After applying all erosion and deposition to the inundated nodes in RG I reduce or increase the remaining flow volume accordingly taking advantage of the Voronoi areas (stored in TIN) of the involved nodes. Finally the elevations in TIN are updated using the modified values in RG.

5.3 Model validation

In this section I validate the debris-flow model presented in the previous sections of this chapter and introduce the reader to a range of model outputs. I do this in three steps: First I show how the model handles single flows and assess whether resulting deposit geometry is reasonable. Second I introduce the model geometry that is adopted for the rest of the chapter and perform a base run to show the general properties of an experiment with 30,000 debris flows. Third I define and show results of a series of experiments to validate the model against field and laboratory observations of fan behaviour in response to variations in sediment flux, sediment concentration and bed water content. For the model runs presented subsequently in the validation and application I used a model space with a fan of 500 m radius with a 100 m long chute feeding the fan and an initially flat topography. To adequately represent channels and levees I chose a node spacing of 3 m. To represent relief in a down-fan direction I decided that an arc spacing of 9 m was sufficient, because from my own observations on natural fans down-fan profile roughness is smaller than across fan, and because lobes and channels are mostly oriented in a radial fashion.

This resulted in 10 straight cross sections in the chute and 55 arcs on the fan. The total number of nodes in each run was 15,019 with 7 nodes per cross section in the chute, 17 nodes in the first fan arc and 526 nodes in the last fan arc. All model runs I present in the subsequent analysis are summarized in the appendix (Appendix: Table D.1).

5.3.1 Behaviour of single flows

Before considering multiple events I need to assess the performance of the model in reproducing individual flows. I used a base topography consisting of a smooth fan with a chute of 100 m, a radius of 200 m, an initial slope of 5% and a channel. The channel is 1 m deep and 15 m wide for the first 100 m from the apex; between 100 m and 150 m it is 0.5 m deep and 20 m wide; and beyond 150 m until the toe of fan at 200 m from the apex there is no channel (Figure 5.3A–D). The chute is not shown in Figure 5.3 and the origin of the length scale is at the fan apex. The four model runs of one debris flow each shown in Figure 5.3A–D were designed to show the interaction of debris flows with topography, and the effect of entrainment on sediment concentration and flow behaviour. Flow volumes were chosen so that the two smaller flows (1,200 m^3, Figure 5.3A and B) would be contained in the channel while the two larger flows (7,000 m^3, Figure 5.3C and D)

would exceed the channel capacity. Initial flow cross section areas A were 11 m^2 and 36 m^2 (with $\varepsilon = 0.1$). Initial sediment concentrations $C_0 = 0.5$ for flows A and C were chosen so that large volumes of sediment could be entrained without reaching the critical sediment concentration of $C_{crit} = 0.8$. For flows B and D in Figure 5.3 initial sediment concentration was chosen so that critical sediment concentration of $C_{crit} = 0.8$ would be reached with only limited entrainment ($C_0 = 0.79$).

Flow A traveled the first 70 m with almost no net volume change, indicated by a lag rate of almost zero (Figure 5.3F). No over-bank deposition occurred as the flow was contained in the channel. At 70 m the channel becomes wider and as a result the flow depth dropped below $d_{crit} = 0.7$ m estimated from Equation 5.3 and the flow became net depositional although still contained within the channel. This transition is indicated by a drop in lag rate to ≈-10 m^3/m. Between 140 m and the fan toe the flow was no longer contained by the channel and spread laterally, depositing an elongated lobe. The resulting channel in the upper part of the fan has undergone only small modifications but in the lower part was filled completely.

Flow B in Figure 5.3 started with an initial sediment concentration much closer to C_{crit}. Entrainment of dry bed material along the chute (not shown) allowed the flow to reach the threshold sediment concentration C_{crit} already at the fan apex. As a result the flow switched to deposition at the maximum possible lag rate calculated with Equation 5.2. Consequently the flow volume decreased continually in down fan direction (Figure 5.3E) causing a decline in deposition (Figure 5.3F). In the upper third of the fan this flow almost completely filled the channel with sediment. The lobe in the lowermost part of the fan is narrower than in flow A because at that point the flow volume was already smaller due to a higher rate of deposition upstream (Figure 5.3A and B). Where the channel is preserved it is shallower than prior to the flow.

Flow C and D were not contained in the channel (Figure 5.3C and D) and deposited levees along the flow margins. At 70 m where the channel widened, flow C was almost completely contained in the channel, leading to a sharp rise in lag rate to positive values and indicating net volume growth of the flow due to entrainment. This net growth in volume in combination with a channel shallowing around 100 m triggered renewed levee deposition, indicated by a drop in lag rate (Figure 5.3F). The resulting channel in Figure 5.3C is deeper than prior to the flow due to in-channel entrainment and lateral levee deposition. Despite simultaneous deposition of levees, in-channel entrainment caused flow D (Figure 5.3D) to reach the threshold sediment concentration.

This resulted in deposition at maximum lag rate from 60 m onwards indicated by a sharp drop in lag rate to nearly -40 m^3/m. The total volume declined much faster after this transition than in flow C (Figure 5.3D), which continued to entrain material along the centerline of the channel. Flow D preserved only a short stretch of channel near the fan head, and further downstream deposition caused topographic inversion (Figure 5.3D).

In summary I find that the model fulfills my expectations in reproducing the main features of debris-flow erosion and deposition as observed in the field (Chapter 4; Blair and McPherson, 1998; Kim and Lowe, 2004). The dynamic interaction between flows and topography gives rise to changes in channel geometry that over multiple events will lead to the feedback mechanisms hypothesised in Chapter 4. What I have shown here for four single flows is repeated thousands of times in the experiments that follow, where I explore whether model behaviour over multiple flows still complies with the understanding of the behaviour of fans.

Figure 5.3: *Next page: Illustration of single-flow behaviour on a fan of 200 m radius, 3 m arc and node spacing, with a chute of 100 m (not shown) for flow volumes of 1,200 and 7,000 m^3, for initial sediment concentrations C_0 of 0.50 and 0.79 ($C_{crit} = 0.8$), α of 15 and ε of 0.1. Initial topography for all four simulations was identical and is shown by black solid contour lines spaced at 1 m. Dotted, black contour lines and the shaded topography with lighting from top right represent the surface modified by the debris flow. A–D: Model runs for four single events with initial volume and initial sediment concentration C_0 as indicated next to sub-figure labels. Flow direction from by arrow. Coloured line identifies these model runs in sub-figures E and F. E: Down-fan volume evolution from fan apex onwards for four events shown in sub-figures A–D. F: Down-fan evolution of lag rate from fan apex onwards for four events shown in sub-figures A–D.*

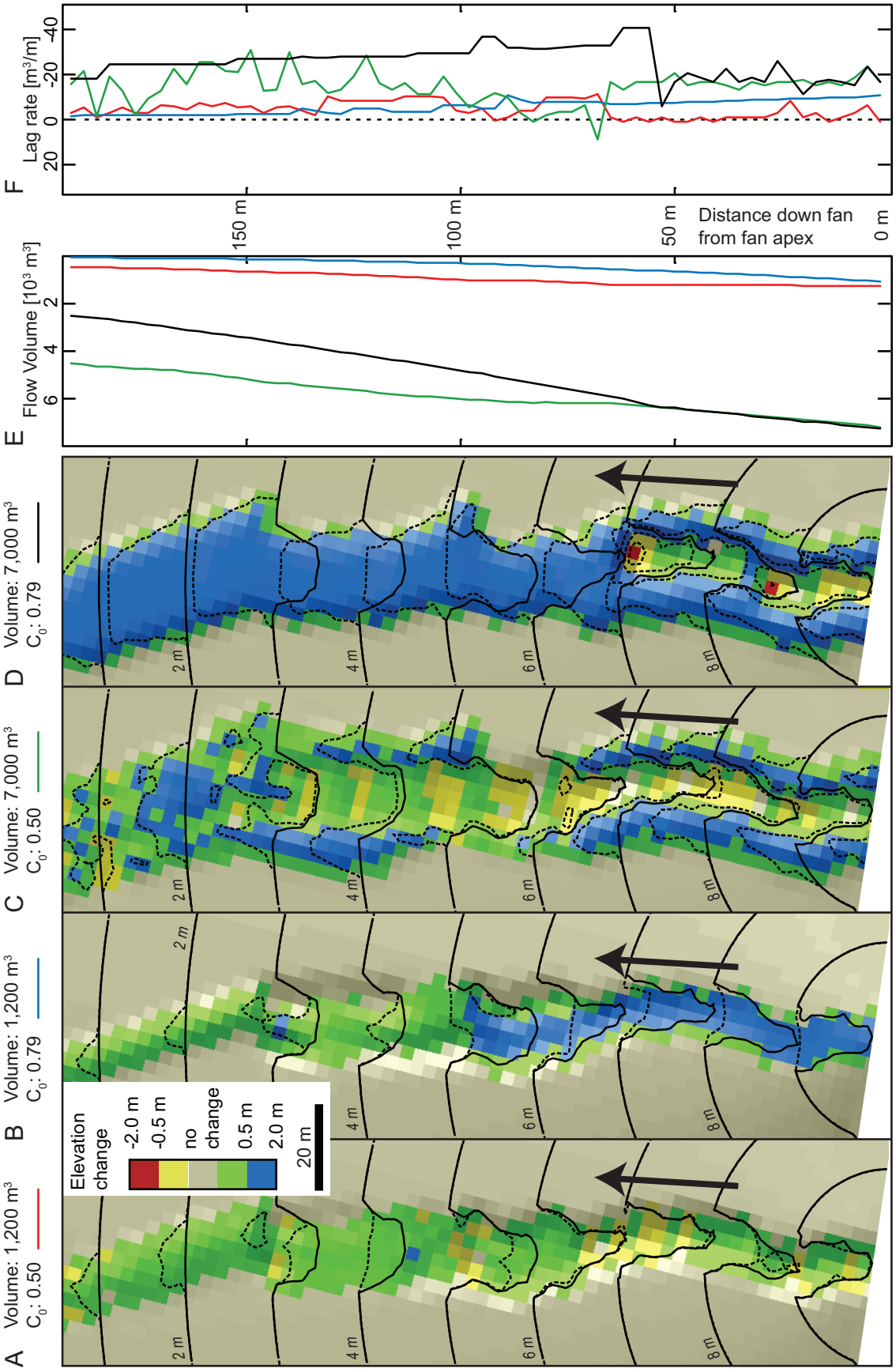
F
Lag rate [m³/m]
20
0
-20
-40
150 m
100 m
50 m
0 m
Distance down fan from fan apex
E
Flow Volume [10³ m³]
6
4
2
A
Volume: 1,200 m³
C₀: 0.50
B
Volume: 1,200 m³
C₀: 0.79
C
Volume: 7,000 m³
C₀: 0.50
D
Volume: 7,000 m³
C₀: 0.79
Elevation change
-2.0 m
-0.5 m
no change
0.5 m
2.0 m
20 m
2 m
4 m
6 m
8 m

5.3.2 Analysis of model output and base run

When running the model over thousands of events, large amounts of data are generated and tools are required to visualize the temporal and spatial performance of the model. I introduce these tools in Figure 5.4 and refer back to them later in the chapter. In Figure 5.4A I trace the flow direction through time: I derive the radial position of the intersection of each flow path with the last arc, where flows that flow in a northerly direction from the apex plot at the top of the diagram. Figure 5.4B shows the resulting fan topography after 30,000 events. From the model output I also retrieve the temporal evolution of fan slope (Figure 5.4C). I calculate the fan slope for a total of 102 corresponding pairs of nodes in arc 21 and arc 66, and the standard deviation of fan slope. The calculation is repeated every 100 events on the current topography. Also shown is surface roughness calculated as the standard deviation of slope, where slope is measured over a moving window of 3x3 cells (Frankel and Dolan, 2007) (Figure 5.4C). In Figure 5.4D, left axis, I plot the cumulative volume of the fan. On the right axis in Figure 5.4D I show the temporal evolution of fan surface age calculated every 100 events. To visualize the erosional or depositional behaviour of flows, I calculate the relative volume change between fan apex and fan toe (Figure 5.4E) as the difference in volume normalized by input volume for each event (gray dots). For bins of 100 events I calculate the *relative volume change* at percentile levels of 25%, 50% and 75% (dashed and solid lines). When the solid line plots on the zero-volume-change level, this means that per 100 events, 50 flows were erosional and 50 depositional (Figure 5.4D).

I illustrate the general model features using run E38 as a base run; an animation of this model run is provided in Appendix D. The parameters were: $\alpha = 20$, $\varepsilon = 0.06$, $C_{min} = 0.3$, $C_{max} = C_{crit} = 0.8$ and $p_{wet} = 0.5$ and a log-normal volume input distribution with a mean volume of 3,000 m^3 and a standard deviation of 1,500 m^3 (Figure 5.4). Most model runs show a division into three phases of fan development. Phase I, which in model run E38 took approximately 7,500 events, is characterized by a frequent shifting in flow direction. The frequent resurfacing of the fan surface kept the median age of the emerging surface low (Figure 5.4D). In this phase the fan grew to the margin of the model space at a radial distance of 500 m from the apex and rapidly steepened (Figure 5.4C). Most flows were depositional (Figure 5.4E) and the fan grew at high rates (Figure 5.4D) to reach about 2/3 of its final volume.

Phase II started at 7.5k events and continued until about 20,000 events. In this phase the depocenter swept several times back and forth across the fan. This resulted in a distinctively different pattern of surface aging (Figure 5.4D). Median surface age increased faster than previously, indicating that only small areas of the fan surface were active at any one time. Major avulsion are marked by a sharp drop in median surface age (e.g. at 25k events) and indicate substantial resurfacing of the fan. Fan slope (Figure 5.4C) and volume (Figure 5.4D) grew at much lower rates, due to an increasing number of erosive flows or flows that were routed without much erosion or deposition (Figure 5.4E) due to the emergence of channels on the fan surface.

Phase III covers the last 10,000 events. Here avulsions led to unpredictable jumps in depocenter location (Figure 5.4A). The final topography in Figure 5.4B shows a resulting fan of about 5% slope with the apex 25 m above base level. This is a relatively gentle fan, which is a result of the low sediment concentration that varied uniformly between 0.3 and 0.8 (mean of 0.55), as I will assess in more detail in Section 5.3.3. Over the model run a number of channels formed that were re-occupied by flows repeatedly. One example is the channel with an azimuth of $\approx 105^{\circ}$ (ESE) which was also active at the end of the model run (Figure 5.4B). The establishment of channels and the increase in fan slope increased the efficiency of flow routing, which meant less sediment was deposited per event, and hence the non-linear growth in fan volume. In phases II and III the solid black line in Figure 5.4E plots on the line of zero relative volume change, which indicates that similar numbers of flows are erosional and depositional. Figure 5.4E shows also that most erosive flows grew in volume by 25% or less.

Figure 5.4: *Next page: Model results for run E38 with 30,000 events, a log-normal flow volume distribution with mean volume (water + sediment) of 3,000 m^3 and a standard deviation of 1,500 m^3, $\alpha = 20$, $\varepsilon = 0.06$, $C_{min} = 0.3$, $C_{max} = C_{crit} = 0.8$ and $p_{wet} = 0.5$. A: Variation of flow path direction from north to south (from top to bottom on vertical axis), number of events on horizontal axis. B: Fan topography at end of model run, contours are shown every 4 m, north is up. Maximum fan elevation is 25 m above base level. C: Average fan slope, standard deviation of fan slope, surface roughness and relative jump distance at 99% non-exceedence probability (RJD_{99}) over time. RJD_{99} is the relative change in flow direction between successive events at 99% non-exceedence probability. It can be understood as the width of the active corridor on the fan. A detailed explanation and rational for this measure is given in Section 5.4.2. D, left axis: Total fan volume over time (solid line). D, right axis: fan surface median age (solid line) and median age plus 1 standard deviation (dashed line). E: Relative volume change of each event between fan apex and toe (gray dots). Erosive debris flows plot above the line of zero volume change and depositional flows below. The solid black line represents the median (50^{th} percentile) outcome per 100 events. The dashed lines are the 25^{th} and 75^{th} percentiles.*

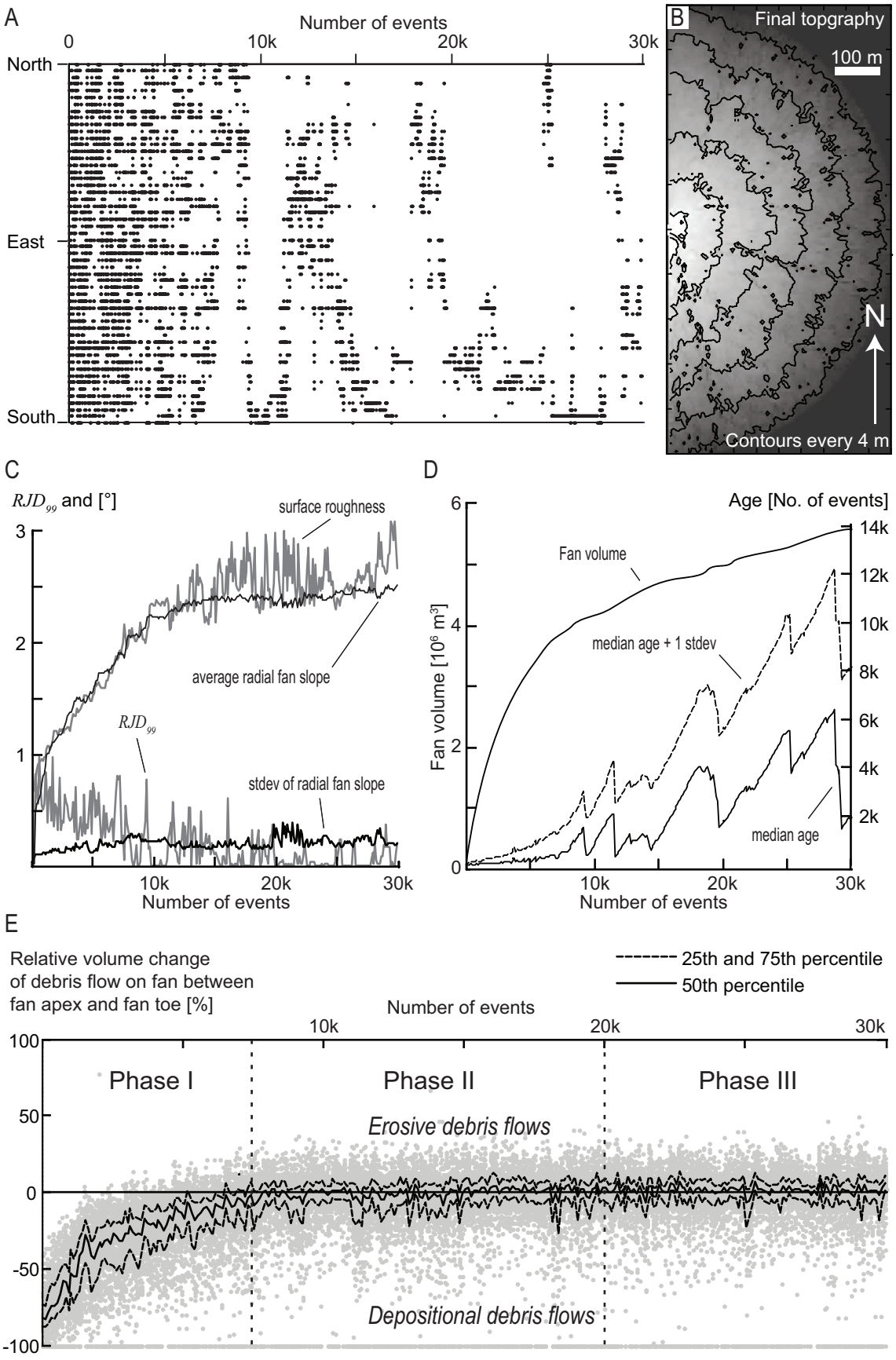
A
Number of events
0
10k
20k
30k
North
East
South
B
Final topgraphy
100 m
N
Contours every 4 m
C
RJD_{99} and [°]
surface roughness
average radial fan slope
RJD_{99}
stdev of radial fan slope
Number of events
D
Age [No. of events]
Fan volume
median age + 1 stdev
median age
Fan volume [10^6 m^3]
Number of events
E
Relative volume change of debris flow on fan between fan apex and fan toe [%]
25th and 75th percentile
50th percentile
Number of events
Phase I
Phase II
Phase III
Erosive debris flows
Depositional debris flows

5.3.3 Validation experiments

I validated the model against field and laboratory observations of fan behaviour. For this purpose I first defined a series of experiments, which I briefly describe below. Initial sediment concentration was varied between C_{min} and C_{max} according to a uniform random distribution. The critical sediment concentration was kept constant at 0.8 throughout all experiments. The runtime reported in the appendix (Appendix: Table D.1) depends on the computer used, but on average each 10,000 events required about 1.2 hours.

In the first set of experiments I primarily focused on fan slope as a function of model parameters. Specifically I wanted to test whether the model replicates fundamental behaviour observed in flume experiments and on natural fans.

In run E1 to E4 I wanted to assess whether fan slope decreases with increasing sediment flux as suggested by Clarke et al. (2010), Bull (1962) and Harvey (2002). For this reason I kept sediment concentration constant at 0.6 and performed four model runs of 10,000 events each with constant flow volumes of 1,000, 2,000, 4,000 and 8,000 m^3 respectively (Appendix: Table D.1).

In run E5 to E10, E11 to E14 and E11 to E22 I wanted to test whether the model would reproduce the findings of Milana and Ruzycki (1999), Schumm et al. (1987) and Whipple et al. (1998) that indicate that fan slope should increase with increasing sediment concentration independent of any changes in sediment flux. For each event in run E5 to E10 I set the initial sediment concentration constant at 0.2, 0.3, 0.4, 0.5, 0.6 and 0.7 respectively and used a ratio of $\alpha/\varepsilon = 100$. In order to keep the sediment flux constant at $\approx 4,000$ m^3 per event I varied the mean flow volume per model run. The flow volumes were sampled from a log-normal distribution with a standard deviation of half the mean (Appendix: Table D.1).

In run E11 to E14 I allowed the initial sediment concentration to vary uniformly over a range of ± 0.1 around 0.2, 0.4, 0.6 and 0.7 with $\alpha/\varepsilon = 100$ (Appendix: Table D.1). The mean flow volumes of the log-normal distribution for each model run were chosen to yield the same sediment flux of $\approx 4,000$ m^3. The standard deviation was again set to half the mean (Appendix: Table D.1).

In run E11 to E22 I introduced more variability in the initial sediment concentration. I allowed the initial sediment concentration to vary between a minimum value (0.1, 0.3, 0.5, 0.7) and the maximum value of 0.8 which was identical with the critical sediment concentration. I also used this group of experiments to test the influence of the ratio of α/ε on fan slope with run E11 to

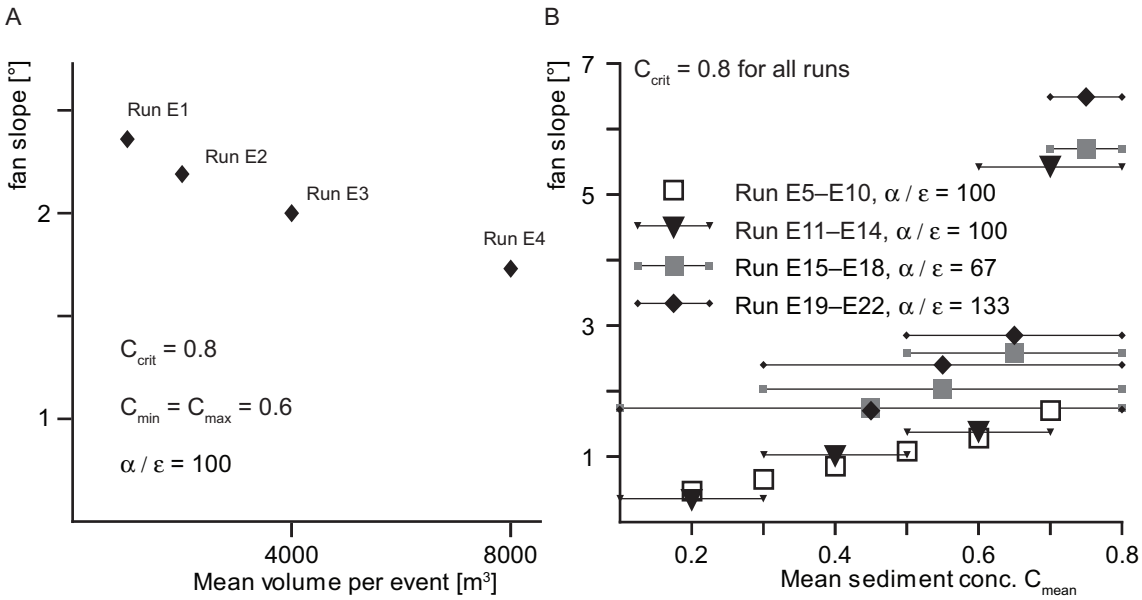

Figure 5.5: *Controls on fan slope. See Appendix D.3 for tabulated values of mean radial slope and standard deviation of radial slope at end of each model run. A: Fan slope after 10,000 events for model run E1–E4. Volume per event in each run was kept fixed at 1,000, 2,000, 4,000 and 8,000 m^3 respectively. B: Fan slope as a function of mean sediment concentration (large symbols) and range (horizontal bars). Run numbers increase from left to right in the plot for each symbol category; e.g. left most white square is run E5, next to the right is run E6.*

E18 using $\alpha/\varepsilon = 67$ and run E19 to E22 using $\alpha/\varepsilon = 133$. I used a log-normal distribution for flow volumes with a mean of 5,714 m^3 and a standard deviation of half the mean. In the previous groups of experiments I had varied either sediment flux or sediment concentration, but by using the same volume distribution for all experiments in this group the mean sediment flux increased from 2,571 m^3 to 4,285 m^3 with increasing mean sediment concentration (Appendix: Table D.1). As increasing sediment flux and increasing sediment concentration are believed to have opposite effects on fan slope (Bull, 1962; Clarke et al., 2010; Harvey, 2002; Milana and Ruzycki, 1999; Schumm et al., 1987; Whipple et al., 1998), these experiments should give indication on the relative importance of the two competing processes.

In run E35, E37 to E39 and E57 to E63 I examined the effect of varying the probability of the channel bed being saturated (p_{wet}) at a water content of 0.1 to assess the influence on runout distance (Iverson et al., 2011). All runs were identical apart from varying p_{wet} in increments of 0.1 between 0 and 1 (Appendix: Table D.1).

5.3.4 Validation results

In Figure 5.5A I show the resulting fan slope for runs with different debris flow volumes. For identical sediment concentrations in all runs and all events encouragingly I find a decrease in fan slope with increasing debris-flow volume. In Figure 5.5B I show fan slope as a function of mean sediment concentration. The main difference between the four groups of model runs shown in this figure is the range over which initial sediment concentration was varied: For run E5 to E10 I allowed no variation of initial sediment concentration and it was always smaller than the critical sediment concentration. I find an almost linear increase in resulting fan slope for increasing sediment concentration, but the final fan slope remains below 2°. It is important to note that in these runs I kept the sediment flux constant at 4,000 m^3 by varying the mean flow volume (Appendix: Table D.1). The observed increase in fan slope is therefore only related to the increase in sediment concentration.

For run E11 to E14, I also find an increase in fan slope with increasing sediment concentration although the initial sediment concentration in each run was allowed to vary over a range of ± 0.1 around the mean (Figure 5.5B). Run E14 stands out with a final fan slope of $\approx 5.5°$ because the range of initial sediment concentration of 0.7 ± 0.1 for the first time allowed flows to start with values equal to or very close to the critical sediment concentration. The result was that flows either immediately (or after entraining only very small amounts of sediment) entered lobe deposition mode (Section 5.2.5). This behaviour leads to a faster build-up of material near the fan head and consequently results in a steeper fan slope.

In run E15 to E18 and E19 to E22, I allowed the sediment concentration to vary over larger ranges, with the maximum possible sediment concentration always identical to the critical sediment concentration. The general finding is that fan slope increases faster with increasing sediment concentration than in the previous runs (Figure 5.5B). It is also important to notice that fan slope increases with increasing sediment concentration despite a simultaneous increase in sediment flux (compare with Figure 5.5A). The difference between the first (run E15–E18) and the second group (run E19–E22) was that I doubled α from 20 to 40. α determines the minimum deposit thickness (Equation 5.3). Higher values of α result in thinner but wider deposits and in a smoother, less channelized fan surface. As a result flows are routed less efficiently and hence deposit more material closer to the fan apex. This results in an increase in fan slope with increasing α, but the effect is not very strong (Figure 5.5B).

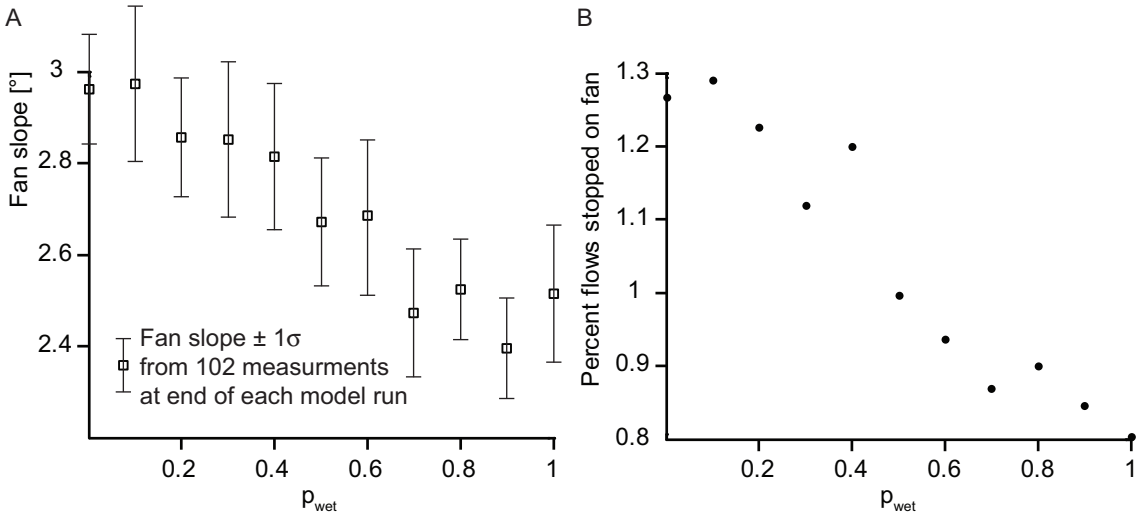

Figure 5.6: *Fan slope and percentage of flows stopping on the fan for runs E35, E37–E39 and E57–E63 (Appendix: Table D.1). See Appendix D.3 for tabulated values of mean radial slope and standard deviation of radial slope at the end of each model run. Model parameters were identical apart from p_{wet}, which I varied between 0 and 1 in increments of 0.1. A: Fan slope measured between arcs 21 and 66 (distance of 405 m) for 102 different directions down-fan (see Section 5.3.2) after 30,000 events as a function of p_{wet}. B: Percentage of flows stopped on fan as function of p_{wet}.*

In Figure 5.6 I show the effect of varying the probability of a saturated bed with a water content of 0.1. First I find a small decrease of fan slope with increasing p_{wet} (Figure 5.6A). This is essentially equivalent with decreasing the average sediment concentration of the flows and is compatible with findings from earlier runs (Figure 5.5). If I consider the percentage of flows that stop on the fan (i.e. all material deposited on the fan), I find that this metric decreases with increasing probability of a saturated bed, which indicates an average increase in flow mobility (Figure 5.6B).

I conclude the model validation here, and note that the model reproduces field and laboratory observations in a qualitatively correct manner. An increase in sediment flux causes a decrease in fan slope (Bull, 1962; Clarke et al., 2010; Harvey, 2002), and an increase in sediment concentration leads to an increase in fan slope (Milana and Ruzycki, 1999; Schumm et al., 1987; Whipple et al., 1998). Varying the probability of a saturated bed also influences the sediment concentration, and the reduced fan slope at higher values of p_{wet} is therefore reassuring. Iverson et al. (2011) found that increased bed saturation enhanced debris-flow runout distance. This effect is also reproduced by this model. In phase II of fan development, (e.g. run E38, Figure 5.4) channels emerge from the fan surface in response to the boundary condition at the fan toe. This boundary condition imitates a non-incising river keeping the fan toe in a fixed lateral and vertical position whilst aggradation

continues on the fan leading to a slow but continuous steepening of the surface. This behaviour is compatible with field evidence (Leeder and Mack, 2001) from alluvial fans that are laterally limited by axial rivers. I also briefly investigated the influence of α and ε on fan slope, but I did not find a strong effect (Appendix D.4). Unfortunately I did not find any validation data in the literature that link these two parameters to overall fan geometry, and therefore I cannot comment on this aspect of the model behaviour with confidence.

5.4 Model applications

In the previous section I have demonstrated that the model presented uniquely reproduces debris-flow deposition and erosion at the level of single flows, and over thousands of events compatible with field observations and laboratory experiments. This allows one to use the model to address questions that require detailed model output from single flow behaviour for thousands of flows. Here I focus on three specific applications, but other applications are inevitably possible.

Whilst debris-flow hazard assessment is conducted by professional consultants on a regular basis, work on the long-term evolution of debris-flow fans is mostly an academic concern, and there is little exchange of concepts and results between the two communities. With the first two of the following experiments I want to explore what the implications of a better understanding of the long-term behaviour of debris-flow fans are for hazard on debris-flow fans. The last experiment is motivated by findings in chapter 2 where the effects of a rock avalanche blocking the fan apex on fan morphology are discussed. However, in everything that follows it is important to remember that the model is not calibrated to reproduce the behaviour of a specific debris-flow fan, but the experiments are meant to stimulate the formulation of hypotheses testable through fieldwork.

5.4.1 Fan evolution and influence on debris-flow magnitude-frequency relationship

Natural hazards, for example rock fall and debris flows are often quantified by magnitude–frequency or magnitude–cumulative frequency distributions (Grossi et al., 2005; Helsen et al., 2002; Hungr et al., 2008; Jakob and Friele, 2010; Lim et al., 2010; Malamud et al., 2004). Debris flow magnitude at the level of a single event, is not only a function of the size of the initial failure but is also strongly controlled by the amount of along-flowpath entrainment and deposition, and by network topology (Benda and Cundy, 1990; Coe et al., 2011; Fannin and Wise, 2001; Hungr

et al., 2005, 2008; Jakob et al., 2005; Scheuner et al., 2009). Therefore building a magnitude–frequency distribution from initial failures of debris flows over a catchment or a region will not yield an accurate picture of the debris-flow magnitudes to be expected at a particular point along the channel network. It can be expected that the shape of the magnitude–frequency distribution is strongly modified by process-form feedback along the flow path (Chapter 4). For this reason regional debris-flow magnitude–frequency relationships are hard to interpret and of little practical use locally (Innes, 1985; van Steijn, 1996; Zimmermann et al., 1997). For hazard assessment at a particular point along the flow path, for example on a debris-flow fan, one needs to constrain the magnitude–frequency distribution locally. Only detailed and long-term monitoring of debris-flow channels (Kean and Staley, 2011; Marchi et al., 2002; McArdell et al., 2007; McArdell and Berger, 2010; Suwa et al., 2009) and detailed mapping and dating of fan surfaces (Dühnforth et al., 2007; Helsen et al., 2002; Jakob and Friele, 2010) can yield the necessary data to understand specific systems. In the first model application I demonstrate how a given, theoretical magnitude–frequency distribution of debris flow volumes released onto a fan, is modified by the emergent fan topography over time and across space. Specifically, I am interested whether there are systematic changes in mean and standard deviation of flow volumes compared to the input distribution when measured at the fan toe.

I considered four model runs (E25, E40, E71 and E89, see Appendix: Table D.1 and Figure 5.7 for details on parameters). The model runs were performed on the standard model space defined in Section 5.3 and over a duration of 30,000 events. I divided the model run into two phases based on the temporal evolution of flow behaviour shown in Figure 5.4D and E. The model evolution is clearly separated into phase I when a large percentage of flows is depositional and the fan growth is rapid, and phase II when fan growth is slower and equal numbers of flows are net erosive and depositional. I define the transition between phase I and phase II as the moment when the line of median flow behaviour (50^{th}-percentile line in Figure 5.4E) reaches zero-volume change. In the base run E38 this transition occurred after around 7,500 events (Figure 5.4E). For both phases I calculated the magnitude–frequency distribution, the mean and the standard deviation of flow volumes from the model output at the fan toe. I also derived the mean and standard deviation of flow volumes as a function of radial distance downstream.

In Figure 5.7 and Table 5.1 I show the results of four experiments where I varied α and ε (run E25 vs. run E40), the standard deviation of the log-normal input distribution (run E89 vs. run

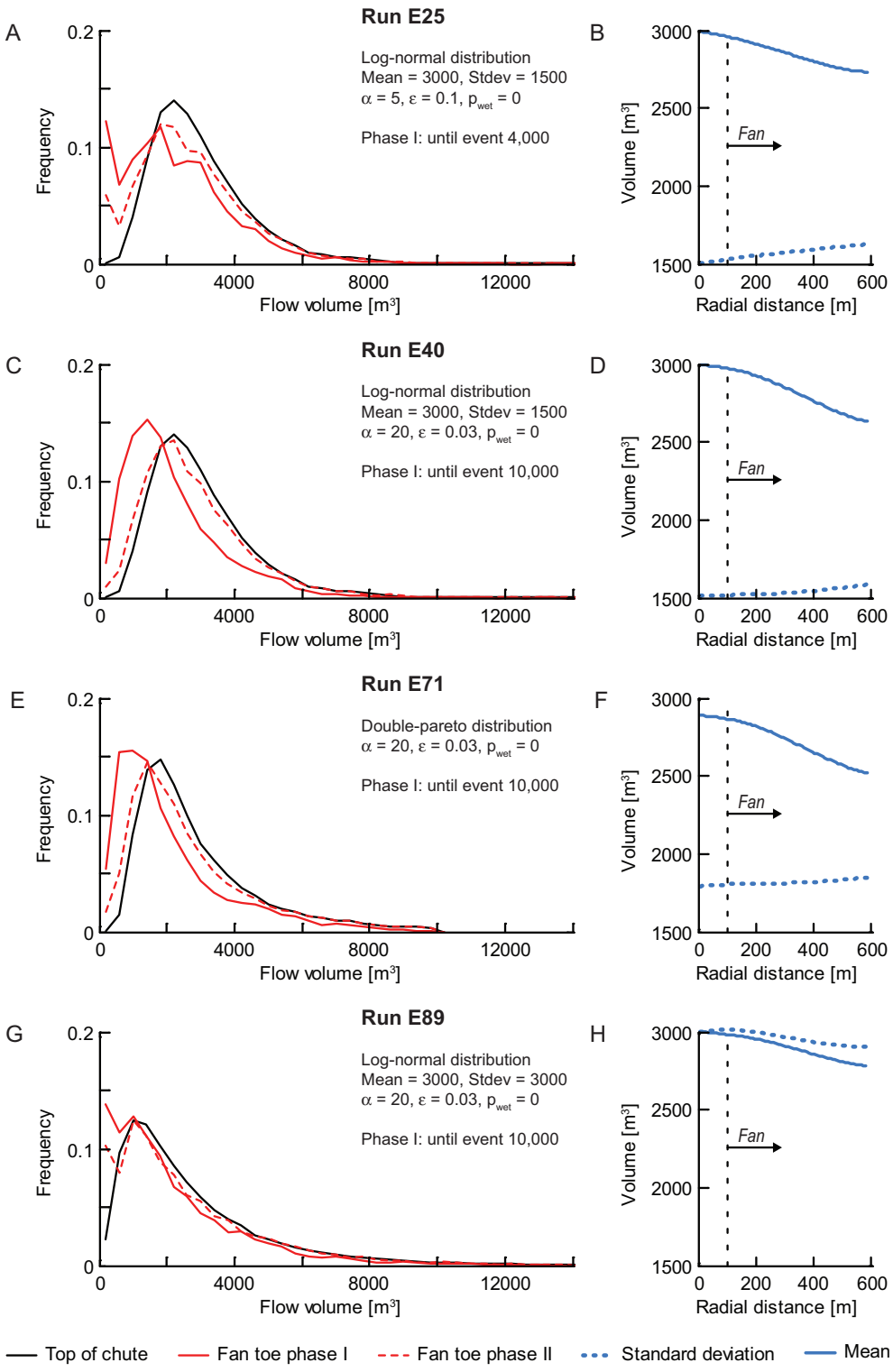

Figure 5.7: *Modification of magnitude–frequency distributions of flow volumes by emerging fan topography in space and time. Panels on left side (A, C, E and G): comparison between input at top of chute and output at toe of fan for phase I and phase II (see text). Important model parameters are indicated in the figure, full details are shown in Appendix, Table D.1. Panels on right side (B, D, F and H): down-fan variation in mean and standard deviation of flow volumes over total model run (30,000 events); vertical dashed line denotes boundary between the chute and the fan.*

E40) and the input distribution (run E40 vs. run E71). Generally I find that in phase I the mean volume measured at the fan toe is only between 62% and 79% of the input at the top of the chute (Table 5.1). With respect to standard deviation of flow volumes measured in phase I the picture is less clear, with output magnitude–frequency distribution similar to that of the input. In phase II the mean flow volumes at the fan toe increased and were between 89% and 94% of the input mean volume. The standard deviation of flow volumes measured at the fan toe in phase II were consistently larger than in that of the input with ratios ranging from 104% (run E25) to 110% (run E71) (Table 5.1). The spatial pattern of mean and standard deviation of flow volumes is shown in Figure 5.7B, D, F and H. I find that in all runs the mean volume decreased down-fan. However, the standard deviation of input volumes only increased in runs E25, E40 and E71 whilst it slightly decreased in run E89 in the down-fan direction.

Table 5.1: *Mean and standard deviation of flow volumes for phase I and II measured at fan toe and in comparison to input distributions.*

Location	Mean [m^3]	Relative to input [%]	Relative to phase I [%]	Standard deviation [m^3]	Relative to input [%]	Relative to phase II [%]
			run E25			
Top of chute	3,006	–	162	1,501	–	94
Toe phase I	1,851	62	–	1,605	107	–
Toe phase II	2,665	89	144	1,667	111	104
			run E40			
Top of chute	3,005	–	138	1,506	–	101
Toe phase I	2,176	72	–	1,486	98	–
Toe phase II	2,832	94	130	1,579	105	106
			run E71			
Top of chute	2,898	–	138	1,791	–	105
Toe phase I	2,105	73	–	1,706	95	–
Toe phase II	2,610	90	124	1,875	104	110
			run E89			
Top of chute	3,026	–	127	3,013	–	112
Toe phase I	2,387	79	–	2,696	89	–
Toe phase II	2,807	93	118	2,918	97	108

Using run E25 and E40 I can investigate the specific effects of deposit geometry by considering two opposing combinations of α and ε. A low ratio of $\alpha/\varepsilon = 50$ in run E25 (Figure 5.7A and B) gives rise to thick deposits and flows that deposit at high lag rates, similar to behaviour documented for flows with high concentrations of coarse clasts (Berti and Simoni, 2007). A ratio of $\alpha/\varepsilon = 667$ as in run E40 (Figure 5.7C and D) results in thinner deposits and flows depositing at lower lag rates that tend towards 'lahar-type' behaviour with a lower concentration in coarse clasts (Iverson et al., 1998). For run E25 I find that mean volumes measured at the fan toe for phases I and II are smaller than in run E40.

A comparison of run E40, E71 and E89 shows the effect of changing the input volume distribution on the output volume distribution measured at the fan toe. When comparing run E40 and E89, where I doubled the standard deviation (at identical mean) of input volumes, I find that higher standard deviation led to a higher proportion of flows not reaching the fan toe (compare solid red line in Figure 5.7C and G). Considering the difference between a log-normal and a double-pareto distribution (run E40 vs. E71, Figure 5.7, Table 5.1) I find no striking differences.

Model experiments had a down-stream boundary condition that is very common in mountain valleys: the lateral growth of the model fans was radially limited by the model boundaries (Section 5.3). When the fan reaches this radial limit (i.e. the transition between phase I and II), it can only grow further in volume or height by becoming steeper. The emergence of channels in this phase (see also Section 5.3) leads to an increase in flow depth, and as a result entrainment along channels on the fan becomes more likely. Therefore mean volumes measured in phase II at the fan toe approached the mean flow volume of the input and were between 118% and 144% of the volumes measured in phase I (Table 5.1). This means that when fans go through the transition from phase I to II the channel system that developed in phase I for comparatively smaller flows might temporarily have a conveyance capacity insufficient to accommodate the increasing flow volumes during the transition to phase II. Whilst this process probably operates on most natural fans over timescales too long to be of relevance for hazard consideration, the spatial trends in mean and standard deviation of flow volumes might be more relevant.

Conveyance capacity has been reported to decrease down-fan (Whipple and Dunne, 1992), probably in response to a downstream decrease in mean flow volume. The decrease in mean flow volume is reproduced reliably by this model (Figure 5.7B, D, F and H). But results also suggest that there is a possibility for the standard deviation of volumes to increase in the down-fan direction (run E25, E40 and E71). This raises an interesting hypothesis that should be tested in the field: If channel conveyance capacity scales with mean flow volume, and standard deviation of flow volumes increases downstream, then channel capacity is more likely to be exceeded near the fan toe than near the fan head once fans have reached phase II of their life cycle.

Interestingly, when raising the standard deviation to the same value as the mean (run E89) as opposed to half the mean (run E40), the standard deviation of flow volumes shows almost no down-fan variation and the decline in mean flow volumes is less pronounced. This indicates that the behaviour of natural fan systems might be sensitive to the shape of the magnitude–frequency

distribution, and underlines first the need to better understand and characterize the magnitude–frequency distributions on natural fans, and second the need to verify these results in the field or with flume experiments.

5.4.2 The influence of fan morphology on inundation patterns

The temporal evolution of inundation patterns and depocenter location on alluvial fans controls the distribution of surface age and location of areas prone to inundation (Dühnforth et al., 2007; Helsen et al., 2002; Jakob and Friele, 2010). For debris-flow hazard assessment the prediction of future flow paths and inundation area is crucial (Gamma, 1999; Iverson et al., 1998; Scheidl and Rickenmann, 2011; Scheuner et al., 2011), but it is inherently difficult due to the convex topography of fans and their divergent channel network. Further uncertainties that deteriorate the ability to predict flow behaviour are related to the event properties such as total volume, peak discharge and velocity. In order to tackle the uncertainty related to flow paths many models include a random algorithm to generate a set of likely flow paths (Favalli et al., 2009; Gamma, 1999; Scheidl and Rickenmann, 2011) which are then used to inform the spreading behaviour of flows. The second major unknown in debris-flow hazard assessment is the magnitude-frequency distribution of flow volumes at a particular location. Therefore the analysis is often limited to a few scenarios that seem reasonable based on past events, or on an assessment of sediment availability in the catchment or comparison with comparable locations (Scheidl and Rickenmann, 2011; Scheuner et al., 2011). The assessment of sediment availability is a very difficult task in itself, yielding large uncertainties (Abanco and Hürlimann, 2011; Gertsch, 2009; Jakob et al., 2005) partly because the controls on debris-flow erosion are still poorly understood with many questions remain unsolved (Chapter 4; Berger et al., 2011; Iverson et al., 2011).

In this application I propose a different approach to tackle the issues of flow-path and inundation-area uncertainty. Rather than limiting the assessment to predefined scenarios with unknown uncertainties, I explore the statistical properties of flow path switching over thousands of events and for a broad range of flow types, varying in volume, sediment concentration and deposit geometry. Flow path switching results from channel avulsion (Field, 2001; Reitz et al., 2010; Whipple and Dunne, 1992). For the purpose of hazard assessment the question arises, once avulsion has occurred, how different will the likely new flow path will be from the previous flow path, as this determines the at-risk area to both sides of active channels on fans. The degree of change in flow

direction in such a scenario is likely to depend on the micro-topography in vicinity of the active channel, e.g. the presence of an abandoned channel nearby could be crucial in capturing the flow (Jerolmack and Paola, 2007). I therefore hypothesize that over many events, the change in flow direction should, to some degree, be a function of fan surface morphology, or more specifically a function of the presence or absence of local relief in the form of relic channels and lobes.

In order to pursue this idea, I need to define a measure to quantify the change in flow direction that can be calculated from the model output. In Figure 5.4A I have introduced a visualization of flow direction over time. Now I take this further, and quantify the changes in flow direction between successive events. I define the relative jump distance *RJD* as:

$$RJD = \frac{j}{J} \tag{5.6}$$

where j is the distance between the intersection points of two successive flows with an arbitrary arc, and J is the length of this arc (Figure 5.8).

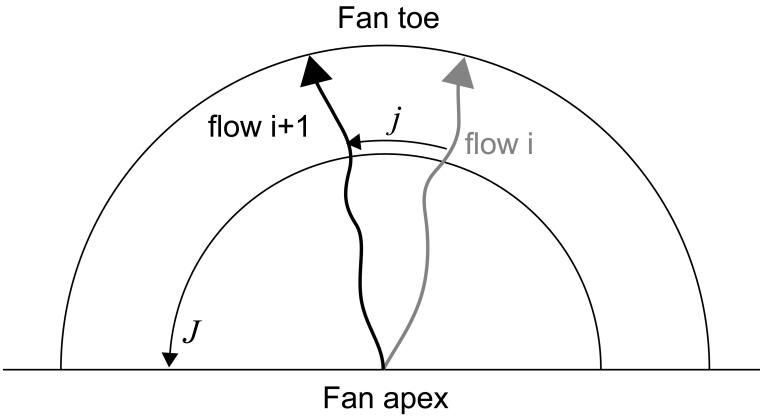

Figure 5.8: *Definition of relative jump distance (RJD) between sucessive events. i is the event number, j is the distance between the intersection points of two successive flows with an arbitrary arc, and J is the length of this arc.*

RJD varies between 0 and 1; a value of $RJD = 0.5$ would indicate a change in flow direction by 90°. For a single pair of subsequent flows this is not a very useful piece of information, but when calculated over a larger number of events or over all events in a model run, I can make probabilistic statements about the system behaviour. A useful visualization is the cumulative probability distribution of a number of measurements of *RJD* (Figure 5.9), as this measure quantifies the probability of a switch in flow direction of a certain magnitude between successive events. I calculate *RJD* only for arc 50, which is at 2/3 of the distance between fan apex and toe, as the

cumulative probability distribution of *RJD* does not vary significantly by distance from the fan apex. From the cumulative probability distribution I can read the relative jump distance *RJD* for a given non-exceedance probability. In the subsequent analysis I will always quote the relative jump distance at a 99% non-exceedance probability, RJD_{99}, as a measure of likely maximum flow direction change between successive events. In the model deposit geometry and local relief are primarily controlled by the parameter α and to a lesser extent by ε. α determines the critical flow depth or minimal deposit thickness when flows are spreading over-bank (Equation 5.3). ε determines the maximum lag rate (Equation 5.2) and width of depositional lobes. In the next step of the analysis I show how variations in α and ε influence RJD_{99} (Figure 5.10). Lastly I use the model to generate fan topography at intervals of 100 events, calculate RJD_{99} for the same intervals, and compare the RJD_{99} data to two measures of fan surface roughness to explore their potential value as predictors of RJD_{99}:

1. local roughness (Frankel and Dolan, 2007): defined as the standard deviation of slope, where slope is calculated across a 3x3 cell moving window across the fan surface.

2. standard deviation of radial slope (Section 5.3.2)

For two model runs (E25 and E40) I calculate the linear regression of RJD_{99} against local roughness and standard deviation of radial slope.

I carried out 50 model runs to constrain the model response with respect to RJD_{99} to variations in α and ε. In model run E24 to E36, E40 to E56 and E64 to E88 I varied α and ε to cover the ranges reported in the literature for debris flows (Berti and Simoni, 2007; Crosta et al., 2003; Griswold and Iverson, 2008; Iverson et al., 1998). Input sediment concentration was always allowed to vary between 0.3 and 0.8, and the latter was also taken as the critical sediment concentration. Half of the runs used a log-normal input volume distribution and the other half used a double-pareto input volume distribution (Appendix:z Table D.1) due to a fundamental difference between a log-normal and a double-pareto distribution; The mean of an increasing number of values sampled form a log-normal distribution converges at large sample sizes, while the mean of an increasing number of values sampled from a double-pareto distribution is non-stationary (Schumer and Jerolmack, 2009).

I use model runs E25 and E40 to test the hypothesis that measures of surface roughness are potential predictors of relative jump distance. In Figure 5.9 I show the cumulative probability

distribution of *RJD* of all 30,000 events in two contrasting model runs. In run E25 I set $\alpha = 5$ and $\varepsilon = 0.1$ (run E40 $\alpha = 20$ and $\varepsilon = 0.03$) and find that at any given probability level *RJD* is smaller than in run E40. At 99% non-exceedence probability I find that RJD_{99} is 0.26 for run E25 and 0.57 for run E40 (Figure 5.9).

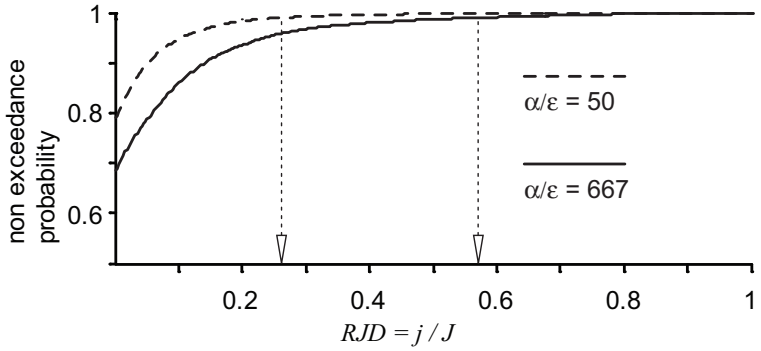

Figure 5.9: *Cumulative probability distribution of relative jump distance (RJD) for run E25 (dashed line, with $\alpha = 5$ and $\varepsilon = 0.1$) and run E40 (solid line, with $\alpha = 20$ and $\varepsilon = 0.03$) measured at arc 50. RJD_{99} for run E25 and E40 is indicated by dashed arrows.*

In Figure 5.10 I have aggregated all results from the 50 model runs into a plot of RJD_{99} as a function of α and ε. I find a similar pattern for the log-normal (Figure 5.10A) and double Pareto input volume distribution (Figure 5.10B). RJD_{99} increases from a minimum of 0.1 for $\alpha = 5$ to a maximum of 0.6 for $\alpha = 40$. With respect to ε the dependence is not as strong, but RJD_{99} seems to be smallest when $\varepsilon \approx 0.1$.

In Figure 5.11 I show the results from the next step in the analysis, the comparison of RJD_{99} with fan surface roughness, again for run E25 and run E40 (see Figure 5.9 for the cumulative probability distribution). Fan slope, roughness, standard deviation of radial slope and RJD_{99} are shown for time slices of 100 debris flows over the model duration of 30,000 events in both runs. First I find that run E25 with a low ratio of $\alpha/\varepsilon = 5/0.1 = 50$ yielded a rough fan surface compared to run E40, where the ratio of $\alpha/\varepsilon = 20/0.03 = 667$ was much higher (Appendix D). Resulting fan slopes for both runs (E25 and E40) are comparable (Figure 5.11). Fan surface roughness increased in both cases rapidly during the first 10,000 events, which reflects the fan evolution in phase I (Section 5.4.1), and then stabilized for the remainder of the model run. Standard deviation of radial slope reached a stable level much earlier and showed only minor fluctuations through time, but there were prolonged periods where standard deviation of slope was higher or lower than the average (e.g. between 18,000 and 26,000 events in run E40). RJD_{99} in run E25 decayed rapidly from a maximum of 1 up to 10,000 events to a maximum of 0.5 between 10,000 and 30,000

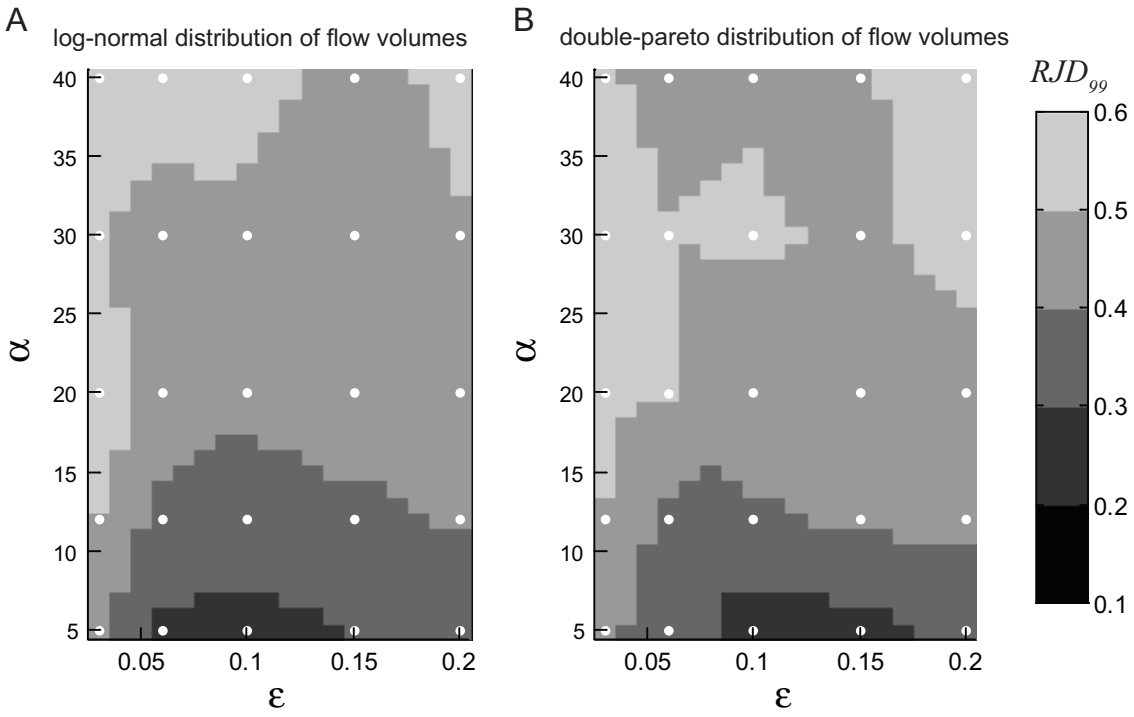

Figure 5.10: *Influence of* α *and* ε *on relative jump distance. White dots represent the combinations of* α *and* ε *used in the model runs. The map in gray-shades is the linear interpolation of the resulting* RJD_{99} *values. A: Log-normal input volume distribution, runs E24–E30, E40–E56 . B: Double Pareto input volume distribution, runs E64–E88.*

events (Figure 5.11A). In run E40 periods of RJD_{99} close to 1 occurred throughout the run, but became less frequent as time progressed (Figure 5.11B). Note the period in the last third of this model run when RJD_{99} was zero, coinciding with a relatively high standard deviation in radial slope and indicating the presence and influence of a stable channel.

In Table 5.2 I show the results of the regression analysis of RJD_{99} against local surface roughness (x_1) and standard deviation of radial slope (x_2). I find that in run E25 surface roughness x_1 measured at 100 event time intervals, explains 55% (61% for run E40) of the variability in RJD_{99} during the 100 events following the roughness measurement. Standard deviation of radial slope is a worse predictor of RJD_{99}, but in run E25 still accounts for 43% of the variability in RJD_{99} during the 100 events following the measurement (28% for run E40).

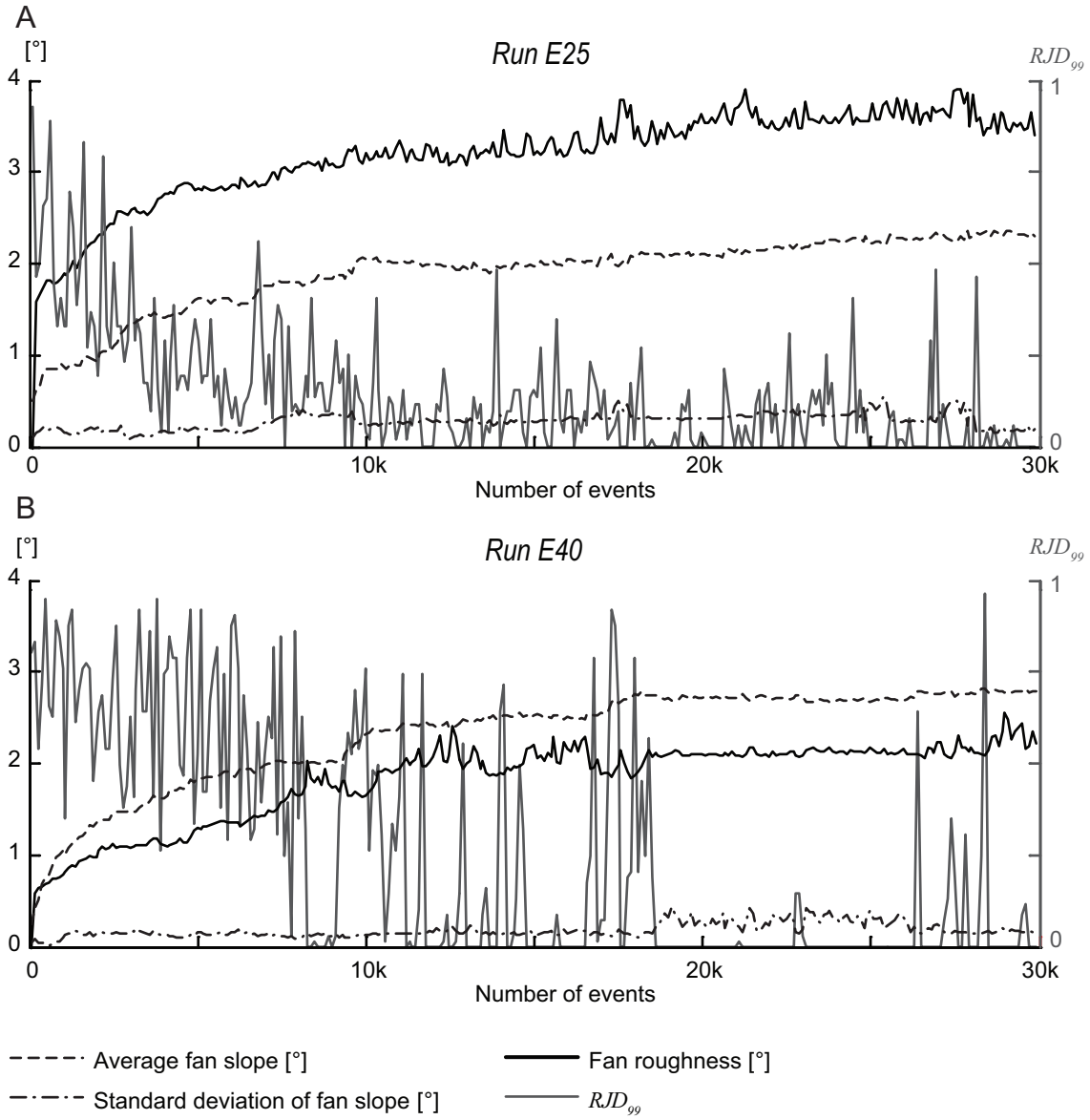

Figure 5.11: *Left y-axis: Fan slope [°] and fan surface roughness [°], standard deviation of radial slope calculated every 100 events. Right y-axis: RJD_{99} calculated for time slices of 100 events. A: Run E25. B: Run E40.*

Table 5.2: *R^2 values of linear regression between relative jump distance at 99% non-exceedence probability RJD_{99} for time slices of 100 events and surface roughness x_1 or standard deviation of radial slope x_2 calculated from fan topography just before first event in a time slice.*

	Run E25	Run E40
Regression model: Surface roughness	$\hat{RJD}_{99} = a + b \cdot x_1$	
R^2	0.55	0.61
Regression model: Standard deviation of radial slope	$\hat{RJD}_{99} = a + b \cdot x_2$	
R^2	0.43	0.28

5.4.3 The influence of apex disturbance on fan surface age and debris-flow magnitudes

In the last application I want to consider the effect of sediment input by a rock avalanche on fan morphology. Rock avalanche deposits emplaced on the fan head disturb the pattern of debris-flow inundation and depostion on fans (e.g. at Illgraben, Chapter 2; Blair and McPherson, 2008). In both cases the rock avalanche blocked the catchment outlet, which resulted in a down-fan shift in apex position and abandonment of the peripheral fan segments near the mountain front. Davies and Korup (2007) found that large and infrequent sediment input by rock avalanches caused fan head aggradation due to increased sediment flux and subsequent incision as sediment flux returned to background levels. With this application I want to investigate how suitable this model is to investigate such a scenario by making a qualitative comparison between model output and these case studies. Specifically I am interested in the emerging patterns of surface age on the fan, and in sediment output measured at the fan toe compared with the sediment input.

I performed a standard model run of 10,000 events with a log-normal input volume distribution (mean volume of 3,000 m^3 and standard deviation of 1,500 m^3), $\alpha = 10$, $\varepsilon = 0.1$, $C_{min} = 0.3$, $C_{max} = C_{crit} = 0.8$ and $p_{wet} = 0$ (Run E23 in Appendix, Table D.1). After 10,000 events I placed a rock avalanche deposit at the fan apex. It covered a semi-circular area with a radius of 50 m around the fan apex (Figure 5.12F) and had a thickness of 20 m. I then filled the accommodation upstream of the rock avalanche dam to form a horizontal surface. This procedure yielded a total added volume of $230,000$ m^3, which was equivalent to about 5% of the total fan volume $\approx 4 \cdot 10^6$ m^3 at that time. I then restarted the model for another 10,000 events with unchanged model parameters. In addition to the data analysis and visualizations shown before (Section 5.3.2, Figure 5.4A and D) I show statistics on sediment flux at the fan toe, long profile evolution in the first 100 events following the rock avalanche (Figure 5.12D) and visualizations of surface age after 10,000 and 20,000 events (Figure 5.12E, F and G). In Figure 5.12A I show the sediment flux measured at the fan toe normalized by the input over a moving window of 50 event. An animation of topographic and surface age evolution of this experiment is archived on the data CD (Appendix D).

In Figure 5.12A I show a comparison of input flow volumes with flow volumes that reach the fan toe. I averaged output volumes over a moving window of 20 events and normalized this by the average input volume over the same moving window. The time window of 20 events is

approximately one third of the response time needed for the channel to adjust to an equilibrium profile after the rock avalanche (see discussion below, Figure 5.12D). I normalized the output by the input to enhance the visualization of the relative difference between the two, otherwise fluctuations in sediment flux are dominated by the noise generated by the log-normal input distribution. Initially only 20% of input volume reached the fan toe, but after about 5,000 events output volumes stabilised at $\approx 80\%$ of input and fluctuated by $\pm 10\%$. With regard to the standard deviation of output volumes normalized by the input standard deviation I find that during the first 1,000 events standard deviation in the output was smaller than in the input, but afterwards was mostly larger, eventually stabilising at $\approx 110\%$. The rock avalanche at 10,000 events and subsequent incision did not significantly impact the output distribution, as indicated by a mean and standard deviation of normalized flow volumes that does not change significantly before and after 10,000 events (Figure 5.12A). Incision into the rock avalanche deposit was completed after only ≈ 60 events (Figure 5.12D) resulting in a slightly steeper but more or less uniformly sloping fan (Figure 5.12F), and a very narrow (9 m) and deep (26 m) gorge cut into the rock avalanche deposit. The net volume removed from the deposit calculated as the difference between topography at 20,000 events and at 10,000 events was $\approx 20,000 \mathrm{m}^3$.

However, I found significant changes in the debris-flow inundation patterns. After emplacement of the rock avalanche deposit, debris-flow activity was focused on the central segment of the fan (Figure 5.12C). The abandonment of the peripheral west and east segments of the fan resulted in a rapid increase in median fan surface age after 10,000 events (Figure 5.12B). At the end of the model run at 20,000 events, I find that the peripheral fan segments have been completely sheltered from subsequent debris flows due to the down-fan shift in apex position (Figure 5.12E and F) leading to a bi-modal age surface distribution (Figure 5.12G).

Figure 5.12: *Next page: Summary of results from apex disturbance by rock avalanche. A: Temporal evolution of mean and standard deviation of output volume distribution averaged over 20 events and normalized by corresponding mean and standard deviation of input volumes. B: Median fan surface age every 100 events. C: Temporal variation of flow path direction from west to east (from left to right). D: Temporal evolution of talweg elevation at apex, rock avalanche at 10,000 events resulted in 17 m elevation increase, decline to pre-rock avalanche level within the next ≈ 60 events as indicated by arrow. E: Map of fan surface age with contours every 4 m immediately after rock avalanche (RA) at 10,000 events. F: Map of fan surface age at end of model run with contours every 4 m. G: Frequency distributions of fan surface age for situations in E and F, RA: rock avalanche.*

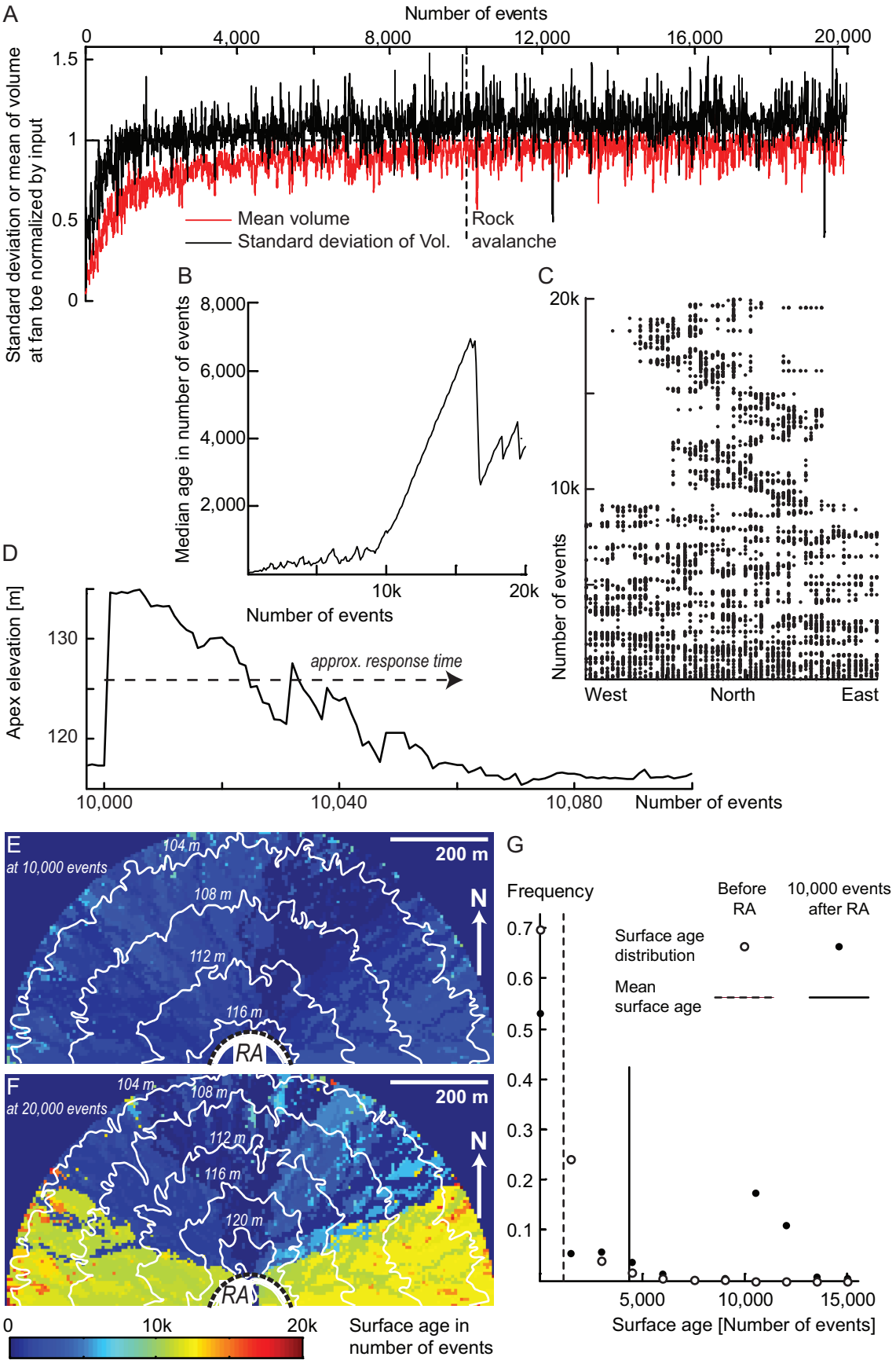
A
Number of events
0
4,000
8,000
12,000
16,000
20,000
Standard deviation or mean of volume at fan toe normalized by input
1.5
1
0.5
0
Mean volume
Standard deviation of Vol.
Rock avalanche
B
Median age in number of events
8,000
6,000
4,000
2,000
10k
20k
Number of events
C
20k
10k
Number of events
West
North
East
D
Apex elevation [m]
130
120
approx. response time
10,000
10,040
10,080
Number of events
E
at 10,000 events
104 m
108 m
112 m
116 m
RA
200 m
N
F
at 20,000 events
104 m
108 m
112 m
116 m
120 m
RA
200 m
N
0
10k
20k
Surface age in number of events
G
Frequency
0.7
0.6
0.5
0.4
0.3
0.2
0.1
Before RA
10,000 events after RA
Surface age distribution
Mean surface age
5,000
10,000
15,000
Surface age [Number of events]

In this application I have shown how this model could be used to investigate external forcing and how output data could be visualized, but I also note some model limitations that warrant further attention. The external forcing incurred by the rock avalanche surprisingly did not impact on the sediment volume output at the fan toe. There are two possible explanations for this; first, the disturbance was too small in comparison to the system inherent noise introduced by the input volume distribution and subsequent erosion and deposition on the fan (Humphrey and Heller, 1995; Jerolmack and Paola, 2010; Kim et al., 2006; Nicholas and Quine, 2007b). Second, and perhaps more relevant explanation, relates to a current limitation of the model. Figure 5.12D and F show that incision into the deposit was extremely rapid and localized, resulting in only limited removal of the rock avalanche deposit. This is in disagreement with field examples such as the Illgraben fan (Chapter 2) or Rose Creek Fan (Nevada, USA, Blair and McPherson, 2008), where incision by debris flows into the rock avalanche deposit resulted in a breach of several 100 meter width. But because the model does not allow for lateral erosion and bank collapse when channel side walls become too steep, the resulting channel was very narrow. Both mechanisms, lateral erosion and bank collapse are clearly relevant on fans (Chapter 4, Appendix A.1 Figure A.12) and could be included in future models. Nonetheless, this application demonstrates that a down-fan shift in apex position leads to the abandonment of peripheral fan segments (Blair and McPherson, 2008, Chapter 2). Because these fan segments are sheltered from further inundation, their surface age will be on average older than the surface age of active fan segments. Surface age distributions of fans, obtained by mapping and dating of fan surfaces (e.g. Chapter 2, Dühnforth et al., 2007), contain interesting information on the history of the fan. A bi-modal age distribution might be the result of drastic changes in inundation patterns in the past, and the age difference of the two modes (at zero and 10,000 events in Figure 5.12) should match the time passed since the disturbance.

5.5 Discussion

In the discussion I want to consider three areas: the underlying principles and the general framework of the model, the model validation, and lessons learnt from the applications shown previously.

5.5.1 Model principles

To my knowledge I have presented the first numerical debris-flow fan evolution model. It consists of seven components that determine its capabilities and limitations:

- Model space geometry
- Flow routing
- Relationship between flow volume and shape of hydrograph
- Relationship between flow volume and deposit geometry
- Lateral inundation algorithm
- Erosion and deposition rule
- Rule for transition from levee- to lobe-deposition mode

Unlike other models that operate over large spatial extents (Berti and Simoni, 2007; Gamma, 1999; Iverson et al., 1998; Scheidl and Rickenmann, 2011), I opted for a grid consisting of a series of cross sections, inspired by Nicholas and Quine (2007a), and handling of topographic data and network topology inspired by Tucker et al. (2001). This has a number of advantages with regard to the remaining six components, but most importantly provides a very efficient and flexible way of parameterising topography. In this chapter the model space consisted of a series of straight cross sections along the chute followed by semi-circular cross sections, termed arcs, for the fan area (Figure 5.1). Within the model framework there is only one constraint on the shape of these cross sections: The trace of the cross sections should be approximately perpendicular to the expected flow direction. Therefore the parameterization of a sinuous valley would not be a problem. Cross section and node spacing are independent and a relatively fine node spacing compared to the arc spacing can be used to account for the larger cross-flow variability in topography. Whilst it is clear that the shape of the cross sections predetermines the overall shape of the resulting landform over the long-term, the shape of the cross sections could be adapted repeatedly to minimize this geometric effect.

The proposed flow routing follows the true steepest slope, always moving outwards from one to the next arc, but the algorithm only considers nodes in the next arc that fall within the search angle ζ (Figure 5.1). Larger values for ζ allow for more abrupt changes in flow direction between arcs. The flow routing proposes one single flow path along the talweg that forms the starting point for the inundation algorithm. This is an important difference to some fluvial fan models that allow for flow splitting (e.g. Nicholas and Quine, 2007a; Pelletier et al., 2005), which is also observed in surging debris flows (Blair and McPherson, 1998). But unlike Scheidl and Rickenmann (2011) or Gamma (1999), the flow routing in this model does not contain any random components and flow paths do not stop when reaching a pit, instead pits are filled and flows continue when the remaining volume is sufficiently large.

The actual flow behaviour is inspired by the LAHARZ model and its derivatives (Berti and Simoni, 2007; Griswold and Iverson, 2008; Iverson et al., 1998), with an important difference beeing that erosion and deposition along the flow path are allowed, which in turn alters the total flow volume. The underlying assumptions are that debris-flow hydrographs can be approximated by a triangular shape and that the propagation velocity is independent of slope but follows $u \approx \sqrt{g \cdot h_r}$, where g is gravitational acceleration and h_r is hydraulic radius. Under these assumptions Iverson et al. (1998) showed that a power-law relationship exists that links total flow volume to flow cross section area and total inundation area. In essence this means that runout distance in the LAHARZ model and in this model is therefore only controlled by mass-conservation and the empirical parameters α and ε in Equations 5.2 and 5.3, and that flow hydrographs do not attenuate when the flow volume remains constant, which may lead to an over-prediction of inundation width.

The lateral inundation algorithm in combination with the erosion and deposition rules is a novel aspect of this model as it provides a mechanism for the deposition of levees. So far only more sophisticated two-phase models have achieved this, but only for very small model-domains of single channels (e.g. Pudasaini et al., 2005). Levees are important topographic features because they guide subsequent flows, make inundation of inter-channel areas much less likely (Chapter 4; Blair and McPherson, 1998; Dühnforth et al., 2007; Whipple and Dunne, 1992). The crucial component of the inundation algorithm is the value of d_c that determines the thickness of deposits when flows spread over-bank. In the current implementation d_c scales with flow volume to the power $1/3$ (Equation 5.3), following Berti and Simoni (2007). This is one of many options. An alternative approach would be to link d_c to the size of coarse boulders in the flow as detailed field

studies of debris-flow deposits suggest that deposit dimensions might be related to the size of the most coarse clasts (Blair and McPherson, 1998); however, to date no simple formulations have been proposed that could be easily adapted. I suggest that a substantial improvement with respect to deposit thickness should include the introduction and tracking of a coarse particle concentration in the model framework.

With regard to erosion and deposition when flow depth exceeds d_c I assume that they are a function of basal shear stress. I further assume that I can estimate basal shear stress beneath the debris flow by calculating the Coulomb friction ($\tau_b = \rho_b g h$; Iverson, 1997; Takahashi, 2007). This approximation is valid for debris flows where friction forces dominate over collision forces (Savage number $N_{Sav} < 0.1$). As long as mixtures of water and rock (i.e. with a strong density contrast) are considered this assumption only breaks down at very low bulk internal friction angles ($\phi \ll 30°$) of the granular material or at very high shear rates ($\dot{\gamma} \gg 100$ 1/s) (Iverson, 1997). I use the basal shear stress to determine the amount of erosion or deposition by sampling from a data set of 565,344 paired observations of maximum flow depth and associated bed elevation change from the Illgraben channel (Chapter 4). This procedure assumes that I can use $\tau_b = \rho_b g h$ to convert the flow-depth in the field data to basal shear stress, which then becomes independent of the slope of the study reach where the data was obtained. It is important to note that my approach to erosion does not favor any particular entrainment or erosion mechanism (e.g.: Berger et al., 2011; Hsu et al., 2008; Hungr et al., 2005; Papa et al., 2004; Sassa and Wang, 2005; Stock and Dietrich, 2006) so long as that mechanism shows a monotonic functional dependence on basal shear stress.

The last model component is the rule that controls the levee-lobe transition. The decision to link this transition to a critical sediment concentration is based on Takahashi (2007) and Rickenmann et al. (2003) who found that entrainment in debris flows decreases with increasing sediment concentration. In essence I make the assumption that once entrainment becomes difficult, because of high sediment concentration, lobe deposition starts. However, Blair and McPherson (1998) suggested that the transition between levee and lobe deposition might also be related to a depletion in coarse clasts that are left behind in levees, supported by observations of a distinct decrease in maximum clast size from levees to lobes. This finding could, in addition to the potential role of coarse clasts in setting the minimum deposit thickness, motivate a more sophisticated treatment of grain size in the model.

5.5.2 Model validation

The validation of a debris-flow fan model poses a major challenge due to a lack of good long-term records of the evolution of for example slope or volume on debris-flow fans. For the moment I can only confirm that the proposed model produced reasonable debris-flow deposits at the level of single flows (Figure 5.3), and that over thousands of events general expectations on the interplay between fan slope on one hand and sediment flux or sediment concentration on the other hand were fulfilled. Model fan slope increased with increasing sediment flux (Bull, 1962; Clarke et al., 2010; Harvey, 2002), and with increasing sediment concentration at nearly constant sediment flux (Milana and Ruzycki, 1999; Schumm et al., 1987; Whipple et al., 1998) (Figure 5.5). During the validation experiments I found that fan slope was very sensitive to the proportion of flows entering lobe-deposition mode high up on the fan, which is a function of the difference between the initial sediment concentration and the critical sediment concentration. Model runs with a mean initial sediment concentration close to the critical sediment concentration produced the steeper fans than those runs where the difference between the two was larger. This confirmed a hypothesis formulated by Whipple and Dunne (1992) suggesting that catchments producing a high proportion of flows with a high sediment concentration should build steep fans, while catchments producing more low-concentration flows should build gentle fans.

In this chapter I have run the model with only one type of boundary condition imitating an axial, non-incising river that limited the radial fan growth and maintained a constant base level. This is a typical boundary conditions for mountain valleys, and is similar to the boundary condition in (Clarke et al., 2010), and I found that the model underwent the same phases of fan building as their flume experiments. Based on these comparisons I am confident that the model, although it is strictly speaking not calibrated, provides a reasonable platform to investigate debris-flow fan evolution.

One important pattern that was seen in all validation experiments is the non-linear growth in volume and slope despite constant sediment flux (Figure 5.4C and D). The main reason for this is not that the fan becomes larger, but that with increasing slope the fan becomes more efficient in routing sediment from fan apex to toe (Figure 5.4E). In other words, after a while debris-flow fans start to behave more like hillslopes that convey sediment rather than storing it, and can be described as being in a state of ‘dynamic equilibrium’ (Davies and Korup, 2007). This is an

important finding for the temporal evolution of connectivity of headwater catchments with the higher-order fluvial stream network in mountain belts, because alluvial fans are the bottleneck between the two process domains. It suggests that over time, e.g. following the deglaciation of a mountain valley, connectivity increases as fans prograde out into the valley floor and approach their state of dynamic equilibrium.

The model should not be used to reproduce the behaviour of a specific debris-flow catchment and fan system, and model results should not be applied to a specific location. However, I used the model to perform three experiments to enhance the understanding of basic process–form feedback that rely on the capability to model thousands of flows and that require flows to erode and deposit.

5.5.3 Model application

With the first two applications I demonstrated why fan evolution over thousands of debris-flows is relevant for debris-flow hazard. If one can read fan surface morphology in a quantitative way with respect to the underlying process, we have a useful tool at hand to learn about the behaviour of a debris-flow fan system. After all, fan surface morphology (e.g. location of channels or geometry of depositional lobes) is the only record of past debris-flow activity, increasingly so with the wide availability of high-resolution topography. Because the focus in hazard assessment lies on the formulation of 'reasonable scenarios' with defined recurrence intervals and flow volumes (e.g. Petrascheck and Kienholz, 2003), there is a tendency to undervalue the long-term information recorded on the fan surface in the form of deposits and channels about the behaviour of past events. However, formulation of scenarios is the crucial step for the outcome of the hazard assessment and the same time it is also the most uncertain step in the work flow unless there is a good event archive. With the model presented here I have shown examples how I can model a debris-flow fan system to gain a probabilistic insight into the behaviour without limiting the analysis to specific scenarios of flow volume and properties, but by drawing flows from a broad population of possible flows.

Fan evolution and influence on debris-flow magnitude–frequency relationship

In the first application I have shown how the magnitude–frequency distribution may change between fan apex and fan toe when debris flows are allowed to dynamically interact with the emerging topography involving entrainment and deposition. The model results suggest that the standard deviation of flow volumes may increase from fan apex to fan toe while the mean flow volumes

decrease (Figure 5.7), causing a down-fan decrease in channel conveyance capacity (Whipple and Dunne, 1992). This finding highlights the need to better understand those debris flows that are erosional on the fan (Chapter 4; Berger et al., 2011; Scheuner et al., 2009), increase the conveyance capacity of the channel in the upper part of the fan and thereby are less likely to avulse near the apex. However, when these flows reach the lower part of the fan, their peak discharge is likely to exceed channel conveyance capacity leading to avulsion near the fan toe (Arattano et al., 2010; Badoux et al., 2008; Scheuner et al., 2009). Very specifically, the implication is that it is dangerous to assume in debris-flow models used in hazard assessment that flows have to deposit once reaching the fan (Gamma, 1999; Scheidl and Rickenmann, 2011).

The influence of fan morphology on inundation patterns

In the second application I have shown that there may be an important link between fan surface morphology and hazard zonation that has been overlooked in the past. Beside the formulation of relevant scenarios with respect to event magnitude, hazard zonation on debris-flow fans also requires a prediction of future flow paths, which allows a prediction of likely inundation areas (Gamma, 1999; Iverson et al., 1998; Scheidl and Rickenmann, 2011; Scheuner et al., 2011). However, flow path prediction on fans is inherently difficult due to the overall convex topography, the divergent channel network Pelletier et al. (2005) and uncertainties related to the event properties such as total volume, entrainment along the flow path (see above), peak discharge and velocity. The flow path uncertainty has been approached in the past by a random generation of likely flow tracks (Favalli et al., 2009; Gamma, 1999; Scheidl and Rickenmann, 2011). Geomorphic mapping has been used widely and reliably to identify the signature of past debris-flow activity in the landscape, and as such is systematically used in hazard mapping (e.g. Kienholz and Krummenacher, 1995). However, little effort has been spent on making quantitative use of topographic information now widely available, to improve understanding of likely flow behaviour.

With the relative jump distance at 99% non-exceedence probability (RJD_{99}) I introduced a measure of the 'volatility' of a debris flow fan system. RJD_{99} can be utilised as a measure of the width to both sides of an active channel that is likely (with 99% probability) to be inundated by debris flows. I have shown that RJD_{99} is most strongly related to fan surface roughness, which is controlled by deposit geometry and presence or absence of channels. In my model deposit geometry and channel scaling are a function of the two parameters α and ε. In experiments where

channels were formed frequently and where debris-flow deposits were thick (low α) the volatility RJD_{99} was found to be smaller than in systems where channels were rare and deposits were thin and wide (large α). This second point confirms my initial hypothesis that changes in flow direction should be a function of fan surface morphology and this has practical implications for hazard mapping. I therefore explored the potential of two measures of fan surface morphology, surface roughness and standard deviation of radial slope, to act as predictors of future RJD_{99}. I found that two simple measures of fan morphology, local surface roughness and standard deviation of radial slope, explained between 28% and 61% of the observed volatility in RJD_{99} in events following the surface morphology measurements. But it is important to note that the quality of the prediction of RJD_{99} is based on a snapshot of fan morphology, and that it must decay over time as the surface is modified by subsequent flows. Another process that is currently not implemented in the model, but is likely to influence the system volatility on the long term, is post-depositional modifications to the surface such as weathering, bank collapse and development of fluvial drainage networks on abandoned fan surfaces (Dühnforth et al., 2007; Frankel and Dolan, 2007; Pelletier et al., 2005). From the results of this application it is clear that other measures of surface morphology could and should be tested to see whether the correlation between fan morphology and system volatility (RJD_{99}) can be improved, and verification of this proposed correlation should be undertaken in the field.

If the finding that fan surface morphology contains statistical information about future flow behaviour also holds true in natural environments, then this has interesting implications for the interpretation of fan surface morphology. A smooth fan, with only a few channels and a vague debris-flow signature, traditionally interpreted as having experienced little debris-flow activity and being dominated by fluvial processes, might counter-intuitively indicate two things. First, debris flows from this catchment might exhibit a different flow behaviour favouring thin and wide deposits, and second, wide-spread inundation might be the rule rather than the exception. An example how the temporal evolution of such an 'unpredictable' fan might look with regard to RJD_{99} is shown in Figure 5.11B. This figure shows a system where the active channel remains in the same place for a long time ($RJD_{99} \approx 0$) and then suddenly becomes extremely volatile ($RJD_{99} \approx 1$). In such a system there is also no decay over time in the maximum value of RJD_{99}.

The contrary example of a fan with closely spaced channels and thin and elongated lobes might indicate a much more predictable behaviour, because flows that avulse from the active channel are

much more likely to be captured by pre-existing channels (Jerolmack and Paola, 2007) or other roughness elements. The evolution of such a system is shown in Figure 5.11A. Compared to the previous example there is a clear difference between phase I (until $\approx 10,000$ events) where RJD_{99} decays rapidly and phase II where RJD_{99} remains low with a maximum of ≈ 0.5.

Clearly this finding should not be over interpreted, but rather highlights the need for future research in two specific areas: First, one needs to understand what controls deposit geometry in nature. In the current implementation of the model, deposit geometry is controlled mainly by α and ε. However, published values of α and ε are the result of regression analysis from multiple events, from multiple catchments (Berti and Simoni, 2007; Crosta et al., 2003; Griswold and Iverson, 2008). For practical purposes it would be preferable if deposit geometry could be understood in the framework of more physically based parameters that could be established for specific catchments. Possible starting points would be the relationship between debris-flow hydrographs and grain size distribution in the flow front (Chapter 4), the relationship between deposit geometry and grain size distribution of the flow, and discrete particle modeling considering the effect of grain size distribution on the flow hydrograph (Hill et al., 2011; Martinez et al., 2011). Second, fan evolution should be investigated using calibrated debris-flow models that conserve both mass and momentum such as the RAMMS model (Christen et al., 2010; Scheuner et al., 2009) or two-phase models (Iverson and Denlinger, 2001; Pudasaini et al., 2005), and they should be run over multiple events and over real topography, preferably in places where the magnitude–frequency distribution of flow volumes is well known.

The influence of apex disturbance on fan surface age and debris-flow magnitudes

In the last application I investigated the effect of an external disturbance to the apex position, on sediment discharge, long-profile response and surface age distribution on the fan. In this scenario I placed a rock avalanche deposit near the fan apex, blocking the catchment outlet. Large and infrequent sediment input into catchments has been reported to significantly influence sediment discharge downstream (Davies and Korup, 2007; Hewitt et al., 2008; Korup, 2004). I wanted to see how such a scenario would impact on the magnitude–frequency distribution of debris-flow volumes measured at the fan toe. Surprisingly it did not have a discernable impact, which is most likely attributed to a current limitation of the model. The model in its current form does not allow for lateral channel erosion or bank failure. This meant that debris flows in this experiment rapidly

incised an unrealistically narrow and deep gorge into the deposit without removing significant amounts of the actual deposit. The wide breach in the rock avalanche deposit at Illgraben (Chapter 2, Figure 2.5) or on the Rose Creek fan (Blair and McPherson, 2008) demonstrate that lateral migration of debris-flow channels by undercutting and subsequent collapse (Chapter 4, Figure 4.2) are important processes that should be included in a fan evolution model. Inclusion of these processes might exacerbate the modification of magnitude–frequency distributions of flow volumes, as shown in the first application, or reduce surface roughness, which would have an influence on the results of the second application. Despite the unrealistic incision behaviour, this experiment confirmed a hypothesis formulated in Chapter 2, that a shift in apex position should result in the preservation of old fan surfaces near the fan apex and along the mountain front (Figure 5.12F). In Chapter 2 (Figure 2.2) I hypothesized based on relative chronology that lobe L1 should be older than the rock avalanche. The resulting map of fan surface age from modeling (Figure 5.12F) looks similar in the sense that two peripheral fan segments developed that are older than the rock avalanche induced at 10,000 events. The resulting surface age distribution from modeling (Figure 5.12G) shows a bi-modal pattern where the separation between the two modes broadly matches the time passed since the rock avalanche.

5.6 Conclusions

In this chapter I present a debris-flow fan evolution model that is based on an attempt to integrate qualitative observations of debris-flow deposit geometry on the fan, semi-empirical relationships of flow behaviour, and monitoring data on the relationship between flow depth and bed elevation change. I have included a mechanism for entrainment along the flow path, which makes this approach different from most other approaches of modeling debris flows. Flow mobility is mainly controlled by lag rate[2] which is a function of cross section geometry, flow cross-sectional area and sediment concentration. The model fulfills general expectations on the relationship between sediment concentration, sediment flux and fan slope, and fan evolution is compatible with observations made during flume experiments of alluvial fans. Channels emerge and disappear from the fan surface over time in absence of external forcing, entirely as a result of process–form feedback, and act as efficient sediment routing pathways. I find a general increase in sediment routing ef-

[2] volume change of the debris flow per unit downstream distance (Cannon, 1989)

ficiency of the fans over time, which means that over time the connectivity between headwater catchments and the higher-order fluvial network in mountain belts should increase. In model applications I show how understanding of debris-flow hazard can be improved by considering the mechanics of long-term fan evolution. I show that contrary trends of declining mean flow volumes and increasing standard deviation of flow volume in the down-fan direction may explain channel avulsion near the fan toe documented in case studies elsewhere. A novel probabilistic measure for the 'volatility' of debris-flow fans is proposed on the basis of the relative change in flow path direction between successive flows termed relative jump distance. I found that the relative jump distance is controlled by surface morphology with smoother fans being more likely to experience substantial changes in flow path direction between successive events than comparatively rough fans. I suggest that my probabilistic modeling approach may be used in conjunction with more physically based, but computationally expensive, models, where flow properties and magnitude–frequency relationships of flow volumes are poorly constrained.

Chapter 6

Conclusions

6.1 General findings

With this thesis I have investigated debris-flow erosion and deposition dynamics on spatial scales ranging from single channels to a catchment-fan system, and on temporal scales covering single events and millennia. Fieldwork was conducted at the Illgraben, Switzerland, and data used to build a numerical fan evolution model.

Understanding erosion and deposition in debris flows requires tools to map, measure and quantify these processes in the field. Accurate measurement of debris-flow erosion and deposition at channel scale is often hindered by a lack of information about the pre-event topography, hence improved understanding of controls on debris-flow erosion at the field-scale is impossible. I have shown that at reach scale (300 m) terrestrial laser scanning is a viable technique to gather high-resolution topographic data to quantify geomorphic change in debris-flow channels. However, challenges arise from unfavorable scan geometries and accessibility issues that dictate scan station positioning, and result in point clouds with highly variable point densities and ambiguous elevation information. Ambiguous elevation information arises from three sources: imperfect point cloud matching, surface roughness and erroneous measurements. I have shown that when such data is used for change detection by pair-wise comparison of subsequent surveys, results may be substantially biased by the process of point cloud processing. When two inhomogeneous and ambiguous point clouds are to be compared against each other, some transformation is necessary to make them comparable. For this work I opted for the popular approach of gridding the data to a rectangular raster of constant resolution. Traditionally this would have involved choosing an

elevation from a range of options for each grid cell, e.g. by applying a filter to the raw data. I have demonstrated first, that this choice introduces unexpected bias in the result of the change detection and hereby obliterates the true geomorphic change, and second how this gridding error can be mitigated and quantified.

Debris flows interact with their bed through often simultaneous erosion and deposition. As debris-flow models improve to a stage where they are increasingly able to reproduce the observations from real debris flows with respect to the combined behaviour of solids and fluid, the depositional morphology and stresses, high resolution data on channel change with known uncertainties becomes an invaluable resource for model building and validation. In a combined analysis of data on bed elevation change from terrestrial laser scanning and maximum per-event flow depth from field mapping of mudlines, I have compiled a probabilistic relationship between the two. Main features of this relationship include an equal likelihood of erosion and deposition for low flow depths of up to ≈ 1.5 m, and a dramatic increase in the likelihood of erosion of 75% and more, for flow depths of ≈ 2.5 m and above. These findings are corroborated by observations at the fan-scale where I found debris flows with high flow fronts to be more erosive than those with average or low front heights. My results also show that at the Illgraben field site debris-flow front height is uncorrelated with total flow volume. This means that the total expected flow volume should not be used as a universal proxy for flow magnitude in hazard assessments for two reasons: Low-volume flows with high flow fronts might unexpectedly exceed channel conveyance capacity and cause damage through over-bank sedimentation. In a situation where erosion is the main concern, hazard might be better assessed by formulating 'peak discharge scenarios' that would give indications of the flow depth in a given channel geometry.

Still many questions remain open with regard to the mechanics of debris flow erosion and it would be misleading to conclude that flow depth controls erosion, however, flow depth can serve as a proxy for three processes that are likely to operate more efficiently provided a higher flow front. Basal shear stress exerts a drag force to the bed and is proportional to the flow depth. The stress state of the bed is further influenced by grain agitation and recirculation of grains within the flow front creating an inertial stress, and also by the hydrostatic pressure underneath the saturated body of the flow. If flow depth is influencing the efficiency of these processes, then a process form feedback must exist, because maximum flow depth is partly controlled by peak discharge but also by cross section geometry with flow depth decreasing towards the flow margins. My observations

of the spatial pattern of debris flow erosion and deposition support the postulated feedback with simultaneous erosion along the center line of the flow and deposition along the flow margins leading to a better confined channel over time, unless channel geometry is reset by a major event.

I hypothesized that over cycles of multiple flows, feedback between patterns of bed elevation change, channel geometry and flow depth may be crucial for the emergence of autogenic behaviour, channel incision and for inundation patterns of debris-flow fans. I explored this idea by implementation of a 2D reduced complexity model that is based on semi-empirical relationships between flow volume and flow cross section area and inundation area, qualitative observations on debris-flow deposit geometry and my own data on the relationship between flow depth and bed elevation change. I showed that the model fulfills general expectations on the behaviour of alluvial fans detailed in case studies and flume experiments by a range of researchers. In particular I showed that model fan slope increases with decreasing sediment flux and increasing sediment concentration, and I showed that distinct phases of fan building observed in flume experiments appear in my model in the same order. These distinct phases are characterized by a high frequency of channel avulsions, a rapid lateral shifting of the depocenter and rapid fan volume growth at the beginning of fan development, followed by the emergence of channels on the fan surface, a lower avulsion frequency, a lower rate of fan volume growth and an overall increased efficiency in sediment routing across the fan domain. These results suggest that with a set of simple rules the characteristic behaviour of debris-flow fans could be captured.

Hazard on debris-flow fans is often described in terms of inundation extent under given scenarios. The fan evolution model presented in this thesis can be used as a tool to look at the statistical properties of the outcomes of many thousands of flows. I considered two aspects relevant for hazard: down-fan modification of flow volume distributions and lateral flow direction change between successive events. Not surprisingly, deposition on the fan lead to a reduction in the mean flow volume measured at the fan toe but in some cases an increase in standard deviation of flow volume was noted. The increase in standard deviation of flow volumes was partly due to flows that grew in volume whilst crossing the fan and partly due to flows that deposited all or almost all of their load. In practical terms these results indicate that knowledge about the flow magnitude-frequency distribution at the fan head is one important part in hazard assessment, but understanding how this distribution is modified when filtered by a particular debris-flow fan could help to define strategies of channel maintenance and design.

Major changes in flow path direction on fans (or the constriction of flows) often poses the greatest challenge for managing authorities. Model results showed a statistical correlation between deposit geometry, defined by lateral extent and thickness, and maximum likely change in flow direction between successive events. Fan surfaces built by narrow but thick deposits, creating high local roughness and numerous channels, experienced smaller maximum likely changes in flow path direction than fans with a smooth surface built by thin and extended deposits. This finding suggests a link between fan surface morphology and likely flow behaviour could be used to inform novel techniques of hazard mapping. As a result of differences in maximum likely flow direction change between successive events, differences in modeled fan surface age distributions arose. Smooth fans were of uniform age and had relatively young median ages due to the frequent resurfacing, whilst rough fan surfaces exhibited large age differences and relatively older median ages due to slow resurfacing. This result highlights that understanding fan surface morphology with respect to the geometry and extent of individual deposits, the cross cutting relationships between different deposits and constraining absolute age not only serves fan reconstruction but should also yield meaningful information about likely future inundation and deposition dynamics.

6.2 Findings relevant for Illgraben

To understand erosion and deposition dynamics of debris flows at fan-scale I performed a geomorphic analysis of the Illgraben fan in the form of a case study. I found that the combined approach of analysis of de-trended high-resolution digital topography and field mapping proved useful for the identification of coherent low relief depositional lobes. Depositional lobes at Illgraben consist of several amalgamated individual debris-flow deposits conveyed in the same feeder system over a defined period of time. By mapping cross cutting relationships of these depositional lobes and associated channels I identified the chronological order in which these feeder systems were active. With cosmogenic exposure dating I constrained absolute surface ages, which are in good agreement with the relative chronology derived from mapping. I also mapped and dated a rock avalanche deposit near the fan head to an age of $3,080 \pm 410$ yr. The rock avalanche enforced a down-fan shift in apex position, which I documented trough an analysis of linear trends of channel fragments preserved on the fan surface. Mapping and exposure dating indicate that the Illgraben fan was almost completely resurfaced within the past $\approx 1,600$ yr. However, for a few depositional

lobes the cross cutting relationship with adjacent depositional lobes suggest an age older than the rock avalanche; due to a lack of suitable material, dating has not been successful so far. The presence of patches of fan surface predating the rock avalanche is reasonable given my model results predicting preservation of old fan surfaces near the mountain front.

The lower boundary condition of the Illgraben fan (toe cutting by the Rhone river) is similar to the boundary conditions I used in the model experiments. My model fans went through a phase of rapid volume growth followed by volume growth at lower rates due to the emergence of channels increasing the routing efficiency of the fan surface. Currently the Illgraben fan is efficient at routing sediment to the fan toe and sediment accumulation is limited to the incised active channel and inset terraces. This behaviour is partly the result of human attempts of controlling the channel position on the fan since at least one century. Because the fan has grown to the opposite valley wall, and is being eroded by the Rhone river at the fan toe, it is suggested that the fan has probably reached the second phase of its development. This second phase by implication should encompass stable channel configurations over prolonged periods of time.

6.3 Future work

My thesis highlights two distinct areas for potential further research with regard to erosion and deposition dynamics of debris flows. First the lack of correlation between total flow volume and front height or peak discharge and the lack of explanation why this might be, demonstrates that there is a gap between idealized models of debris flows (discrete element and continuum constituent models), and their extremely complex natural counterparts. As of yet we do not even have established procedures to monitor the temporal and spatial evolution of flow fronts at a meaningful scale, let alone linking their evolution to catchment or channel parameters. In particular the role of coarse clasts and their size distribution in flow front formation has not been clarified beyond the general observation that coarse clasts accumulate at the flow front and are forming a high-friction mobile dam. Flow front formation is closely related to grain segregation (Iverson, 1997; Zanuttigh and Lamberti, 2007). Complete grain segregation requires a minimal travel distance (Zanuttigh and Lamberti, 2007), therefore static flumes might be too short to yield reasonable results. Davies (1990) experimented with a 2 m long and 50 mm wide conveyor belt apparatus and a mixture of water and PVC particles. As a first step a similar but larger apparatus could be built from indus-

trial conveyor belts, where larger quantities and realistic material mixtures could be tested. In a series of experiments I would vary the concentration and grain size distribution of coarse clasts within a slurry of water, sand and clay, comparable to the liquid phase of debris flows. Observable variables should include flow front height, distribution and concentration of coarse grains in the flow, and travel distance until complete grain segregation. This experimental work could be combined with discrete particle modelling (Hill et al., 2011, 2003). In a second step a suitable field site should be identified to monitor flow front formation in natural debris flows. The first question to answer would be how flow fronts of different height differ with respect to the content and distribution of coarse clasts. Photogrammetric monitoring as in Berger et al. (2011) would be one option, high-frequency repeat laser scanning of the progressing flow front an other option. Ideally this data should be combined with information on entrainment, amount and size of coarse clasts in the channel upstream of the monitoring site.

Second, controls on debris-flow erosion at channel-reach scale are still poorly constrained. Although my research has yielded some data at channel-reach scale, and revealed some control by flow depth, there is clearly scope to take my analysis further to cover different flow types, channel substrates, and geometries. Because many researchers have highlighted the importance of the flow front for erosion, channel bed monitoring should also be combined with flow front monitoring at the same spatial scales. My modeling suggests that in confined settings lateral debris flow erosion over multiple events can not be ignored. This is a related field where little research has been done so far, but would deserve further attention, particularly when including debris flows within landscape evolution models.

The results from the investigations described above should then be used to improve the model I presented in Chapter 5. The direct link between flow volume and flow cross sectional area could be replaced by direct empirical data on flow front behaviour. A grain size component could be introduced, which could potentially be a very powerful way of calibrating the model with field data, as grain sizes available for debris flow transport can be measured manually in the field or from aerial imagery (e.g. Carbonneau et al., 2005).

Notation

Note: [1] means that a quantity is dimensionless, otherwise its dimension is given in suitable units.

A	flow cross sectional area	[m^2]
A_c	catchment area	[m^2]
B	channel width	[m]
C	bulk sediment concentration	[1]
C_∞	equilibrium coarse particle concentration	[1]
C_{crit}	critical sediment concentration for onset of deposition	[1]
D	difference model, grid value: elevation change	[m]
E_i	DEM, grid value of cell i: true elevation	[m]
E_i'	DEM, grid value of cell i: elevation from last return filter	[m]
F	long axis of the laser beam footprint	[m]
N	number of grains above slip surface	[1]
N_{Sav}	Savage number	[1]
N_{Bag}	Bagnold number	[1]
N_{Dar}	Darcy number	[1]
Q_s	input sediment flux	[m^3/s]
R	radius	[m]
R_i	topographically corrected range in elevation in grid cell i	[m]
S	channel slope $S = \tan\theta$	[1]
T	granular temperature	[(m/s)^2]
T_A	avulsion period	[s]
T_s, T_f	shear stress in solid and fluid phase	[Pa]
dV	volume change	[m^3]
V	flow volume	[m^3]
$\vec{b}$	vector connecting laser scanner and object	[m]
d_c	critical flow depth or averave deposit thickness	[m]

g	gravity	[m/s^2]
h	flow depth or channel depth	[m]
h_r	hydraulic radius	[m]
k	hydraulic permeability	[1/m^2]
l	grid resolution	[m]
m	number of slices across the channel	[1]
m_f	rate of added fluid mass to unit volume	[kg/s]
m_s	rate of added solid mass to unit volume	[kg/s]
n	number of grid cells in a slice of width dx across the channel	[1]
p_c	particle collision stress	[Pa]
p_t	total fluid pressure	[Pa]
p_h	hydrostatic fluid pressure	[Pa]
p_e	excess fluid pressure	[Pa]
r	fan radius	[m]
s	bed porosity	[1]
t	time	[s]
u	velocity	[m/s]
$\vec{u}$, $\vec{v}$	components of the long axis of laser beam footprint	[m]
u_f	fluid velocity	[m/s]
u_s	solid velocity	[m/s]
$\bar{u}$	mean fluid velocity	[m/s]
w	water content of bed material	[1]
w_c	channel width	[m]
dx	width of slice across channel, unit downstream length	[m]
x_1	local surface roughness	[°]
x_2	standard deviation of radial slope	[°]
α	inundation area coefficient	[1]
α	dip direction of surface (only in Chapter 3)	[radians]
α_i	collision angle	[radians]
β	opening angle of laser beam (only in Chapter 3)	[radians]
δ	representative grain diameter	[m]
η	viscosity of the Bingham fluid	[Pa s]
γ	shear strain rate	[1/s]
μ	dynamic viscosity of pore fluid with suspended fine sediment	[kg/m s]
λ	linear grain concentration	[1]

ρ_b	bulk density $= (\rho_s - \rho_f)C + \rho_f$	[kg/m^3]
ρ_f	density of fluid	[kg/m^3]
ρ_s	density of solids	[kg/m^3]
ρ_i	a value on the interval $[0; R_i]$,	[m]
ϕ	bulk internal friction angle	[radians]
σ	normal stress	[Pa]
τ	shear stress	[Pa]
τ_b	basal shear stress	[Pa]
τ_c	shear stress due to grain collisions	[Pa]
τ_y	yield strength	[Pa]
θ	slope angle	[radians]
ε	lag rate or flow cross section coefficient	[1]
ε	incidence angle of laser beam (only in Chapter 3)	[radians]

Bibliography

Abanco, C. and Hürlimann, M. (2011). Simple geomorphologic approach to estimate debris-flow entrainment. Applications to the Pyrenees and the Alps, *in* R. Genevois, D. Hamilton and A. Prestininzi (eds), *5th International Conference on Debris-Flow Hazards – Mitigation, Mechanics, Prediction and Assessment; Padua, Italy 14–17 June 2011*, Casa Editrice Università La Sapienza, p. 183–191.

Abellán, A., Jaboyedoff, M., Oppikofer, T. and Vilaplana, J. (2009). Detection of millimetric deformation using a terrestrial laser scanner: experiment and application to a rockfall event, *Natural Hazards and Earth System Science* **9**: 365–372.

Alfimov, V. and Ivy-Ochs, S. (2009). How well do we understand production of ^{36}Cl in limestone and dolomite?, *Quaternary Geochronology* **4**(6): 462–474.

Arattano, M. and Franzi, L. (2010). On the application of kinematic models to simulate the diffusive processes of debris flows, *Natural Hazards and Earth System Science* **10**(8): 1689–1695.

Arattano, M., Giordan, D., Luino, F., Conte, R., Lazzari, A. and Franzi, L. (2010). Risk management on an alluvial fan: A case study of the 2008 debris-flow event at Villar Pellice (Piedmont, N-W Italy), *Natural Hazards and Earth System Science* **10**(5): 999–1008.

Arattano, M. and Savage, W. (1994). Modelling debris flows as kinematic waves, *Bulletin of the International Association of Engineering Geology* **49**(1): 3–13.

Armanini, A., Fraccarollo, L. and Larcher, M. (2008). Liquid-granular channel flow dynamics, *Powder Technology* **182**(2): 218–227.

Badoux, A., Graf, C., Rhyner, J., Kuntner, R. and McArdell, B. W. (2008). A debris-flow alarm system for the alpine Illgraben catchment: design and performance, *Natural Hazards* **49**: 517–539.

Bagnold, R. A. (1954). Experiments on a gravity-free dispersion of large solid spheres in a newtonian fluid under shear, *Proceedings of the Royal Society of London. Series A, Mathematical and Physical Sciences* **225**(1160): 49–63.

Balco, G. (2009 and updates). Cronus-Earth Be-10 – Al-26 exposure age calculator, version 2.2, http://hess.ess.washington.edu/math (accessed 6 May 2011).

Bardou, E., Fournier, F. and Sartori, M. (2003). Paleoflood reconstruction at Illgraben torrent (Switzerland): a current need for event frequency estimation, *in* V. Thorndycraft, G. Benito, M. BArriendos and C. Llasat (eds), *Palaeofloods, Historical Data & Climatic Variability: Applications in Flood Risk Assessment*, Proceedings of the International PHEFRA Workshop, Centro de Ciencias Medioambientales, Barcelona, Spain, p. 53–59.

Bardou, E. and Jaboyedoff, M. (2008). Debris flows as a factor of hillslope evolution controlled by a continuous or a pulse process?, *in* K. Gallagher, S. J. Jones and J. Wainwright (eds), *Landscape Evolution: Denudation, Climate and Tectonics over different Time and Space Scales*, Vol. 296 of *Special Publications*, Geological Society, London, p. 63–78.

Barnes, H. H. J. (1967). *Roughness Characteristics of Natural Channels.*, number 1849 in *U.S. Geological Survey Water-Supply Paper*, Geological Survey (U.S.).

Bater, C. and Coops, N. (2009). Evaluating error associated with lidar-derived DEM interpolation, *Computers and Geosciences* **35**(2): 289–300.

Benda, L. and Cundy, T. (1990). Predicting deposition of debris flows in mountain channels, *Canadian Geotechnical Journal* **27**: 409–417.

Benda, L. and Dunne, T. (1997a). Stochastic forcing of sediment routing and storage in channel networks, *Water Resources Research* **33**(12): 2865–2880.

Benda, L. and Dunne, T. (1997b). Stochastic forcing of sediment supply to channel networks from landsliding and debris flow, *Water Resources Research* **33**(12): 2849–2863.

Bennett, G., Eisenbeiss, H., Molnar, P., McArdell, B. W., Schlunegger, F. and Burlando, P. (2011). The Illgraben sediment cascade, 1963–2009, *Geophysical Research Abstracts*, Vol. 13, EGU, Vienna, pp. EGU2011–8500.

Berger, C., McArdell, B. W., Fritschi, B. and Schlunegger, F. (2010). A novel method for measuring the timing of bed erosion during debris flows and floods, *Water Resources Research* **46**(2).

Berger, C., McArdell, B. W. and Schlunegger, F. (2010). Sediment transfer patterns at the Illgraben catchment, Switzerland: Implications for the time scales of debris flow activities, *Geomorphology* **125**(3): 421–432.

Berger, C., McArdell, B. W. and Schlunegger, F. (2011). Direct measurement of channel erosion by debris flows, Illgraben, Switzerland, *Journal of Geophysical Research F* **116**(F1): F01002.

Berti, M. and Simoni, A. (2007). Prediction of debris flow inundation areas using empirical mobility relationships, *Geomorphology* **90**(1-2): 144–161.

Besl, P. and McKay, N. (1992). A method for registration of 3-D shapes., *IEEE Transactions on Pattern Analysis and Machine Intelligence* **14**(2): 239–256.

Bevington, P. R. (1969). *Data reduction and error analysis for the physical sciences*, McGraw-Hill, New York.

Bezzola, G., Hegg, C. and Koschni, A. (2008). *Synthesebericht zur Ereignisanalyse – Hochwasser 2005 in der Schweiz*, Eidgenössisches Departement für Umwelt, Verkehr, Energie und Kommunikation, Bern.

Blair, T. and McPherson, J. (1998). Recent debris flow processes and resultant form and facies of the Dolomite alluvial fan, Owens valley, California, *Journal of Sedimentary Research. Section A, Sedimentary Petrology and Processes* **68**(5): 800–818.

Blair, T. and McPherson, J. (2008). Quaternary sedimentology of the Rose Creek fan delta, Walker lake, Nevada, USA, and implications to fan-delta facies models, *Sedimentology* **55**(3): 579–615.

Bonnard, C. (2004). Technical and human aspects of historic rockslide dammed lakes and landslide dam breaches, *in* K. Abdrakhmatov, S. Evans, R. Hermanns, G. Scarascia-Mugnozza and A. Strom (eds), *Security of Natural and Artificial Rocikslide Dams*, Proceedings NATO Advanced Research Workshop, Springer, Bishkek.

Brasington, J., Langham, J. and Rumsby, B. (2003). Methodological sensitivity of morphometric estimates of coarse fluvial sediment transport, *Geomorphology* **53**(3): 299.

Bryant, M., Falk, P. and Paola, C. (1995). Experimental study of avulsion frequency and rate of deposition, *Geology* **23**(4): 365–368.

Buckley, S., Howell, J., Enge, H. and Kurz, T. (2008). Terrestrial laser scanning in geology: data acquisition, processing and accuracy considerations, *Journal of the Geological Society* **165**: 625–638.

Bull, W. (1962). *Relations of alluvial fan size and slope to drainage basin size and lithology in western Fresno County*, number 450-B, U.S. Geological Survey, Washington D.C., pp. 51–53.

Bull, W. B. (1977). The alluvial-fan environment, *Progress in Physical Geography* **1**(2): 222 –270.

Bundesamt für Landestopographie (1954). Landeskarte der Schweiz 1:25,000, Blatt Sierre, Wabern, Switzerland.

Bundesamt für Landestopographie (2005). DTM-AV (digital elevation model for Switzerland), Wabern, Switzerland.

Bundesamt für Landestopographie (2006a). Formulas and constants for the calculation of the swiss conformal cylindrical projection and for the transformation between coordinate systems, Bundesamt für Landestopographie.

Bundesamt für Landestopographie (2006b). Sierre – Siders (Sheet 1287).

Cannon, S. H. (1989). *An evaluation of the travel-distance potential of debris flows*, Utah Geological and Mineral Survey, [Salt Lake City, Utah].

Carbonneau, P. E., Bergeron, N. and Lane, S. N. (2005). Automated grain size measurements from airborne remote sensing for long profile measurements of fluvial grain sizes, *Water Resources Research* **41**(11): W11426.

Chen, Y. and Medioni, G. (1992). Object modeling by registration of multiple range images, *Image and Vision Computing* **10**(3): 145–155.

Chmeleff, J., von Blanckenburg, F., Kossert, K. and Jakob, D. (2010). Determination of the ^{10}Be half-life by multicollector ICP-MS and liquid scintillation counting, *Nuclear Instruments and Methods in Physics Research Section B: Beam Interactions with Materials and Atoms* **268**(2): 192–199.

Christen, M., Bartelt, P. and Kowalski, J. (2010). Back calculation of the in den Arelen avalanche with RAMMS: interpretation of model results, *Annals of Glaciology.* **51**(54): 161–168.

Clarke, L., Quine, T. A. and Nicholas, A. (2010). An experimental investigation of autogenic behaviour during alluvial fan evolution, *Geomorphology* **115**(3): 278.

Coe, J., Reid, M., Brien, D. and Michael, J. (2011). Assessment of topographic and drainage network controls on debris-flow travel distance along the west coast of the United States, *in* R. Genevois, D. Hamilton and A. Prestininzi (eds), *5th International Conference on Debris-Flow Hazards – Mitigation, Mechanics, Prediction and Assessment; Padua, Italy 14–17 June 2011*, Casa Editrice Università La Sapienza, p. 199–209.

Costa, J. E. and Fleisher, P. J. (1984). Physical geomorphology of debris flows, *Developments and Applications of Geomorphology*, Springer-Verlag, Berlin; New York, p. 268–317.

Costa, J. E. and Garnett, P. (1984). Debris-flow dynamics (video tape), open file report 84/606.

Coulthard, T. J., Kirkby, M. J. and Macklin, M. G. (2000). Modelling geomorphic response to environmental change in an upland catchment, *Hydrological Processes.* **14**: 2031–2046.

Crosta, G. B., Cucchiaro, S. and Frattini, P. (2003). Validation of semi-empirical relationships for the definition of debris-flow behavior in granular materials, *in* D. Rickenmann and C. Chen (eds), *Proceedings of the 3rd International Conference on Debris-Flow Hazards Mitigation: Mechanics, Prediction, and Assessment*, Vol. 2, Millpress, Davos, Switzerland, p. 821–832.

Dade, W. B. and Huppert, H. E. (1998). Long-runout rockfalls, *Geology.* **26**(9): 803.

Dalbey, K., Patra, A., Pitman, E., Bursik, M. and Sheridan, M. (2008). Input uncertainty propagation methods and hazard mapping of geophysical mass flows, *Journal of Geophysical Research B* **113**(5): B05203.

Dalley, G. and Flynn, P. (2002). Pair-Wise range image registration: A study in outlier classification, *Computer Vision and Image Understanding* **87**: 104–115.

Davies, T. (1990). Debris-flow surges – experimental simulation, *Journal of Hydrology (N.Z.)* **29**(1): 18–46.

Davies, T. R. and Korup, O. (2007). Persistent alluvial fanhead trenching resulting from large, infrequent sediment inputs, *Earth Surface Processes and Landforms* **32**(5): 725–742.

De Chant, L. J., Pease, P. P. and Tchakerian, V. P. (1999). Modelling alluvial fan morphology, *Earth Surface Processes and Landforms* **24**(7): 641–652.

Denlinger, R. P. and Iverson, R. M. (2001). Flow of variably fluidized granular masses across three-dimensional terrain, 2, numerical predictions and experimental tests (Paper 2000JB900330), *Journal of Geophysical Research* **106**: 553–566.

Densmore, A. L., Allen, P. A. and Simpson, G. (2007). Development and response of a coupled catchment fan system under changing tectonic and climatic forcing, *Journal of Geophysical Research F* **112**(F1): F01002.

Desilets, D., Zreda, M., Almasi, P. F. and Elmore, D. (2006). Determination of cosmogenic 36cl in rocks by isotope dilution: innovations, validation and error propagation, *Chemical Geology* **233**(3-4): 185–195.

Dufour, G.-H. (1845). Topographische Karte der Schweiz (Dufourkarte), sheet XVII, Swisstopo, Bundesamt für Landestopographie, Wabern. http://map.geo.admin.ch/, accessed 7 July 2011.

Dufresne, A. and Davies, T. (2009). Longitudinal ridges in mass movement deposits, *Geomorphology* **105**(3-4): 171–181.

Dühnforth, M., Densmore, A. L., Ivy-Ochs, S. and Allen, P. A. (2008). Controls on sediment evacuation from glacially modified and unmodified catchments in the eastern Sierra Nevada, California, *Earth Surface Processes and Landforms* **33**(10): 1602–1613.

Dühnforth, M., Densmore, A. L., Ivy-Ochs, S., Allen, P. A. and Kubik, P. W. (2007). Timing and patterns of debris flow deposition on Shepherd and Symmes creek fans, Owens valley, California, deduced from cosmogenic 10-Be, *Journal of Geophysical Research F* **112**(F3): F03S15.

Dunne, J., Elmore, D. and Muzikar, P. (1999). Scaling factors for the rates of production of cosmogenic nuclides for geometric shielding and attenuation at depth on sloped surfaces, *Geomorphology* **27**(1-2): 3–11.

Dunning, S., Mitchell, W., Rosser, N. and Petley, D. (2007). The Hattian Bala rock avalanche and associated landslides triggered by the Kashmir earthquake of 8 October 2005, *Engineering Geology* **93**(3-4): 130–144.

Elmore, D., Ma, X., Miller, T., Mueller, K., Perry, M., Rickey, F., Sharma, P., Simms, P., Lipschutz, M. and Vogt, S. (1997). Status and plans for the PRIME Lab AMS facility, *Nuclear Instruments and Methods in Physics Research Section B: Beam Interactions with Materials and Atoms* **123**(1-4): 69–72.

Fabryka-Martin, J. (1988). *Production of Radionuclides in the Earth and their Hydrogeologic Significance, with Emphasis on Chlorine-36 and Iodine-129*, PhD thesis, University of Arizona, Tucson, USA.

Fannin, R. J. and Wise, M. P. (2001). An empirical-statistical model for debris flow travel distance, *Canadian Geotechnical Journal* **38**(5): 982–994.

Favalli, M., Mazzarini, F., Pareschi, M. and Boschi, E. (2009). Topographic control on lava flow paths at Mount Etna, Italy: Implications for hazard assessment, *Journal of Geophysical Research F* **114**(F1): F01019.

Field, J. (2001). Channel avulsion on alluvial fans in southern Arizona, *Geomorphology* **37**(1): 93–104.

Frankel, K. and Dolan, J. (2007). Characterizing arid region alluvial fan surface roughness with airborne laser swath mapping digital topographic data, *Journal of Geophysical Research F* **112**(F2): F02025.

Fuller, I., Large, A., Charlton, M., Heritage, G. and Milan, D. (2003). Reach-Scale sediment transfers: An evaluation of two morphological budgeting approaches, *Earth Surface Processes and Landforms* **28**: 889–904.

Gabus, J., Weidmann, M., Sartori, M. and Burri, M. (2008). *Feuille 1287 Sierre. – Atlas géol. Suisse 1:25 000*, number 111 in *Notice explicative*, Office federal de topographie, Wabern.

Gamma, P. (1999). *dfwalk – Ein Murgang-Simulationsprogramm zur Gefahrenzonierung*, PhD, Universität Bern, Bern.

Gertsch, E. (2009). *Geschiebelieferung alpiner Wildbachsysteme bei Grossereignissen - Ereignisanalysen und Entwicklung eines Abschätzverfahrens*, PhD thesis, Universität Bern, Bern.

Gray, J. and Kokelaar, B. (2010). Large particle segregation, transport and accumulation in granular free-surface flows, *Journal of Fluid Mechanics* **652**: 105–137.

Griswold, J. and Iverson, R. (2008). Mobility statistics and automated hazard mapping for debris flows and rock avalanches, *U.S. Geological Survey Scientific Investigations Report 2007–5276*, USGS.

Grossi, P., Kunreuther, H. and Patel, C. C. (2005). *Catastrophe modeling: a new approach to managing risk*, Huebner international series on risk, insurance, and economic security, 25, Springer Science+Business Media, New York.

Hardy, S. and Gawthorpe, R. (1998). Effects of variations in fault slip rate on sequence stratigraphy in fan deltas: Insights from numerical modeling, *Geology* **26**(10): 911–914.

Harvey, A. (1984). Aggradation and dissection sequences on spanish alluvial fans: Influence on morphological development, *Catena* **11**(4): 289 – 304.

Harvey, A. M. (2002). The role of base-level change in the dissection of alluvial fans: case studies from southeast Spain and Nevada, *Geomorphology* **45**(1): 67.

Heim, A. (1882). Der Bergsturz von Elm, *Zeitschrift der Deutschen Geologischen Gesellschaft* **34**(1): 74–115.

Heim, A. (1932). Bergsturz und Menschenleben, *Beiblatt zur Vierteljahresschrift der Naturforschenden Gesellschaft Zürich* **20**: 1–214.

Helsen, M., Koop, P. and Van Steijn, H. (2002). Magnitude-frequency relationship for debris flows on the fan of the chalance torrent, Valgaudemar (French Alps), *Earth Surface Processes and Landforms* **27**: 1299–1307.

Heritage, G., Milan, D., Large, A. and Fuller, I. (2009). Influence of survey strategy and interpolation model on DEM quality, *Geomorphology* **112**(3-4): 334 – 344.

Hewitt, K., Clague, J. J. and Orwin, J. F. (2008). Legacies of catastrophic rock slope failures in mountain landscapes, *Earth-Science Reviews* **87**(1-2): 1–38.

Hill, K., Bereket, Y., Dietrich, W. and Hsu, L. (2011). Discrete element modeling and large scale studies of bouldery debris flows, *in* R. Genevois, D. Hamilton and A. Prestininzi (eds), *5th International Conference on Debris-Flow Hazards – Mitigation, Mechanics, Prediction and Assessment; Padua, Italy 14–17 June 2011*, Casa Editrice Università La Sapienza, p. 435–447.

Hill, K., Gioia, G. and Tota, V. (2003). Structure and kinematics in dense free-surface granular flow, *Physical review letters* **91**(6).

Hodge, R., Brasington, J. and Richards, K. (2009). In situ characterization of grain-scale fluvial morphology using terrestrial laser scanning, *Earth Surface Processes and Landforms* **34**(7): 954–968.

Hornung, J., Pflanz, D., Hechler, A., Beer, A., Hinderer, M., Maisch, M. and Bieg, U. (2010). 3-D architecture, depositional patterns and climate triggered sediment fluxes of an alpine alluvial fan (Samedan, Switzerland), *Geomorphology* **115**(3): 202.

Hovius, N., Stark, C. P. and Allen, P. A. (1997). Sediment flux from a mountain belt derived by landslide mapping, *Geology* **25**(3): 231–234.

Hsu, L., Dietrich, W. and Sklar, L. (2008). Experimental study of bedrock erosion by granular flows, *Journal of Geophysical Research F* **113**(2): F02001.

Humphrey, N. F. and Heller, P. L. (1995). Natural oscillations in coupled geomorphic systems: An alternative origin for cyclic sedimentation, *Geology -Boulder-* **23**(6): 499.

Hungr, O., McDougall, S. and Bovis, M. (2005). Entrainment of material by debris flows, *in* M. Jakob and O. Hungr (eds), *Debris-flow Hazards and Related Phenomena*, Springer-Praxis books in geophysical sciences, Springer, Berlin; New York, p. 135–158.

Hungr, O., McDougall, S., Wise, M. and Cullen, M. (2008). Magnitude-frequency relationships of debris flows and debris avalanches in relation to slope relief, *Geomorphology* **96**(3-4): 355–365.

Hungr, O., Morgan, G. and Kellerhals, R. (1984). Quantitative analysis of debris torrent hazards for design of remedial measures, *Canadian Geotechnical Journal* **21**(4): 663–677.

Hürlimann, M., Rickenmann, D. and Graf, C. (2003). Field and monitoring data of debris-flow events in the Swiss Alps, *Canadian Geotechnical Journal* **40**: 161–175.

Innes, J. L. (1985). Magnitude-Frequency relations of debris flows in northwest Europe, *Geografiska Annaler. Series A. Physical Geography* **67**(2): 23–32.

Iverson, R. H. (1997). The physics of debris flows, *Reviews of Geophysics* **35**(3): 245–296.

Iverson, R. M. and Denlinger, R. P. (2001). Flow of variably fluidized granular masses across three-dimensional terrain, 1, coulomb mixture theory, *Journal of Geophysical Research* **106**: 537–552.

Iverson, R. M., Logan, M., LaHusen, R. and Berti, M. (2010). The perfect debris flow? Aggregated results from 28 large-scale experiments, *Journal of Geophysical Research F* **115**(F03005): 1–29.

Iverson, R. M., Reid, M. E., Logan, M., LaHusen, R. G., Godt, J. W. and Griswold, J. P. (2011). Positive feedback and momentum growth during debris-flow entrainment of wet bed sediment, *Nature Geoscience* **4**(2): 116–121.

Iverson, R. M., Schilling, S. P. and Vallance, J. W. (1998). Objective delineation of lahar-inundation hazard zones, *Geological Society of America Bulletin* **110**(8): 972–984.

Iverson, R. M. and Vallance, J. W. (2001). New views of granular mass flows, *Geology.* **29**(2): 115.

Ivy-Ochs, S. (1996). *The dating of rock surface using in situ produced Be-10, Al-26, and Cl-36, with examples from Anatarctica and the Swiss Alps*, PhD thesis, Swiss Federal Institute of Technology Zurich, Zürich.

Ivy-Ochs, S., Kerschner, H., Reuther, A., Preusser, F., Heine, K., Maisch, M., Kubik, P. W. and Schluchter, C. (2008). Chronology of the last glacial cycle in the european Alps, *Journal of Quaternary Science* **23**(6-7): 559–573.

Ivy-Ochs, S., Maisch, M., Poschinger, A. and Synal, H. (2009). Surface exposure dating of the Flims landslide, Graubünden, Switzerland, *Geomorphology* **103**(1): 104–112.

Ivy-Ochs, S. and Schaller, M. (2009). Examining processes and rates of landscape change with cosmogenic radionuclides, *in* K. Froehlich (ed.), *Environmental Radionuclides: Tracers and Timers of Terrestrial Processes*, Vol. Volume 16, Elsevier, pp. 231–294.

Ivy-Ochs, S., Synal, H.-A., Roth, C. and Schaller, M. (2004). Initial results from isotope dilution for cl and ^{36}cl measurements at the PSI/ETH Zurich AMS facility, *Nuclear Instruments and Methods in Physics Research Section B: Beam Interactions with Materials and Atoms* **223-224**: 623–627.

Jakob, M. (2010). State of the art in debris-flow research: the role of dendrochronology, *in* M. Stoffel (ed.), *Tree rings and natural hazards: a state-of-the-art*, Springer, Dordrecht; New York, p. 183–192.

Jakob, M., Bovis, M. and Oden, M. (2005). The significance of channel recharge rates for estimating debris-flow magnitude and frequency, *Earth Surface Processes and Landforms* **30**(6): 755–766.

Jakob, M. and Friele, P. (2010). Frequency and magnitude of debris flows on Cheekye river, British Columbia, *Geomorphology* **114**(3): 382–395.

Jakob, M. and Hungr, O. (2005). *Debris-flow hazards and related phenomena*, Springer-Praxis books in geophysical sciences, Springer, Berlin; New York.

Jakob, M., Porter, M., Savigny, K. and Yaremko, E. (2004). A geomorphic approach to the design of pipeline crossings of mountain streams, *Proceedings of the 5th Biennial International Pipeline Conference: presented at the International Pipeline Conference (IPC 2004)*, American Society of Mechanical Engineers, Calgary, Alberta, Canada, pp. IPC04–0239.

Jerolmack, D. J. and Paola, C. (2010). Shredding of environmental signals by sediment transport, *Geophysical Research Letters* **37**(19): L19401.

Jerolmack, D. and Paola, C. (2007). Complexity in a cellular model of river avulsion, *Geomorphology* **91**(3-4): 259–270.

Julien, P. and Paris, A. (2010). Mean velocity of mudflows and debris flows, *Journal of Hydraulic Engineering, New York* **136**(9): 676–679.

Kaasalainen, S., Kukko, A., Lindroos, T., Aeby, P., Kaartinen, H., Brasington, J. and Ahokas, E. (2008). Brightness measurements and calibration with airborne and terrestrial laser scanners, *IEEE Transactions on Geoscience and Remote Sensing* **46**(2): 528.

Kean, J. and Staley, D. (2011). Direct measurements of the hydrologic conditions leading up to and during post-fire debris flow in southern California, USA, *in* R. Genevois, D. Hamilton and A. Prestininzi (eds), *5th International Conference on Debris-Flow Hazards – Mitigation, Mechanics, Prediction and Assessment; Padua, Italy 14–17 June 2011*, Casa Editrice Università La Sapienza, pp. 685—694.

Kienholz, H. and Krummenacher, B. (1995). Empfehlungen: Symbolbaukasten zur Kartierung der Phänomene, *Empfehlung VU-7502-D*, Bundesamt für Umwelt, Wald und Landschaft; Bundesamt für Wasser und Geologie.

Kim, B. C. and Lowe, D. R. (2004). Depositional processes of the Gravelly debris flow deposits, South Dolomite alluvial fan, Owens valley, California, *Geoscience Journal – Seoul* **8**: 153–170.

Kim, W. and Jerolmack, D. J. (2008). The pulse of calm fan deltas, *The Journal of Geology* **116**(4): 315–330.

Kim, W. and Muto, T. (2007). Autogenic response of alluvial-bedrock transition to base-level variation: Experiment and theory, *Journal of Geophysical Research F* **112**(F3): F03S14.

Kim, W., Paola, C., Swenson, J. and Voller, V. (2006). Shoreline response to autogenic processes of sediment storage and release in the fluvial system, *Journal of Geophysical Research F* **111**(F4): F04013.

Kohl, C. and Nishiizumi, K. (1992). Chemical isolation of quartz for measurement of in-situ-produced cosmogenic nuclides, *Geochimica et Cosmochimica Acta* **56:9**: 3583–3587.

Korschinek, G., Bergmaier, A., Faestermann, T., Gerstmann, U., Knie, K., Rugel, G., Wallner, A., Dillmann, I., Dollinger, G., von Gostomski, C. L. and et al. (2010). A new value for the half-life of ^{10}Be by Heavy-Ion Elastic Recoil Detection and liquid scintillation counting, *Nuclear Instruments and Methods in Physics Research Section B: Beam Interactions with Materials and Atoms* **268**(2): 187–191.

Korup, O. (2004). Landslide-induced river channel avulsions in mountain catchments of southwest New Zealand, *Geomorphology* **63**(1-2): 57–80.

Korup, O., Clague, J., Hermanns, R., Hewitt, K., Strom, A. and Weidinger, J. (2007). Giant landslides, topography, and erosion, *Earth and Planetary Science Letters* **261**(3-4): 578–589.

Korup, O., Densmore, A. and Schlunegger, F. (2010). The role of landslides in mountain range evolution, *Geomorphology* **120**(1-2): 77–90.

Kubik, P. W. and Christl, M. (2010). ^{10}Be and ^{26}Al measurements at the Zurich 6 MV Tandem AMS facility, *Nuclear Instruments and Methods in Physics Research Section B: Beam Interactions with Materials and Atoms* **268**(7-8): 880–883.

Lancaster, S. T. and Casebeer, N. E. (2007). Sediment storage and evacuation in headwater valleys at the transition between debris-flow and fluvial processes, *Geology.* **35**(11): 1027.

Lane, S. N., Westaway, R. M. and Hicks, D. M. (2003). Estimation of erosion and deposition volumes in a large, Gravel-Bed, braided river using synoptic remote sensing, *Earth Surface Processes and Landforms* **28**: 249–272.

Lee, J., Davies, T. and Bell, D. (2009). Successive holocene rock avalanches at lake Coleridge, Canterbury, New Zealand, *Landslides* **6**(4): 287–297.

Leeder, M. R. and Mack, G. H. (2001). Lateral erosion ('toe cutting') of alluvial fans by axial rivers: Implications for basin analysis and architecture, *Journal of the Geological Society.* **158**(6): 885.

Lichtenhahn, C. (1971). Zwei Betonmauern: die Geschieberückhaltesperre am Illgraben (Wallis)., *F.f.v. Hochwasserbekämpfung*, Vol. 3, Villach, Kärnten, Austria, p. 451–456.

Lichti, D., Gordon, S. and Stewart, M. (2002). Ground-based laser scanners: Operation, systems and applications, *Geomatica* **56**(1): 21–33.

Lim, M., Mills, J. P. and Rosser, N. (2009). Laser scanning surveying of linear features: considerations and applications, *in* G. Heritage and A. Large (eds), *Laser Scanning for the Environmental Sciences*, Wiley-Blackwell, Chichester, UK; Hoboken, NJ, p. 245–261.

Lim, M., Petley, D. N., Rosser, N. J., Allison, R. J., Long, A. J. and Pybus, D. (2005). Combined digital photogrammetry and Time-of-Flight laser scanning for monitoring cliff evolution, *Photogrammetric Record* **20**(110): 109–129.

Lim, M., Rosser, N. J., Allison, R. J. and Petley, D. N. (2010). Erosional processes in the hard rock coastal cliffs at Staithes, North Yorkshire, *Geomorphology* **93**(1): 12.

Liu, B., Phillips, F. M., Fabryka-Martin, J. T., Fowler, M. M. and Stone, W. D. (1994). Cosmogenic ^{36}Cl accumulation in unstable landforms: 1. effects of the thermal neutron distribution, *Water Resources Research* **30**(11): 3115–3125.

Major, J. (1997). Depositional processes in large-scale debris-flow experiments, *The Journal of Geology* **105**(3): 345–366.

Major, J. J. and Iverson, R. M. (1999). Debris-flow deposition: Effects of pore-fluid pressure and friction concentrated at flow margins, *Geological Society of America Bulletin.* **111**(10): 1424–1434.

Major, J. and Pierson, T. (1992). Debris-flow rheology – experimental-analysis of fine-grained slurries, *Water Resources Research* **28**(3): 841–857.

Malamud, B. D., Turcotte, D. L., Guzzetti, F. and Reichenbach, P. (2004). Landslides, earthquakes, and erosion, *Earth and Planetary Science Letters* **229**(1-2): 45–59.

Marchand, A. (1871). Les torrents des Alpes, *Revue des eaux et forêts.* **10**: 77–95.

Marchi, L., Arattano, M. and Deganutti, A. (2002). Ten years of debris-flow monitoring in the Moscardo Torrent (Italian Alps), *Geomorphology* **46**(1-2): 1–17.

Martinez, C., Miralles-Wilhelm, F. and Garcia-Martinez, R. (2011). Quasi-three dimensional two-phase debris flow model acounting for boulder transport, *in* R. Genevois, D. Hamilton and A. Prestininzi (eds), *5th International Conference on Debris-Flow Hazards – Mitigation, Mechanics, Prediction and Assessment; Padua, Italy 14–17 June 2011*, Casa Editrice Università La Sapienza, p. 457–466.

McArdell, B. W., Bartelt, P. and Kowalski, J. (2007). Field observations of basal forces and fluid pore pressure in a debris flow, *Geophysical Research Letters* **34**(7): L07406.

McArdell, B. W. and Berger, C. (2010). Field measurements of debris flow properties and channel-bed elevation change, *Geological Society of America Abstracts with Programs*, Vol. 42, GSA, Denver, p. 384.

McCoy, S. W., Kean, J. W., Coe, J. A., Staley, D. M., Wasklewicz, T. A. and Tucker, G. E. (2010). Evolution of a natural debris flow: In situ measurements of flow dynamics, video imagery, and terrestrial laser scanning, *Geology* **38**(8): 735 –738.

Milan, D., Heritage, G. L. and Hetherington, D. (2007). Application of a 3D laser scanner in the assessment of erosion and deposition volumes and channel change in a proglacial river, *Earth Surface Processes and Landforms* **32**(11): 1657–1674.

Milana, J. P. and Ruzycki, L. (1999). Alluvial-fan slope as a function of sediment transport efficiency, *Journal of Sedimentary Research. Section A, Sedimentary Petrology and Processes* **69**(3): 553.

Nakamura, F. and Kikuchi, S. (1996). Some methodological developments in the analysis of sediment transport processes using age distribution of floodplain deposits, *Geomorphology* **16**(2): 139.

Nicholas, A. P. and Quine, T. A. (2007a). Crossing the divide: Representation of channels and processes in reduced-complexity river models at reach and landscape scales, *Geomorphology* **90**(3): 318.

Nicholas, A. P. and Quine, T. A. (2007b). Modeling alluvial landform change in the absence of external environmental forcing, *Geology* **35**(6): 527–530.

Nishiizumi, K., Imamura, M., Caffee, M., Southon, J., Finkel, R. and McAninch, J. (2007). Absolute calibration of ^{10}Be AMS standards, *Nuclear Instruments and Methods in Physics Research Section B: Beam Interactions with Materials and Atoms* **258**(2): 403–413.

NLT Study Bible (2008). *NLT Study Bible*, Tyndale House Publishers, Carol Stream, Ill.

Norton, K., von Blanckenburg, F., Schlunegger, F., Schwab, M. and Kubik, P. (2008). Cosmogenic nuclide-based investigation of spatial erosion and hillslope channel coupling in the transient foreland of the Swiss Alps, *Geomorphology* **95**(3-4): 474–486.

Ochs, M. and Ivy-Ochs, S. (1997). The chemical behavior of Be, Al, Fe, Ca and Mg during AMS target preparation from terrestrial silicates modeled with chemical speciation calculations, *Nuclear Instruments and Methods in Physics Research Section B* **123**(1/4): 235–240.

Okuda, S., Suwa, H., Okunishi, K., Nakano, K. and Yokoyama, K. (1977). Synthetic observation on debris flow, part 3; observation at valley Kamikamihorizawa of Mt. Yakedake in 1976, *Annuals Desaster Prevention Research Institute* **21B-1**: 277–296.

O'Neal, M. and Pizzuto, J. (2011). The rates and spatial patterns of annual riverbank erosion revealed through terrestrial laser-scanner surveys of the South river, Virginia, *Earth Surface Processes and Landforms* **36**(5): 695–701.

Papa, M., Egashira, S. and Itoh, T. (2004). Critical conditions of bed sediment entrainment due to debris flow, *Natural Hazards and Earth System Science* **4**(3): 469–474.

Parker, G., Paola, C., Whipple, K. X., Mohrig, D., Toro-Escobar, C. M., Halverson, M. and Skoglund, T. W. (1998). Alluvial fans formed by channelized fluvial and sheet flow. II: application, *Journal of Hydraulic Engineering, New York* **124**(10): 996–1004.

Patra, A. K., Bauer, A. C., Nichita, C. C., Pitman, E. B., Sheridan, M. F., Bursik, M., Rupp, B., Webber, A., Stinton, A. J. and Namikawa, L. M. (2005). Parallel adaptive numerical simulation of dry avalanches over natural terrain, *Journal of Volcanology and Geothermal Research* **139**(1-2): 1–21.

Pelletier, J. D., Mayer, L., Pearthree, P. A., House, P. K., Demsey, K. A., Klawon, J. E. and Vincent, K. R. (2005). An integrated approach to flood hazard assessment on alluvial fans using numerical modeling, field mapping, and remote sensing, *Geological Society of America Bulletin* **117**(9-10): 1167 –1180.

Petrascheck, A. and Kienholz, H. (2003). Hazard assessment and mapping of mountain risks in Switzerland, *in* D. Rickenmann and C. L. Chen (eds), *Proceedings of the 3rd International Conference on Debris-Flow Hazards Mitigation: Mechanics, Prediction, and Assessment. Davos, Switzerland, September 10–12, 2003*, Millpress, Rotterdam, Netherlands, p. 25–38.

Petrie, G. and Toth, C. K. (2008). Terrestrial laser scanners, *in* J. Shan and C. K. Toth (eds), *Topographic laser ranging and scanning : principles and processing*, CRC ; Taylor & Francis, Boca Raton, Fla.; London, pp. 87–126.

Phillips, F. M., Stone, W. D. and Fabryka-Martin, J. T. (2001). An improved approach to calculating low-energy cosmic-ray neutron fluxes near the land/atmosphere interface, *Chemical Geology* **175**(3-4): 689–701.

Pratt-Sitaula, B., Burbank, D. W., Heimsath, A. and Ojha, T. (2004). Landscape disequilibrium on 1000-10,000 year scales Marsyandi river, Nepal, central Himalaya, *Geomorphology* **58**(1): 223ï¿½241.

Pudasaini, S. P., Wang, Y. and Hutter, K. (2005). Modelling debris flows down general channels, *Natural Hazards and Earth System Science* **5**(6): 799–819.

Reitz, M., Jerolmack, D. and Swenson, J. (2010). Flooding and flow path selection on alluvial fans and deltas, *Geophysical Research Letters* **37**(6): L06401.

Remaitre, A., Malet, J., Van Asch, W. and Maquaire, O. (2008). Influence of check dams on debris-flow run-out intensity, *Natural Hazards and Earth System Science* **8**(6): 1403–1416.

Rickenmann, D. (1999). Empirical relationships for debris flows, *Natural Hazards* **19**(1): 47–77.

Rickenmann, D. (2005). Runout prediction methods, *in* M. Jakob and O. Hungr (eds), *Debris-flow hazards and related phenomena*, Springer-Praxis books in geophysical sciences, Springer, Berlin; New York, p. 305–321.

Rickenmann, D. and Chen, C. L. (2003). *Proceedings of the 3rd International Conference on Debris-Flow Hazards Mitigation: Mechanics, Prediction, and Assessment. Davos, Switzerland, September 10–12, 2003*, Millpress, Rotterdam, Netherlands.

Rickenmann, D., Weber, D. and Stepanov, B. (2003). Erosion by debris flows in field and laboratory experiments, *in* D. Rickenmann and C. L. Chen (eds), *Proceedings of the 3rd International Conference on Debris-Flow Hazards Mitigation: Mechanics, Prediction, and Assessment. Davos, Switzerland, September 10–12, 2003*, Millpress, Rotterdam, Netherlands, p. 883–894.

Rickenmann, D. and Zimmermann, M. (1993). The 1987 debris flows in Switzerland: documentation and analysis, *Geomorphology* **8**(2-3): 175–189.

Rosser, N., Lim, M., Petley, D., Dunning, S. and Allison, R. (2007). Patterns of precursory rockfall prior to slope failure, *Journal of Geophysical Research F* **112**(F4): F04014.

Sassa, K. and Wang, G. (2005). Mechanism of landslide-triggered debris flows: liquefaction phenomena due to the undrained loading of torrent deposits, *in* M. Jakob. and O. Hungr. (eds), *Debris flow hazards and related phenomena*, Springer, Berlin; Heidelberg; New York, p. 81–103.

Savage, S. B. and Lun, C. K. K. (1988). Particle size segregation in inclined chute flow of dry cohesionless granular solids, *Journal of Fluid Mechanics* **189**: 311–335.

Scheidl, C. and Rickenmann, D. (2011). TopFlowDF – a simple GIS based model to simulate debris-flow runout on the fan, *in* R. Genevois, D. Hamilton and A. Prestininzi (eds), *5th International Conference on Debris-Flow Hazards – Mitigation, Mechanics, Prediction and Assessment; Padua, Italy 14–17 June 2011*, Casa Editrice Università La Sapienza, p. 253–262.

Scheuner, T., Keusen, H., McArdell, B. W. and Huggel, C. (2009). Murganmodellierung mit dynamisch-physikalischem und GIS-basiertem Fliessmodell, *Wasser Energie Luft* **101**(1): 15—21.

Scheuner, T., Schwab, S. and McArdell, B. W. (2011). Application of a two-dimensional numerical model in risk and hazard assessment in Switzerland, *in* R. Genevois, D. Hamilton and A. Prestininzi (eds), *5th International Conference on Debris-Flow Hazards – Mitigation, Mechanics, Prediction and Assessment; Padua, Italy 14–17 June 2011*, Casa Editrice Università La Sapienza, p. 993–1001.

Schlunegger, F., Badoux, A., McArdell, B. W., Gwerder, C., Schnydrig, D., Rieke-Zapp, D. and Molnar, P. (2009). Limits of sediment transfer in an alpine debris-flow catchment, Illgraben, Switzerland, *Quaternary Science Reviews* **28**(11): 1097–1105.

Schlunegger, F., Norton, K. and Caduff, R. (accepted). Hillslope processes in temperate environments, *in* J. Shroder, R. Marston and M. Stoffel (eds), *Treatise on geomorphology*, Vol. 7, Academic press, San Diego.

Schumer, R. and Jerolmack, D. J. (2009). Real and apparent changes in sediment deposition rates through time, *Journal of Geophsical Research* **114**: F00A06.

Schumm, S. A., Mosley, M. P. and Weaver, W. E. (1987). *Experimental Fluvial Geomorphology*, Wiley, New York.

Schürch, P., Densmore, A. L., McArdell, B. W. and Molnar, P. (2006). The influence of landsliding on sediment supply and channel change in a steep mountain catchment, *Geomorpholopy* **78**(3-4): 222–235.

Schürch, P., Densmore, A. L., Rosser, N. and McArdell, B. W. (2009). Quantifying surface change in a debris flow channel with terrestrial laser scanning – what is the volumetric error?, *Proceedings of RSPSoc 2009 Annual Conference*, Nottingham: RSPSoc, Leicester, UK, p. 586–574.

Schürch, P., Densmore, A., Rosser, N. and McArdell, B. W. (2011). Dynamic controls on erosion and deposition on debris-flow fans, *Geology* .

Siegfried, H. (1886, 1907, 1915, 1924 and 1933). Topographischer Atlas der Schweiz (Siefgriedkarte), sheet 482, digital edition, Swisstopo, Bundesamt für Landestopographie, Wabern. digital edition published 2003.

Stock, G. and Uhrhammer, R. (2010). Catastrophic rock avalanche 3600 years BP from el Capitan, Yosemite valley, California, *Earth Surface Processes and Landforms* **35**(8): 941–951.

Stock, J. D. and Dietrich, W. E. (2006). Erosion of steepland valleys by debris flows, *Geological Society of America Bulletin* **118**(9/10): 1125–1148.

Stock, J. and Dietrich, W. E. (2003). Valley incision by debris flows: Evidence of a topographic signature, *Water Resources Research* **39**: ESG 1.

Stock, J., Schmidt, K. and Miller, D. (2008). Controls on alluvial fan long-profiles, *Geological Society of America Bulletin* **120**(5/6): 619–640.

Stoffel, M., Bollschweiler, M., Leutwiler, A. and Aeby, P. (2008). Tree-ring reconstruction of debris-flow events leading to overbank sedimentation on the Illgraben cone (Valais Alps, Switzerland), *The Open Geology Journal* **2**: 18–29.

Stojic, M., Chandler, J., Ashmore, P. and Luce, I. (1998). The assessment of sediment transport rates by automated digital photogrammetry, *Photogrammetric Engineering and Remote Sensing.* **64**(5): 387.

Stone, J., Allan, G., Fifield, L. and Cresswell, R. (1996). Cosmogenic chlorine-36 from calcium spallation, *Geochimica et Cosmochimica Acta* **60**(4): 679–692.

Stone, J., Evans, J., Fifield, L., Allan, G. and Cresswell, R. (1998). Cosmogenic Chlorine-36 production in calcite by muons, *Geochimica et Cosmochimica Acta* **62**(3): 433–454.

Sun, T., Paola, C., Parker, G. and Meakin, P. (2002). Fluvial fan deltas: Linking channel processes with large-scale morphodynamics, *Water Resources Research* **38**: 26–26.10.

Suwa, H. (1988). Focusing mechanism of large boulders to a debris-flow front, *Transactions of the Japanese Geomorphological Union* **9**(3): 151–178.

Suwa, H., Okano, K. and Kanno, T. (2009). Behavior of debris flows monitored on test slopes of Kamikamihorizawa Creek, Mount Yakedake, Japan, *International Journal of Erosion Control Engineering* **2**(2): 34–45.

Suwa, H. and Okuda, S. (1983). Deposition of debris flows on a fan surface, Mt. Yakedake, Japan, *Zeitschrift für Geomorphologie* **Suppl.-Bd. 46**: 79–101.

Suwa, H. and Okuda, S. (1988). Seasonal variation of erosional processes in the Kamikamihori valley of Mt. Yakedake, northern Japan Alps, *Catena Supplement* **13**: 61–77.

Takahashi, T. (2007). *Debris Flow: Mechanics, Prediction and Countermeasures*, Balkema-proceedings and monographs in engineering, water and Earth sciences, Taylor & Francis, London; New York.

Taylor, J. R. (1982). *An introduction to error analysis: the study of uncertainties in physical measurements*, A series of books in physics, University Science Books, Mill Valley, Calif.

Törnqvist, T. E. (1994). Middle and late holocene avulsion history of the river Rhine (Rhine-Meuse delta, Netherlands), *Geology* **22**(8): 711 –714.

Trimble (2005). Datasheet for trimble GS series 3D scanners (GS 200).

Trimble (2006). Trimble RealWorks survey, user guide.

Tsai, Y. (2006). Three-Dimensional topography of Debris-Flow fan, *Journal of hydraulic engineering.* **132**(3): 307.

Tucker, G. E., Lancaster1, S. T., Gasparini, N. M., Bras, R. L. and Rybarczyk, S. M. (2001). An object-oriented framework for distributed hydrologic and geomorphic modeling using triangulated irregular networks, *Computers and Geosciences* **27**(8): 959–973.

van Steijn, H. (1996). Debris-flow magnitude–frequency relationships for mountainous regions of central and northwest Europe, *Geomorphology* **15**(3-4): 259–273.

Varnes, D. (1978). Slope movement types and processes, *Landslides, Analysis and Control*, Vol. 176 of *Transport Research Board Special Reports*, National Academy of Sciences, Washington, p. 11–33.

Volker, H., Wasklewicz, T. and Ellis, M. (2007). A topographic fingerprint to distinguish alluvial fan formative processes, *Geomorphology* **88**(1-2): 34–45.

von Blanckenburg, F., Belshaw, N. S. and ONions, R. K. (1996). Separation of ^{9}Be and cosmogenic ^{10}Be from environmental materials and SIMS isotope dilution analysis, *Chemical Geology* **129**(1-2): 93–99.

von Hansen, W. (2007). Registration of agia sanmarina LiDAR data using surface elements, *ISPRS Workshop on Laser Scanning 2007 and SilviLaser 2007*, Finland, p. 178–183.

von Poschinger, A. (2005). Der Flimser Bergsturz als Staudamm, *Bulletin für angewandte Geologie* **10**(1): 33–47.

Wessels, M. (1998). Natural environmental changes indicated by late glacial and holocene sediments from lake Constance, Germany, *Palaeogeography, Palaeoclimatology, Palaeoecology* **140**(1-4): 421–432.

Wheaton, J., Brasington, J., Darby, S. E. and Sear, D. (2010). Accounting for uncertainty in DEMs from repeat topographic surveys: improved sediment budgets, *Earth Surface Processes and Landforms* **35**(2): 136–156.

Whipple, K. X. (1992). Predicting debris-flow runout and deposition on fans: the importance of the flow hydrograph, *IAHS-AISH Publication* **209**: 337–345.

Whipple, K. X. and Dunne, T. (1992). The influence of debris-flow rheology on fan morphology, Owens valley, California, *Geological Society of America Bulletin* **104**(7): 887—900.

Whipple, K. X., Parker, G., Paola, C. and Mohrig, D. (1998). Channel dynamics, sediment transport, and the slope of alluvial fans: experimental study, *The Journal of Geology.* **106**(6): 677.

Wu, C. and Chang, Y. (2003). Debris-trapping efficiency of crossing-truss open-type check dams, *in* D. Rickenmann and C. Chen (eds), *Debris-Flow Hazards Mitigation: Mechanics, Prediction, and Assessment*, Vol. 2, Millpress, Davos, Switzerland, p. 1315–1325.

Xu, Q., Fan, X.-M., Huang, R.-Q. and Westen, C. (2009). Landslide dams triggered by the Wenchuan earthquake, Sichuan province, south west China, *Bulletin of Engineering Geology and the Environment* **68**(3): 373–386.

Zanuttigh, B. and Lamberti, A. (2007). Instability and surge development in debris flows, *Reviews of Geophysics* **45**(3): RG3006.

Zimmermann, M. (2000). Geomorphologische Analyse des Illgraben, *Technical report*, Geo 7 AG, Bern.

Zimmermann, M., Mani, P. and Romang, H. (1997). Magnitude-frequency aspects of alpine debris flows, *Eclogae Geologicae Helvetiae* **90**(3): 415–420.

Appendix A

Supplementary material for Chapter 2

A.1 Photo documentation of the Illgraben fan and catchment

Figure A.1: *Illgraben, looking upstream: on the left the deposit of the 1961 rock avalanche, right side rock slope of the Gorwetsch Grat.*

Figure A.2: *Illgraben, looking upstream, standing on CD1: mound of soft sediments in central part of photograph is the deposit of the 1961 rock avalanche.*

Figure A.3: *Illgraben, looking downstream from top of CD1.*

Figure A.4: *The sediment retention dam (CD1) seen from downstream, total height is 40 m. Note abrasion of concrete structure by debris flows.*

Figure A.5: *Sample sites for wood embeded in valley fill (S1 and S2, Figure 2.3).*

Figure A.6: *The Illgraben channel looking downstream from sample sites for wood (S1 to S3).*

Figure A.7: *The upper Illgraben catchment seen from the Güetji terrace, note CD1 marked by arrow.*

Figure A.8: *Illgraben channel upstream of CD10 (Figure 4.1).*

Figure A.9: *View downstream from the catchment outlet. Rock avalanche deposit from 3,080 years ago (arrow).*

Figure A.10: *Exposed inner structure of the rock avalanche deposit from 3,080 years ago. Note highly compacted lower part with preserved rock mass structure (arrow) and coarse top layer.*

Figure A.11: *Downstream view of study reach between CD16 and CD19 (Chapter 4). Levee deposits from event 14 (Appendix, Table C.1) indicated by arrows.*

Figure A.12: *Deeply incised active channel on the Illgraben fan. Stabilization and protection of damaged check dam due to lateral erosion and bank collapse with ring net barriers.*

Figure A.13: *Illgraben fan: Snout with boulder C26 (Figure 2.2) behind person for scale in shallow channel (≈ 15 m wide and 2 m deep).*

Figure A.14: *Illgraben fan seen from opposite valley side. The houses of Susten (Figure 2.1) and confluence of the Illgraben with the Rhone can be seen on the left side. Rock avalanche deposit from 3,080 years ago indicated by arrow.*

A.2 Laboratory report for radiocarbon dating of wood samples

University Bern
Physics Institute
Prof. T. Stocker
CH-3012 Bern, Sidlerstrasse 5
ph +41-31- 631 44 62, fx +41-31- 631 87 42
rfischer@climate.unibe.ch
http://www.climate.unibe.ch

20.05.11

UNI Bern / Geologisches Institut
Fritz Schlunegger
Baltzerstr. 1
3012 Bern

Betrifft: Radiocarbondatierung Ihrer Holz-Proben

Sehr geehrter Herr Schlunegger

Wir freuen uns, Ihnen nachstehende Resultate unserer Analysen mitteilen zu können. Diese enthalten unsere Labornummer, Ihre Probenbezeichnungen, das konventionelle Radiocarbonalter sowie $D^{14}C$ und $\delta^{13}C$-Angaben.

B-9629 **Holz S1 Illgraben VS (CH)** **1950 ± 20 Jahre BP**
$D^{14}C$ = (-215,9± 2,2)‰ **$\delta^{13}C$ = (-23,6 ± 0,2)‰**
Fundort: Illgraben, in der rechten Zuflussrinne 8m oberhalb der Sperre 4; aus dem **westlichen Anriss** dieser Rinne (CH-Koordinaten: 614124/125848, 982 m ü.M., in ca. 20m Tiefe) April 2009

B-9630 **Holz S2 Illgraben VS (CH)** **1970 ± 20 Jahre BP**
$D^{14}C$ = (-217,8 ± 2,3)‰ **$\delta^{13}C$ = (-23,8 ± 0,2)‰**
Fundort: Illgraben, in der rechten Zuflussrinne 8m oberhalb der Sperre 4; aus der **östlichen Flanke**, April 2009

B-9631 **Holz S3 Illgraben VS (CH)** **1990 ± 20 Jahre BP**
$D^{14}C$ = (-219,3 ± 2,2)‰ **$\delta^{13}C$ = (-24,9 ± 0,2)‰**
Fundort: Illgraben, aus einer Seitenrinne (2 Rinnen flussabwärts der Rinne aus welcher S1 uns S2 entnommen wurden) ca. 12,2 m oberhalb der Sperre 4

Als zusätzliche Information legen wir ein Merkblatt mit technischen Erklärungen bei.

Bemerkung:
Wir bitten Sie, uns im Falle einer Veröffentlichung des obigen ^{14}C Alters ein Exemplar der Publikation oder ein Separatum des Artikels zu überlassen. Bei Publikationen ist folgender Absatz an geeigneter Stelle im Text einzufügen: "Die für Altersbestimmung erforderliche Präparation, die Aufbereitung und Datierung des Probenmaterials erfolgten im Radiocarbonlabor des Physikalischen Institutes der Universität Bern". Wir danken Ihnen für Ihr Verständnis.
Es würde uns freuen, Ihre eventuellen Fragen beantworten, bzw. die Resultate mit Ihnen besprechen zu dürfen. Bitte nehmen Sie Kontakt auf mit

T. Stocker
Tel. 031 631 44 62

oder

R. Fischer
Tel. 031 631 44 78

Mit freundlichen Grüssen

T. Stocker

UNIVERSITÄT BERN

Radiocarbon-Labor
Physikalisches Institut-Universität Bern
Sidlerstrasse. 5 , CH-3012 Bern
Tel. 031- 631 44 64 Labor: 031- 631 44 78
FAX: 031- 631 87 42
rfischer@climate.unibe.ch

Altersbestimmung nach der ^{14}C-Methode

Holz-, Holzkohle-, Torf-, Laubproben, etc. werden nach einer Vorbehandlung, die probenfremdes Material nach Möglichkeit entfernt, unter Luftabschluss im O_2-Strom zu CO_2 verbrannt.
Diesem CO_2 werden ca. 15 cm^3 STP entnommen und massenspektrometrisch auf den Gehalt an ^{13}C untersucht. Der gemessene δ**^{13}C**-Wert gibt an, wie weit es in der Natur und/oder im Labor zu einer Verschiebung in der isotopenmässigen Zusammensetzung des Kohlenstoffes, d.h. zu einer Fraktionierung gekommen ist. Dieser ^{13}C-Wert ist repräsentativ für das Zählgas und gibt nicht unbedingt die isotopenmässige Zusammensetzung der ursprünglichen Probe wieder.
Der Hauptteil des aus der Probe gewonnenen CO_2 wird katalytisch unter Zugabe von H_2 zu CH_4 reduziert, dem Füllgas der Proportionalzähler zur Bestimmung der ^{14}C-Aktivität der Probe. Die mit dem Zähler gemessene ^{14}C-Aktivität wird mit der Aktivität eines Eichgases verglichen. Die Abreicherung an ^{14}C der Probe verglichen mit diesem Standard wird in Promill ausgedrückt und als **D^{14}C** bezeichnet. Bei der Berechnung von D^{14}C werden durch Normierung auf δ^{13}C = -25 ‰ mögliche Fraktionierungen berücksichtigt.
Aus dem ^{14}C-Gehalt der Probe kann unter Annahme gewisser Voraussetzungen (wie etwa der Konstanz des atmosphärischen ^{14}C-Gehaltes), welche von Stuiver und Polach in der Zeitschrift RADIOCARBON, Vol. 19, No. 3, 1977, S. 355-363, beschrieben sind, das **konventionelle Radiocarbon- oder ^{14}C-Alter** der Probe berechnet werden. Das konventionelle Radiocarbon-Alter wird mit der **Libby-Halbwertszeit** (5568 Jahre) berechnet und gerundet in Jahren vor 1950 (Jahren BP (before present)) ausgedrückt.
Da die oben erwähnten Annahmen nur unter gewissen Umständen berechtigt sind, stimmt das Radiocarbon-Alter nicht unbedingt mit dem wahren ("Kalender"-) Alter der Probe überein. Das Radiocarbon-Alter kann aber mittels **Kalibrierungskurven**, die aus hochpräzisen Messungen an absolut datierten Baumringen und anderen Probenmaterialien gewonnen wurden, in **Kalenderalter** umgerechnet werden. Allerdings muss bei der Umrechnung z.T. mit Mehrdeutigkeiten gerechnet werden.
Kalibrationskurven werden u.a. in RADIOCARBON, Vol. 35, No. 1, 1993, S.215-230, in RADIOCARBON, Vol. 46, No.3, 2004, S.1029-1058 (INTCAL04 RADIOCARBON AGE CALIBRATION, 26'000-0 cal BP) und in RADIOCARBON, Vol.51, Nr.4, 2009, S. 1111-1150 (INTCAL09, Calibration Curves, 0-50'000 Years cal BP) beschrieben. Das Kalibrationsprogramm kann direkt genutzt oder heruntergeladen werden (www.calib.org).

Randbemerkung für die Angabe von Resultaten in Publikationen:

Da die Umrechnung auf das wirkliche Alter (Kalibration) künftig noch verfeinert werden könnte, darf in Publikationen die Angabe des konventionellen Alters nie fehlen.

Ebenfalls nicht fehlen sollte die Probenummer des Messlabors (B-…… für die Uni Bern). Gemäss einer internationalen Abmachung werden jedem Labor andere Buchstaben zugeteilt. In Publikationen sind unsere B-Nummern jeweils aufzuführen. Sie erschliessen den Weg zu den Originalproben im Archiv sowie zu den ausführlichen Probenakten (Koordinaten des Fundortes etc.)

R.Fischer, 20.5.2011

Appendix B

Supplementary material for Chapter 3

Derivation of the equation for expected standard deviation of elevation (Equation 3.3).

$$\begin{aligned}\sigma_{elv,exp} &= \sqrt{\frac{1}{2}((z_{max}-\bar{z})^2+(z_{min}-\bar{z})^2)} \\ &= \sqrt{\frac{1}{2}(z_{max}^2-2z_{max}\bar{z}+\bar{z}^2+z_{min}^2-2z_{min}\bar{z}+\bar{z}^2)}\end{aligned} \tag{B.1}$$

with substitution $\bar{z}=\frac{z_{max}+z_{min}}{2}$ Equation B.1 can be writen as:

$$\begin{aligned}\sigma_{elv,exp} &= \sqrt{\frac{1}{2}(\frac{1}{2}z_{max}^2-z_{max}z_{min}+\frac{1}{2}z_{min}^2)} \\ &= \sqrt{\frac{1}{4}(z_{max}-z_{min})^2} \\ &= \frac{1}{2}(z_{max}-z_{min})\end{aligned} \tag{B.2}$$

Appendix C

Supplementary material for Chapter 4

C.1 Calculation of debris flow volumes from hydrographs

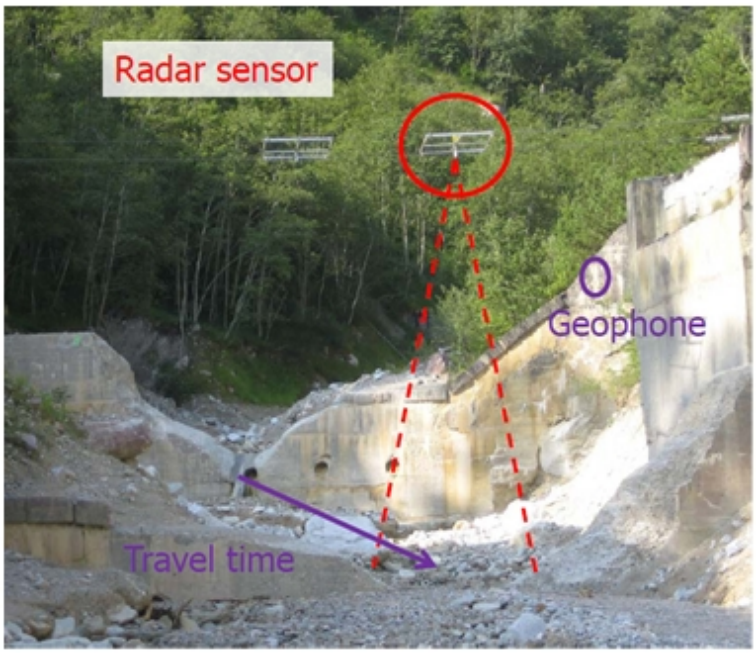

Figure C.1: *Upper gauging station at CD9 and CD10. The distance between CD9, where the geophone is mounted, and CD10, where the radar is mounted, is 39 m (purple arrow). Channel slope is 10%.*

I estimate debris flow volumes from flow hydrographs of individual events, using the method in (Schlunegger et al., 2009) to calibrate a simple Manning-type friction relation (Barnes, 1967). Estimates are made at two gauging stations, one in the catchment at check dam (CD) 9 and 10, and the second at the fan toe at CD28 and 29. At the upstream station, a geophone at CD9 (Figure C.1) records the passage of the flow front and triggers a radar sensor $\approx$ 39 m downstream at CD10, which records the debris flow hydrograph. I estimate front velocity using the time difference between detection of the flow front at both stations and

calibrate the Manning equation according to the procedure described below. At the downstream station (CD29), a laser and a radar unit record debris flow hydrographs. I estimate front velocity from the front arrival times at geophones mounted on CD28 and CD29, and calibrate the Manning equation as below. To quantify the uncertainty in the velocity estimate, average debris flow velocities are calculated for the channel reaches CD1 to 9 and CD9 to 29 and the resulting flow volumes. Results for all flows are shown in Table C.1. Below the volume calculations using data from the upper station at CD9/10 for event 9 on 1 July 2008 is illustrated (Table C.1). The necessary calculation steps in detail are:

1. Estimate front velocity from travel time between CD9 and CD10:

$$u_{local} = \frac{\Delta l}{\Delta t} = \frac{39m}{8s} = 4.9m/s \tag{C.1}$$

2. Measure front height from radar recordings (Figure C.2): $h_f = 4.5m$.

3. Estimate the hydraulic radius for the passage of the flow front based on a channel cross profile surveyed with a hand level on 25 May 2009: $h_r(h_f = 4.5m) \approx 2.1$.

4. Calculate the coefficient for the Manning friction relation using front velocity, hydraulic radius and channel slope:

$$k = \frac{u_{local}}{h_r^{2/3} \cdot S^{1/3}} = \frac{4.9m/s}{(2.1m)^{2/3} \cdot 0.1^{1/3}} = 6.5m^{1/3}/s \tag{C.2}$$

5. Integrate along the hydrograph (Figure C.2) to obtain the total flow volume.

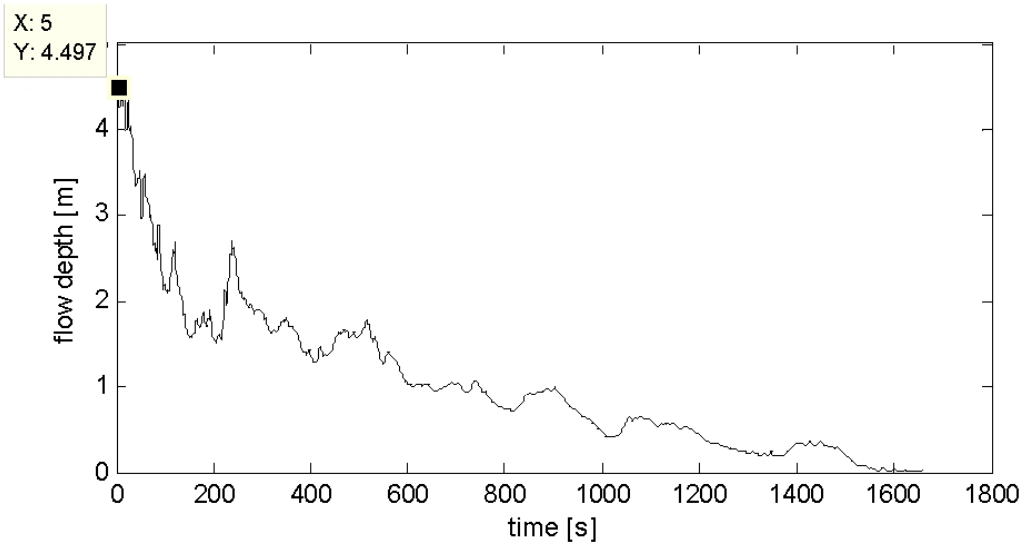

Figure C.2: *Hydrograph of event 9 at CD10. Front height (see data tip) is 4.5 m measured 5 s after recording of the front at CD9.*

At every recording of flow depth, $h(t)$, I calculate the corresponding hydraulic radius, $h_r(t)$, and then calculate the mean velocity, $u(t)$, for each time step. I multiply the velocity with the flow cross section area, $A(t)$, which is a function of flow stage, $h(t)$, and the channel cross-sectional profile, to obtain discharge. The flow volume is the sum of the discharge time series, $Q(t)$, over the duration of the event.

$$V = \sum_{t=0}^{t=t_{max}} Q(t) = \sum_{t=0}^{t=t_{max}} A(t) \cdot u(t) = \sum_{t=0}^{t=t_{max}} A(t) k h_r(t)^{2/3} S^{1/3} \approx 27,000 m^3 \tag{C.3}$$

In Table C.1 I show the calculated volumes at CD10 and at CD29 for all 14 events. For the analysis in Chapter 4 I use the volumes calculated according to the workflow detailed above. As a check I have also calculated the average velocities between CD1 and CD9 and between CD9 and CD29 from front arrival times at CD1 and CD29 respectively. Then I calculated the friction coefficient (step 4 above) using these velocities and then integrated along the hydrograph to obtain flow volume (step 5 above, using same cross section geometry as in step 3). For five events (flows 2, 4, 8, 11 and 12) the average velocities are significantly lower and would, if used for the volume calculation, lead to substantially smaller volumes at CD10 (Table C.1). These events would change from being dominantly depositional to having no net volume change whilst traversing the fan. For all other events the dominant behaviour would not change. Therefore I conclude that the uncertainties in the local velocity estimate are small enough to warrant our analysis in the paper.

Table C.1: *Debris flow velocities, front height and volumes. Channel slopes used for calculating k at the gauging stations are 0.1 (CD10) and 0.086 (CD29) respectively. * Only for these events the use of alternative calculations for the flow volume have a significant effect on the fan-scale flow behaviour. ** A second surge with a front height of 5.2m arrived 17s after passage of the flow front. n/a: debris flow not detected at CD1 (Events 1 and 11) or debris flow did not trigger lower gauging station due to full deposition on fan (Events 3, 6, 7, 10, 12).*

		gauging station at CD10 measured velocity u, front height hf and calculated Strickler coefficient k, volume V and peak discharge Q													gauging station at CD29 measured velocity u, front height hf and calculated Strickler coefficient k, volume V and peak discharge Q				
			based on travel time CD9–CD10				based on travel time CD1–CD9				based on travel time CD9–CD29				based on travel time CD27–CD29				
No.	Date	h_f	u_{local}	k	V	Q	u_{1-9}	k	V	Q	u_{9-29}	k	V	Q	h_f	u_{27-29}	k	V	Q
		m	m s^{-1}	m$^{2/3}$ s$^{-1/3}$	m^3	m^3 s^{-1}	m s^{-1}	m$^{2/3}$ s$^{-1/3}$	m^3	m^3 s^{-1}	m s^{-1}	m$^{2/3}$ s$^{-1/3}$	m^3	m^3 s^{-1}	m	m s^{-1}	m$^{2/3}$ s$^{-1/3}$	m^3	m^3 s^{-1}
1	2007/05/28	1.6	7.8	17.6	27800	80	n/a	n/a	n/a	n/a	6.6	14.9	23500	70	1.5	6.6	21.5	18600	70
2*	2007/06/15	0.7	5.6	19.3	68800	130	0.7	2.4	8600	16	2.2	7.6	27200	50	3.8	2.5	5.3	10200	140
3	2007/07/01	2.0	3.3	6.3	9400	40	1.5	2.9	4400	17	n/a	n/a	n/a	n/a	n/a	n/a	n/a	0	0
4*	2007/07/21a	2.7	4.9	7.8	15600	90	1.0	1.6	3200	17	0.9	1.4	2900	15	1.0	0.4	1.7	4600	3
5	2007/07/21b	2.8	2.6	4.3	11700	60	10.8	17	48600	220	7.0	11	31000	140	1.9	6.8	20.2	67400	100
6	2007/08/08	0.5	3.9	16.7	28400	20	0.3	1.3	2200	2	n/a	n/a	n/a	n/a	n/a	n/a	n/a	0	0
7	2007/08/29	0.6	4.9	20.2	1600	7	0.5	2.1	200	1	n/a	n/a	n/a	n/a	n/a	n/a	n/a	0	0
8*	2008/06/16	1.3	3.9	10.5	15900	50	1.5	4.0	6100	20	2.1	5.4	8200	30	1.1	2.4	9.1	7700	17
9	2008/07/01	4.5	4.9	6.5	27000	200	7.6	10.1	41500	310	6.5	8.6	35500	270	2.2	5.3	14.4	60000	90
10	2008/08/19	1.0	4.3	12.6	4100	20	0.9	2.6	850	3	n/a	n/a	n/a	n/a	n/a	n/a	n/a	0	0
11*	2008/08/31	2.5	3.9	6.7	10600	60	n/a	n/a	n/a	n/a	2.6	4.4	7100	40	1.45	1.9	6.3	8200	19
12*	2009/07/17	1.8	4.3	9.1	7200	40	3.6	7.8	6100	40	n/a	n/a	n/a	n/a	n/a	n/a	n/a	0	0
13	2009/07/28	2.3	3.3	6.1	5300	40	5.4	9.8	8500	70	3.0	5.4	4700	40	1.0	2.2	9.1	13500	20
14	2009/08/09	2.3**	7.8	14.4	106300	630	5.9	10.9	80400	480	6.8	12.5	92700	550	2.6	5.9	15.1	56800	130

C.2 Quantitative comparison of elevation change and flow depth

Here, I briefly explain the processing that lead to the visualization of our data in Figure 4.3A. First maps of elevation change were created (termed difference models) with a cell size of 0.2 x 0.2 m from subsequent surveys and the models of maximum flow depth for each event (as explained in the main text). Crucial here is that for each grid cell in the difference model there is a corresponding grid cell in the flow-depth model. I then produced a scatter plot of flow depth vs. elevation change combining all four events into one data set. Because of the large number of data points – as illustrated by the density plot (Figure 4.3A and Figure C.3) – the structure of the data is not immediately obvious. Therefore I subdivided the data in bins with a width of 0.5 m along the flow-depth axis (i.e. $[0m-0.5m[\,;[0.5m-1.0m[\cdots[3.0m-3.5m]$). I choose a bin width of 0.5 m, because this reflects the estimated uncertainty on the maximum flow depth. Any bin width smaller than 0.5 m would yield a percentile plot that over interprets the data. Next I calculated the corresponding elevation change value for the 1, 10, 25, 50, 75, 90 and 99 percentile based on the data in each bin. This gave the vertical position of the respective percentile line at the centre of each bin (0.25 m, 0.75 m, 1.25 m ... 3.25 m) in Figure 4.3A.

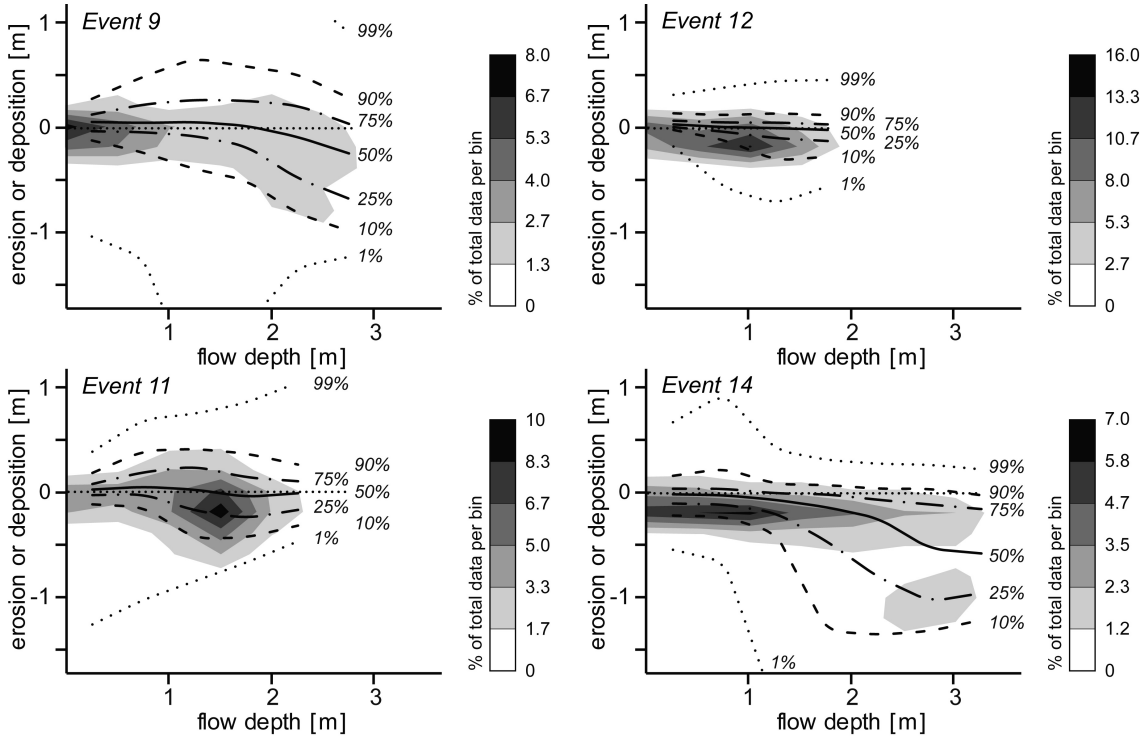

Figure C.3: *Percentile and density plot of cell by cell (0.2 x 0.2 m) comparison of elevation change (erosion or deposition) from TLS vs. maximum flow depth as mapped in the field for individual events 9, 11, 12 and 14). The percentiles are calculated based on a bin width of 0.5 m of flow depth.*

Appendix D

Supplementary material for Chapter 5

D.1 Technical documentation

D.1.1 Model execution

Synopsis for the model on the MATLAB command prompt is:

```
dfmodel2d_v4_2('params.txt','Fan.mat',OutputOption,BreakOption)
```

where `params.txt` is the file name of the parameter file and `Fan.mat` is the file name of the *.mat file containing the model space. `OutputOption` can be 'each' (DEM and AGE are saved at each interval specified in params.txt) or 'onlysummary' (only summary output file is written). `BreakOption` can be 'nogrowth' (model is stopped when fan growth rate is zero for the first time) or 'none' (model stoppes when the specified number of iterations is accomplished).

A standalone executable can be compiled by typing

```
>> mcc -mv dfmodel2d_v4.m -R -nojvm -d path_for_output
```

on the Matlab command prompt. The resulting executable can be run on any windows machine. Follow the instructions in the readme file that is generated by the `mcc` command. Command line syntax on the windows command prompt is:

```
dfmodel2d_v4.exe parameterfile.txt fanfile.mat OutputOption BreakOption
```

D.1.2 List of matlab routines

This is the list of functions called by `dfmodel2d_v4_2`, which is the main model routine. A short explanation and synopsis of each function can be found in the header of the source code on the data CD (Appendix E).

- `dfmodel2d_v4_2`
- `tin2grid_ps`
- `curvature_along_arcs_v2`
- `tin_flow_path_v3`
- `FindMinFillElevation`
- `slope_alongpath_v2`
- `flowprops_ps`
- `modifytopo_2d_v3_ps`
- `update_elevation`
- `FindInChannel`
- `FillPits`
- `fillchannel2d_ps`
- `simdiscr`
- `grd2array_no_nan_ps`
- `depositflowcrosssec_2d_ps`

D.1.3 Definition of the model space

A custom model space can be defined with the file `template_radialgrid.m`. A sample model space is on the data CD. All units are in meter or degrees (fan azimuth) or dimensionless (fan and chute slope). In the first 13 lines of the file the geometry of the model space is defined. Specify name of output file on line 25. The output file contains five variables which I briefly explain below:

RGREF is a 1 x 4 array that defines the basic geometry of the model space with: X-, Y-coordinates of apex, node spacing along arc, arc spacing, fan azimuth.

ApexArc is the number of the last chute arc, counted from the top of the chute.

TINbkp is a data base (structured array) containing for each node information on parent arc, position within arc, cartesian x-y coordinates, elevation, IDs of neighboring nodes and area of the voronoi polygon associated with the node.

RGbkp is a matrix with as many columns as there are arcs in the model space. The cell values contain the node elevation.

TRI is the triangulation database in MATLABs own format.

It is important that the variables have exactly the names as above, otherwise subroutines will not work! `template_radialgrid.m` calls the following functions, the source code contains some comments for further reference.:

- `make_model_space`
- `makeradialgrid`
- `make_chute`
- `create_tin_ps`
- `make_cone`
- `make_axes_from_dem`

The model can be restarted based on the output of a former model run. Variables have to be renamed as follows: **RGnew** to **RGbkp**, and **TINnew** to **TINbkp**. This is done by calling `OutToInFile(DumpFile,NewFanFile)`, which will gather the relevant variables from the summary output file, rename and save them to a NewFanFile for the next model run. This function will also transfer the fan age from the previous run, so the new run starts with actual surface age from when the previous model run stopped. It is possible to sample elevations from an existing DEM. The procedure for this is as follows:

1. create a model space with the appropriate geometry using `template_radialgrid.m`.
2. use function `[RGsamp, TINsamp] = sample_grid_at_nodes(DEM,VREF,TIN,RG)` to sample elevations from DEM at nodes defined in TIN and RG. VREF is the reference vector for DEM defined as [Grid spacing, Xmin, Ymin].

D.1.4 Description of output variables

Below is a list and description of the variables in the output summary file, *MaxEvents* stands for the maximum number of events specified in the parameter file. *NoArcs* stands for the number of arcs in the model space. Remember, first and last arc are not occupied by flows:

ApexArc arc number of last arc in chute.

BedEvol MaxEvents x 1 array of bed water content.

BedPorosity porosity of sediment in the model. This variable appears again in the output summary file because it is needed by some of the analysis tools described below.

CsedEvol NoArcs x MaxEvents matrix. Sediment concentration of flow at each arc (rows) for each event (columns).

Interval each Interval time steps a DEM and AGE matrix are written to disk. This variable appears again in the output summary file because it is needed by some of the analysis tools described below.

PathEvol NoArcs x MaxEvents matrix. IDs of the talweg nodes of each event (events in columns). IDs refer to lines in TIN1,1.

ProfEvol NoArcs x 2*MaxEvents matrix. Elevations of talweg nodes before and after debris flow. The first MaxEvents columns contain the pre-event talweg elevations and the second MaxEvents columns the post-event talweg elevations.

RGREF see above.

RGbkp input radial grid matrix, see above.

RGnew output radial grid matrix at end of model run, see above.

RunTime model run time in hours.

StopEvol NoArcs x MaxEvents matrix. With flow status for each arc and each event. Flow status is coded as: -1 node not occupied by flow (stoped further upstream), 0 occupied but not stopped, 1 sediment concentration Crit was reached and now depositing full flow cross sectional area at each arc, 2 flow ended at this node.

TINbkp output TIN database at end of moedl run.

TNInew input TIN database.

TRI triangulation of TIN in MATLABs own format.

VolEvol NoArcs x MaxEvents matrix. Volume change in each arc. positive=deposition, negative=erosion. Volumes are water+sediment!

VolumeLast Volume in last arc. Zero when flow stopped on fan.

VolumeTop Volume as drawn from input volume distribution.

AGE surface age (in time steps) at end of model run.

D.1.5 Sample parameter file

```
% model run specific
%%%%%%%%%%%%%%%%%%%%
dt = 1 ;            % time step, only relevant if including e.g. diffusion
df_pbb= 1 ;         % probability of debris flow ocurring in time step
NoIt = 5 ;          % total number of time steps
SAng = 90 ;         % downstream search angle (degrees) for flow routing
Interval = 10 ;     % interval at which DEM and AGE matrix are written to disk
                    % output is written to directory ./output as
                    % *dem.mat or *age.mat where * stands for the time step

% environmental parameters
%%%%%%%%%%%%%%%%%%%%%%%%%%
BedPorosity = 0.1 ; % porosity of fan deposits
Pwet = 0 ;          % probability of bed beeing 100% saturated

% next three lines are examples how to specify the input distribution
% uncomment one of them or change as needed
%VolumeGenerator = 'lognrnd_ps(5714,2857,NoIt)' ;
%VolumeGenerator = 'doubleparetovol_ps(1.8,9,1200,100,50000,NoIt)' ;
VolumeGenerator = 'ones(NoIt,1)*5000' ;

% path to flow depth - erosion PDF
EroPDF = 'load z:\flowdepth_vs_change\pdf_fd_vs_change\ProbDFstruct.mat' ;

% debris flow parameters
%%%%%%%%%%%%%%%%%%%%%%%%%
% Power law coefficient for flow cross section area,
% for debris flows ~0.03 to 0.11
% see Iverson et al., 1998; Griswold & Iverson, 2008;
% Berti & Simoni, 2007; Crosta et al.,2003
EpsilonGenerator = 'ones(NoIt,1)*0.03' ;
% Power law coefficient for planimetric inundation area
% for debris flow ~6 to 40, 200 for lahars
AlphaGenerator = 'ones(NoIt,1)*20' ;
MinConc = 0.6 ; % minimum initial sediment concentration
MaxConc = 0.6 ; % maximum initial sediment concentration
Crit = 0.8 ;    % critical sediment concentration, to trigger lobe deposition mode

% What to do with output
%%%%%%%%%%%%%%%%%%%%%%%%
DumpFile = 'dumpresults.mat' ; % file name for summary output, will be written
                               % to directory from where model function is called
```

D.2 Table of model experiments and parameters

See next page.

Table D.1: *Model runs with parameter settings. Bed porosity was 0.1 for all model runs.* α *see Equation 5.3,* ε *see Equation 5.2.* C_{min} *and* C_{max}*: minimum and maximum initial sediment concentration.* C_{crit}*: critical sediment concentration.* p_{wet}*: probability of bed being wet (water content of 0.1). logn: lognormal input volume distribution with mean* μ_V *and standard deviation* σ_V*. dbp: double pareto input volume distribution with positive power law slope a and negative power law slope b, q roll-over volume,* V_{min} *minimum and* V_{max} *maximum volume (Volumes in [*m^3*]). unirnd[value1...value2]: random sampling from uniform distribution between value1 and value2 for each event in model run. NoIt: number of events in thousands. Runtime: model runtime after NoIt events [h].*

Run ID	Model parameters							NoIt	Runtime
	α	ε	C_{min}	C_{max}	C_{crit}	p_{wet}	Volume distribution		
E1	10	0.1	0.6	0.6	0.8	0	$\mu_V = 1,000$, $\sigma_V = 0$	10k	1.2
E2	10	0.1	0.6	0.6	0.8	0	$\mu_V = 2,000$, $\sigma_V = 0$	10k	1.2
E3	10	0.1	0.6	0.6	0.8	0	$\mu_V = 4,000$, $\sigma_V = 0$	10k	1.2
E4	10	0.1	0.6	0.6	0.8	0	$\mu_V = 8,000$, $\sigma_V = 0$	10k	1.2
E5	10	0.1	0.2	0.2	0.8	0	logn, $\mu_V = 20,000$, $\sigma_v = 10,000$	30k	4
E6	10	0.1	0.3	0.3	0.8	0	logn, $\mu_V = 13,333$, $\sigma_v = 6,666$	16k	1.2
E7	10	0.1	0.4	0.4	0.8	0	logn, $\mu_V = 20,000$, $\sigma_v = 10,000$	30k	1.2
E8	10	0.1	0.5	0.5	0.8	0	logn, $\mu_V = 8,000$, $\sigma_v = 4,000$	30k	1.2
E9	10	0.1	0.6	0.6	0.8	0	logn, $\mu_V = 6,667$, $\sigma_v = 3,334$	30k	1.2
E10	10	0.1	0.7	0.7	0.8	0	logn, $\mu_V = 5,714$, $\sigma_v = 2,857$	30k	1.2
E11	10	0.1	0.1	0.3	0.8	0	logn, $\mu_V = 20,000$, $\sigma_v = 10,000$	2.9k	1.2
E12	10	0.1	0.3	0.5	0.8	0	logn, $\mu_V = 20,000$, $\sigma_v = 10,000$	6.8k	1.2
E13	10	0.1	0.5	0.7	0.8	0	logn, $\mu_V = 6,667$, $\sigma_v = 3,334$	8.5k	1.2
E14	10	0.1	0.6	0.8	0.8	0	logn, $\mu_V = 5,714$, $\sigma_v = 2,857$	20k	1.2
E15	20	0.3	0.1	0.8	0.8	0	logn, $\mu_V = 5,714$, $\sigma_v = 2,857$	9.9k	1.6
E16	20	0.3	0.3	0.8	0.8	0	logn, $\mu_V = 5,714$, $\sigma_v = 2,857$	8.8k	1.4
E17	20	0.3	0.5	0.8	0.8	0	logn, $\mu_V = 5,714$, $\sigma_v = 2,857$	11k	1.9
E18	20	0.3	0.7	0.8	0.8	0	logn, $\mu_V = 5,714$, $\sigma_v = 2,857$	40k	25
E19	40	0.3	0.1	0.8	0.8	0	logn, $\mu_V = 5,714$, $\sigma_v = 2,857$	7.6k	1.3
E20	40	0.3	0.3	0.8	0.8	0	logn, $\mu_V = 5,714$, $\sigma_v = 2,857$	11k	1.9
E21	40	0.3	0.5	0.8	0.8	0	logn, $\mu_V = 5,714$, $\sigma_v = 2,857$	10k	1.9
E22	40	0.3	0.7	0.8	0.8	0	logn, $\mu_V = 5,714$, $\sigma_v = 2,857$	40k	18
E23	10	0.1	0.3	0.8	0.8	0	logn, $\mu_V = 3,000$, $\sigma_v = 1,500$	20k	3
E24	5	0.03	0.3	0.8	0.8	0	logn, $\mu_V = 3,000$, $\sigma_v = 1,500$	30k	4

Run ID	Model parameters							NoIt	Runtime
	α	ε	C_{min}	C_{max}	C_{crit}	p_{wet}	Volume distribution		
E25	5	0.1	0.3	0.8	0.8	0	logn, $\mu_V = 3{,}000$, $\sigma_v = 1{,}500$	30k	4
E26	5	0.2	0.3	0.8	0.8	0	logn, $\mu_V = 3{,}000$, $\sigma_v = 1{,}500$	30k	4
E27	20	0.1	0.3	0.8	0.8	0	logn, $\mu_V = 3{,}000$, $\sigma_v = 1{,}500$	30k	4
E28	20	0.2	0.3	0.8	0.8	0	logn, $\mu_V = 3{,}000$, $\sigma_v = 1{,}500$	30k	4
E29	40	0.1	0.3	0.8	0.8	0	logn, $\mu_V = 3{,}000$, $\sigma_v = 1{,}500$	30k	4
E30	40	0.2	0.3	0.8	0.8	0	logn, $\mu_V = 3{,}000$, $\sigma_v = 1{,}500$	30k	4
E31	20	0.06	0.3	0.7	0.7	0	logn, $\mu_V = 3{,}000$, $\sigma_v = 1{,}500$	30k	4
E32	20	0.06	0.5	0.7	0.7	0	logn, $\mu_V = 3{,}000$, $\sigma_v = 1{,}500$	30k	4
E33	20	0.06	0.3	0.75	0.75	0	logn, $\mu_V = 3{,}000$, $\sigma_v = 1{,}500$	30k	4
E34	20	0.06	0.5	0.75	0.75	0	logn, $\mu_V = 3{,}000$, $\sigma_v = 1{,}500$	30k	4
E35	20	0.06	0.3	0.8	0.8	0	logn, $\mu_V = 3{,}000$, $\sigma_v = 1{,}500$	30k	4
E36	20	0.06	0.5	0.8	0.8	0	logn, $\mu_V = 3{,}000$, $\sigma_v = 1{,}500$	30k	4
E37	20	0.06	0.3	0.8	0.8	0.1	logn, $\mu_V = 3{,}000$, $\sigma_v = 1{,}500$	30k	4
E38	20	0.06	0.3	0.8	0.8	0.5	logn, $\mu_V = 3{,}000$, $\sigma_v = 1{,}500$	30k	4
E39	20	0.06	0.3	0.8	0.8	0.9	logn, $\mu_V = 3{,}000$, $\sigma_v = 1{,}500$	30k	4
E40	20	0.03	0.3	0.8	0.8	0	logn, $\mu_V = 3{,}000$, $\sigma_v = 1{,}500$	30k	4
E41	40	0.03	0.3	0.8	0.8	0	logn, $\mu_V = 3{,}000$, $\sigma_v = 1{,}500$	30k	4
E42	30	0.03	0.3	0.8	0.8	0	logn, $\mu_V = 3{,}000$, $\sigma_v = 1{,}500$	30k	4
E43	30	0.06	0.3	0.8	0.8	0	logn, $\mu_V = 3{,}000$, $\sigma_v = 1{,}500$	30k	4
E44	30	0.1	0.3	0.8	0.8	0	logn, $\mu_V = 3{,}000$, $\sigma_v = 1{,}500$	30k	4
E45	30	0.15	0.3	0.8	0.8	0	logn, $\mu_V = 3{,}000$, $\sigma_v = 1{,}500$	30k	4
E46	30	0.2	0.3	0.8	0.8	0	logn, $\mu_V = 3{,}000$, $\sigma_v = 1{,}500$	30k	4
E47	12	0.03	0.3	0.8	0.8	0	logn, $\mu_V = 3{,}000$, $\sigma_v = 1{,}500$	30k	4
E48	12	0.06	0.3	0.8	0.8	0	logn, $\mu_V = 3{,}000$, $\sigma_v = 1{,}500$	30k	4
E49	12	0.1	0.3	0.8	0.8	0	logn, $\mu_V = 3{,}000$, $\sigma_v = 1{,}500$	30k	4
E50	12	0.15	0.3	0.8	0.8	0	logn, $\mu_V = 3{,}000$, $\sigma_v = 1{,}500$	30k	4
E51	12	0.2	0.3	0.8	0.8	0	logn, $\mu_V = 3{,}000$, $\sigma_v = 1{,}500$	30k	4
E52	5	0.06	0.3	0.8	0.8	0	logn, $\mu_V = 3{,}000$, $\sigma_v = 1{,}500$	30k	4
E53	5	0.15	0.3	0.8	0.8	0	logn, $\mu_V = 3{,}000$, $\sigma_v = 1{,}500$	30k	4
E54	20	0.15	0.3	0.8	0.8	0	logn, $\mu_V = 3{,}000$, $\sigma_v = 1{,}500$	30k	4

Run ID	Model parameters							NoIt	Runtime
	α	ε	C_{min}	C_{max}	C_{crit}	p_{wet}	Volume distribution		
E55	40	0.06	0.3	0.8	0.8	0	logn, $\mu_V = 3{,}000$, $\sigma_v = 1{,}500$	30k	4
E56	40	0.15	0.3	0.8	0.8	0	logn, $\mu_V = 3{,}000$, $\sigma_v = 1{,}500$	30k	4
E57	20	0.06	0.3	0.8	0.8	1	logn, $\mu_V = 3{,}000$, $\sigma_v = 1{,}500$	30k	4
E58	20	0.06	0.3	0.8	0.8	0.8	logn, $\mu_V = 3{,}000$, $\sigma_v = 1{,}500$	30k	4
E59	20	0.06	0.3	0.8	0.8	0.7	logn, $\mu_V = 3{,}000$, $\sigma_v = 1{,}500$	30k	4
E60	20	0.06	0.3	0.8	0.8	0.6	logn, $\mu_V = 3{,}000$, $\sigma_v = 1{,}500$	30k	4
E61	20	0.06	0.3	0.8	0.8	0.4	logn, $\mu_V = 3{,}000$, $\sigma_v = 1{,}500$	30k	4
E62	20	0.06	0.3	0.8	0.8	0.3	logn, $\mu_V = 3{,}000$, $\sigma_v = 1{,}500$	30k	4
E63	20	0.06	0.3	0.8	0.8	0.2	logn, $\mu_V = 3{,}000$, $\sigma_v = 1{,}500$	30k	4
E64	5	0.03	0.3	0.8	0.8	0	dbp, $a = 2$, $b = 9$, $r = 1{,}000$, $V_{min} = 100$, $V_{max} = 10{,}000$	30k	4
E65	5	0.1	0.3	0.8	0.8	0	dbp, $a = 2$, $b = 9$, $r = 1{,}000$, $V_{min} = 100$, $V_{max} = 10{,}000$	30k	4
E66	5	0.2	0.3	0.8	0.8	0	dbp, $a = 2$, $b = 9$, $r = 1{,}000$, $V_{min} = 100$, $V_{max} = 10{,}000$	30k	4
E67	20	0.1	0.3	0.8	0.8	0	dbp, $a = 2$, $b = 9$, $r = 1{,}000$, $V_{min} = 100$, $V_{max} = 10{,}000$	30k	4
E68	20	0.2	0.3	0.8	0.8	0	dbp, $a = 2$, $b = 9$, $r = 1{,}000$, $V_{min} = 100$, $V_{max} = 10{,}000$	30k	4
E69	40	0.1	0.3	0.8	0.8	0	dbp, $a = 2$, $b = 9$, $r = 1{,}000$, $V_{min} = 100$, $V_{max} = 10{,}000$	30k	4
E70	40	0.2	0.3	0.8	0.8	0	dbp, $a = 2$, $b = 9$, $r = 1{,}000$, $V_{min} = 100$, $V_{max} = 10{,}000$	30k	4
E71	20	0.03	0.3	0.8	0.8	0	dbp, $a = 2$, $b = 9$, $r = 1{,}000$, $V_{min} = 100$, $V_{max} = 10{,}000$	30k	4
E72	40	0.03	0.3	0.8	0.8	0	dbp, $a = 2$, $b = 9$, $r = 1{,}000$, $V_{min} = 100$, $V_{max} = 10{,}000$	30k	4
E73	30	0.03	0.3	0.8	0.8	0	dbp, $a = 2$, $b = 9$, $r = 1{,}000$, $V_{min} = 100$, $V_{max} = 10{,}000$	30k	4
E74	30	0.06	0.3	0.8	0.8	0	dbp, $a = 2$, $b = 9$, $r = 1{,}000$, $V_{min} = 100$, $V_{max} = 10{,}000$	30k	4
E75	30	0.1	0.3	0.8	0.8	0	dbp, $a = 2$, $b = 9$, $r = 1{,}000$, $V_{min} = 100$, $V_{max} = 10{,}000$	30k	4
E76	30	0.15	0.3	0.8	0.8	0	dbp, $a = 2$, $b = 9$, $r = 1{,}000$, $V_{min} = 100$, $V_{max} = 10{,}000$	30k	4
E77	30	0.2	0.3	0.8	0.8	0	dbp, $a = 2$, $b = 9$, $r = 1{,}000$, $V_{min} = 100$, $V_{max} = 10{,}000$	30k	4
E78	12	0.03	0.3	0.8	0.8	0	dbp, $a = 2$, $b = 9$, $r = 1{,}000$, $V_{min} = 100$, $V_{max} = 10{,}000$	30k	4
E79	12	0.06	0.3	0.8	0.8	0	dbp, $a = 2$, $b = 9$, $r = 1{,}000$, $V_{min} = 100$, $V_{max} = 10{,}000$	30k	4
E80	12	0.1	0.3	0.8	0.8	0	dbp, $a = 2$, $b = 9$, $r = 1{,}000$, $V_{min} = 100$, $V_{max} = 10{,}000$	30k	4
E81	12	0.15	0.3	0.8	0.8	0	dbp, $a = 2$, $b = 9$, $r = 1{,}000$, $V_{min} = 100$, $V_{max} = 10{,}000$	30k	4

Run ID	Model parameters							NoIt	Runtime
	α	ε	C_{min}	C_{max}	C_{crit}	p_{wet}	Volume distribution		
E82	12	0.2	0.3	0.8	0.8	0	dbp, $a = 2$, $b = 9$, $r = 1,000$, $V_{min} = 100$, $V_{max} = 10,000$	30k	4
E83	5	0.06	0.3	0.8	0.8	0	dbp, $a = 2$, $b = 9$, $r = 1,000$, $V_{min} = 100$, $V_{max} = 10,000$	30k	4
E84	5	0.15	0.3	0.8	0.8	0	dbp, $a = 2$, $b = 9$, $r = 1,000$, $V_{min} = 100$, $V_{max} = 10,000$	30k	4
E85	20	0.15	0.3	0.8	0.8	0	dbp, $a = 2$, $b = 9$, $r = 1,000$, $V_{min} = 100$, $V_{max} = 10,000$	30k	4
E86	40	0.06	0.3	0.8	0.8	0	dbp, $a = 2$, $b = 9$, $r = 1,000$, $V_{min} = 100$, $V_{max} = 10,000$	30k	4
E87	40	0.15	0.3	0.8	0.8	0	dbp, $a = 2$, $b = 9$, $r = 1,000$, $V_{min} = 100$, $V_{max} = 10,000$	30k	4
E88	20	0.06	0.3	0.8	0.8	0	dbp, $a = 2$, $b = 9$, $r = 1,000$, $V_{min} = 100$, $V_{max} = 10,000$	30k	4
E89	20	0.03	0.3	0.8	0.8	0	logn, $\mu_V = 3,000$, $\sigma_v = 3,000$	40k	5

D.3 Results from validation experiments

Mean radial fan slope M_{sl} and standard deviation of radial fan slope S_{sl} for model validation experiments (Section 5.3). Events: Time when slope measurement was taken, usually when fan volume growth rate, averaged over 100 events, reached zero for the first time. * In these runs average fan volume growth did not reach zero. ** Slope measurement after 30,000 events.

Run ID	M_{sl} [°]	S_{sl} [°]	NoIt	Run ID	M_{sl} [°]	S_{sl} [°]	NoIt
E1	2.36	0.03	4,400	E18*	5.70	0.07	40,000
E2	2.19	0.10	2,800	E19	1.70	0.03	7,662
E3	2.00	0.07	3,300	E20	2.40	0.06	11,146
E4	1.73	0.07	3,500	E21	2.85	0.04	10,992
E5	0.46	0.13	11,900	E22*	6.49	0.13	40,000
E6	0.64	0.18	16,100	E35**	2.96	0.12	30,000
E7	0.84	0.11	7,195	E37**	2.97	0.17	30,000
E8	1.07	0.13	10,749	E38**	2.67	0.14	30,000
E9	1.27	0.12	11,421	E39**	2.40	0.11	30,000
E10	1.69	0.10	13,081	E57**	2.51	0.15	30,000
E11	0.32	0.12	2,908	E58**	2.53	0.11	30,000
E12	0.99	0.12	6,848	E59**	2.47	0.14	30,000
E13	1.36	0.08	8,546	E60**	2.69	0.18	30,000
E14*	5.41	0.34	20,000	E61**	2.81	0.16	30,000
E15	1.74	0.05	9,443	E62**	2.85	0.17	30,000
E16	2.03	0.06	8,807	E63**	2.86	0.13	30,000
E17	2.58	0.06	11,141				

D.4 Influence of α and ε on fan slope

In Appendix Figure D.1 I show the relationship between fan slope after 30,000 events and different settings for α and ε (Appendix Table D.1). In each of the sub-panels I show results from 10 experiments were I kept α constant and varied ε (Appendix Figure D.1A) and vice versa (Appendix Figure D.1B). ε sets the flow cross section area and the maximum rate at which a flow can deposit material as it travels across the fan, flows with high ε can be thought of having a high flow front (Equation 5.2). α is the parameter responsible for the spreading of the flow and hence the average deposit thickness, where larger values of α result in wider spreading and thiner deposits (Equation 5.3).

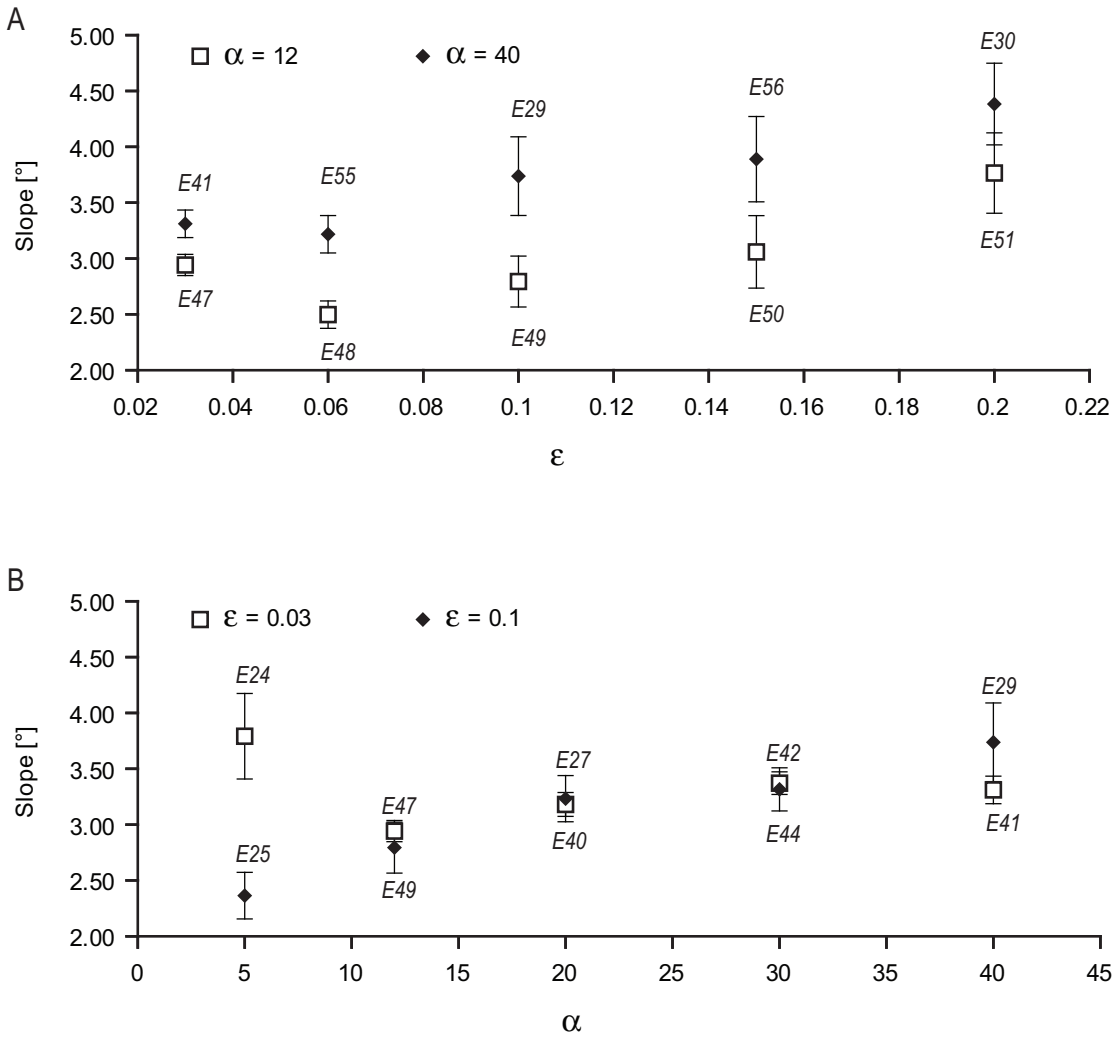

Figure D.1: *Influence of* α *and* ε *on fan slope* ± *one standard deviation. Labels in italics next to symbols indicate model run (Appendix, Table D.1). A: Fan slope as function of* ε *for fixed* α*. B: Fan slope as function of* α *for fixed* ε*.*

For fixed α I find a small increase in fan slope of about 1° when increasing ε from 0.03 to 0.2, and for higher α values the resulting fan slope is also between 0.5° and 1° higher (Appendix Figure D.1A). It is important to note that the reported range of ε in the literature only spans the interval 0.03 to 0.11 (Berti and Simoni, 2007), and over this range the influence of ε is less clear. For fixed ε I find no consistent change in resulting fan slope when varying α between 5 and 40 (Appendix Figure D.1B). When keeping $\varepsilon = 0.03$ fixed, marking the lower end of reported values for this parameter (Berti and Simoni, 2007), I find a weak trend to lower fan slopes with increasing α; for $\varepsilon = 0.1$, at the upper end of the reported range (Berti and Simoni, 2007), I find the opposite. In summary I note that the influence of α and ε on fan slope on its own is weak with a trend to higher slopes for combinations high α and ε, but partly inconsistent (run E24, Figure D.1).

Appendix E

Content of data DVD

The DVD contains data and program code for Chapters 2, 4 and 5, which I describe below. The path to each directory is given, followed by an itemized list of the content.

```
/SCHUERCH2011
├── /Chapter2
│   ├── ReportCosmoSamplingIllgraben.pdf ...  Description of sample locations,
│   │                                         shielding and block geometry;
│   │                                         photographs of each sampled boulder
│   │                                         are included.
│   ├── /BoulderLocations
│   │   ├── boulder.shp ...  ESRI shape file with locations of all candidate boulders.
│   │   ├── samp_locations.csv ...  Text file with coordinates of sample locations
│   │   │                           in swiss national coordinates.
│   │   ├── samp_loactions_wgs1984.csv ...  Text file with coordinates of
│   │   │                                   sample locations in WGS1984 lat-lon
│   │   │                                   coordinates.
│   │   └── samploc_elv.shp ...  ESRI shape file with sample locations and
│   │                            elevations from the DEM see text for details.
│   └── /LobeFieldmap
│       └── lobe_fieldmap.shp ...  ESRI shape file with mapped lobe boundaries.
├── /Chapter4
│   ├── README.txt ...  text file with information about file format and elevation
│   │                   datum of DEMs obtained from terrestrial laser scanning.
│   │                   Information on which DEMs relate to which debris flow
│   │                   events listed in Appendix C, Table C.1 is included.
│   └── e0*_asc.grd ...  six DEMs in Surfer ASCII grid format, see README.txt.
└── /Chapter5
    ├── ProbDFstruct.mat ...  MATLAB data file containing the probability
    │                         distribution function of elevation change vs.  flow
    │                         depth (based on data from Chapter 4) read by the
    │                         model to inform erosion and deposition behaviour.
    ├── dfmodel2d_v4_3.exe ...  Windows executable of the model, command line
    │                           syntax see Appendix D.1.1.
    ├── fan.mat ...  Standard model space as described in main text.
    ├── /MatlabRoutines ...  20 MATLAB routines, description and synopsis in file
    │                        header of each *.m file.
    └── /ModelRuns
        ├── /E01
        ├── ...
        └── /E89
            ├── params.txt ...  Parameter file for model run E89.
            ├── dumpresults.mat ...  Summary outputfile for model run E89.
            ├── *age.mat ...  Final map of surface age.
            ├── *dem.mat ...  Final topography.
            └── *.avi ...  Animations of topographic and surface age evolution,
                           only for model runs E23, E25, E38 and E40.
```